UNIVERSITÀ
DEGLI STUDI
DI BRESCIA

CORSO DI DOTTORATO IN

Technology for Health

CICLO XXXVI

ING-IND/22 Scienza e Tecnologia dei Materiali

DEVELOPMENT OF TUNABLE CORE-SHELL COMPOSITE SCAFFOLDS FOR TISSUE ENGINEERING

Primo supervisore: Prof. Luciana Sartore
Co-supervisore: Prof. Stefano Pandini
Tutor: Prof. Francesco Baldi

Dottoranda:

Chiara Pasini

Anno Accademico 2023/2024

Sintesi della tesi di dottorato

Gli *scaffold* per l'ingegneria tissutale sono tenuti a rispondere a un'impegnativa combinazione di requisiti fisici, meccanici e biologici, che orientano la ricerca verso lo sviluppo di nuovi materiali ibridi e l'utilizzo di processi di biofabbricazione non convenzionali. Infatti, i sistemi compositi permettono di coniugare i vantaggi dei materiali che li compongono, mentre tecniche avanzate come la fabbricazione additiva (*additive manufacturing*) e l'elettrofilatura (*electrospinning*) sono in grado di produrre strutture complesse fibrose e ad architettura controllata per affrontare la ricostruzione di specifici tessuti biologici.

Questo studio introduce innovativi *scaffold* bioriassorbibili che presentano una struttura *core-shell*, in cui un nucleo (*core*) polimerico stampato in 3D ha lo scopo di garantire un supporto meccanico temporaneo, mentre un guscio (*shell*) di idrogelo bioattivo è incorporato per offrire un miglior ambiente per l'adesione e la proliferazione delle cellule. Grazie alla versatilità della progettazione *core-shell* e della fabbricazione additiva, le proprietà dello *scaffold* possono essere personalizzate attraverso un'opportuna progettazione della struttura del *core* stampato in 3D e del rapporto *core/shell*, in base all'applicazione designata e all'anatomia del paziente. Particolare attenzione è dedicata al caso della rigenerazione del tessuto osseo, qui affrontato sviluppando *scaffold core-shell* in cui una rigida struttura reticolare (*lattice*) di acido polilattico (PLA) è innestata con un idrogelo osteogenico a base di gelatina e chitosano.

Il primo capitolo fornisce un'introduzione ai biomateriali e alle tecniche di biofabbricazione utilizzate nel campo dell'ingegneria tissutale, con particolare enfasi sulla rigenerazione dell'osso e della cartilagine, sulla modulazione e modellizzazione delle proprietà degli *scaffold* e su innovativi compositi polimerici intelligenti.

In seguito, viene descritto in dettaglio il lavoro sperimentale sugli *scaffold* compositi *core-shell*, esplorando inizialmente la possibilità di modulare le loro proprietà meccaniche e il contenuto di idrogelo considerando un ampio insieme di variabili (Capitolo 2), per poi concentrarsi sulla possibilità di affrontare la rigenerazione dell'osso con *scaffold* di PLA-idrogelo, che sono stati sottoposti a esperimenti di degradazione idrolitica e *in vitro* (Capitolo 3) e infine customizzati ai fini di studi *in vivo* in un modello animale di coniglio (Capitolo 4). Questi test preclinici mirano a studiare le potenziali applicazioni traslazionali nella medicina rigenerativa dell'osso.

Oltre a questi studi sperimentali, vengono presentati approcci basati su equazioni analitiche, modelli semi-empirici, reti neurali artificiali e simulazioni numeriche come strumenti per la previsione delle proprietà meccaniche delle strutture *core* degli *scaffold* (Capitolo 5).

Infine, viene presentato un nuovo metodo di fabbricazione per produrre compositi polimerici modulabili in grado di cambiare forma in modo reversibile, con la prospettiva di future applicazioni per gli *scaffold*, come il rilascio intelligente di farmaci o la stimolazione meccanica dinamica di colture cellulari (Capitolo 6).

Contents

Abstract

Scaffolds for tissue engineering are expected to respond to a challenging combination of physical, mechanical and biological requirements, guiding the research towards the development of novel hybrid materials and the use of unconventional biofabrication processes. In fact, composite systems can bring together the advantages of their constituent materials, while advanced techniques such as additive manufacturing and electrospinning can produce complex architected and fibrous structures to address the reconstruction of specific biological tissues.

This study introduces innovative bioresorbable scaffolds presenting a core-shell structure, in which a 3D-printed polymeric core is meant to ensure temporary mechanical support, while a bioactive hydrogel shell is incorporated to provide a better environment for cell adhesion and proliferation. Thanks to the versatility of the core-shell design and of additive manufacturing, the scaffold properties can be tailored by properly designing the 3D-printed core structure and the core/shell ratio, based on the target application and on patient anatomy. Special attention is dedicated to the case of bone tissue regeneration, here addressed by developing core-shell scaffolds in which a stiff poly(lactic acid) (PLA) lattice structure is grafted with an osteogenic gelatin-chitosan hydrogel.

The first chapter provides an introduction to biomaterials and biofabrication techniques employed in the field of tissue engineering, with particular focus on bone and cartilage regeneration, on scaffold property tunability and modeling, and on innovative smart polymeric composites.

Thereafter, the experimental work on core-shell composite scaffolds is described in detail, first exploring the tunability of their mechanical properties and hydrogel content by considering a vast set of variables (Chapter 2), and then focusing on the

possibility to address bone regeneration with PLA-hydrogel scaffolds, which were subjected to hydrolytic degradation and *in vitro* experiments (Chapter 3) and finally tailored for *in vivo* studies in a rabbit animal model (Chapter 4). These preclinical tests aim at investigating potential translational applications in bone regenerative medicine.

In addition to these experimental studies, approaches based on analytical equations, semi-empirical models, artificial neural networks and numerical simulations are presented as tools for predicting the mechanical properties of scaffold core structures (Chapter 5).

Finally, a novel fabrication method to produce tunable polymeric composites capable of reversible shapeshifting is reported, envisioning future scaffold applications such as smart drug release or dynamic mechanical stimulation of cell cultures (Chapter 6).

1. Introduction

Scaffold-based tissue engineering is a valid alternative to autologous and allogeneic transplants, allowing to replace and regenerate damaged or diseased tissues. Scaffolds are biomaterial-based platforms that should mimic the functionality of native extracellular matrix (ECM), both acting as physical support for cell attachment and promoting cell growth and new ECM deposition [1].

Spontaneous tissue regeneration is typically inefficient, except for gut epithelium, cornea, skin and liver, therefore many applications of scaffolds were explored, including interstitial, connective, vascular, nerve, visceral and musculoskeletal tissue engineering [2]. Depending on the target tissue, the choice of the scaffold material and fabrication process demands careful consideration of several requirements. Since it is often difficult to match all these needs with a single biomaterial, the research is going in the direction of multifunctional hybrid materials.

This chapter provides a general introduction to scaffold requirements, manufacturing techniques and main material classes (paragraph 1.1), followed by a more detailed discussion regarding bone and cartilage tissue engineering, with special focus on the use of composite biomaterials (paragraph 1.2). Further insights concern advanced scaffolds with tailorable shapes and functions (paragraph 1.3).

1.1. Scaffold requirements, fabrication and materials

1.1.1. Scaffold requirements

In order to efficiently substitute the ECM during tissue regeneration, scaffolds have to fulfil several requirements [3], listed hereafter.

(i) Biocompatibility: it is intended as "the ability of a material to perform with an appropriate host response in a specific application" (D. F. Williams, 1986 [4]); in particular, scaffolds must be non-cytotoxic and avoid any inflammatory response or adverse interaction with the hosting tissue.

(ii) Biodegradability: though non-biodegradable porous implants are still largely considered in some fields such as orthopedics [5], the ultimate goal is the full replacement of scaffolds with new functional tissue; ideally, bioresorption should occur at the same rate as new tissue formation, releasing non-toxic and easily removable products.

(iii) Bioactivity: scaffolds should not be bioinert but actively promote tissue regeneration, therefore they require adequate chemical and topographical features; indeed, properties such as surface charge, wettability, free energy and roughness can greatly influence cell adhesion, proliferation and differentiation.

(iv) Open interconnected porous structure: interconnected macro-pores with proper size and high surface area-to-volume are needed to ensure cell growth and migration, while additional micro-pores can improve the diffusion of oxygen, nutrients, and metabolism products.

(v) Mechanical properties close to the native tissue: providing adequate stiffness and strength is not only needed for temporary load bearing, but also because biomimetic mechanical properties have been demonstrated to stimulate proper cell differentiation [6,7].

(vi) Safe and convenient fabrication technique: a simple method to obtain a controlled porous structure should be employed, possibly avoiding the use of substances that could harm the cells, such as organic solvents.

1.1.2. Scaffold fabrication technologies

A variety of manufacturing technologies can be used to produce porous scaffolds. A major distinction can be drawn between more conventional processes using different kinds of porogens and advanced techniques such as electrospinning and additive manufacturing [8].

Conventional methods employ water-soluble particles, foaming agents or solvents as porogens, *i.e.* substances that are dispersed throughout the scaffold material and then removed, leaving a network of interconnected pores. Many of these techniques (*e.g.*, solvent casting/particulate leaching, gas foaming, thermally induced phase separation – see Figure 1.1a-c) involve the use of organic solvents or foaming agents, which would be better to avoid so to reduce the risk of toxicity. A safer process is melt molding/particulate leaching (Figure 1.1a), though it may be difficult to remove the particles at the center of the scaffold and obtain a uniform porosity. Another one is freeze-drying (Figure 1.1d), in which only water is used as solvent: the pores are created in a frozen aqueous solution by sublimation of ice crystals under vacuum, and their size can be adjusted by controlling the freezing temperature and the polymer content. [8,9]

A completely different fabrication approach consists of electrospinning (Figure 1.1e), which uses electrostatic forces to produce micro- and nano-fibers. The obtained fibrous structures are porous and flexible and have great potential to mimic native ECM and influence cellular behavior. The high tunability of process parameter and recent advances in electrospinning setup further increased the control over scaffold architecture, mechanical properties and bioactivity. Viceversa, it is still necessary to improve reproducibility and cellular infiltration, and achieving clinically relevant dimensions is still a challenge. [10]

Finally, a vast group of advanced techniques enabling the production of 3D scaffolds is based on additive manufacturing (AM) processes, which provide unparalleled spatial control over both the internal structure and the external shape

of the scaffolds. These processes have in common a layer-by-layer realization of the final object, according to computer-aided design (CAD) or computed tomography (CT) data. Alongside some common AM techniques (Figure 1.1f), the field of tissue engineering has favored the evolution of alternative processes such as melt electrowriting (Figure 1.1g), with additional application of an electric potential, or bioprinting (Figure 1.1h), with simultaneous deposition of living cells.

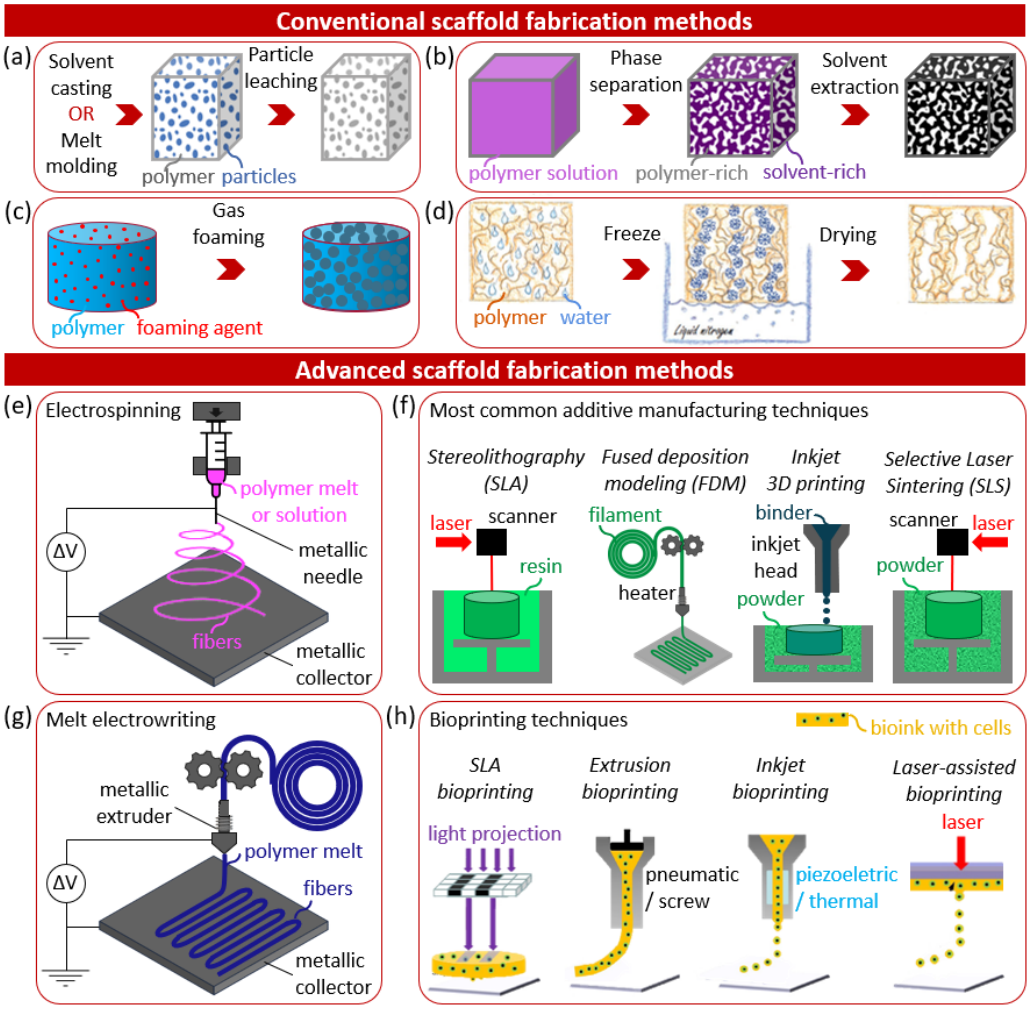

Figure 1.1. Scheme of the main conventional and advanced fabrication techniques employed in the realization of scaffolds; bioprinting techniques (h) have been adapted from [11].

Each fabrication technique has different strengths and drawbacks. For example, inkjet 3D printing can process a variety of powders (made of metals, ceramics, polymers, or composites) by selective deposition of a binder, but typically produces objects with poor resolution and mechanical properties. Conversely, stereolithography (SLA) has excellent resolution but can only be applied to photocrosslinkable resins, few of which have the necessary biocompatibility and biodegradability. Selective laser sintering (SLS) also offers a limited choice of materials, consisting of expensive metallic or polymer powders resistant to the high processing temperatures; moreover, though enabling manufacturing of very complex geometries without support structures, it produces rather rough surfaces. Similarly, high temperatures and limited resolution are issues in fused deposition modeling (FDM), but in this case the raw materials are much cheaper thermoplastic filaments, many of which exhibit good biocompatibility, biodegradability and mechanical strength. [11–13]

An innovative technique that is receiving special attention in tissue engineering is melt electrowriting (MEW, Figure 1.1g), bridging the gap between electrospinning of molten polymers and direct-write AM processes; with respect to melt electrospinning, the electrified jet is stable and a precise layer-by-layer material deposition is obtained [14–16]. As a result, precise control over fiber arrangement and increased scaffold volumes are achieved, with potential applications especially in soft tissue regeneration, where high compliance and flexibility are required [17]. Current literature mainly reports MEW of poly(ε-caprolactone), but a growing number of papers is demonstrating the possibility to process other polymers [18], including thermoplastic elastomers [19–21].

The possibility of including living cells directly during AM of scaffolds (*i.e.* bioprinting, Figure 1.1h) is also particularly attractive. The main advantage is the achievement of a controlled cell distribution, for instance having a specific alignment or combining regions with different cell types. However, maintaining cells alive can

be challenging and is not compatible with the use of high temperatures. For this reason, alongside SLA bioprinting and inkjet-based bioprinting, *ad hoc* extrusion-based and laser-assisted techniques have been developed to avoid or limit heat-induced cell damages. [11,12]

1.1.3. Scaffold materials

A proper material selection is essential for the creation of scaffolds having suitable properties for tissue engineering applications. The biomaterials can be chosen from different classes, listed in Table 1.1, which reports some examples and the main advantages and disadvantages for each class [3,12,22].

Table 1.1. Main classes of biomaterials: examples, advantages and disadvantages for the production of scaffolds.

Class	Examples	Advantages	Disadvantages
Metals	biodegradable metals (magnesium and alloys), non-biodegradable metals (titanium and alloys), …	biocompatibility, high strength and stiffness	too fast biodegradation accumulating H or no biodegradation
Ceramics	hydroxyapatite (HA), tri-calcium phosphate (TCP), bioglass (BG)...	high stiffness, biocompatibility and bioactivity	brittleness, difficulty of shaping
Natural polymers	proteins (collagen, elastin, silk), polysaccharides (cellulose, chitosan, alginate, hyaluronic acid), decellularized ECMs...	biocompatibility and bioactivity	poor mechanical properties, low reproducibility
Synthetic polymers	polyesters (PLA, PGA, PLGA, PCL), polyether esters (PEG, PBT), polyurethanes...	processability, versatility, better control over shape and properties	lacking bioactivity
Hybrids/ composites	synthetic polymers + natural polymers, polymers + ceramics...	combining the advantages of different material classes, property tunability	more complex design/realization

Metals are typically considered for bone tissue engineering because of their high mechanical properties. In particular, titanium-based scaffolds have excellent biocompatibility and have been proposed for load-bearing applications, but they are not biodegradable; conversely, biodegradable metals such as magnesium degrade too fast and rise hydrogen accumulation issues.

Ceramic biomaterials are also most commonly employed in scaffolds addressing the regeneration of mineralized tissues. In fact, calcium phosphate-based ceramics have stiffness and composition similar to the mineral component of bone; on the negative side, their main weaknesses are brittleness and shaping difficulties.

Polymers are the most variegated class of scaffold materials, allowing to address the regeneration of a variety of tissues. They can be classified as natural polymers, including several proteins and polysaccharides, or synthetic polymers, usually consisting of polyester, polyether ester or polyurethanes. Natural polymers are especially appreciated for the biocompatibility and bioactivity but display poor mechanical properties and reproducibility, whereas synthetic polymers lack bioactivity but offer improved processability and control over their degradation rate, microstructure, and mechanical properties.

Among biopolymers, hydrogels have gained extraordinary popularity in the field of tissue engineering. Hydrogels are crosslinked polymeric networks exhibiting high water content and permeability, absorbing amounts of water comparable to biological tissues and facilitating the exchange of oxygen, nutrients, and metabolites. They can have natural or synthetic origin and are particularly valued for their biocompatibility, biodegradability, fabrication versatility, tunable properties, and excellent physicochemical mimicry of the ECM; their mechanical properties are rather low, which better match those of soft tissues. [23,24]

Considering the advantages and disadvantages of the various classes of biomaterials, and the numerous requirements of scaffolds (paragraph 1.1.1), it is often difficult to identify a suitable material for this kind of application. Therefore,

a growing research trend is that developing of hybrid scaffolds composed of two or more materials, usually belonging to different classes, in order to better combine their advantageous characteristics [2,9].

For instance, three main types of reinforcement have been reported for hydrogels, according to their expected main biological effect: (i) structural reinforcement, improving mechanical properties (e.g. interpenetrating networks, fibres, particles, stiff porous cores); (ii) spatial patterning and guidance, influencing directional migration and alignment of cells (e.g. aligned nanofibers, magnetic particles, spatial positioning of bioactive cues); (iii) stimuli responsiveness, for instance providing the scaffolds with electrical, optical or thermal conductivity (e.g. conductive carbon nanotubes, graphene oxide) [25].

Moreover, scaffolds are usually combined with cells, laying down new ECM, and biomolecules such as growth factors and morphogenetic signals, enhancing cell proliferation and differentiation [8]. In particular, mesenchymal stromal cells (MSCs) are the most frequently used stem cells in regenerative medicine approaches thanks to their immunomodulation, tissue regeneration, and protective functions [26]. MSCs can be derived from different sources, such as bone marrow, adipose tissue, and oral tissues, and they can differentiate into various mesodermal cells, such as bone and cartilage lineages [27]. To consider these cells in different clinical situations, MSCs must fulfill the definition criteria requested by the International Society for Cellular Therapy (ISCT) [28].

1.2. Scaffolds for bone and cartilage tissue regeneration

1.2.1. Bone and cartilage tissue regeneration treatments

Regeneration of osseous and cartilaginous tissue has gained particular attention, since the regenerative capability of cartilage is very low and that of bone is limited when extensive injuries or bone diseases are involved [2].

Bone morbidities represent a serious medical burden and heavily affect the quality of life. Though the bone has inherent regeneration capability, there are several clinical conditions that need regeneration treatments, such as severe traumas, bone infections, osteoporosis or sarcoma resection resulting in large bone defects. Autografts harvested from the patients are considered the clinical gold standard to treat these defects, however they are associated to limited availability, donor site pain and possibility of donor site morbidity. Allografts are more available, but they can cause immune rejection or pathogen transmission from the donor. Therefore, the use of biocompatible scaffolds and artificial bone substitutes is a promising alternative strategy. Moreover, in order to prevent fibrous tissue invasion of the defect and promote the revascularisation of bone grafts, a temporary cement spacer can be inserted during the first weeks before implantation, inducing formation of a vascularised membrane (induced membrane technique) [29].

As regards cartilage, its regeneration is even more complicated due to the absence of nerves and vascularisation. Damages can derive from traumas, an unhealthy style or various diseases (e.g. obesity, osteoporosis, osteochondritis dissecans, juvenile idiopathic arthritis, osteoarthritis). If conservative treatments such as rehabilitation, dieting or drug administration are insufficient, surgical intervention is needed. A safe, cheap and minimally invasive method is the microfracture technique, consisting in perforations of the subchondral bone aimed at gathering blood to promote tissue regeneration, but instead of promoting the formation of healthy hyaline cartilage, it produces fibrocartilage, more susceptible to further damage. Cell-based approaches (scaffolds seeded with autologous chondrocytes or, more recently, with

mesenchymal stem cells, MSCs, and growth factors) are considered more promising, though current treatments still cannot recreate native hyaline cartilage [9].

1.2.2. Biomaterials for bone and cartilage tissue engineering

Prosthesis for the substitution of bones and joints are typically produced with biocompatible metals and ceramics that provide excellent physical support due to their mechanical properties, but do not promote tissue regeneration, being bioinert materials. Therefore, other biomaterials have been investigated in bone and cartilage tissue engineering, aiming at producing scaffolds that biodegrade as new tissue grows. At present, commercially available materials for bone reconstruction are mostly calcium-based cements, which are easily replaced by bone tissue because their composition is close to that of the mineral component of ECM; however, their main purpose is usually to fill defects and they are still not optimized to promote bone regeneration [29]. As for cartilage, commercial scaffolds are mostly made of collagen (i.e. the main ECM component), but they quickly lose their structure in aquatic environment, transforming in a gel-like form that cannot mechanically support the cells during regeneration; as a result, non-valuable fibrous cartilage is obtained [9]. With these premises, many scientific studies have been working on new scaffolds with higher bioactivity, composed by biomaterials belonging to the following three classes [9,29,30].

(i) Calcium-based ceramics (*e.g.*, tricalcium phosphate, TCP; hydroxyapatite, HA; bioactive glasses, BGs; …): they are used for their bioactivity, since they mimic the mineral component of bone ECM, mainly composed of natural hydroxyapatite; particularly, they have been used in scaffolds for bone and osteochondral tissue; on the downside, bioceramics are brittle, and bioresorption of TCP and BGs may occur too fast.

(ii) Natural polymers (*e.g.*, collagen; gelatine; elastin; fibrin; chondroitin sulphate; silk fibroin; hyaluronic acid; chitosan; alginate; agarose; …): they exhibit excellent biocompatibility and bioactivity, being or resembling typical polysaccharides and

proteins of the ECM; however, their success is limited by their poor mechanical properties and degradation control, as well as low resistance to some process parameters such as high temperatures.

(iii) Synthetic polymers (*e.g.*, poly(lactic acid), PLA; poly(glycolic acid), PGA; poly(ε-caprolactone), PCL; poly(ethylene glycol), PEG; polyurethanes, PUs; …): these polymers, together with their blends and copolymers, are characterized by good processability and better control of their mechanical and degradation properties compared to natural polymers; on the other hand, they present inferior cell adhesion and bioactivity and their degradation products are usually acidic.

Among the proposed biomaterials, hydrogels are considered to be favorite candidates also in view of cartilage and bone regeneration, due to their ability to closely mimic native ECM features, good fabrication versatility, tunable properties, and water absorption comparable to biological tissues [31,32]. However, improving their low strength and stiffness is particularly important in the case of cartilage and bone tissue engineering, both for mechanical reasons (temporary mechanical support should be provided until new tissue formation, especially in load bearing applications) and for regenerative purposes (biomimetic scaffolds with mechanical behavior close to the native tissue are believed to affect stem cells differentiation and promote new tissue growth) [7,33,34].

As a consequence, stiffer synthetic biopolymers have been explored with much interest, above all polyesters such as polylactic acid (PLA) and poly(ε-caprolactone) (PCL), which are already commercially available for clinical applications such as resorbable sutures and fixation devices [35–38]. Their good mechanical properties and slow resorption rate are particularly interesting for targeting mineralized tissues. For example, rigid porous scaffolds for bone tissue have been produced by Sartore *et al.* [39–41] with different thermoplastic PLA-based blends. These scaffolds were endowed with the necessary porous structure by mixing the blends with superabsorbent particles and by subsequent water immersion, leading the particles

to swell and leach from the matrix; in this way, interconnected porosity was achieved safely, avoiding solvents. The obtained materials exhibited morphology and stiffness comparable to those of bones, and allowed good adhesion and proliferation of fibroblasts, especially when PLA was combined with PCL. Still, while being promising in terms of osteoconductivity, polyesters do not exhibit specific bioactive properties to stimulate osteogenic differentiation of cells (osteoinductivity) [12].

1.2.3. Hybrid scaffolds for bone and cartilage tissue engineering

Understanding that all biomaterials, even the most promising ones, present some shortcomings, led to the development of composite scaffolds for bone and cartilage tissue engineering. Combining multiple biomaterials not only enables the so-called "one-matches-all concept", meaning that a small group of materials can be applied to match the properties of many different tissues [2], but is particularly targeted in the case of bone ECM, which consists of a hybrid polymer nanostructure, comprising various biopolymers and hydroxyapatite nanocrystals.

Many examples of composite scaffolds for bone and cartilage tissues are based either on the enhancement of the bioactivity of stiff synthetic polyesters, thanks to the combination with bioceramics and/or hydrogels, or on the use of reinforced hybrid hydrogels; various hybridization solutions have been employed, including surface-modified polymers [42], interpenetrating/semi-interpenetrating networks [43], embedded particles/nanoparticles [44–47], incorporation of fibrous meshes [48,49], co-axial composite fibers [50–53], 3D-printed structures made of co-axial composite struts [54–56], and other 3D-printed composite systems [57–59].

1.2.3.1. Examples of composite scaffolds for bone and cartilage obtained by combining different biomaterials and fabrication techniques

Many production technologies have been employed to create hybrid structures, including but not limited to conventional freeze-drying method and advanced electrospinning and 3D printing techniques. More detailed examples are provided heareafter.

Some examples of freeze-dried scaffolds were prepared and characterized by Haaparanta *et al.*, who incorporated a mesh of melt-spun PLA fibers into collagen and/or chitosan before freeze-drying. While collagen and chitosan were chosen for their ability to closely mimic the ECM and absorb high amounts of water, PLA improved the scaffold stiffness and mechanical stability. Especially chitosan/PLA systems appeared potentially suitable for cartilage tissue engineering, exhibiting superior water uptake and penetration of chondrocytes [48]. The freeze-drying technique has also been used to produce a commercial cartilage scaffold, Chondrotissue®, composed of PGA and hyaluronic acid. Preclinical trials on sheep demonstrated that the PGA skeleton allowed early loading of treated articular defects, while hyaluronic acid supported chondrogenic differentiation of MSCs [60]. In human patients Chondrotissue® was applied after microfracture treatment, leading to complete defect filling after 8 to 12 months in condylar articular cartilage of the knee [49].

Sartore *et al.* developed hybrid scaffolds by using both freeze-drying and particle swelling and leaching. They started from the development of hybrid hydrogels, since these materials allow combining the advantages of synthetic and natural components [61]. In particular, they studied gelatin-based scaffolds, strengthened by crosslinking with poly(ethylene glycol) diglycidyl ether (PEGDGE), and with bioactivity improved by adding natural polysaccharides such as chitosan or dextran, which were found to induce osteogenic or chondrogenic differentiation of human MSCs [62–67]. Gelatin-chitosan hydrogels were also efficiently sterilizable [68] and displayed faster and higher stress relaxation, which can improve cell spreading, proliferation and differentiation [69]. Their soft mechanical properties (stiffness lower than 1 MPa) appear more suitable for cartilage than for bone tissue, but non-load bearing applications may be still considered in light of their good osteogenic performance.

Aiming at combining the bioactive properties of their hybrid hydrogels [62] with the good mechanical properties and biomimetic morphology of their PLA-PCL

porous scaffolds [40] (obtained by superabsorbent particle swelling and leaching, paragraph 1.2.2), Sartore *et al.* created scaffolds for bone tissue engineering by grafting a PLA-PCL porous core with gelatin-chitosan hydrogel [70,71] (Figure 1.2). The hydrogel homogeneously covered both the outer surface and the inner voids of PLA-PCL with a thin bioactive layer (ca. 3 wt%), leading to promising results in terms of vitality, proliferation and osteogenic differentiation of human MSCs.

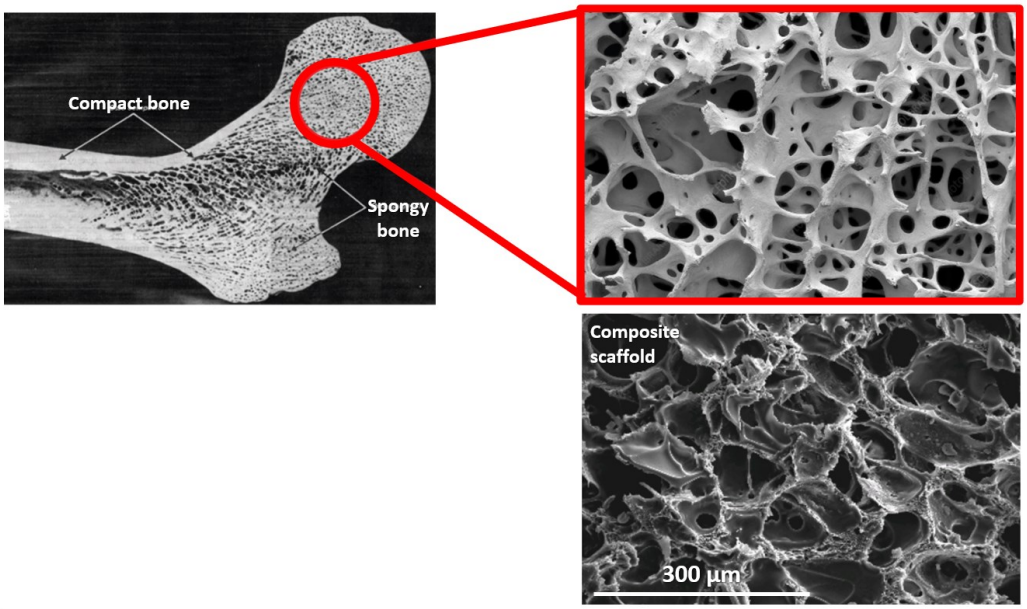

Figure 1.2. Similarity between the porous interconnected structure of bone tissue and a composite scaffold with PLA-PCL core and gelatin-chitosan hydrogel shell (SEM micrograph).

Other composite scaffolds were produced thanks to electrospinning techniques. Nanofibrous scaffolds are appreciated for their high specific surface area, promoting cell adhesion and proliferation, but such thin fibres have limitations for manufacturing of 3D structures and if pores are too small they may hinder cell migration inside the scaffold. Therefore, Beom *et al.* deposited conventionally electrospun silk fibroin nanofibers on a microfibrous PCL skeleton obtained by melt-electrospinning, producing highly porous 3D scaffolds with the ability to promote both cell proliferation and infiltration. These hybrids appeared promising

for bone tissue engineering, as demonstrated by new bone formation and angiogenesis in rabbit calvarial defects [53].

In other studies, natural and synthetic components were directly combined by co-electrospinning. For instance, Sharifi *et al.* employed co-electrospinning of a synthetic polymer, PCL, and a solution containing two natural polymers, gelatin and chondroitin sulphate, obtaining nanofibrous systems capable of supporting MSC proliferation and chondrogenic differentiation [52].

With the aim of controlling scaffold porous microstructure, 3D printing techniques were also extensively used, especially FDM of polyesters. For example, Dong *et al.* printed a PCL porous scaffold by FDM and impregnated it with a chitosan solution. PCL degraded slowly, ensuring long-term mechanical support, with compressive strength similar to the cancellous bone, whereas chitosan improved biocompatibility and had a faster degradation rate, supporting new bone tissue formation after subcutaneous implantation in a nude mice model [58].

By means of multiple-tool bioprinting it was also possible to simultaneously print different materials, as shown by Daly *et al.* for PCL and an alginate bioink containing MSCs and specific adhesion peptides. The result was an anatomically accurate, mechanically reinforced, hypertrophic cartilage template that mimicked the geometry of a vertebral body. This bone precursor was implanted in nude mice and successfully developed over time into a vascularized bone organ, containing trabecular-like and marrow-like tissue [59].

1.3. Advanced scaffolds with tailorable shapes and functions

1.3.1. Advanced manufacturing approaches to scaffold realization

1.3.1.1. Examples of advanced composite scaffolds for multiple-tissue defects, electroactive stimulation, and drug/biomolecules delivery

The realization of hybrid structures combining different materials becomes even more necessary when addressing simultaneous regeneration of different types of tissues, or when the inclusion of specific bioactive cues (electroactive materials, drugs, biomolecules) is desired. Some examples of advanced composite scaffolds developed for these applications are here provided.

In design of a composite scaffold for bone regeneration, Wang *et al.* were inspired by the natural bone architecture, combining a strong dense cortical shell and a porous trabecular core. Their medical device contained a PLA/PEG/PLA stereocomplex hydrogel within a gelatin shell, which was strengthened by crosslinking and hydroxyapatite addition, and its evaluation in vivo in rat calvarial defects provided encouraging results [72]. Other bilayered scaffolds were proposed for osteochondral tissue engineering, whose aim is to repair both articular cartilage and the underlying subchondral bone with a single construct. Pure naturally-derived polymers were usually employed in the cartilage-like layer (e.g. silk fibroin or gellan gum), whereas in the bone-like layer the polymers were reinforced with inorganic particles (e.g. TCP or HA), that promoted the mineralization process. By seeding chondrocytes and osteoblasts separately in the corresponding layers, markers of chondrogenic and osteogenic activity were observed as expected [73,74].

Other advanced scaffolds incorporated electroactive materials such as graphene [75] and oligopyrrole [76], so to achieve the possibility of exploiting electrical stimulation for the promotion of bone tissue regeneration. Moreover, composite scaffolds, often created with a core-shell spherical or fibrous structure, have been enhanced with drug/biomolecule delivery functionalities [77]. For example, electrospun gelatin-PCL fibers have been produced by co-axial electrospinning for

controlled release of specific proteins; both mechanical properties and release rate were controlled by adjusting gelatin/PCL ratio and the degree of crosslinking [78].

1.3.1.2. Additive manufacturing and modeling approaches for tailoring of scaffold structure, with focus on bone tissue engineering

Recent developments in tissue engineering are driven by additive manufacturing (AM) technologies, which are deemed strategic for reproducing anatomical shapes and for tailoring the scaffold internal structure to customize their properties [57,79–82]. The influence of geometrical parameters on scaffold properties was studied for few geometrical configurations, usually adopting a basic 0°/90° lay-up and varying the spacing between filaments along the printing direction (xy) [83,84] or designing lattice structures with simple cubic cells of variable size [85,86], but some alternative lattice designs have recently begun to be explored [87,88]. Moreover, some composite scaffolds for bone tissue repair have been partially or fully produced by AM, either incorporating melts or solutions into 3D-printed structures [54,58], adopting dual-extrusion systems [59] or directly extruding composite filaments [55].

Still, the effect of the specifical structural arrangement of the rigid polymer on the properties of hybrid systems has been little investigated [89–91], but deserves further attention. In fact, understanding structure-property correlations for this type of scaffolds would greatly ease their design optimization and customization. Structure-property correlations can be derived either analytically [92,93] or by fitting results of experiments and FEM simulations [84,94–98]. It is useful to represent stiffness and strength as a function of relative density or porosity and to look for equations fitting experimental data or the results of proper FEM simulations [84,94]. Helpful knowledge may also be provided by several works about lattice metamaterials, in which the relationship between mechanical properties and relative density is typically described with a power law equation [96–98]. Moreover, the value of the exponent in the equation provides information about the deformation behavior of the lattice, which may be bending-dominated or stretching-dominated

[92,93]. Further help in optimizing the scaffold design can be provided by other numerical approaches, such as machine learning methods (e.g., neural networks [99,100]), and topology optimization based on proper constraints and multiple objectives (e.g., aiming at a compromise between stiffness and permeability [101], considering the layered structure of 3D-printed objects [102] or the tissue ingrowth process [103]).

1.3.2. Smart shapeshifting materials for biomedical applications

Another important innovative trend in tissue engineering is the use of smart materials to produce scaffolds capable of changing their shape and/or functionality upon application of specific external stimuli. For example, smart hydrogels can respond to various stimuli (pH, light, ions, small molecules, temperature) with reversible swelling, shape/volume changes, or sol-gel transitions, and have been employed for the engineering of different tissues, as well as other biomedical applications (targeted drug delivery, biosensing, actuators, cell culture…) [104,105]. Other smart polymers are supramolecular materials that exploit non-covalent bonds to achieve self-healing capabilities, proposed for applications such as scaffolds, wound healing, electronic skin and drug delivery [106]. Furthermore, shape memory polymers (SMPs) have been used to create self-deploying, self-expanding, or self-fitting scaffolds for tissue defect filling, usually employing thermoresponsive or hydroresponsive SMPs [107].

1.3.2.1. Thermoresponsive SMPs for tissue engineering and other biomedical applications

Thermoresponsive SMPs have been particularly attracting the attention of materials researchers with their shapeshifting capabilities, or shape memory effect (SME). Thanks to such peculiar property, these materials can be deformed and stored in a temporary shape until a specific thermal stimulus activates the recovery of their original (permanent) shape [108]. In regenerative medicine, this behavior has been exploited to obtain scaffolds to face problems of special restriction in bone tissue engineering [109], injectable scaffolds that recover their shape after injection

[110] or sel-fitting implants [111]; in bone regeneration applications, the SME is advantageous not only in view of minimally invasive implantation, but also to provide self-adaptation of the scaffold to the defect shape [112].

Shape memory capabilities can become even more attractive by considering the use of advanced fabrication techniques as electrospinning and additive manufacturing.

In particular, combining electrospinning and SMPs is reported to bring several advantages to biofabrication: micro- and nanofibers exhibit improved and faster shape recovery than the bulk material because of higher mobility and larger specific surface area for heat exchange; by controlling micro- and nanoscale features of materials it is possible to influence cell behavior; fibrillar structures with highly interconnected porosity and shape memory properties are suitable for minimally invasive implantation as scaffolds, thanks to their similarity with the extracellular matrix [113,114]. For these reasons, a variety of biomedical applications is listed in reviews about SMP fibers, especially addressing tissue engineering and drug delivery, but also wound healing, cell culturing, biomedical devices, medical imaging, bioactuators and implantable electronics [115,116].

Concerning additive manufacturing of SMPs, it is a winning strategy to gain control over their shape and its transformation. Indeed, 4D printing, intended as 3D printing of objects capable of changing shape, property, or functionality as a function of time, can greatly increase design freedom and facilitate the realization of complex 3D structures, often starting from 2D printed patterns [117]. For instance, the deposition of aligned PCL filaments on planar hydrogel substrates is an effective method to create tubular structures for the regeneration of tissues characterized by uniaxial cell orientation, such as skeletal muscle, cardiac, or neural tissues; such scaffolds can be seeded with cells in their planar form and then take on a tubular shape in water, due to the hydrogel swelling [118,119]. In other researches, more complex patterns were printed on pre-stretched textiles or sheets, forming curved

surfaces such as domes, saddles, or triply periodic minimal surfaces after load removal [120,121]. Adaptive and personalized vascular grafts made of poly(glycerol dodecanoate) acrylate have also been proposed for minimally-invasive implantation, thanks to their ability to recover their original shape at body temperature [122].

1.3.2.2. Insights on two-way SMPs realization and applications

Most studies about SMPs deal with thermoresponsive one-way SME. However, some applications require reversibility of shapeshifting, which has led to the development of two-way SMPs, being able to undergo dimensional variations between two different shapes by applying proper heating-cooling cycles [123]. In the biomedical sector, for example, smart materials with two-way SME have been suggested in applications such as smart drug delivery, dynamic mechanical stimulation of cell cultures, active devices to help disabled people, bandages, and temporary fixation parts [124–126].

From the molecular point of view, the two-way SME relies on the presence of net-points, responsible for the memorization of the permanent shape, and of switch segments, undergoing a reversible transition between a stable coil conformation and a metastable oriented conformation around a specific transition temperature; the main molecular strategies involve liquid crystalline elastomers, semicrystalline networks, two-way shape memory composites, and interpenetrated polymer networks [123].

Among these approaches, the realization of polymeric composites stands out for the straightforward preparation, simply consisting in attaching a deformed one-way SMP to an elastomer polymer, and for the stress-free actuation of SMPs that would normally exhibit two-way SME only under a constant external load [127]. In fact, when the SMP recovers its deformation upon heating above its transition temperature, the elastomer stores elastic strain energy, which is then released upon cooling below the transition temperature, providing an internal stress that deforms the SMP once again [128,129]. SMP-elastomer composites described in literature

[127–129] are typically obtained in three steps: (i) realization of the shape memory component by conventional techniques, such as film casting, hot press molding or compression molding; (ii) deformation of the SMP; (iii) integration of the elastomer component through adhesives, by coating or by casting in a second mold.

The production of two-way shape memory fibrous structures has also been investigated with interest, employing electrospinning for their fabrication. For instance, He *et al.* obtained liquid crystal elastomer microfibers by electrospinning under UV light, and employed them as actuators for a microtweezer, a microrobot, and a microfluidic pump [130]. In another work, Ahn *et al.* produced smart polyurethane membranes with temperature tunable pores under constant stress, that could selectively separate substances of different sizes [131]. Modulation of pore size and fiber orientation was also investigated by Pandini *et al.* in scaffolds prepared by electrospinning and sol-gel crosslinking of poly(ε-caprolactone) (PCL), that were suggested as smart supports for cell culture but also for controlled drug delivery [132].

2. Tailoring the Properties of Composite Scaffolds with a 3D-Printed Lattice Core and a Bioactive Hydrogel Shell for Tissue Engineering

Recent research in the field of tissue engineering is focusing on the realization of hybrid scaffolds as multi-material systems which allow to successfully combine the advantages of different biomaterials, as discussed in Chapter 1. The regenerative potential of hydrogels has strikingly emerged, together with their recurrent need of reinforcement or prolonged durability when structural support is required, which has led to consider them often in combination with other biopolymers. In addition, additive manufacturing technologies have demonstrated superior design flexibility in the realization of scaffolds with controlled and personalized 3D structure.

Although a lot of research activity has been developed out of this background, several pathways are still open, and it remains difficult to match all scaffold requirements and address specific patient needs. The approach presented in this thesis may contribute to the progress in this field, thanks to its versatility and to the auspiciousness of its results. In particular, this chapter[1] presents the innovative core-shell design at the base of the proposed scaffolds and investigates in depth the correlations between scaffold structure and mechanical properties.

The developed composite scaffolds have a core consisting of a rigid thermoplastic lattice realized by fused deposition modeling, and a shell consisting of a bioactive

[1] Most of the work presented in this chapter is published in reference [138]: C. Pasini, S. Pandini, G. Ramorino, L. Sartore, *Tailoring the properties of composite scaffolds with a 3D-Printed lattice core and a bioactive hydrogel shell for tissue engineering*, Journal of the Mechanical Behavior of Biomedical Materials 150 (2024) 106305.
Reference [91] is also based on the first results of this study: C. Pasini, L. Sartore, S. Pandini, G. Ramorino, *Hybrid scaffolds with a 3D-printed polymer lattice core and a bioactive hydrogel shell for bone regeneration*, Materials Today: Proceedings 70 (2022) 230-236.

hydrogel, grafted upon the core and freeze-dried to develop porous microstructure. Different lattice structures are designed and finely realized thanks to additive manufacturing, so to better tailor the scaffold architecture and composition, and thereby tuning its mechanical, degradation and biological features according to specific tissue engineering applications.

For the core, poly-L-lactic acid is selected to provide stiffness and strength, with the dual purpose of obtaining biomimetic properties and dealing with the temporary substitution of mineralized tissues, also thanks to its slow biodegradation rate, which may help retaining sufficient mechanical stability despite the long healing time of bone tissue. A softer material, a thermoplastic elastomer, is also investigated to consider the case of softer tissues.

On the other hand, the hydrogel shell should improve the biocompatibility and bioactivity of the scaffold thanks to its high hydrophilicity, to the similarity between its macromolecular network and the bone extracellular matrix, and to its ability to support osteogenic and chondrogenic differentiation.

The correlation between structure, mechanical properties and hydrogel content is here explored by varying both the lattice unit cell geometry and its size, and considering various external shapes and loading conditions. Mechanical tests reveal the suitability of the mechanical properties of the scaffolds for bone and cartilage tissue regeneration, and the possibility to modulate their stiffness and strength upon the lattice parameters. Moreover, the interconnected porous structure of the shell, assessed by morphological analysis at the microscope[2], may promote cell colonization and proliferation, while its composition may support osteogenic/chondrogenic differentiation.

[2] Images obtained by Scanning Electron Microscopy were kindly taken by Prof. Giovanna Conacchia (Metallurgy Laboratory, Department of Mechanical and Industrial Engineering, University of Brescia, Via Branze 38, 25123 Brescia, Italy).

2.1. Materials and methods

2.1.1. Materials

Poly-L-lactic acid (PLA) filament of commercial grade (Raise3D Premium PLA [133]) was provided by Raise 3D Technologies, Inc. (Irvine, CA, USA); its precise composition is not revealed by producers, only disclosing a purity higher than 90%.

Thermoplastic elastomer (TPE) filament (FILOALFA® BioFlex) was purchased by Maip Compounding S.r.l. (Torino, Italy); according to its data sheet [134] and its list of biocompatibility certifications [135], it is copolyester-based, non-cytotoxic, and compliant to hemolysis, intracutaneous and systemic injection tests.

Type A gelatin (pharmaceutical grade, 280 bloom, viscosity 4.30 mPs) was kindly supplied by Italgelatine (Cuneo, Italy). Poly(ethylene glycol) diglycidyl ether (PEGDGE) (molecular weight 526 Da) and chitosan (molecular weight between 50,000 and 190,000 Da and degree of deacetylation 75–85%) were provided by Sigma-Aldrich Co (Milan, Italy). Ethylene diamine (EDA) and acetic acid were obtained by Fluka (Milan, Italy).

2.1.2. Preparation of core-shell composite scaffolds

The manufacturing process of the scaffolds consisted of three main steps, represented in Scheme 2.1 and detailed in the following paragraphs:

1. 3D printing of the PLA (or TPE) core as a lattice structure;
2. preparation of a hydrogel-forming solution;
3. integration of the core with the hydrogel shell, completed by freeze-drying and post-curing.

2.1.2.1. Core realization by fused deposition modeling (FDM)

The software Solidworks (Dassault Systèmes, Vélizy-Villacoublay, France) was used to create CAD models for the scaffold core, which consisted of variously arranged lattice structures. The slicing of the model was performed without adding any supports, by means of the software IdeaMaker (Raise 3D Technologies). The core specimens were obtained by additive manufacturing by means of the FDM 3D

printer Raise3D Pro2 (Raise 3D Technologies). Table 2.1. summarizes PLA and TPE printing conditions, specifying layer thickness, nozzle diameter, nozzle temperature, bed temperature, and printing speed employed for each material.

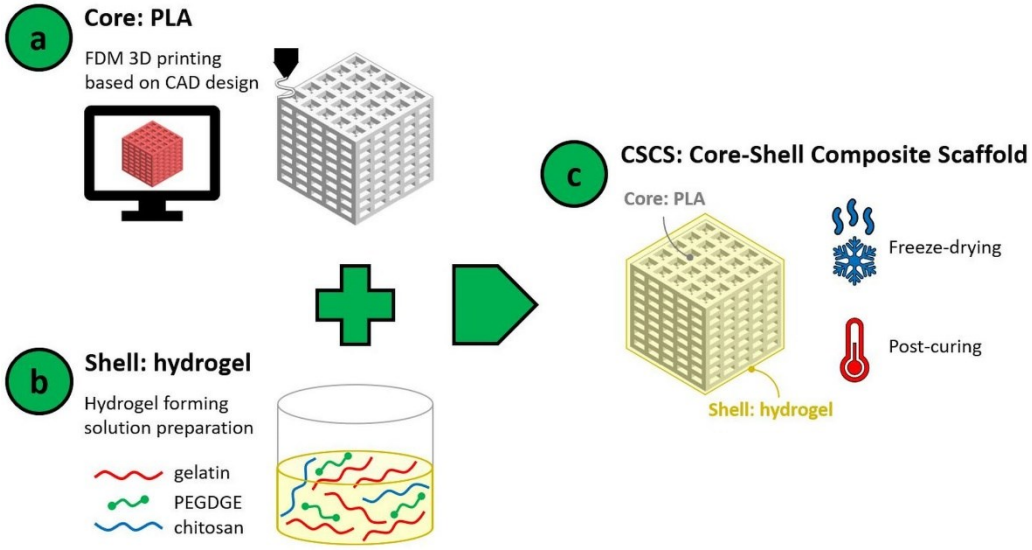

Scheme 2.1. main steps for the preparation of 3D-printed core-shell composite scaffolds: (a) *3D printing of the core as a lattice structure; (b) preparation of a hydrogel-forming solution; (c) integration of the core with the hydrogel shell.*

Table 2.1. Printing parameters for PLA and TPE filaments.

Material	Layer thickness [mm]	Nozzle diameter [mm]	Nozzle temp. [°C]	Bed temp. [°C]	Printing speed [mm/s]
PLA (Raise3D Premium PLA)	0.1	0.2	205	60	15 ÷ 60
TPE (FILOALFA® BioFlex)	0.2	0.4	210	60	5 ÷ 35

Various specimen types were created, all having core struts of fixed thickness (t = 0.6 mm) but different external shape (cubic or cylindrical) and different internal structure of the core, obtaining the eight lattices represented in Figure 2.1 and summarized in Table 2.2. More specifically, all cubic specimens had similar sides of about 10 mm, while cylindrical specimens had a diameter of about 7 mm and a length of about 20 mm. A cartesian coordinate system was defined, the z-axis

corresponding to the build direction and xy being the two directions of the printing plane. Note that the additional horizontal struts in SH+ specimens are parallel to the xy plane, while the additional vertical struts in RV+ lattices are aligned to the z direction. For each lattice type, while strut thickness, t, remains fixed, the hole width, w, and the hole height, h, can be either fixed or variable parameters.

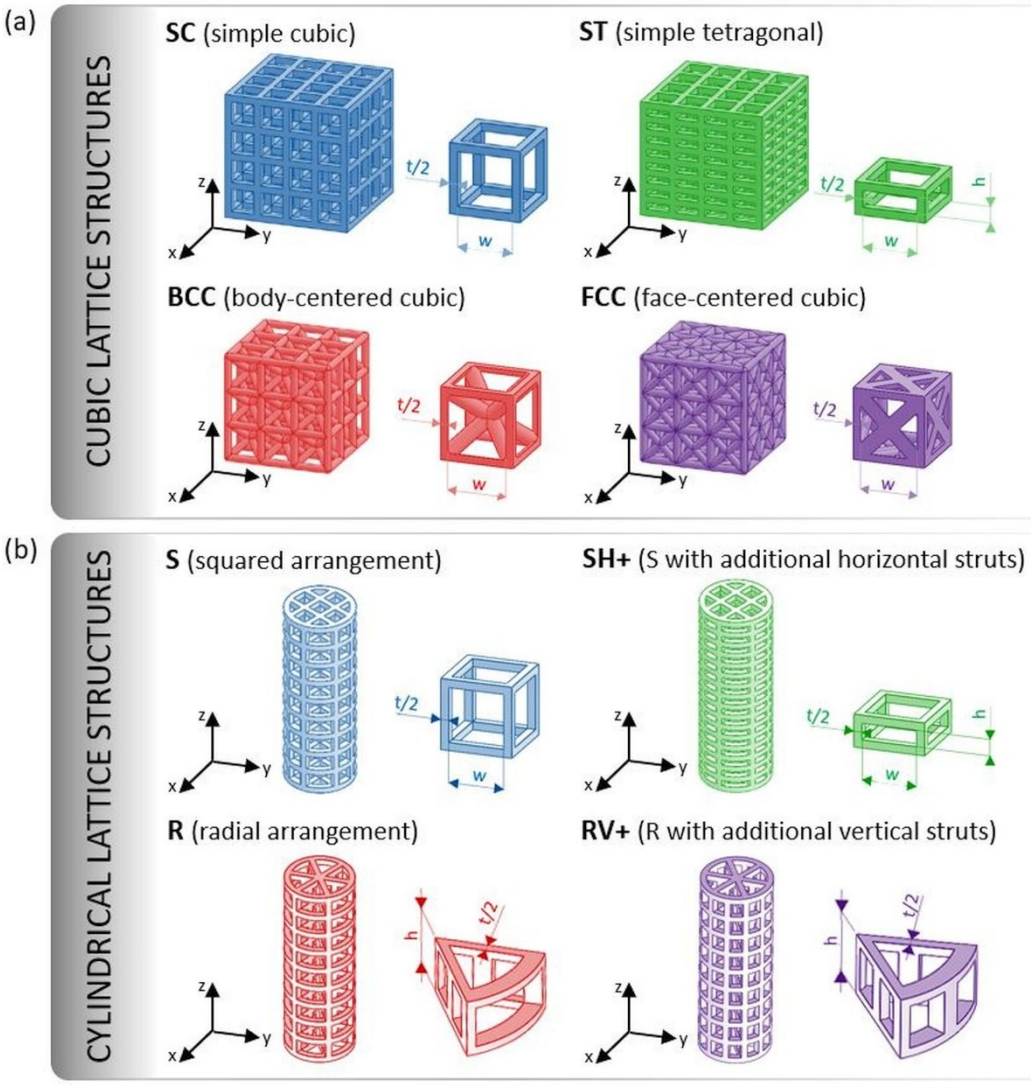

Figure 2.1. CAD models of cubic (a) and cylindrical (b) core specimens with different lattice structures, with indications of the relevant unit cell parameters: t = strut thickness; w = hole width; h = hole height. The z axis corresponds to the build direction.

Table 2.2. Parameters defining the geometry of the unit cells of the core lattice structures.

Unit cell type		Strut thickness t [mm]	Hole width w [mm]	Hole height h [mm]
SC	simple cubic	0.6	0.5; 0.7; 1; 1.5; 2; 3; 4	equal to w
ST	simple tetragonal	0.6	1; 1.5; 2; 3; 4	0.6
BCC	body-centered cubic	0.6	1.4; 2.4; 3.4	equal to w
FCC	face-centered cubic	0.6	1.4; 2.4; 3.4	equal to w
S	squared arrangement	0.6	1.5	equal to w
SH+	squared arrangement with additional horizontal struts	0.6	1.5	0.6
R	radial arrangement	0.6	n.a.	1.5
RV+	radial arrangement with additional vertical struts	0.6	n.a.	1.5

2.1.2.2. Hydrogel forming solution preparation

A concentrated aqueous solution was obtained by dissolution of gelatin (6 g) in distilled water (65 mL) at 40 °C, followed by sequential addition of PEGDGE (1.4 g), chitosan solution (2 wt% in acetic acid 1%; 32.5 g) and EDA (70 mg). The reaction mixture was prepared and maintained under mild magnetic stirring at 40 °C for about 10 minutes, in order to completely dissolve the reactants and to start grafting/crosslinking through condensation reactions between the amino groups of gelatin and chitosan and the epoxy groups of PEGDGE. The composition of the dry hydrogel was 74.3 wt% gelatin, 17.6 wt% PEGDGE and 8.1 wt% chitosan.

2.1.2.3. Core-shell integration

Core specimens were immersed in the hydrogel forming solution at 40 °C, and three cycles of vacuum/air were applied to eliminate entrapped bubbles and ensure the penetration of the hydrogel even into the innermost holes of the core. The product was maintained at 40 °C for about 50 minutes before freezing and freeze-drying in a lyophilizer (HyperCOOL HC3055, LabTech Srl, Italy). The excess hydrogel surrounding the core was removed with a blade and a post-curing

treatment was performed in oven at 45 °C under vacuum for 2 h, to complete the crosslinking reaction of the hydrogel. The obtained core-shell specimens were finally washed with distilled water to remove the unreacted reagents and freeze-dried again to prevent hydrolysis during storage.

2.1.3. Physical-mechanical characterization of core-shell composite scaffolds

2.1.3.1. Core void volume

The core specimens were all weighted on a laboratory balance (Gibertini E42-B, Gibertini Elettronica, Novate Milanese, Italy) to evaluate their mass (m_c), while a caliper was used to measure their total volume (V), considered as cubic for the cubic specimens and as cylindrical for the other ones. From these values, their experimental void volume ($V_{v,exp}$) was calculated as follows:

$$V_{v,exp}[\%] = \left(1 - \frac{m_c}{\rho_c V}\right) \times 100 \quad (2.1)$$

assuming the density of the core (ρ_c) equal to 1.2 g/cm^3 for Raise3D Premium PLA [133] and equal to 1.09 g/cm^3 for FILOALFA® BioFlex [134].

The values obtained were compared to the theoretical void volume ($V_{v,th}$) of the CAD models, expressed as percentage with respect to their total volume.

2.1.3.2. Hydrogel content

The experimental hydrogel content (H_{exp})) of the scaffolds was evaluated by weight as:

$$H_{exp}[\%] = \frac{m_{cs,dry} - m_c}{m_{cs,dry}} \times 100 \quad (2.2)$$

where $m_{cs,dry}$ is the mass of the core-shell specimens in dry conditions.

The obtained values were compared to the theoretical hydrogel content (H_{th}), estimated as:

$$H_{th}[\%] = \frac{\rho_s V_{v,exp}}{\rho_c(100 - V_{v,exp}) + \rho_s V_{v,exp}} \times 100 \quad (2.3)$$

where ρ_s =0.11 g/cm^3 is the density of the hydrogel [62].

2.1.3.3. Water uptake

The water uptake (W) of the composite scaffolds was obtained as:

$$W[\%] = \frac{m_{cs,wet} - m_{cs,dry}}{m_{cs,dry}} \times 100 \quad (2.4)$$

where $m_{cs,wet}$ is the mass of the core-shell specimens in wet conditions (*i.e.* after immersion in water for 24 h).

Considering the water uptake as occurring in the hydrogel shell only (W_s), it was also calculated as:

$$W_s[\%] = \frac{m_{cs,wet} - m_{cs,dry}}{m_{cs,dry} - m_c} \times 100 \quad (2.5)$$

2.1.3.4. Morphology

Core and core-shell specimens were observed with an optical microscope (Leica DMS 300, Leica Microsystems, Wetzlar, Germany), both in dry and wet conditions (*i.e.* after immersion in distilled water for 24 h). Some of them were cryogenically fractured to reveal their inner appearance as well. Moreover, a Scanning Electron Microscope (SEM) (LEO EVO 40, Carl Zeiss AG, Oberkochen, Germany) was employed to better observe the morphology of the section of mechanically sawed specimens.

2.1.3.5. Compression tests

The mechanical properties of core and core-shell specimens were tested under compression with an electromechanical dynamometer (Instron 3366, Illinois Tool Works Inc., Norwood, MA, USA), equipped with a 10 kN load cell. The tests were carried out at room temperature and with a crosshead speed equal to 2 mm/min. In the case of core-shell specimens, they were preceded by immersion in distilled water for 24 h. Specimens were tested both along the build direction and the transverse direction of the core (*i.e.* z-direction and x- or y-direction in Figure 2.1, respectively), performing at least 2 and up to 6 tests for each geometry. The results were represented as apparent stress (σ_{app}) *vs.* apparent strain (ε_{app}), calculated as follows:

$$\sigma_{app}[MPa] = \frac{P}{A} \quad (2.6)$$

$$\varepsilon_{app}[mm/mm] = \frac{u}{L} \quad (2.7)$$

where P is the force measured by the load cell, A is the total area of the specimen cross-section (either squared or circular), u is the crosshead displacement and L is the dimension of the specimen along the loading direction. In these equations the term apparent is used since stress and strain are evaluated as macromechanical parameters for a homogeneous equivalent material, whereas the lattice structures and consequently local stress and strain are actually not homogeneous. For the same reason, also the following stiffness and strength parameters are defined apparent: the initial slope of σ_{app} *vs.* ε_{app} curves was determined, and reported as apparent modulus (E_{app}); similarly, an apparent stress at failure ($\sigma_{app,f}$) was defined, evaluating it at the first peak or knee of the curves.

Only in the case of cylindrical specimens tested along their transverse direction, due to the continuous variation of the cross-section along the testing direction, the results were expressed in terms of normalized load (P_N) *vs.* normalized displacement (u_N), calculated as:

$$P_N[MPa] = \frac{P}{dl} \quad (2.8)$$

$$u_N[mm/mm] = \frac{u}{d} \quad (2.9)$$

where d and l are the diameter and the length of the cylinder, respectively. A stiffness parameter (S^*) was evaluated as the initial slope of P_N *vs.* u_N curves, while the normalized load at failure ($P_{N,f}$) was taken at the first peak or knee of the curves.

2.1.3.6. Bending tests

Three-point bending tests were carried out on cylindrical core specimens by means of the electromechanical dynamometer, equipped with a 500 N load cell. They were tested at room temperature and with a crosshead speed equal to 2 mm/min. Two different values were set for the span (s) between lower supports,

namely 80 mm and 30 mm. Therefore, compared to compression specimens, the length of the cylinders along z was increased (about 100 mm) in order to fit the supports. The results were represented as apparent maximum stress ($\sigma_{app,b}$) *vs.* apparent maximum strain ($\varepsilon_{app,b}$), corresponding to the maximum stress and strain that would have characterized an equivalent fully solid cylinder subjected to three-point bending under the same load P and displacement u as the lattice specimen. Also in this case, the term apparent is used for the reasons expressed in paragraph 2.1.3.5. The following equations were employed.

$$\sigma_{app,b}\,[MPa] = \frac{8Ps}{\pi d^3} \tag{2.10}$$

$$\varepsilon_{app,b}\,[mm/mm] = \frac{6ud}{s^2} \tag{2.11}$$

The apparent bending modulus ($E_{app,b}$) was evaluated as the initial slope of $\sigma_{app,b}$ *vs.* $\varepsilon_{app,b}$ curves, while the maximum stress at failure of the equivalent homogeneous beam ($\sigma_{app,b,f}$) was taken at the first peak of the curves.

2.1.3.7. Power-law equations for structure-property correlations

Relative modulus and relative strength of PLA core specimens, calculated as ratio between the mechanical properties of cubic lattices ($P = E_{app};\ \sigma_{app.f}$) and those of bulk PLA ($P_c = E_c;\ \sigma_{c,f}$) [133], were plotted against their relative density, ρ_{rel}, calculated as follows:

$$\rho_{rel} = 1 - V_{v,exp} \tag{2.12}$$

For each lattice type, curve fitting was carried out according to Gibson-Ashby power-law models for cellular materials, with fitting constant C and exponent n [92]:

$$\frac{P}{P_c} = C\rho_{rel}^n \tag{2.13}$$

2.2. Scaffold morphology, composition and water uptake

2.2.1. Core-shell structure and morphological analysis of the scaffolds

The core-shell composite scaffolds are realized as shown in Scheme 2.1, by 3D printing the PLA (or TPE) core (a), preparing the hydrogel forming solution (b), and grafting and integrating the core with the hydrogel shell (c). Additive manufacturing of the core lattice structure enables full control over the arrangement of its struts, having the function of mechanical support, and the distribution of its holes, forming a network of channels to be filled by the hydrogel forming solution. After the shell gelation, a freeze-drying step is performed to create interconnected pores throughout the hydrogel in a cell-friendly way, using only water as solvent. Finally, a post-curing treatment on dry samples ensures completion of crosslinking reactions [62].

The CAD models and unit cell parameters of the core lattice structures examined are shown in Figure 2.1 and Table 2.2, respectively, while the appearance of core and core-shell specimens is displayed in Figure 2.2, reporting an example for each type of PLA lattice structure (a) as well as photographs of a PLA-hydrogel scaffold (b) and of TPE and TPE-hydrogel specimens. Two simple external shapes (cubes/cylinders) are taken into account in order to ease interpretation of the mechanical response of the scaffolds, while several different lattice unit cells are studied: cubic specimens are constituted by cells with different dimensions and strut arrangements; cylindrical specimens are provided with different arrangements of longitudinal and transverse struts.

More in detail, for the set of cubic specimens, the simple cubic (SC) cells arrangement may be considered the starting point, from which other geometries are derived by introducing several variables in the strut arrangement: simple tetragonal (ST) lattices are obtained by selecting a fixed value of strut spacing along the build direction (z), while strut spacing in the xy-plane is free to vary; body-centered cubic (BCC) and face-centered cubic (FCC) lattices are obtained by adding diagonal struts

across the center of the cells or of their faces, respectively. On the other hand, for the set of cylindrical specimens, struts are arranged either along the xyz coordinate axes, forming simple cubic and tetragonal cells (S and SH+, respectively), or according to a cylindrical system, with a radial disposition of struts in the xy-plane (R and RV+, the latter with a higher number of struts parallel to z in the outer ring).

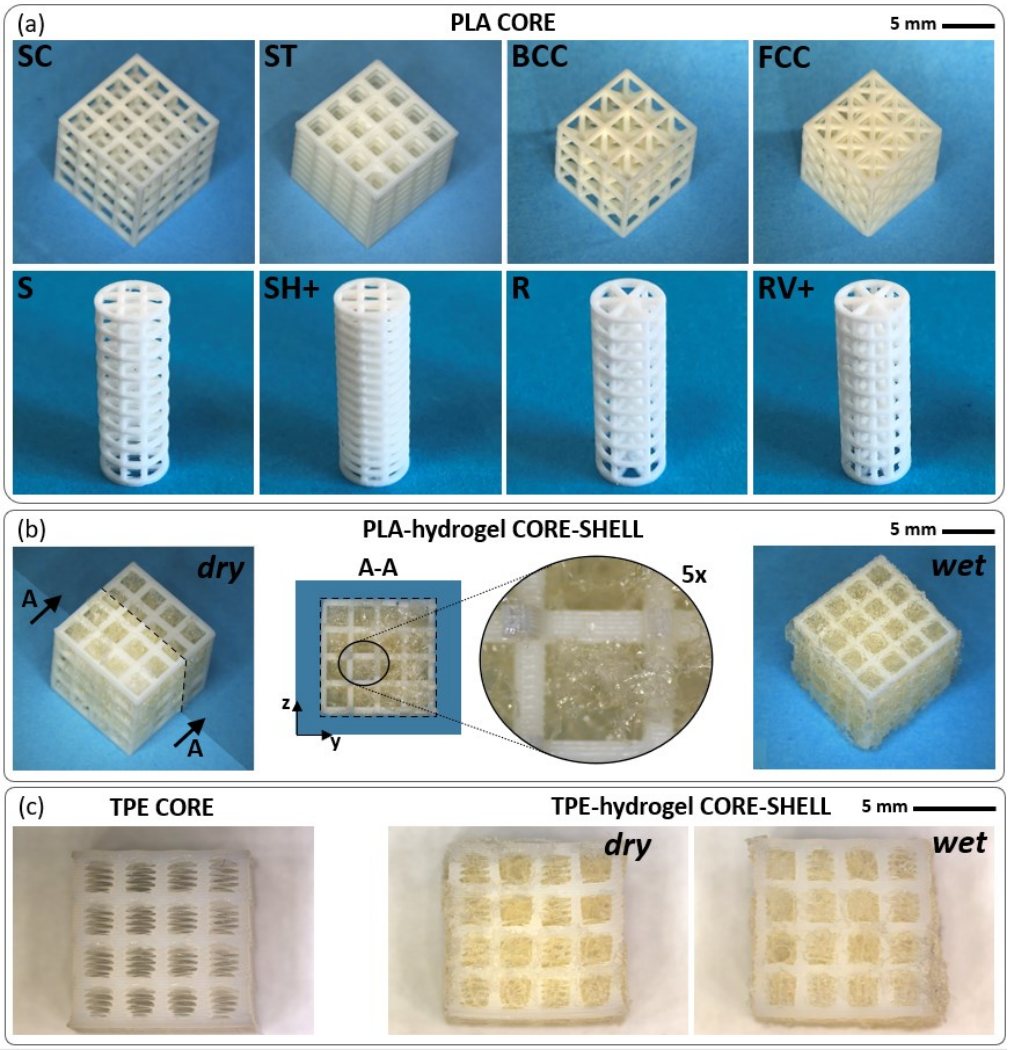

Figure 2.2. (a) Representative core specimens for each type of lattice structure: SC (w = 2 mm); ST (w = 2 mm); BCC (w = 2.4 mm); FCC (w = 2.4 mm); S; SH+; R; RV+. (b) Core-shell specimen (SC: w = 2 mm) in dry conditions (with details of its cross-section A-A) and in wet conditions (after immersion in distilled water for 24 hours). (c) TPE core (SC: w = 2 mm) and corresponding core-shell specimens in dry and wet conditions.

All PLA struts are 0.6 mm thick and formed by smaller filaments having height equal to 0.1 mm, corresponding to the layer thickness, and width equal to 0.2 mm, corresponding to the nozzle diameter. The single filaments can be easily recognized in magnified images of the specimens (Figure 2.2, insert with 5x magnification), highlighting the anisotropic morphology due to FDM layer-by-layer deposition. All geometric features are accurately replicated, also thanks to the adoption of small filament height and width. BCC and FCC structures present some stringing, which may be ascribed to the increased printing difficulty of inclined struts, but it is a limited phenomenon, which does not compromise that lattice holes could remain interconnected and pervious to the flow of the hydrogel forming solution.

Considering the possibility of varying the core material, SC lattices are also 3D-printed with a biocompatible soft copolyester-based TPE (FILOALFA® BioFlex), with the same geometry of PLA core specimens (strut thickness of 0.6 mm and hole width between 0.5 mm and 3 mm; non-supported 4-mm holes could not be printed with this material). These tiny features are not easy to achieve by FDM of elastomeric materials, which have usually lower processability. Indeed, the TPE needs to be printed with a larger nozzle (0.4-mm diameter) and the lattice holes present diffuse stringing (Figure2.2c).

After hydrogel incorporation, the specimens consist of core-shell systems, represented in Figure 2.2b,c as observed under an optical microscope, taking as example the case of SC scaffolds. The hydrogel shell penetration deep inside the core is confirmed, both looking at the external appearance of the specimens and examining their cross-sections, carefully obtained by cryogenic fracture with a sharp blade. The outer surfaces of the lattice appear covered by a thin hydrogel layer, that becomes more clearly visible in wet conditions, displaying a slight swelling after prolonged immersion in water.

The morphology of core-shell composite scaffolds at the micro-scale was more accurately examined by SEM. Figure 2.3a shows part of the cross-section of a

scaffold with ST core, in which PLA struts are differently spaced along z and xy directions. To better guide the eye in reading, the zy section plane and the cross-sections of PLA struts, contoured by a dashed line, are schematically evidenced in Figure 2.3b.

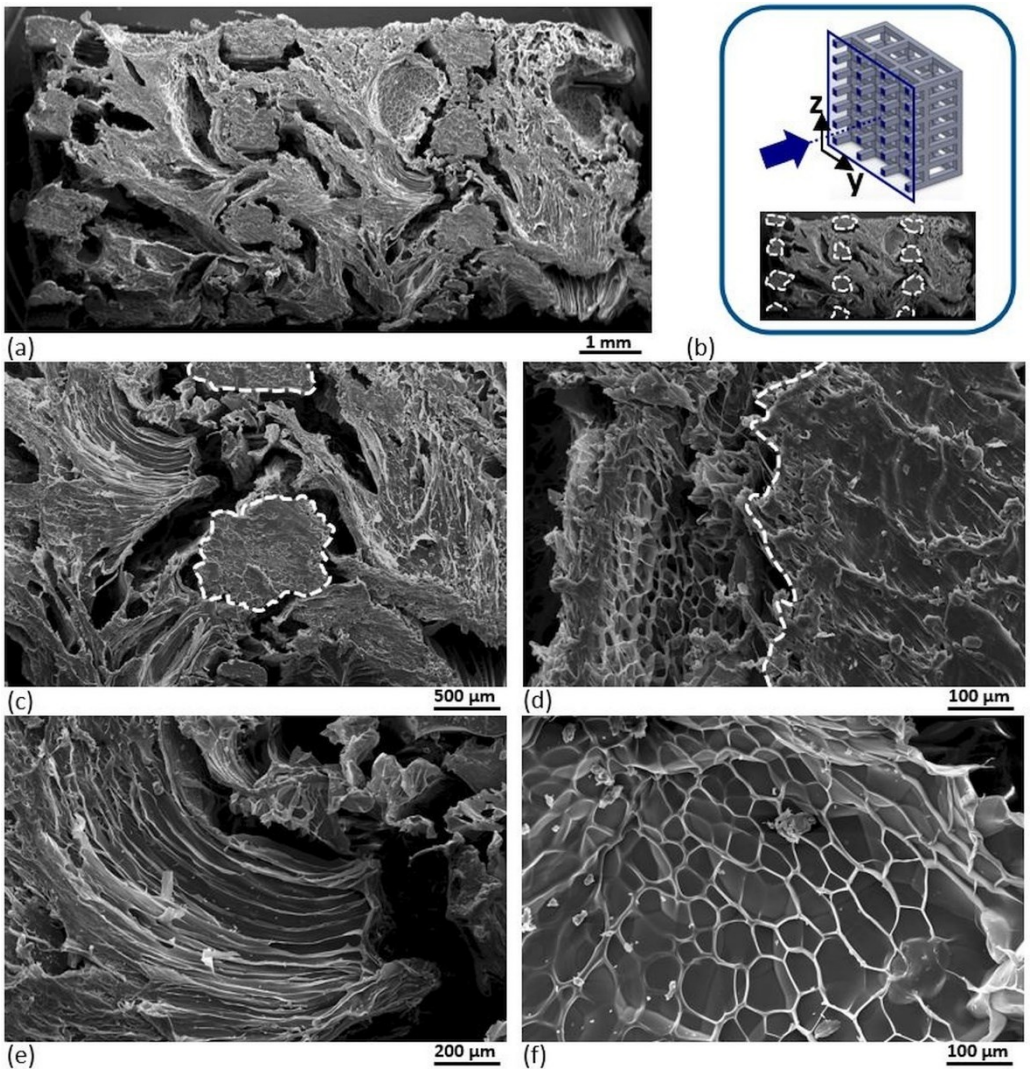

Figure 2.3. SEM analysis of the yz cross-section of a ST core-shell scaffold (w = 3 mm; h = 1 mm): (a) cross-section of the specimen, along with (b) scheme of the yz section plane and highlighting of the PLA struts with a dashed contour on Figure 2.3a; (c) heterogeneous porous structure of the hydrogel surrounding a PLA strut; (d) core-shell interface; (e) detail of channels developed in the hydrogel after penetration in the core and freeze-drying; (f) detail of the hydrogel open cellular structure.

Each strut is surrounded by porous hydrogel (Figure 2.3c), which reveals a structure characterized by interconnected pores of heterogeneous size, from big channels measuring several hundreds of microns and providing easy access to cells, to smaller cavities which provide more surface for cell adhesion and still guarantee exchange of gases, nutrients, and metabolites. The particular of the core-shell interface reported in Figure 2.3d shows that a microporous hydrogel layer seems to adhere to PLA struts. Finally, some details of the shell pores display the presence of a portion of shell with a peculiarly regular open cellular structure, with pore size of about 100 μm (Figure 2.3e), along with a wide cavity next to some thinner but remarkably long channels, originated by the vapor flow in the freeze-drying process (Figure 2.3f). Interestingly, scaffolds with pore size equal to 100 μm or more allowed cell penetration and growth in numerous studies [12]. Overall, pores exhibit heterogeneous size and orientation due to a complex combination of two phenomena: on one side, the hydrogel forming solution flows around PLA struts during the immersion of the core specimens, filling all their void volume; on the other hand, during the freezing and freeze-drying processes, the thermal flow guides the formation and sublimation of ice crystals, creating a highly interconnected porous structure in the dried hydrogel. Such a hierarchical arrangement of the pores may be particularly interesting, considering that both bone and vascular tissues are typically hierarchically organized.

2.2.2. Composition and water uptake of the scaffolds

The composition of the scaffolds is tailored by varying the void volume fraction in the core, V_v, which is the space destined to the hydrogel in core-shell specimens. The correlations between hole width, core void volume fraction, hydrogel content and water uptake are summarized in Figure 2.4. It is useful to remind that V_v is geometrically determined not only by the hole width, but also by the specific strut arrangement, associated with symbols and colors in the legend (Figure 2.4a); symbols refer to experimental data, while dashed lines are theoretical trends.

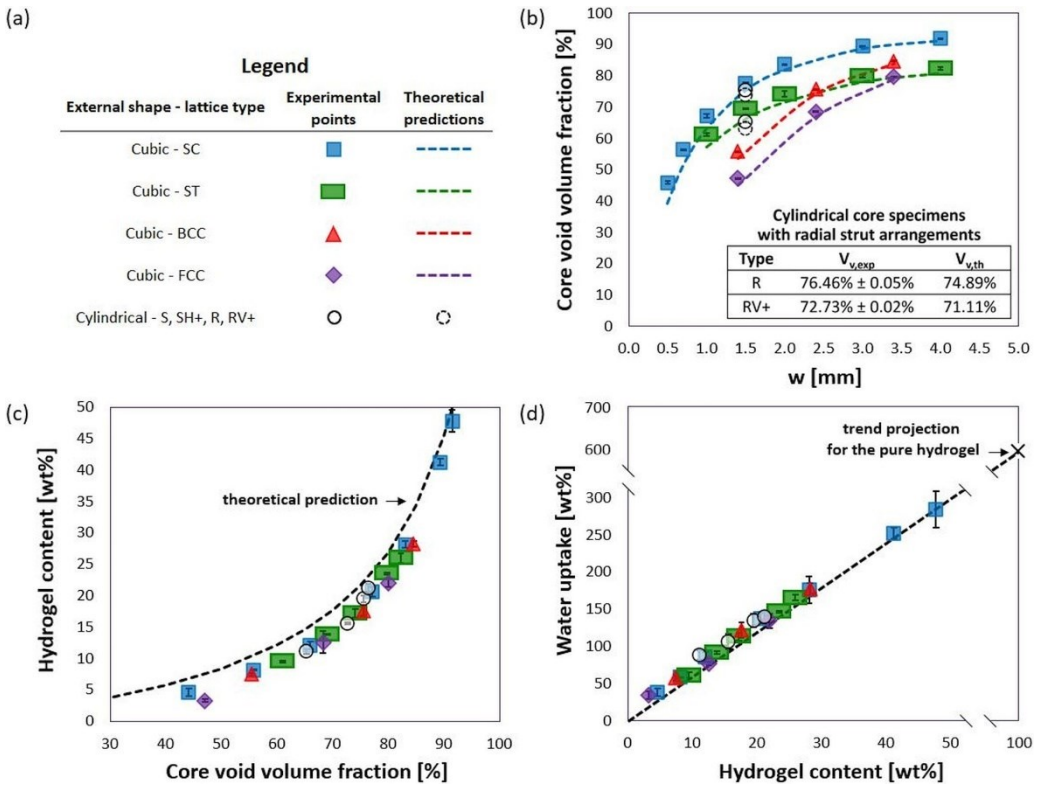

Figure 2.4: Experimental results and theoretical predictions regarding composition and water uptake of the core-shell scaffolds: (a) legend; (b) void volume fraction in the core, V_v, as a function of the hole width, w (for lattices with radial strut arrangements, V_v values are reported in the table); (c) hydrogel content versus *core void volume fraction; (d) water uptake* versus *hydrogel content.*

For all PLA cubic specimens, Figure 2.4b reports V_v values as a function of the hole width, w,. As w grows, varying within an interval between 0.5 mm and 4 mm, the void volume fraction increases, overall ranging from about 45% to more than 90%. Considering a same increment of w, the change in void volume is more limited in tetragonal lattices than it is in cubic lattices, because only two dimensions of the unit cells are free to vary; the biggest variations are obtained in BCC and FCC lattices, due to the higher number of struts per cell. On the other hand, for any given w, SC lattices present the highest core void volume fraction, due to the higher number of struts in ST, BCC and FCC lattices with respect to SC ones. Overall,

experimental measures of V_v are consistent with the expected theoretical values based on CAD models, with small deviations (around 1–5%) that tend to disappear as the cell size increase.

Figure 2.4b also reports void volume fraction values of cylindrical core specimens with squared arrangement (S and SH+, represented graphically in correspondence of w = 1.5 mm) and with radial strut arrangement (R and RV+, reported in a table, since their geometry is not based on the parameter w). S and SH+ lattices present V_v values close to the points corresponding to SC and ST structures with the same value of w, as expected since S ones present in fact SC unit cells and SH+ ones present in fact ST unit cells. R cylinders, in spite of the different strut arrangement, present void volume fraction values similar to S ones, around 76%. The addition of horizontal struts to S lattices (SH+) and of vertical struts to R lattices (RV+) reduces V_v down to 65% and 73%, respectively, once again consistently with the expected theoretical values.

The large overall variation of the void volume fraction for the various examined lattices leads to a broad range of dry hydrogel content, from less than 5 wt% to almost 50 wt%, that were experimentally evaluated through eq. 2.2. Figure 2.4c shows a common increasing trend of the hydrogel content with the core void volume fraction, apparently not influenced by the lattice type. It is also possible to predict this trend with theoretical calculations (eq. 2.3), made on the basis of the density of the porous hydrogel and considering all the void volume in the core as completely filled by the hydrogel shell. Despite the implicit approximations of this method, namely supposing that the presence of PLA struts does not alter the porosity of the hydrogel and that the hydrogel perfectly fills the entire core void volume, the predictive curve in Figure 2.4c is overall close to the experimental points. The hydrogel content tends to be overestimated for low V_v values, probably because narrower core holes are more difficult to permeate; however, significant

amounts of hydrogel can be incorporated into all lattices (V_v down to about 45%) despite the high viscosity of the hydrogel forming solution.

The hydrogel content in these core-shell scaffolds as well as its morphology are held in high consideration because the shell is expected to be the first site of new bone formation, due to its bioactive properties, its faster degradation rate and its open interconnected porosity, allowing penetration of cells and biological fluids. Indeed, the higher is the hydrogel content in the scaffolds, the greater is the amount of water they absorb, as represented in Figure 2.4d. The obtained values of water uptake range between 30 wt% and 300 wt% ca. and their trend projection at a hydrogel content of 100 wt% is consistent with the typical values found for the pure hydrogel [62], confirming that the confinement within the lattice structure does not alter the hydrogel water absorption.

Finally, as regards TPE-hydrogel specimens, analogous considerations can be made in terms of correlations between SC lattice cell size, core void volume fraction, hydrogel content and water uptake. The presence of stringing in the lattice holes causes a reduction in core void volume fractions values (20–85%) with respect to theoretical values, but does not prevent hydrogel penetration inside the core, so that hydrogel content (1–30%) and water uptake (5–200%) are overall close to the expectations for the obtained void volume fractions.

2.3. Mechanical properties of PLA core structures

2.3.1. Compression tests on cubic specimens

The mechanical properties of core and core-shell scaffolds are evaluated under compression along both z and xy directions. The results of compression tests are reported as apparent stress (σ_{app}) *vs.* apparent strain (ε_{app}), from which stiffness and strength were calculated, as described in paragraph 2.1.3.5. In Figure 2.5, the curves of two PLA core specimens (SC with w = 0.5 mm and w = 2 mm) are shown as reference to describe the typical response of the core under compression.

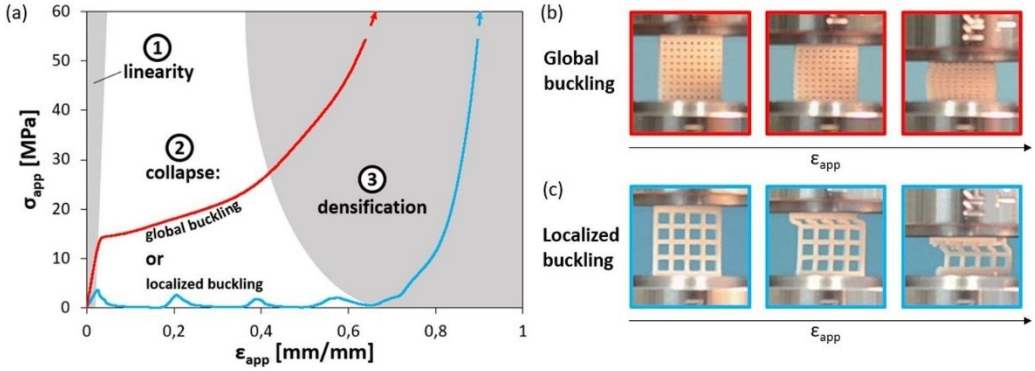

Figure 2.5: Compressive behavior of core specimens: (a) examples of curves plotting the apparent stress, σ_{app}, against the apparent strain, ε_{app}, for lattices displaying either global or localized buckling (a SC PLA lattice with w = 0.5 mm and one with w = 2 mm, respectively); (b) global buckling during the compression test of the SC specimen with w = 0.5 mm along z; (b) localized buckling during the compression test of the SC specimen with w = 2 mm along z.

For all the studied core lattices, like in many cellular materials [92], three separate regions can be recognized in stress-strain curves (examples in Figure 2.5a): (i) an initial linear portion up to apparent strain values of about 2–5%; (ii) a following region associated with collapse of the structure due to an unstable bending deformation (buckling) of the core struts under compression; (iii) a final tract with rapidly increasing slope, ascribed to the densification occurring in the lattice structure after all the walls of the cells come in contact with each other. The buckling phenomena observed during the tests can be reconducted to two main types of behavior: (i) global buckling of the struts throughout the entire specimen, typically

leading to a stress-strain curve with a knee-point followed by a plateau (*e.g.*, SC core with w = 0.5 mm in Figure 2.5b); (ii) localized buckling events, each visible as a stress peak in the curve (*e.g.*, SC core with w = 2 mm in Figure 2.5c). According to Euler-Bernoulli beam theory, the slenderness of a beam favors buckling under compression, therefore longer struts are more prone to local unstable deformations. Indeed, one or more stress peaks are visible in the compression curves of core lattices featuring greater free length of the struts along the loading direction, while specimens with shorter struts tend to exhibit global buckling.

Considering PLA cubic core specimens, Figure 2.6 reports a more detailed representation of stress-strain curves for each different strut arrangement, hole width and testing direction.

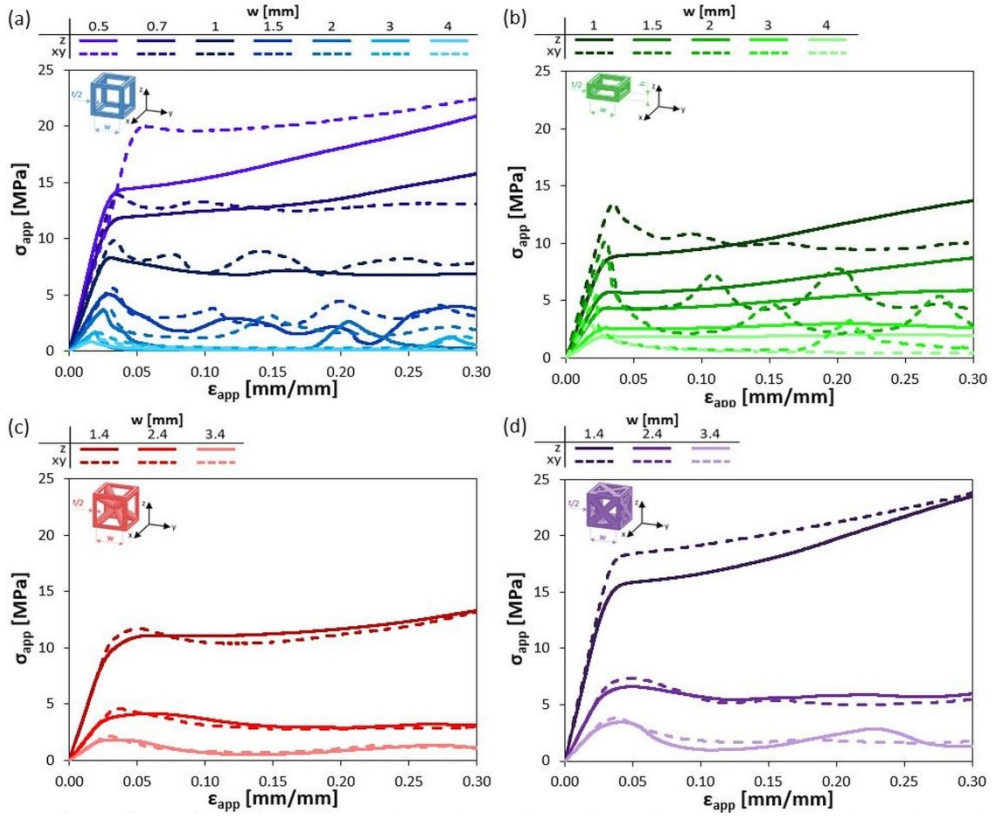

Figure 2.6: Magnification up to 30% strain of apparent stress, σ_{app}, versus *apparent strain, ε_{app}, curves for SC (a), ST (b), BCC (c) and FCC (d) PLA lattices: an example is reported for each value of hole width (w) and for each loading direction (z: build direction; xy: transverse direction).*

For compression test along the build direction, z, the buckling behavior of SC lattices (Figure 2.6a) affects the entire specimen for w = 0.5-0.6 mm, and progressively shifts to a more localized type of response as the hole width increases. A similar trend is also observed in the xy direction, though in this case a higher number of peaks tends to be found in the curves and even the lattices with the smallest holes exhibit a slight peak when entering the second regime; such an effect may be ascribed to differences either in stiffness or strength between struts which are parallel or perpendicular to the printing direction. As one could expect, the anisotropy is much more evident in ST lattices (Figure 2.6b), because of the different free length of the struts under the loading direction: along z, the free length equals to h = 0.6 mm and global buckling prevails; along xy, the free length corresponds to w and takes on values from 1 mm upwards, favoring localized unstable deformations. Finally, the addition of diagonal struts in BCC and FCC (Figure 2.6c,d) specimens slightly reduces the free length of the other struts and overall seems to act as a constraint against buckling, leading to less pronounced peaks in stress-strain curves. Moreover, especially along xy, the behavior of these structures is also characterized by inner splitting of the cores, caused by delamination at the interface between the printed layers of some struts; this may be due to the higher degree of constraint or to weaker adherence between layers possibly caused by the difficulty of printing complex lattices with many overhangs.

The effect of the void volume fraction on the core mechanical properties can be better appreciated by plotting apparent modulus (E_{app}, Figure 2.7a) and apparent failure stress ($\sigma_{app,f}$, Figure 2.7b) of each lattice against its corresponding V_v value. A clear and expected decreasing trend is visible for both strength and stiffness and for all lattice types, highlighting the importance of V_v as tunable parameter for tailoring not only the hydrogel content but also the mechanical response of the scaffolds. From Figure 2.7 it also possible to appreciate the effects of two other key parameters, namely the orientation of the printing layers and the strut arrangement.

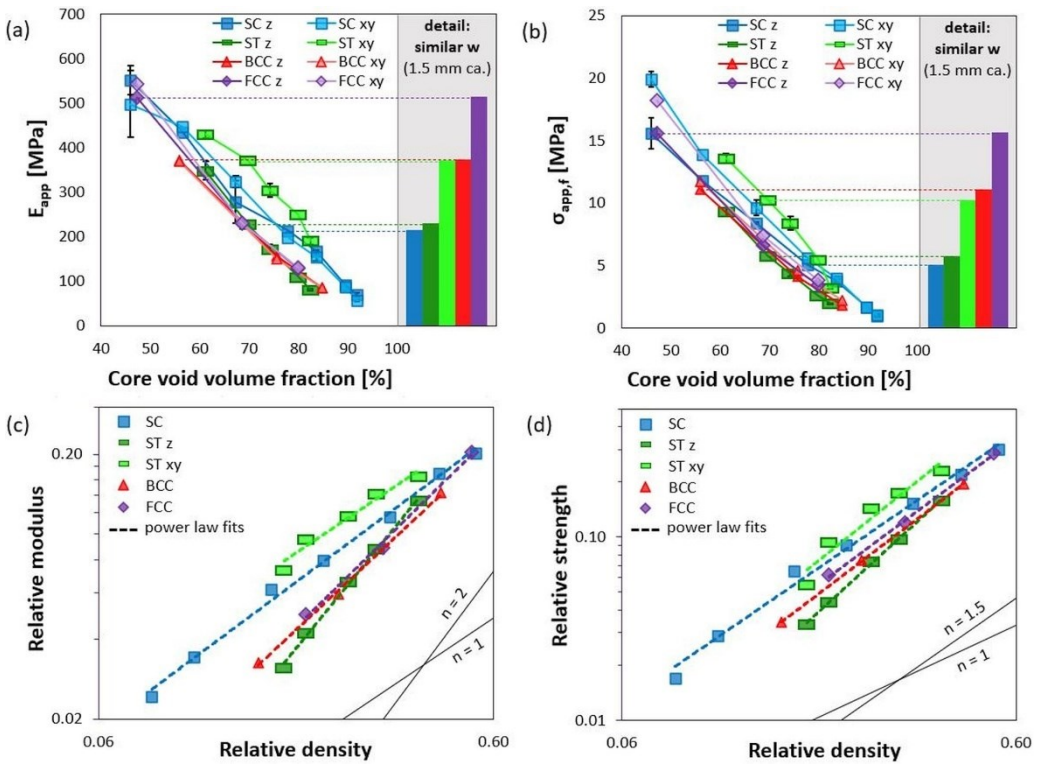

Figure 2.7: (a,b) Apparent modulus, E_{app} (a), and apparent failure stress, $\sigma_{app,f}$ (b), of cubic PLA core specimens, plotted against their void volume fraction; in the details, strength and stiffness are reported for five specimens with similar values of hole width (w = 1.4-1.5 mm) but different lattice cell (left to right: SC z; ST z; ST xy; BCC z; FCC z). (c,d) Relative modulus (c) and relative strength (d) of cubic core lattices plotted against their relative density on a log-log graph; dashed lines are power law fits of experimental average values, with exponent n as slope.

Table 2.3: Values of fitting constant, C, and exponent, n, for power-law fits of relative modulus vs. *relative density and relative strength* vs. *relative density of cubic PLA core specimens.*

Unit cell type	Fitting parameters for power law: $P/P_c = C\rho_{rel}^n$			
	Relative modulus fitting		Relative strength fitting	
	C	n	C	n
SC	0.41	1.11	0.79	1.48
ST (along z)	0.77	1.83	1.03	1.97
ST (along xy)	0.45	1.00	1.31	1.73
BCC	0.44	1.39	0.74	1.63
FCC	0.51	1.46	0.78	1.60
Stretching-dominated	-	1	-	1
Bending-dominated	-	2	-	1.5

For specimens having the same nominal structure along z and xy directions (*i.e.*, formed by SC, BCC and FCC unit cells), the choice of the loading direction has negligible effect on their compressive stiffness (Figure 2.7a). Their compressive strength (Figure 7b) is more affected by the anisotropic arrangement of the printing layers, although still to a moderate extent. In fact, slightly lower $\sigma_{app,f}$ values are found along z, which is likely due to the discontinuous nature of FDM-printed parts at the interface between layers; this difference tends to decrease as the void volume fraction increases. As regards ST specimens, the effect of layer orientation is obscured by the anisotropy of their strut arrangement. In fact, their hole height (h = 0.6 mm) is always lower than their hole width ($w \geq 1$ mm), which results in a higher number of transverse struts and, ultimately, in significantly higher mechanical properties along xy.

To better elucidate the effect of the strut arrangement, E_{app} and $\sigma_{app,f}$ are compared for specimens with similar values of hole width (1.5 mm ca.) but different lattice structure, as shown in the details of Figure 2.7a,b. The addition of transverse struts in ST lattices with respect to SC ones only slightly improves the mechanical properties along z, but greatly increases the performances along xy, whereas diagonal struts act as reinforcement also in the z direction of BCC and, above all, FCC lattices. However, adding struts reduces the core void volume, and thus the available space to host the bioactive hydrogel. Therefore, a proper design of the scaffolds should more conveniently rely on a representation of the properties as a function of V_v, (*i.e.* curves in Figure 2.7a,b). In this way, taking the curves of SC structures as reference, the addition of transverse struts actually improves the mechanical response along xy, but at the cost of a reduction of strength and stiffness along z. Moreover, BCC and FCC lattices show trends close to those of ST lattices tested along the z direction, therefore appearing weaker than SC lattices; nevertheless, they may still be considered in view of reinforcing the scaffolds along their diagonals. Indeed,

struts parallel to the loading direction provide the main contribution to the mechanical properties for all the examined core structures.

For each PLA cubic lattice type, relative modulus and relative strength were represented as a function of relative density (eq. 2.12) and fitted with a Gibson-Ashby power model (eq. 2.13). Fitting curves are represented by dashed lines in Figure 2.7c and Figure 2.7d, respectively, and the values of the fitting constant C and the exponent n are displayed in Table 2.3. Two separate fits were obtained for ST lattices tested along z and along xy directions, due to the anisotropic strut arrangement of ST specimens. All series of data adequately comply with power law models, so that by knowing the core structure and the corresponding values of C and n it is possible to determine the mechanical properties of core-shell scaffolds for any value of core relative density within the range of the power-law fit. Thus, power law fits represent useful tools for the prediction of the core behavior in the design phase of the scaffolds.

In addition, the values of the exponent n provide information about the deformation behavior of each lattice type. Theoretical values of n for stretching-dominated and bending-dominated cellular structures were calculated by Gibson and Ashby and are reported both in Figure 2.7a,b and Table 2.3 for comparison [136]. As one can see, the slope of the power low fits is different for the various systems, depending in particular on the alignment of the struts with respect to the loading direction, as especially observed in ST lattices compressed along different directions. From relative modulus fits, SC lattices result stretching-dominated ($n \sim 1$), consistently with the findings of other works on SC systems (Altamimi *et al.* [96]; Maconachie *et al.* [98]). ST lattices are stretching dominated along xy and mostly bending-dominated along z ($n \sim 2$). Finally, BCC and FCC structures are associated to intermediate values of n, corresponding to a mixed deformation mode, which is also an intermediate result between those of BCC and FCC lattices tested by

Altamimi *et al.* (stretching-dominated) and Maconachie *et al.* (bending-dominated). Relative strength fits are less markedly differentiated, and from their n values they seem more closely associated to the bending-dominated deformation mode. This may be ascribed to a much higher degree of misalignment of lattice struts observed when their cells collapse, showing evident buckling phenomena.

2.3.2. Compression and bending tests on cylindrical specimens

Further analyses on the effect of the number and orientation of struts in the core were conducted on cylindrical PLA specimens, studying several loading conditions: (i) longitudinal compression along the cylinder axis (Figure 2.8a); (ii) transversal compression (Figure 2.8b, also reporting a detail of the orientations adopted for the specimen cross-sections); (iii) three-point bending of a slender specimen, tested with

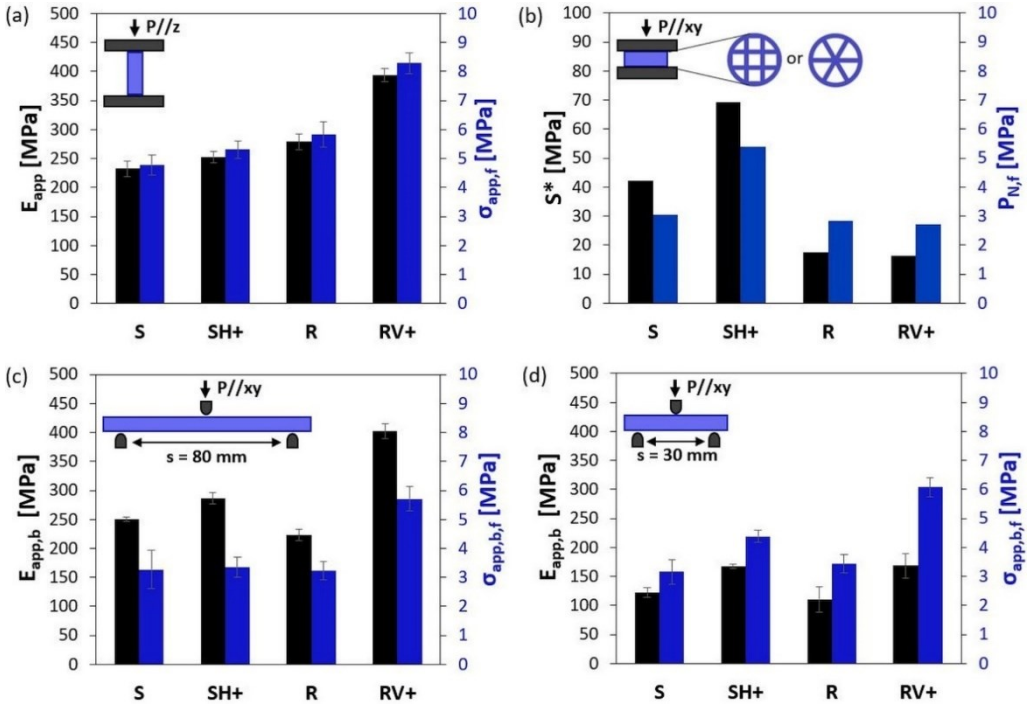

Figure 2.8: Mechanical properties of cylindrical PLA core specimens with S, SH+, R and RV+ strut arrangement: (a) apparent modulus, E_{app}, and apparent failure stress, $\sigma_{app,f}$, under longitudinal compression; (b) stiffness parameter, S, and normalized failure load, $P_{N,f}$, under transversal compression; (c) apparent bending modulus, $E_{app,b}$, and apparent bending failure stress, $\sigma_{app,b,f}$, under three-point bending with span equal to 80 mm; (d) $E_{app,b}$, and $\sigma_{app,b,f}$, under three-point bending with span equal to 30 mm.*

a span equal to 80 mm (Figure 2.8c); (iv) three-point bending of a shorter specimen, tested with a span equal to 30 mm (Figure 2.8d). For each type of test, Figure 2.8 reports the results in terms of stiffness and strength, evaluated as described in the paragraphs 2.1.3.5 and 2.1.3.6. In particular, in the case of transverse compression, they were calculated from normalized load (P_N) vs. normalized displacement (U_N) curves, because the geometrical parameters A and L in eq. 2.6 and eq. 2.7, respectively, have not constant values under this test configuration.

By comparing the results of longitudinal and transversal compression tests (Figure 2.8a,b), the predominant influence of struts parallel to the loading direction can be observed. In fact, SH+ lattices are only slightly stiffer and stronger than S ones along z but much more robust along xy, whereas RV+ lattices have mechanical properties similar to those of R ones along xy but higher stiffness and strength along z. Therefore, reducing the void volume fraction is not sufficient to improve the mechanical performance of the core, which should be carefully designed in order to reinforce the most critical directions for each specific application.

Analogue reasoning can be applied also to loading conditions other than uniaxial loads. The example of a slender beam subjected to three-point bending is reported in Figure 2.8c, showing the superior performance of RV+ specimens. It may be concluded that the best strategy against bending loads is the addition of struts in the outer ring of the cylinder, *i.e.* as far as possible from the neutral axis of the beam. However, scaffolds confined within a bone defect are more likely to undergo a combination of bending and shear rather than pure bending [137], therefore a second set of three-point bending tests (Figure 2.8d) was carried out on shorter lattice beams, which should experience more significant shear effects. With regard to stiffness, this situation seems to reduce the advantage provided by the presence of more struts in the outer ring of the cylinders. Nevertheless, the values of strength obtained for the different strut arrangements are in line with those found in slender beams and confirm the superior resistance of RV+ specimens under bending.

Indeed, both slender and shorter beams fail at the bottom of their middle section, where the bending moment creates the maximum tension; here, a crack propagates between printing layers, rapidly splitting the specimen in two halves.

2.4. Mechanical properties of PLA-hydrogel scaffolds and proof-of-concept of softer core-shell scaffolds

2.4.1. Mechanical properties of PLA-hydrogel scaffolds

The mechanical properties of the PLA specimens were compared with those of the final scaffolds for all types of lattice structures. The stress-strain curve of each core-shell system appears similar to that of its core for all external shapes, strut arrangements, hole dimensions and testing directions under analysis. As examples, some compression curves of core and core-shell specimens are provided in Figure 2.9a for SC lattices and in Figure 2.9b for cylindrical structures, both tested along the build direction. The closest similarity is found in the linear portion of the curves, until failure occurs, whereas the position and shape of later stress peaks associated with buckling may vary, but analogous variations are observed even within the same group of specimens and cannot be attributed to the presence of the hydrogel. Accordingly, the stiffness and strength evaluated for the hybrid scaffolds are entirely comparable with those of the corresponding core structures, as shown in Figure 2.9c in the case of compression tests along z. It may be concluded that the contribution of shell to the mechanical properties of the scaffolds is negligible, which is reasonable because its stiffness is significantly lower compared to that of the core. Indeed, the hydrogel has a Young's modulus in the order of 10^{-2}-10^{-1} MPa [62], while even the most porous PLA lattices have values of apparent modulus at least 2 orders of magnitude higher.

Exactly as the mechanical properties of core specimens, stiffness and strength of the hybrid scaffolds decrease as the core void volume fraction increases, following trends analogous to those of the corresponding lattices. In order to compare the mechanical properties of the scaffolds with those of biological tissues, these results were rewritten as a function of the overall density of the core-shell specimens and reported against density on material property charts showing the typical ranges of

compressive modulus (Figure 2.10a) and strength (Figure 2.10b) of some types of bone and cartilage tissues.

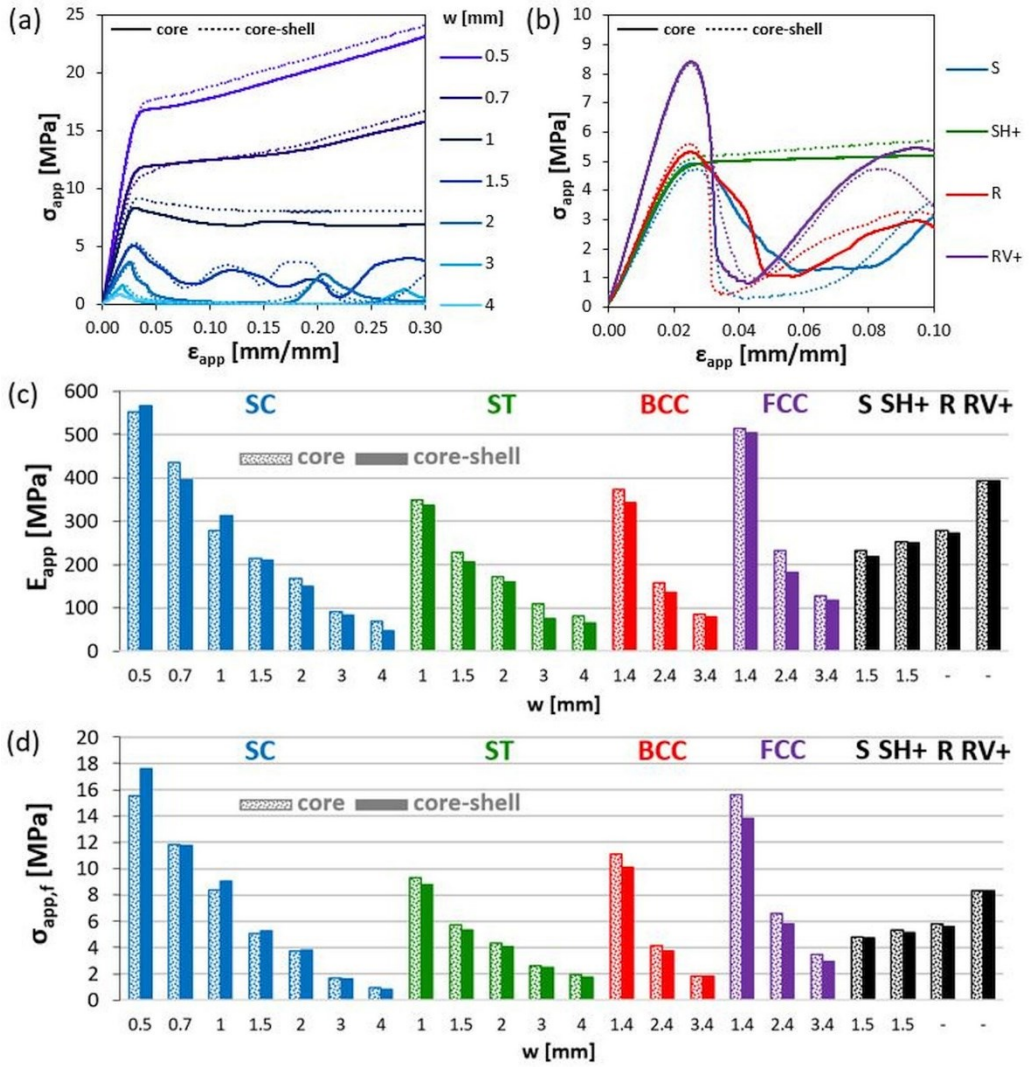

Figure 2.9: Comparison between the mechanical behavior of PLA lattices and that of PLA-hydrogel core-shell specimens, in the case of compression along z: (a) examples of apparent stress versus *apparent strain curves for SC lattices; (b) examples of apparent stress* versus *apparent strain curves for cylindrical lattices; (c) apparent modulus, E_{app}, for all lattice types; apparent failure stress, $\sigma_{app,f}$, for all lattice types.*

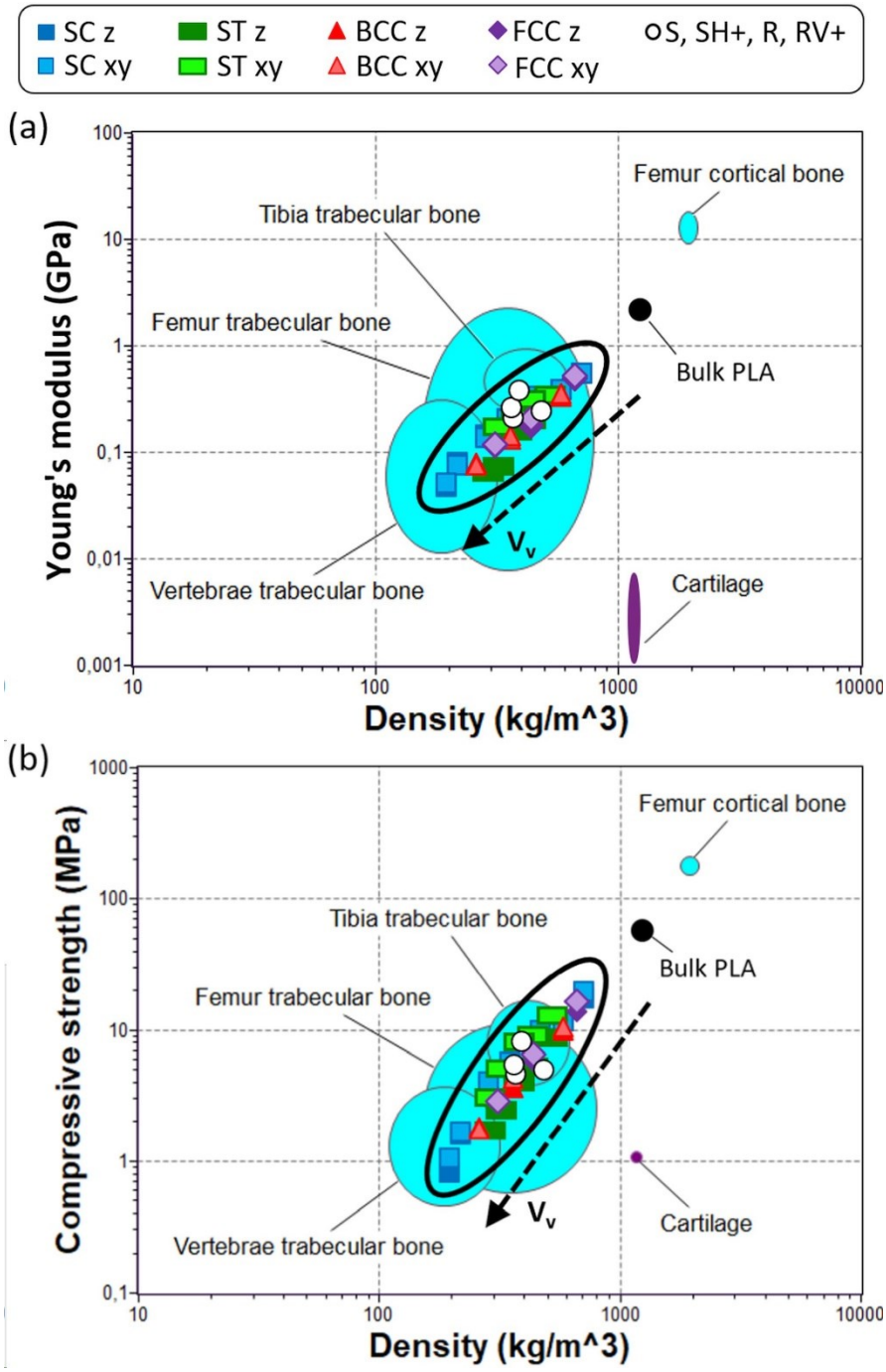

Figure 2.10: Young's modulus (a) and compressive strength (b) plotted against density for all the types of composite scaffolds, for bulk PLA and for a set of biological tissues filed in the database of CES Selector software by Granta Design.

Overall, the hybrid systems examined cover a range between 0.2 and 0.7 g/cm^3 in terms of density, while their modulus varies between about 50 and 550 MPa and their strength is between about 1 and 20 MPa. As the void volume fraction increases, the properties deviate from those of bulk PLA, with decreasing trends that differ from each other according to the core lattice type. While compact bone tissue, such as that of the femur on the charts, is typically stiffer, stronger and denser than bulk PLA, several types of trabecular bone tissue exhibit properties similar to the hybrid scaffolds (spongy bone Young's modulus: 10 ÷ 2000 MPa; spongy bone compressive strength: 0.3 ÷ 50 MPa; spongy bone density: 0.1 ÷ 1.0 g/cm^3 [92]); in addition, the mechanical properties of PLA-hydrogel core-shell specimens can reach higher values with respect to several hybrid scaffolds proposed in literature for bone regeneration (see Table 2.4), and this may be particularly beneficial in load-bearing anatomical sites. As for cartilage, it has usually lower values of elastic modulus, but strength values comparable with those of the lightest core-shell scaffolds.

Table 2.4. Comparison of compressive modulus and strength of PLA-hydrogel core-shell scaffolds with those of other hybrid scaffolds. Each scaffold type is described in terms of component materials and void volume percentage, the latter (*) referred to the rigid component of the scaffold.

Hybrid scaffold components	**Void volume* [%]**	**Compr. modulus [MPa]**	**Compr. strength [MPa]**	**Ref.**
PLA (core) + gelatin-chitosan hydrogel (shell)	40 ÷ 90	50 ÷ 550	1 ÷ 20	[138]
PCL + chitosan hydrogel	62	n.a.	5	[58]
PCL + calcium phosphate	59	n.a.	5 ÷ 10	[54]
PCL + alginate hydrogel with adhesion peptides	67	1.4	n.a.	[59]
Calcium-deficient hydroxyapatite + alginate hydrogel	n.a.	7	n.a.	[55]
PLA + gelatin methacrylate hydrogel with gold nanoparticles	74 ÷ 87	300 ÷ 800	n.a.	[89]
Flexible PLA + alginate hydrogel	60 ÷ 85	0.3 ÷ 4.5	n.a.	[90]

Based on these data, it is hypothesized that scaffolds composed of a PLA core and a hydrogel shell exhibiting osteogenic properties would be best employed in tissue engineering for trabecular bone regeneration. However, when seeded with mesenchymal stromal cells and cultured in an osteogenic medium, new bone tissue soon replaces the hydrogel as it degrades [65], thus gradually reinforcing the material; therefore, the possibility of regenerating portions of cortical bone should be favored. Positive expectations are supported also by cell proliferation and mineralization observed on previous scaffolds developed from the authors using the hydrogel alone or combined with PLA-based blends, in spite of the lower mechanical properties of such materials compared to the present core-shell systems (*e.g.*, Young's modulus of the neat hydrogel: 0.25 ± 0.03 MPa; Young's modulus of a PLA-based core combined with a hydrogel shell: 70 ± 15 MPa) [62,71]. Moreover, considering also the good chondrogenic differentiation results of the gelatin-chitosan hydrogel [63], healing osteochondral defects may be a further application to consider for the scaffolds with the lowest core/shell ratios, though they may be still excessively stiff for cartilage replacement.

Furthermore, it is worth highlighting that the selection of a proper core/shell ratio and of a specific strut arrangement allows tailoring the properties of the hybrid scaffolds according to the exact type of target tissue and to its most stressed directions. In addition, aiming to expand the set of target tissues, the achievable ranges of stiffness, strength and density may be further extended by varying the core material, while different compositions of the hydrogel may be considered in order to attain different bioactive properties. As a proof-of-concept, the following paragraph presents the compression properties of softer scaffolds with a TPE core and a gelatin-chitosan hydrogel shell.

2.4.2. Proof-of-concept of softer TPE-hydrogel core-shell scaffolds

Compression stiffness and strength values of core-shell specimens with soft TPE core are reported and compared to those of PLA-hydrogel specimens in Figure

2.11a and 2.11b, the latter also reporting the properties of cartilage and bone tissues. TPE-hydrogel scaffolds have apparent modulus values between about 1 MPa and 20 MPa and apparent failure stress values between about 0.1 MPa and 4 MPa.

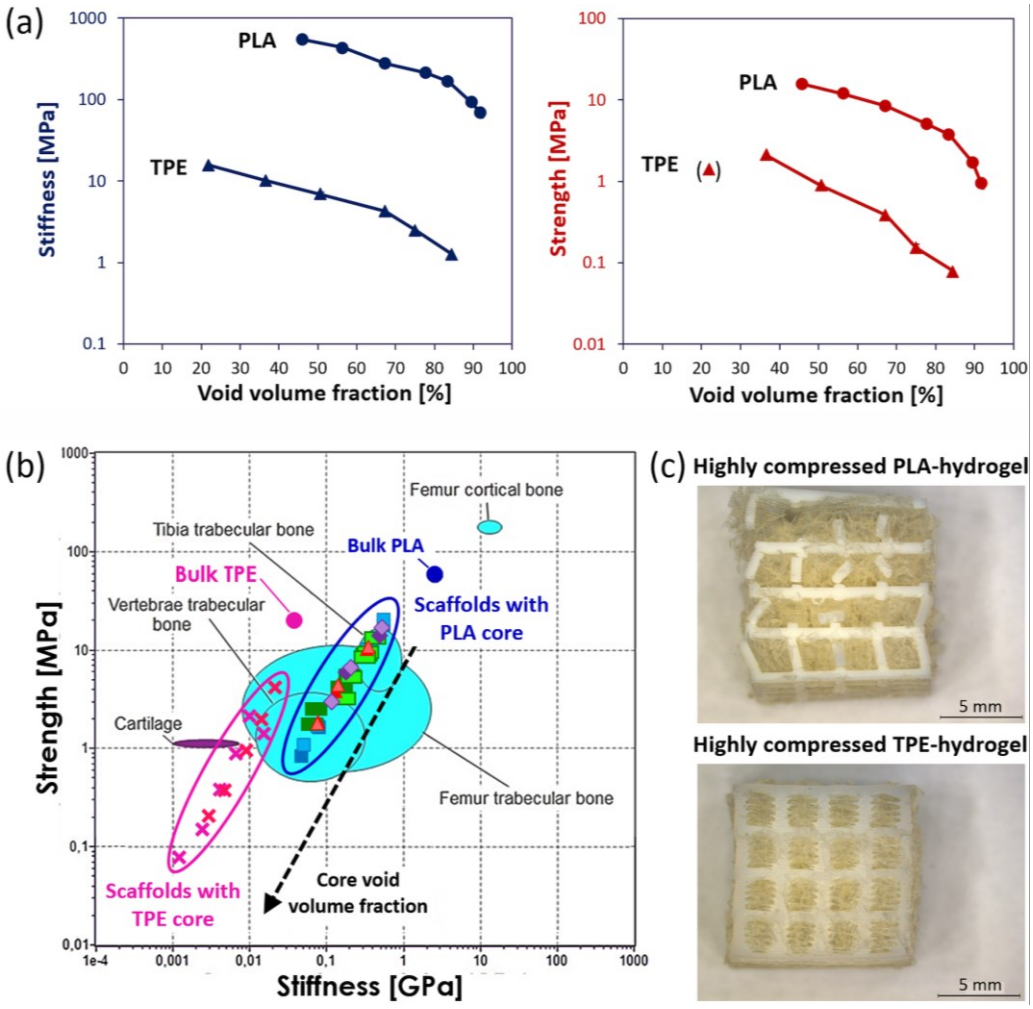

Figure 2.11: (a) Compressive stiffness and strength of TPE-hydrogel scaffolds compared to those of PLA-hydrogel scaffolds tested along z; the out-of-trend datapoint between brackets corresponds to a particularly smooth slope change in stress-strain curves, encountered only for the smallest hole size of the TPE core. (b) Comparison of compressive properties of TPE-hydrogel and PLA-hydrogel scaffolds with those of cartilage and bone tissues filed in the database of CES Selector software by Granta Design. (c) Photographs of scaffolds with PLA and TPE core after compression along z up to 50% apparent strain.

Compared to PLA-hydrogel scaffolds with the same core design (SC lattices), they exhibit much lower stiffness and strength (differences of 1-2 orders of magnitude) due to their softer core material. The mechanical properties of denser TPE lattices are close to those of highly porous trabecular bone tissue, but their values decrease as the core void volume increases, becoming comparable to those typical of cartilage (or even lower). nterestingly, after application of large apparent strain values (50% ca.) and unloading, TPE-hydrogel scaffolds can recover almost all of their deformation, while in PLA-hydrogel scaffolds only the hydrogel is able to recover large deformations (Figure 2.11c).

Furthermore, a more complete comparison of PLA and TPE as core materials is provided in Table 2.5, highlighting their differences not only in terms of composition and mechanical behavior but also concerning their thermal properties, biodegradability and biocompatibility. In light of such differences, possible applications in regenerative medicine vary as well.

The most evident difference is that, at both room and human body temperature, PLA core structures are made of a rigid thermoplastic polymer, whereas TPE lattices behave more similarly to elastomers. In fact, under such temperature conditions, PLA is well below its transition temperatures, whereas TPE soft segments are amorphous and rubbery (past both glass and melting transitions) and the hard ones seem to have rather low crystallinity [133,139]. This is clearly reflected by the mechanical behavior of scaffolds prepared with different core materials, which are stiffer and stronger when presenting a PLA core, softer and capable of recovering rather large deformations when realized with a TPE core.

Moreover, FILOALFA® BioFlex TPE filament is already known to be compliant to several biocompatibility tests (ISO 10993-4,5,10,11 – see Table 2.5 for details) [135], while Raise3D Premium PLA is a commercial product with no medical certification; however, its base material is also biocompatible, so that a medical-grade substitute can be found for *in vivo* applications (see the one used in Chapter 4).

Finally, bioresorption requires long times for both materials [140,141], which is are expected to guarantee mechanical support while the hydrogel leaves space to new tissue growth; on the other hand, it may be not ideal for tissues exhibiting rather fast regeneration rate.

In conclusion, both PLA and TPE are potentially valid core materials for biocompatible and biodegradable composite scaffolds that may provide long-term support during tissue regeneration processes, and they should address different tissue engineering cases based on their specific mechanical properties. On average, PLA-hydrogel core-shell systems appear more suitable for bone regeneration, while softer scaffolds may be more appropriate for cartilage tissue engineering, as suggested also by a work of Gnatowski *et al.* on nasal septum cartilage implants [141].

Table 2.5. Comparison of PLA and TPE as core materials of the scaffolds.

	PLA [133,140] (Raise3D Premium PLA)	**TPE** [135,139,141] (FILOALFA® BioFlex)
Composition	Mostly poly-L-lactic acid (> 90%)	Thermoplastic copolyester based on aromatic polyester-ether compounds
Thermal properties	• Glass transition at 61 °C • Melting at 150 °C	• Glass transition at -69 °C • Melting at 0 °C (soft segments) and 189 °C (hard segments)
Mechanical behavior (scaffolds with SC lattice core)	• Stiffness of 1 ÷ 20 MPa • Strength of 0.1 ÷ 4 MPa • Cannot recover large strains at unloading	• Stiffness of 50 ÷ 500 MPa • Strength of 1 ÷ 20 MPa • Can recover large strains at unloading
Biocompatibility	Not certified biocompatibility (but other PLA-based biocompatible filaments exist, such as the one used in Chapter 4 of this thesis)	Hemolysis tests (ISO 10993-4:2002/Amd 1:2006, ASTM F756 2008); intracutaneous test (ISO 10993-10:2010); systemic injection test (ISO 10993-11:2006, ASTM F 750-82); cytotoxicity (ISO 10993-5:2009)
Bioresorbability	Hydrolytic degradation in 1-2 years	7% mass loss after 2 months in 0.01 M phosphate-buffered saline
Possible target	Bone tissue	Cartilage tissue

2.5. Conclusions

In this chapter, hybrid scaffolds with a core-shell structure are conceived as a versatile strategy to match all fundamental requirements of tissue engineering and potentially address the regeneration of a variety of different biological tissues. More specifically, composite scaffolds consisting of 3D-printed core structures integrated with a hydrogel shell are realized and studied with the aim to provide a better understanding of the correlations between core structure, mechanical performances, and hydrogel content.

Here, bone tissue engineering applications are specifically addressed through a core consisting of 3D-printed PLA lattice structures, mainly offering mechanical support, and a shell composed of a bioactive hydrogel exhibiting osteogenic properties. Aiming to highlight the possibility of extending the approach to cover a broad range of applications, softer scaffolds are also produced by replacing PLA with a thermoplastic elastomer. Noteworthily, lattices differing in void volume fraction and strut arrangement are all thoroughly permeated by the hydrogel forming solution, and the obtained shell maintains interconnected pores and water absorption similar to the free bioactive hydrogel.

The reinforcement provided by the PLA core allows reaching stiffness and strength comparable to those of several spongy bone types, whereas softer core structures display mechanical properties closer to those of cartilage. Moreover, FDM proved to be a suitable AM technique for the customization of the scaffolds, not only in terms of geometry but also as regards their mechanical properties. In fact, this study shows how to draw useful structure-property correlations from experimental data and highlights the possibility to specifically reinforce the scaffolds according to different loading conditions. An extended discussion on possible approaches to model these correlations is provided in Chapter 5.

Finally, by acting on the core void volume fraction, the hydrogel content can also be tailored. This shell fraction is particularly important with respect to the scaffold

degradation and bioactive properties, which should enable new bone tissue formation. Focusing on PLA-hydrogel scaffolds, these aspects are investigated in the following Chapter 3 through *in vitro* experiments. In addition, potential translational applications in maxillofacial regenerative medicine are discussed in Chapter 4.

On a broader perspective, the findings here reported open the possibility of a more versatile scaffold design, based on combining the advantages of different biomaterials and experimenting with many possible configurations, by acting on several variables, such as the nature of the materials and the structure of both the core and the shell, as well as their mutual proportions and mutual arrangement.

3. PLA-Hydrogel Core-Shell Scaffolds for Bone Tissue Engineering: Thermal, Degradation, and *In Vitro* Studies

In this chapter[3], composite scaffolds with a PLA core and a gelatin-chitosan hydrogel shell were prepared by FDM of PLA lattice structures and subsequent grafting of the bioactive hydrogel. As described in detail in Chapter 2, these scaffolds may ensure long-term temporary mechanical support, owing to their stiff core, as well as a favorable environment for cell growth and colonization throughout the hydrogel, which is destined to be faster replaced by new tissue during the regeneration process. Moreover, the performance of the scaffolds can be easily modulated by properly tailoring their 3D-printed core structure and the associated core-shell proportions. While Chapter 2 especially focused on correlations between scaffold structure and mechanical properties, the analysis of the scaffolds is here extended to thermal, degradation, and biological properties.

First, results of differential scanning calorimetry (DSC) are illustrated for PLA before and after 3D printing, and dimensional stability of the core upon heating is assessed. Then, three different types of lattices, hosting different amounts of hydrogel, are investigated upon immersion in water and cell culture. Special attention is dedicated to the effect of hydrolytic degradation on the scaffold strength, stiffness, and hydrogel stability. After sterilization, the composite materials were delivered to the Department of Clinical and Experimental Sciences, where they were seeded with bone marrow-derived human mesenchymal stromal cells (BM-hMSCs) and

[3] Most of the work presented in this chapter is published in reference [163]: C. Pasini, S. Pandini, F. Re, M. Ferroni, E. Borsani, D. Russo, L. Sartore, *New Poly(lactic acid)–Hydrogel Core–Shell Scaffolds Highly Support MSCs' Viability, Proliferation and Osteogenic Differentiation*, Polymers 15 (2023) 4631.

subjected to cell viability, proliferation, morphology and mineralization assessments.[4]

Compression stiffness and strength provided by PLA lattices are overall within the range of values displayed by human bone tissue and remain stable after prolonged immersion in water at body temperature for several weeks; dimensional stability is also verified up to 60 °C, when PLA glass transition occurs. On the other hand, the hydrogel undergoes gradual and homogeneous degradation over time, but the core-shell integrity and structural stability are nevertheless maintained during at least 7-week hydrolytic degradation tests. *In vitro* experiments with BM-hMSCs reveal that the core-shell scaffolds are biocompatible and their physical-mechanical properties and architecture are suitable to support cell growth and osteogenic differentiation, as demonstrated by hydroxyapatite formation.

These results suggest that the bioresorbable core-shell scaffolds can be considered, and further studied, in view of clinically relevant endpoints in bone regenerative medicine. In this thesis, the specific use of these materials in mandibular defects in a rabbit model is addressed in Chapter 4, dealing with the development of *ad hoc* PLA-hydrogel scaffolds and with their potential translational applications.

[4] Collaborations: Federica Re and Prof. Domenico Russo (Unit of Blood Diseases and Bone Marrow Transplantation, Department of Clinical and Experimental Sciences, University of Brescia, ASST Spedali Civili, Piazzale Spedali Civili 1, 25123 Brescia, Italy) for cell culture, as well as cell viability and proliferation assessments; Prof. Elisa Borsani (Division of Anatomy and Physiopathology, Department of Clinical and Experimental Sciences, University of Brescia, 25123 Brescia, Italy) for histomorpholocial analyses; Prof. Matteo Ferroni (Department of Civil, Environmental, Architectural Engineering and Mathematics, University of Brescia, Via Valotti 9, 25123 Brescia, Italy; CNR—Institute for Microelectronics and Microsystems, Bologna, Via Gobetti 101, 40129 Bologna, Italy) for SEM analyses.

3.1. Materials and methods

3.1.1. Materials

Raise3D Premium PLA filament was provided by Raise 3D Technologies, Inc. (Irvine, CA, USA). Pharmaceutical grade type A gelatin (280 bloom, viscosity 4.30 mPs) was provided by Italgelatine (Cuneo, Italy). Poly(ethylene glycol) diglycidyl ether (PEGDGE) (molecular weight 526 Da) and chitosan (molecular weight 50,000 ÷ 190,000 Da, degree of deacetylation 75–85%) were supplied by Sigma-Aldrich Co (Milan, Italy). Ethylene diamine (EDA) and acetic acid were provided by Fluka (Milan, Italy).

Dulbecco's modified Eagle's medium and fetal bovine serum (FBS) were purchased from Sigma Aldrich, USA. Human platelet lysate (hPL) for MSCs expansion was obtained from blood donations belonging to the Blood Bank of ASST Spedali Civili of Brescia, Italy. Hematoxylin–eosin (H&E) stain was purchased from Bio-Optica, Milan, Italy.

3.1.2. Preparation of core-shell composite scaffolds

Core-shell composite scaffolds were prepared following the procedure described in paragraph 2.1.2.

The core structures here investigated are three PLA lattices with parallelepipedal cells having same strut thickness (t = 0.6 mm) but different hole width (w) along x and y and different hole height (h) along z, according to the cartesian coordinate system in Figure 3.1a. They were properly chosen in order to control the amount of hydrogel that may be hosted by the lattice: low (L), medium (M), or high (H).

Cubic specimens were employed in physical-mechanical characterizations and degradation experiments, while bar specimens were produced for biological characterizations. The outer dimensions of the specimens (A, B, C), as well as the lattice parameters (w, h, t) are all summarized in Figure 3.1 for the different types of structures realized. Both cubic and bar-shaped specimens were 3D-printed with build direction along the z axis.

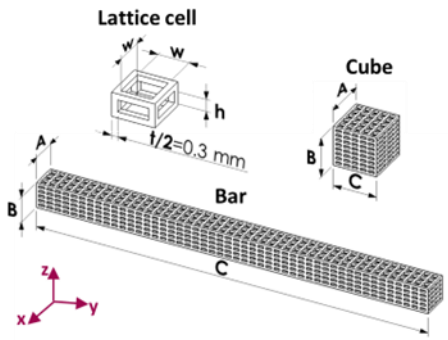

Hydrogel content	w [mm]	h [mm]	Shape	A [mm]	B [mm]	C [mm]
Low (L)	1.5	0.6	Cube	11.1	10.2	11.1
			Bar	6.9	6.6	101.4
Medium (M)	1.5	1.5	Cube	11.1	11.1	11.1
			Bar	6.9	6.9	101.4
High (H)	3.0	1.0	Cube	11.4	10.2	11.4
			Bar	11.4	5.4	101.4

Figure 3.1. Hole dimensions and global dimensions for lattice-structured cubes and bars capable of hosting low, medium or high hydrogel content values.

3.1.3. Physical and mechanical characterization

The physical and mechanical characterization of core-shell composite scaffolds was carried out as described in paragraph 2.1.3, which reports all details of the methods employed (*i.e.*, microscope observations, core void volume fraction and hydrogel content evaluation, water uptake measurements, compression tests).

3.1.4. Thermal characterization and hydrolytic degradation tests

3.1.4.1. Differential scanning calorimetry

Differential scanning calorimetry (DSC) tests were carried out on Raise3D Premium PLA filament, as well as on portions of 3D-printed parts realized with the same material. Samples of about 10 mg were tested by means of a DSC Q100 calorimeter (TA Instruments), using nitrogen as a purge gas (50 mL/min) and applying the following thermal cycle: (i) heating from -50 °C to 200 °C at 10 °C/min; (ii) cooling from 200 °C to -50 °C at 10 °C/min; (iii) heating from -50 °C to 200 °C at 10 °C/min. Using DSC results, PLA crystallinity (X_c) was also calculated, approximating it as 100% poly(L-lactic acid) and applying the following equation:

$$X_c[\%] = \frac{\Delta H_m - \Delta H_{cc}}{\Delta H_m^0} \times 100 \quad (3.1)$$

where ΔH_m is the melting enthalpy, ΔH_{cc} is the cold crystallization enthalpy, and ΔH_m^0 is the reference melting enthalpy (93.6 J/g) for poly(L-lactic acid) crystals having an infinite size [142].

3.1.4.2. Evaluation of dimensional stability upon heating

A dynamical mechanical analysis (DMA) apparatus (DMA Q800 analyzer by TA Instruments, New Castle, DE, USA) was used to record the deformation of cubic PLA lattices during heating. The lattice was positioned between compression plates so that the strain along x could be evaluated. In a first experiment, a thermal ramp from 25 °C to 100 °C was applied, with heating rate of 1 °C/min. A second experiment consisted of a series of isothermal steps (40 °C; 50 °C; 60 °C; 70 °C; 80 °C) of 40 min each. Every time before changing step, pictures of the specimen were collected at the optical microscope in order to measure the deformations along y and z as well, thanks to the image analysis software ImageJ (National Institutes of Health, US).

In addition, small bar-shaped specimens (4.8 mm x 4.8 mm x 51 mm) were subjected to the same series of isothermal steps in an oven. Their photographs were analyzed with ImageJ to measure their curvature at different temperatures.

3.1.4.3. Hydrolytic degradation experiments

The degradation of cubic core-shell scaffolds was studied in distilled water at 37 °C for a total of 7 weeks. The distilled water medium was changed every week.

The evolution of mechanical properties with degradation time was investigated by compression tests on specimens withdrawn at different time points (1 day, 21 days, 35 days, 49 days). Compressive stiffness and strength along degradation time were obtained as described in the previous paragraph.

The mass loss of the specimens was also recorded on scaffolds picked up from the bath at different time points (1 day, 7 days, 21 days, 35 days, 49 days) and dried under vacuum in oven at 40 °C. It was expressed both as percentage of the initial mass of the dry core-shell specimen and as percentage of the initial mass of the dry hydrogel shell:

$$mass\ loss/total\ mass\ [\%] = \frac{m_{cs,dry} - m_{deg}}{m_{cs,dry}} \times 100 \qquad (3.2)$$

$$mass\ loss/hydrogel\ mass\ [\%] = \frac{m_{cs,dry} - m_{deg}}{m_{cs,dry} - m_c} \times 100 \quad (3.3)$$

where $m_{cs,dry}$ is the initial mass of the core-shell specimens in dry conditions, m_{deg} is their mass after degradation and drying, and m_c is the mass of their core.

3.1.5. *In vitro* characterization, optical and electron microscopy

The bar-shaped core-shell specimens were cut along their length into about 20 slices each, obtaining scaffolds with a thickness of about 5 mm. The scaffolds were packed under vacuum into polypropylene bags and sterilized by gamma irradiation by Gammatom Srl (Guanzate, Italy). A dose of 25 kGy of Cobalt 60 gamma rays was used, in compliance with UNI EN ISO 11137 standard for the sterilization of health care products. *In vitro* analyses on sterilized scaffolds were carried out by the Department of Clinical and Experimental Sciences of the University of Brescia.

3.1.5.1. BM-hMSC culture, seeding and osteogenic differentiation

For the purpose of the study, commercial BM-hMSCs (PromoCell, Germany) were expanded, as previously described [65], with growth medium (GM) consisting of Dulbecco's modified Eagle's medium. GM was added to 10% fetal bovine serum (FBS) (hereinafter referred as GM FBS) or 5% human platelet lysate (hPL) (hereinafter referred as GM HPL). Dry scaffolds were seeded with $7x10^5$ viable cells in GM FBS or GM HPL, and the medium was changed three times per week. Each system was analyzed in triplicates on day 28 for cell viability and proliferation.

Additionally, the osteogenic differentiation capability of the scaffolds on day 28 was investigated. For these scaffolds, the GM was substituted with an osteogenic medium (OM) 48 hours after cell seeding. The OM consisted of GM supplemented with dexamethasone, L-ascorbic acid, and NaH_2PO_4. As controls, samples were also maintained in GM for 28 days.

3.1.5.2. BM-hMSC viability and proliferation assay

A Live/Dead kit for mammalian cells and NucBlue® Live reagent (ThermoFisher, USA) were used to evaluate cell viability of BM-hMSCs in the

scaffolds. A fluorescence microscope (Zeiss Observer Z1) was used to observe live cells (stained in green, nuclei in blue) and dead cells (stained in red).

Cell proliferation was determined using the Cell Counting Kit-8 (CCK-8 reagent, Sigma-Aldrich, USA) on day 28 of cell culture on the scaffolds, and measuring the supernatant absorbance at 450 nm, that is proportional to the number of viable cells.

3.1.5.3. Histomorphological analysis at optical microscope

After 28 days of culture, scaffolds were fixed with formaldehyde, dehydrated and embedded in paraffin. 5 μm-thick sections of each sample were cut with a semiautomatic microtome (Diapath S.p.A., Bergamo, Italy). Alternate sections were deparaffinized, rehydrated and stained with H&E stain for analysis of general morphology.

3.1.5.4. Scanning Electron Microscopy observation

Scanning Electron Microscopy (SEM) was used to evaluate both the adhesion and the osteogenic differentiation of the cells. For observation at SEM (ZEISS EVO LS-10), samples have been progressively dehydrated through immersion in alcohol solutions, without deposition of a conductive metal coating, which could be avoided by operating the SEM in environmental mode (0.1-0.2 Torr pressure).

3.2. Physical and mechanical characterization

The composite scaffolds here investigated differ for their core/shell ratio, so they are labelled as PLA-CH(L) (low hydrogel content), PLA-CH(M) (medium hydrogel content), and PLA-CH(H) (high hydrogel content). Core lattices are designed with same strut thickness but different hole size, so that they may host different amounts of hydrogel. The width (w) and height (h) of the holes are defined in Figure 3.1, together with the overall dimensions of the specimens.

The appearance of wet core-shell specimens employed for physical-mechanical characterizations is shown in Figure 3.2a from different viewpoints. Magnified details show that core struts are composed by smaller PLA filaments, with width equal to the nozzle diameter (0.2 mm) in the top view, and height corresponding to the layer thickness (0.1 mm) in the side view. The core struts are surrounded by hydrogel, which is able to penetrate deep into the core through its holes, as further demonstrated by the images of dry sectioned specimens for *in vitro* studies in Figure 3.2b; each slice specimen is displayed next to the original core structure of the bar-shaped specimen from which it was obtained. The porous structure of the hydrogel is better shown in images obtained by SEM (Figure 3.2c), highlighting the presence of a heterogeneous network of interconnected pores, suitable for cell colonization as well as oxygen and nutrients supply.

Since the shell occupies all the voids in the core, the hydrogel content depends on the void volume fraction in the core, which in turns varies according to the lattice hole dimensions. All these parameters are reported in Table 3.1 for cubic scaffolds, together with water uptake values after immersion in water for 24 hours. The experimental values of core void fraction are around 70-80% and only slightly higher than those theoretically expected from the CAD models of the lattices. As these values increase, the hydrogel content also grows, leading to correspondingly higher water uptake values, between 100% and 200%.

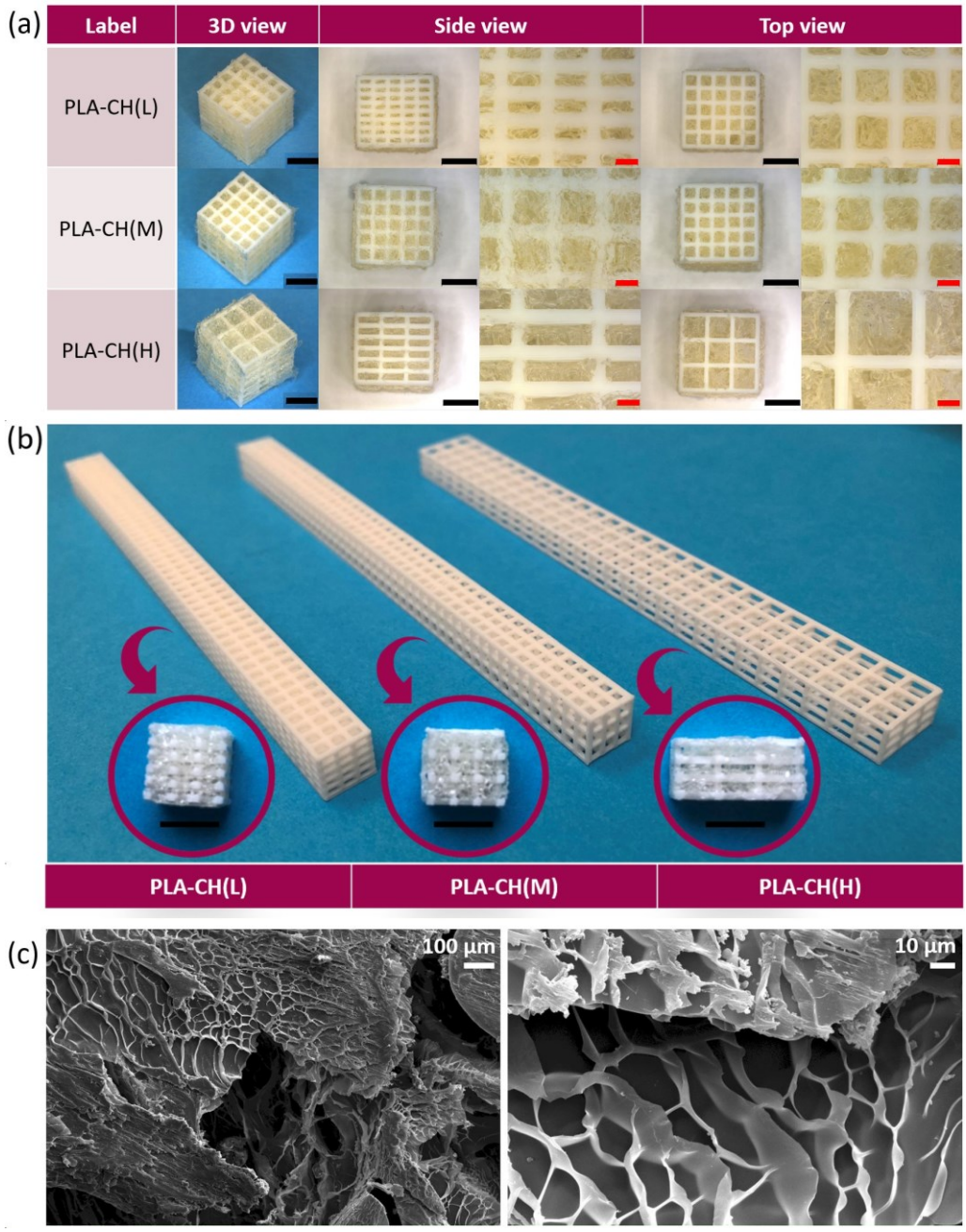

Figure 3.2. Core-shell scaffolds with low (L), medium (M) or high (H) hydrogel content: (a) wet cubic specimens (different viewpoints and magnifications); (b) dry slice specimens for in vitro studies, along with the bar-shaped core specimens from which they were obtained. Markers: 5 mm (black) and 1 mm (red). (c) Porous structure of the hydrogel observed by SEM.

Table 3.1. Dimensions of core holes (w x h), core void volume fraction (theoretical and experimental), hydrogel content (weight fraction) and water uptake of cubic composite scaffolds with low (L), medium (M) or high (H) hydrogel content.

Label	***w* x *h*** **[mm]**	**Core void vol. fraction, th [%]**	**Core void vol. fraction, exp [%]**	**Hydrogel content, exp [%]**	**Water uptake (24 h) [%]**
PLA-CH(L)	1.5 x 0.6	66.3	68.8 ± 0.3	11.6 ± 0.4	102.5 ± 7.4
PLA-CH(M)	1.5 x 1.5	75.3	77.0 ± 0.3	17.6 ± 0.4	137.2 ± 4.3
PLA-CH(H)	3.0 x 1.0	81.9	83.4± 0.2	22.0 ± 0.9	201.4 ± 8.9

More in detail, the increasing trend of the hydrogel content with the core void volume fraction is shown in Figure 3.3, for both cubic and bar-shaped specimens. A theoretical trend is also obtained by means of eq. 2.3, assuming that the porosity of the hydrogel is not affected by the presence of the core struts and that the lattice holes are perfectly filled by the shell. Overall, despite these approximations, the experimental points are only slightly below the theoretical trend (cubes: see Table 3.1; PLA-CH(L) bars: 13.6% ± 0.6%; PLA-CH(M) bars: 19.2% ± 0.4%; PLA-CH(H) bars: 27.1% ± 1.5%).

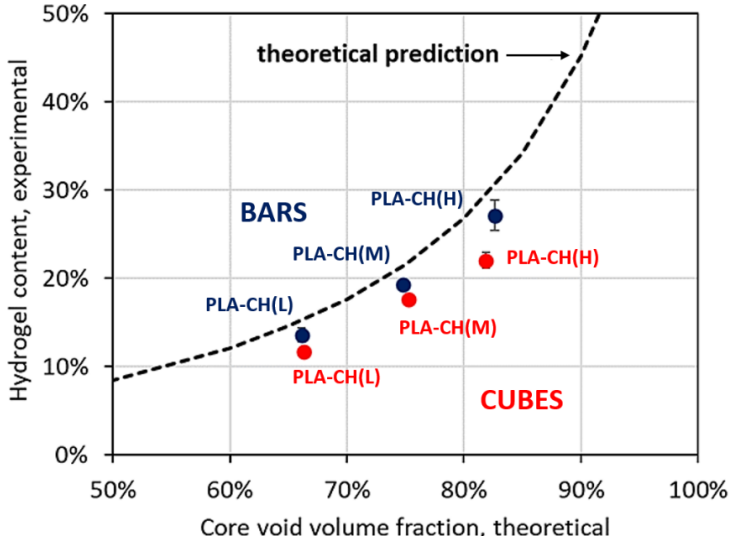

Figure 3.3. Hydrogel content (weight fraction) versus *core void volume fraction for composite scaffolds with either cubic or bar-shaped core and with low (L), medium (M) or high (H) hydrogel content; the dashed line represents the theoretical hydrogel content prediction.*

The mechanical properties of core and core-shell scaffolds were evaluated under compression along the xy direction (more details regarding the effects of the loading direction and of the geometry of the scaffold on its mechanical behavior are reported in Chapter 2). Some examples of the obtained stress-strain curves are reported in Figure 3.4, for PLA-CH(L), PLA-CH(M) and PLA-CH(H) core-shell scaffolds after 1 day in water (continuous lines) and after 7-week hydrolytic degradation experiments reported below (dashed lines). All the curves have the typical characteristics that can be observed in many cellular materials [92]: (i) an initial linear segment up to apparent strain values around 2–5%; (ii) a second region during which the lattice collapses due to buckling phenomena (*i.e.* unstable bending deformation under compression); (iii) a final part during which the slope rises rapidly because of the structure densification that happens as the walls of the cells come in contact with each other (here not shown). More specifically, the structures are observed to progressively collapse through a series of localized buckling phenomena of individual lattice struts, favored by strut slenderness, and associated to stress peaks in compression curves. The first stress peak is considered as the strength of the specimen, while the apparent modulus of the specimens is evaluated as the slope of the first linear tract of the curves.

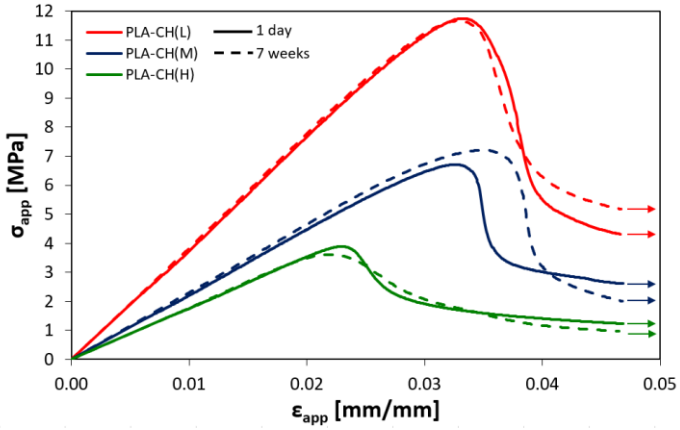

Figure 3.4. Apparent stress (σ_{app}) versus *apparent strain (ε_{app}) curves of cubic core-shell scaffolds with low (L), medium (M) or high (H) hydrogel content tested under compression after 1 day or 7 weeks in water at 37°C.*

Apparent modulus (E_{app}) and apparent failure stress ($\sigma_{app,f}$) are represented in Figure 3.5 for PLA-CH(L), PLA-CH(M) and PLA-CH(H) core-shell scaffolds and for the corresponding core structures.

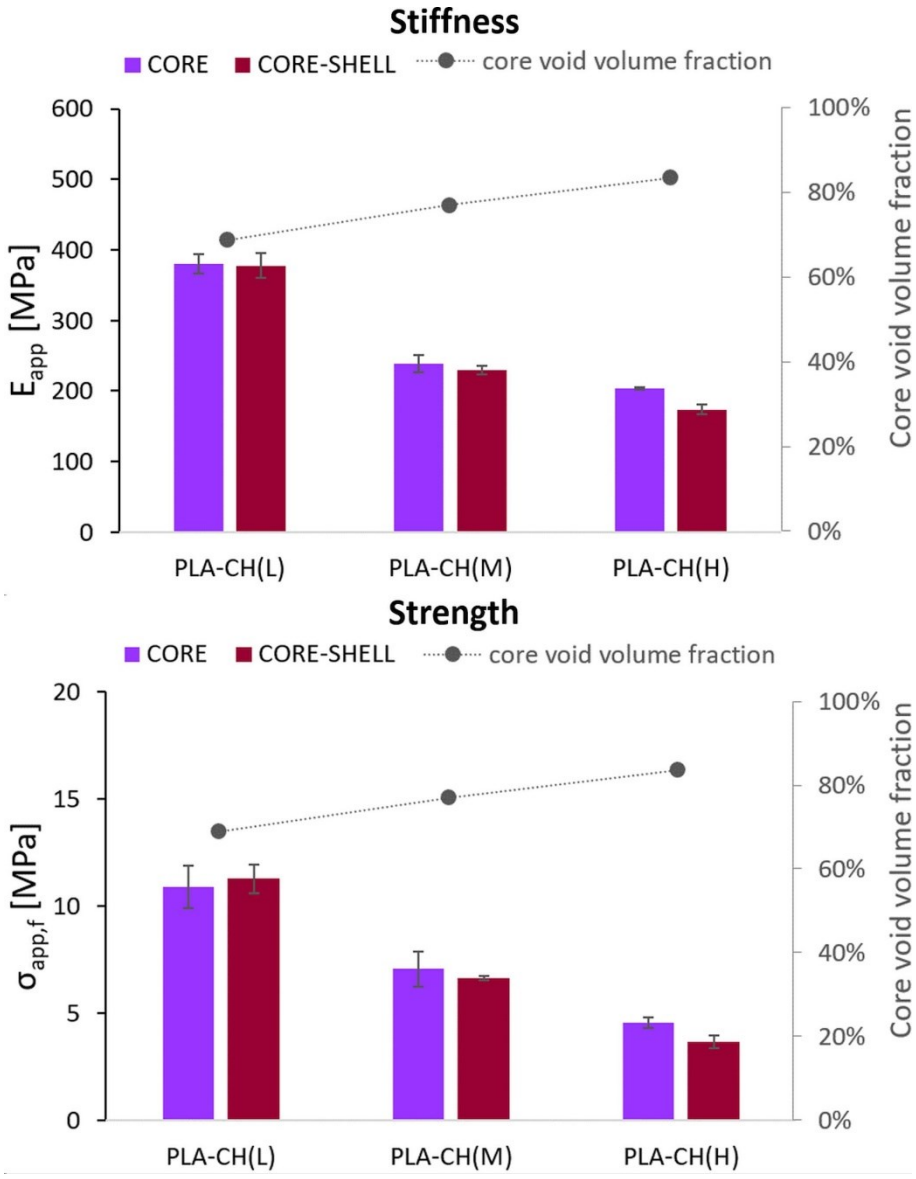

Figure 3.5. Apparent modulus (E_{app}) and apparent failure stress ($\sigma_{app,f}$) for cubic core and core-shell -specimens with low (L), medium (M) or high (H) hydrogel content. The core void volume fraction of the specimens is also reported in both graphs (in grey).

As previously observed in Chapter 2, the contribution of the hydrogel shell to the mechanical properties of the composite systems is negligible, and the mechanical properties of the hybrid scaffolds are comparable with those of several types of trabecular bone tissue [92]. These results are therefore promising in view of bone tissue engineering applications, in which the scaffolds should temporarily provide sufficient mechanical support while new bone gradually replaces them.

Moreover, the graphs in Figure 3.5 also show that both the apparent failure stress and the apparent modulus of the specimens decrease as the hydrogel content increases. These trends are the result of the increase of the void volume fraction in the core, indicated through secondary ordinate axes. The core void volume fraction is thus confirmed as an important parameter for tailoring not only the hydrogel content but also the scaffold mechanical properties, according to the specific bone defect to treat.

3.3. Thermal deformations and hydrolytic degradation

Further investigations were conducted to evaluate the dimensional stability of PLA lattices upon heating and the degradation behavior of PLA-hydrogel scaffolds in aqueous environment at body temperature.

3.3.1. Results of thermal analyses

At first, the main thermal properties of PLA were evaluated by DSC, carried out both on the PLA filament and on 3D-printed PLA. All DSC traces (1st heating, cooling, and 2nd heating) are shown in Figure 3.6, while Table 3.2 reports the properties measured on the two heating scans: glass transition temperature (T_g), cold crystallization temperature (T_{cc}), cold crystallization enthalpy (ΔH_{cc}), melting temperature (T_m), melting enthalpy (ΔH_m), and crystallinity content before the scan (X_c, calculated through eq. 3.1 as difference between the maximum crystallinity that may be developed in the polymer and that developed during cold crystallization).

By considering the filament 1st heating scan, the inflection in the curve around 60 °C corresponds to the typical glass transition of PLA, whereas the subsequent endothermal peak indicates a T_m around 153 °C, which is significantly lower than the usual melting temperature of poly-L-lactic acid (170-190 °C [143]). The low T_m is a sign of reduced enantiomeric purity with respect to pure poly-L-lactic acid, and this could be expected both because the filament producers only declared a purity higher than 90% and because it is common to increase the amorphous phase content in commercial grades by adding between 0.5% and 15% of D,L copolymer; this is usually of help in FDM because a low crystallization ability improves the adhesion between 3D-printed layers [144].

In the beginning, PLA has a crystallinity of about 24% (approximately, since the reference melting enthalpy used in the calculation is valid for pure poly-L-lactic acid); the absence of cold crystallization signals indicates that the crystallinity is fully developed in the pristine filament. However, both the cooling rate of the DSC tests

(10 °C/min) and that experienced during 3D printing are insufficient for crystallization to take place. Therefore, PLA becomes amorphous ($X_c \approx 0$), as confirmed by the subsequent heating scans, presenting additional exothermal signals of cold crystallization around 120-130 °C with $\Delta H_{cc} \approx \Delta H_m$. On the contrary, transition temperature values do not significantly change, and in particular 3D-printed PLA has still T_g and T_m comparable to those of the original filament.

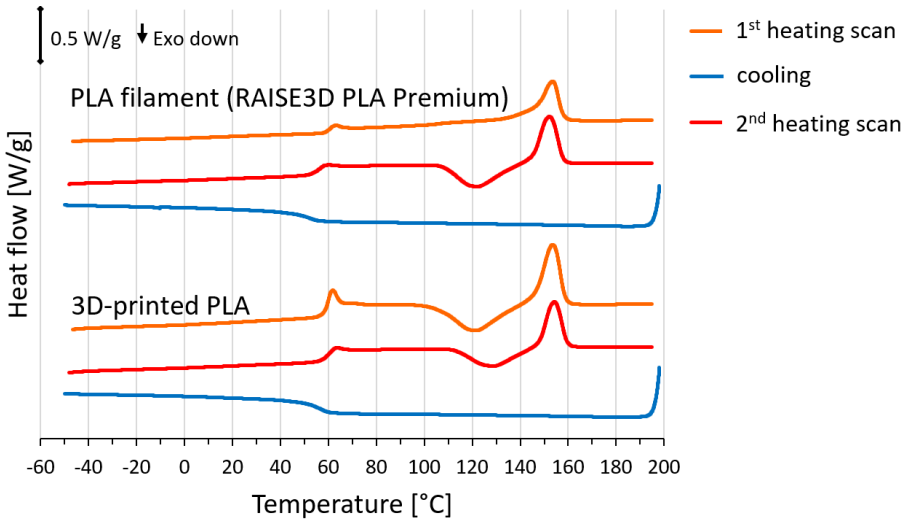

Figure 3.6. DSC traces of the PLA filament and of 3D-printed PLA.

Table 3.2. PLA glass transition temperature (T_g), cold crystallization temperature (T_{cc}), cold crystallization enthalpy (ΔH_{cc}), melting temperature (T_m), melting enthalpy (ΔH_m), and crystallinity (X_c) evaluated by DSC on the filament and after 3D printing.

Material	Heating scan	T_g [°C]	T_{cc} [°C]	ΔH_{cc} [J/g]	T_m [°C]	ΔH_m [J/g]	X_c [%]
PLA filament	1st	60.8	-	-	153.5	22.6	24.1
	2nd	56.2	121.9	22.6	152.2	22.8	≈ 0*
3D-printed PLA	1st	60.0	121.5	29.8	153.6	29.0	≈ 0*
	2nd	60.8	128.9	18.8	154.3	19.6	≈ 0*

*at the beginning of the heating scan, the polymer is completely amorphous

Subsequent thermal tests were performed focusing on PLA dimensional changes. The deformation of a cubic PLA-CH(M) scaffold along x was recorded by means of a DMA apparatus during application of a heating ramp (Figure 3.7a) or a series of isothermal steps of 40 min each, progressively applied at 40 °C, 50 C°, 60 °C, 70 °C, and 80 °C (Figure 3.7b). In both cases, no significant strain along x can be observed before T_g (about 60 °C, as calculated by DSC on 3D-printed PLA, see Table 3.2). Conversely, for temperatures of 60 °C or higher, PLA lattices tend to progressively contract along x.

By comparing pictures at room temperature and after each isothermal step, the values of strain along y and z can also be calculated (Figure 3.7c). For x and y directions, the values are similar to those recorded by DMA apparatus, with a final contraction of about 7% after the isothermal step at 80 °C. On the other hand, the lattice structure expands along the build direction, z (up to nearly 4%).

Finally, the dimensional stability of a small PLA-CH(M) bar-shaped specimen was monitored during a series of isothermal steps carried out in oven (Figure 3.7d). Once again, no shape distortion can be noticed at 40 °C and 50 °C, whereas progressive bending occurs at temperatures from T_g upwards, *i.e.*, at 60 °C, 70 °C, and 80 °C. The main curvature is visible in pictures taken from the side view, showing how the top of the bar contracts more than its bottom; this is caused by the release of frozen stresses that may form during FDM due to the presence of temperature gradients in the 3D printer chamber.

All these experiments highlight the importance of keeping the samples below PLA glass transition temperature. An annealing treatment, to carry out while the part is still attached to the 3D printer bed, may also be helpful in improving dimensional stability. Anyway, both the hydrogel curing temperature and the body temperatures of humans and rabbits are well below 60 °C; therefore, it is sufficient to use a low-temperature sterilization procedure (such as gamma irradiation) and to store the scaffolds properly to avoid any shape alteration.

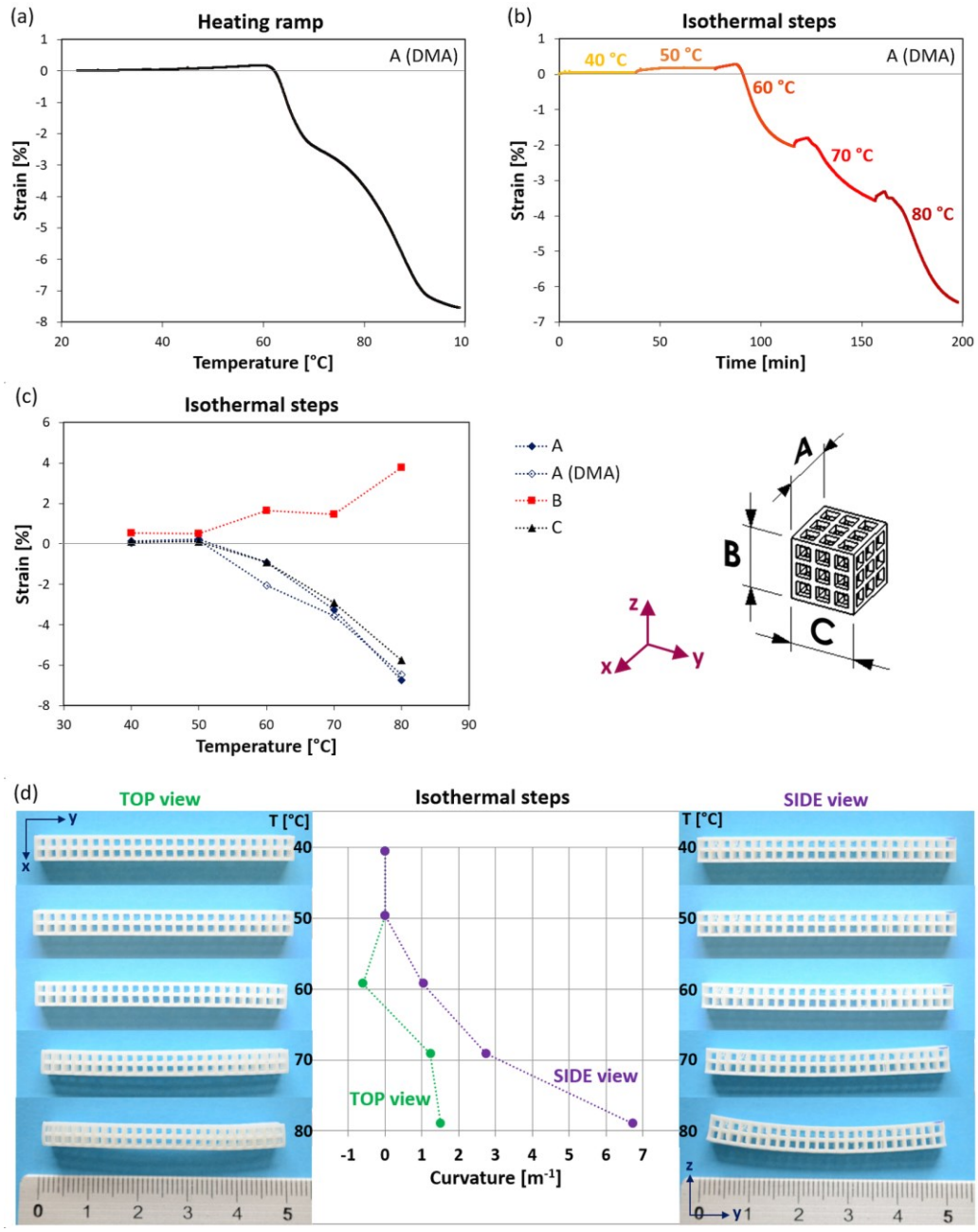

Figure 3.7. Deformation of cubic (a-c) and bar-shaped (d) lattices at high temperatures: (a) strain-temperature plot during a heating ramp; (b) strain-time plot during sequential isothermal steps; (c) total strain values at the end of each isothermal step; (d) curvature values at the end of each isothermal step. The strain in (a-b) is referred to the lattice dimension along the x axis.

3.3.2. Results of hydrolytic degradation experiments

Bone tissue has an excellent self-healing capacity for defects of few millimeters, but for defects beyond the critical-size a clinical intervention with bone grafts or scaffolds is necessary [29]. In these cases, it is important to prolong the permanence of the scaffold and its mechanical action until a sufficient portion of tissue is regenerated. For this reason, degradation experiments were carried out on cubic core-shell scaffolds immersed in distilled water at 37 °C for 7 weeks, aiming to evaluate their mass loss and the evolution of their mechanical properties over time. Both the rigid core and the bioactive shell need an adequate degradation kinetics in order to perform their own function: while the hydrogel should soon start to degrade and be gradually replaced by new bone tissue, PLA should provide mechanical support for a longer duration.

The mass loss of the specimens was calculated according to eq. 3.2 with respect to the initial total mass of the scaffolds, and according to eq. 3.3 with respect to initial mass of their hydrogel shell; the results are represented in Figure 3.8 as a function of time and fitted with second-order polynomial lines to better highlight their trends. All curves show mass loss indicating hydrolytically degradable products and the degradation rate tends to increase over time. Since PLA hydrolysis at body temperature typically occurs in about 1-2 years [140], its mass loss is expected to be negligible during the first weeks with respect to that of the hydrogel. Indeed, the overall mass loss seems to be proportional to the initial hydrogel content, and the trends of the three scaffold types are observed to overlap when the mass loss is normalized to the initial hydrogel mass (Figure 3.8b). For all the systems, about 70% of the hydrogel shell is lost after 7 weeks, corresponding to 6%, 9% and 15% of the total mass for PLA-CH(L), PLA-CH(M) and PLA-CH(H), respectively. However, the core-shell structural integrity is maintained for at least 7 weeks and the hydrogel remains grafted throughout the core.

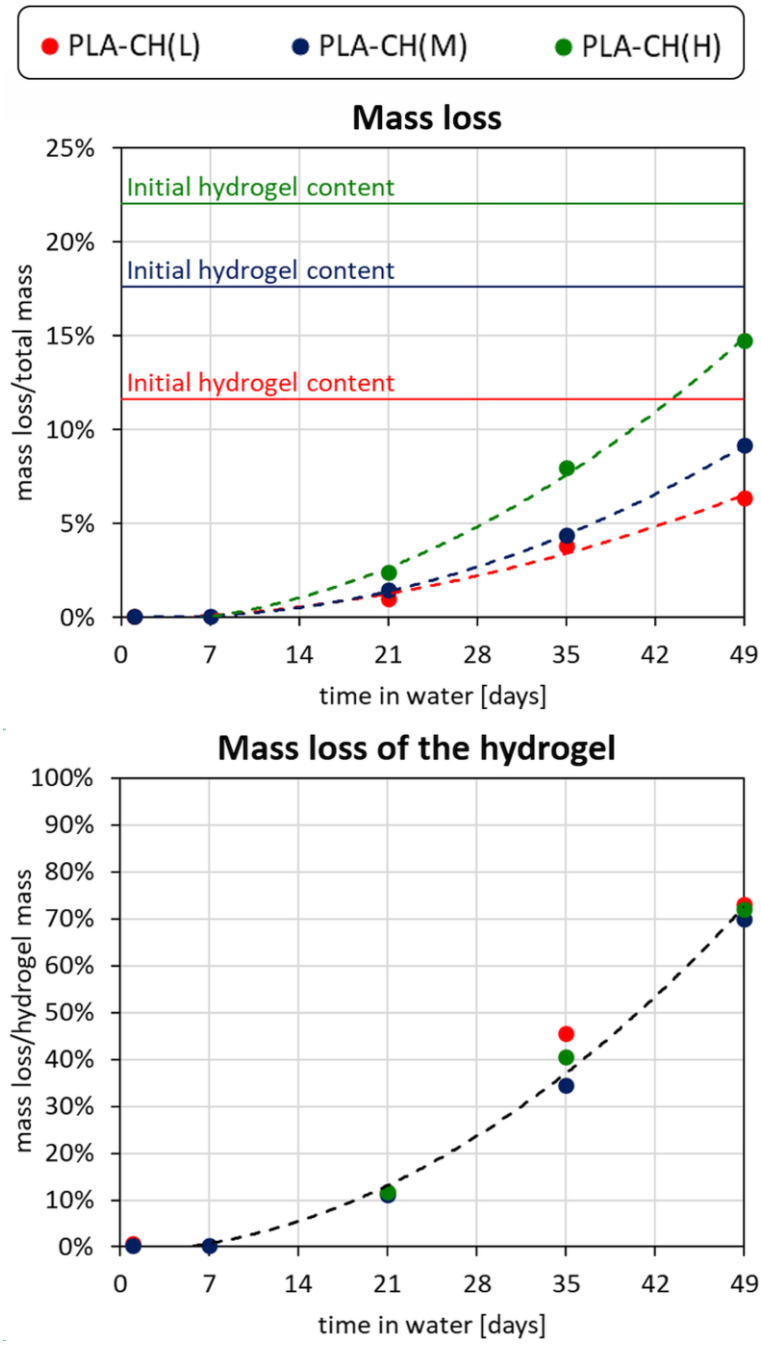

Figure 3.8. Mass loss versus *degradation time for cubic core-shell scaffolds with low (L), medium (M) or high (H) hydrogel content, expressed both as percentage of the initial mass of the dry core-shell specimen and as percentage of the initial mass of the dry hydrogel shell. The trends are fitted with second-order polynomial curves (dashed lines).*

Despite PLA negligible mass loss, prolonged immersion in water at 37°C may still reduce the molecular weight of the polymer chains, and consequently affect the mechanical properties of the lattices. For this reason, degradation experiments also included compression tests of the specimens, whose apparent failure stress and apparent modulus are reported in Figure 3.9 as a function of the immersion time; in addition, complete stress-strain curves after 7-week degradation are shown in Figure 3.4. Both stiffness and strength remain stable up to 7 weeks from the beginning of the tests, when stress-strain curves still display no relevant changes, which is encouraging in view of supporting loads during early bone tissue reconstruction.

As shown previously, scaffold mechanical properties depend on the void volume fraction in the core. Since the void fraction also affects the hydrogel content, a balance should be found between the mechanical properties of the scaffolds and the amount of faster-degrading shell.

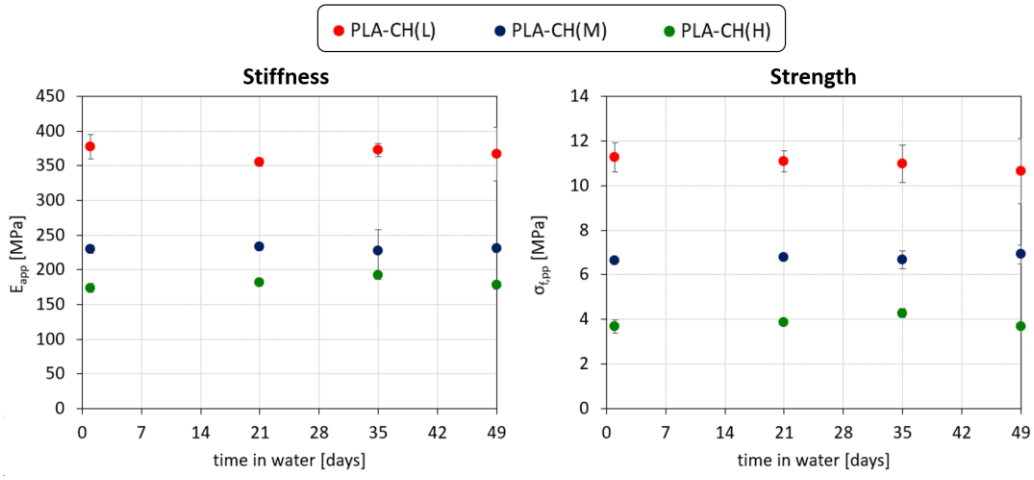

Figure 3.9. Stiffness (E_{app}) and strength ($\sigma_{app,f}$) as a function of degradation time for cubic core-shell scaffolds with low (L), medium (M) or high (H) hydrogel content.

3.4. *In vitro* experiments

Scaffolds for *in vitro* experiments were obtained by slicing the bar-shaped core-shell specimens and performing sterilization by ^{60}Co gamma rays. They were seeded with BM-hMSCs in growth or osteogenic medium, with addition of either fetal bovine serum or human platelet lysate (GM FBS; GM HPL; OM FBS; OM HPL), and observed after 28 days of cell culture.

After 28 days in GM FBS or GM HPL, cells viability in the scaffolds was evaluated in three replicates using a Live/Dead assay. Bright-field and fluorescence images were collected from the same area of PLA-CH(L), PLA-CH(M), PLA-CH(H) specimens and are reported in Figure 3.10, 3.11 and 3.12, respectively. The results achieved from the fluorescence microscopy analysis highlighted that BM-hMSCs were viable within the scaffolds after 28 days of culture. In more detail, the images show the presence of intact cell nuclei (blue staining) and confirm homogeneous cell distribution within the scaffolds (green staining) as well as almost the absence of dead cells (red staining).

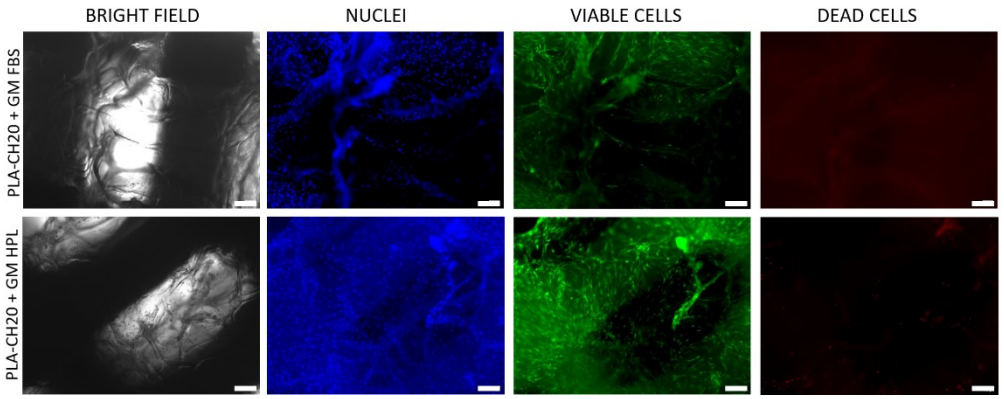

Figure 3.10. Live/dead staining of BM-hMSCs cultivated in slices of PLA-CH (L) bars for 28 days in GM FBS and GM HPL. Scale bar: 200 µm.

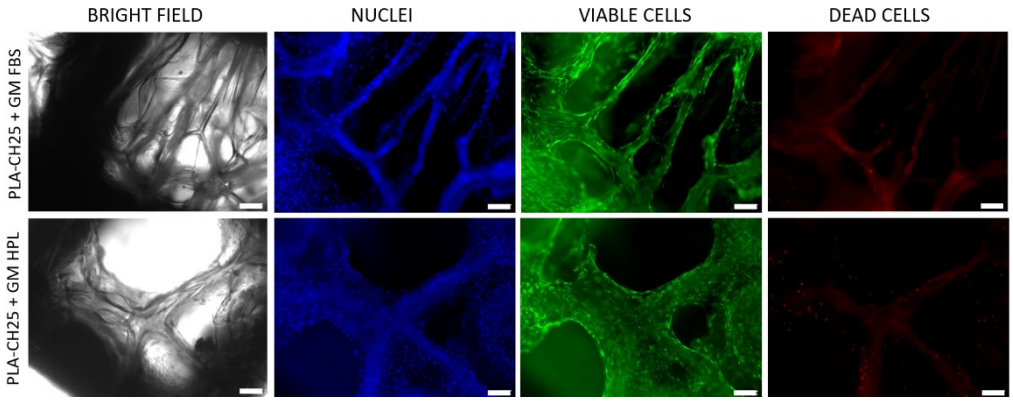

Figure 3.11. Live/dead staining of BM-hMSCs cultivated in slices of PLA-CH (M) bars for 28 days in GM FBS and GM HPL. Scale bar: 200 μm.

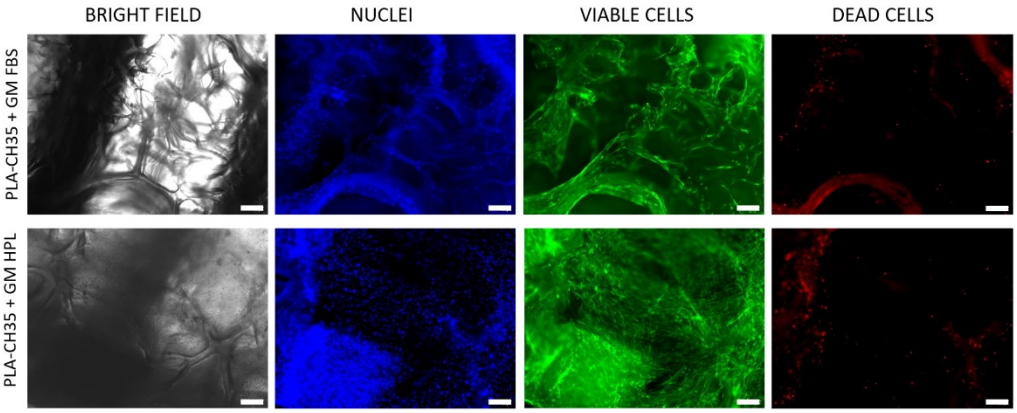

Figure 3.12. Live/dead staining of BM-hMSCs cultivated in slices of PLA-CH (H) bars for 28 days in GM FBS and GM HPL. Scale bar: 200 μm.

In addition to the data obtained with Live/Dead assay, cell proliferation was measured by quantifying viable cells number within the scaffolds at 28 days after cell seeding with Cell Counting Kit-8 colorimetric assay (Figure 3.13). It was previously demonstrated that CCK-8 solution reached all parts of the scaffolds and did not cause any non-specific staining of the scaffold [145]. Results obtained by testing if different types of scaffolds and culture medium (GM FBS and GM HPL) could affect cell proliferation showed no significant differences ($p < 0.05$). Therefore, PLA-CH(L), PLA-CH(M), PLA-CH(H) were considered comparable regardless cells proliferation in different culture media.

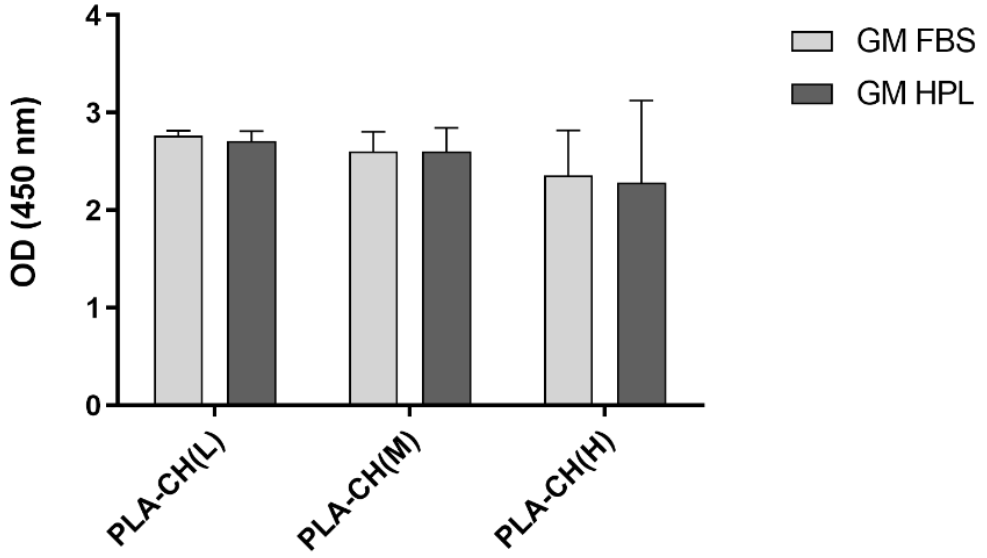

Figure 3.13. Proliferation of BM-hMSCs cultivated in slices of PLA-CH(L), PLA-CH(M) and PLA-CH(H) bars in GM FBS or GM HPL at 28 days measured by CCK-8 assay.

Moreover, SEM analyses were performed on scaffolds seeded with BM-hMSCs in GM or OM, and on scaffolds without cells as control. Micrographs of samples at day 28 of cell culture in GM FBS or GM HPL and relative controls are shown in Figure 3.14 for PLA-CH(L), in Figure 3.15 for PLA-CH(M), and in Figure 3.16 for PLA-CH(H). The images display the attachment and spreading of cells in the scaffolds, preferentially occurring inside the hydrogel pores. Cells develop a large spreading area with elongated fibroblast-like morphology, forming bridges through the pores and showing great affinity with all three types of scaffolds. These results further signify the fact that BM-hMSCs have high affinity to attachment, proliferation, and migration in PLA-CH(L), PLA-CH(M), PLA-CH(H) scaffolds, without differences between the scaffolds. This is confirmed also by histomorphological analyses at optical microscope with H&E stain (Figure 3.17), showing homogeneous colonization of cells inside the hydrogel pores, as well as their good spreading visible at higher magnifications.

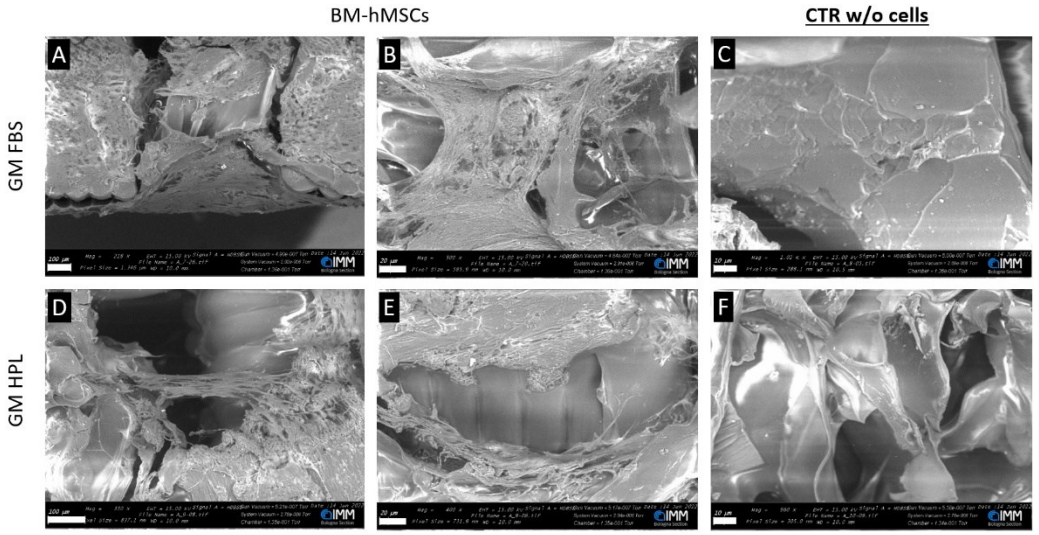

Figure 3.14. SEM micrographs of PLA-CH(L) bar slices with BM hMSCs (A,B,D,E) and without cells (C,F) in the GM FBS (A,B,C) and GM HPL (D,E,F). Scale bar: 100 µm (A,D); 50 µm (B,E); 20 µm (C,F).

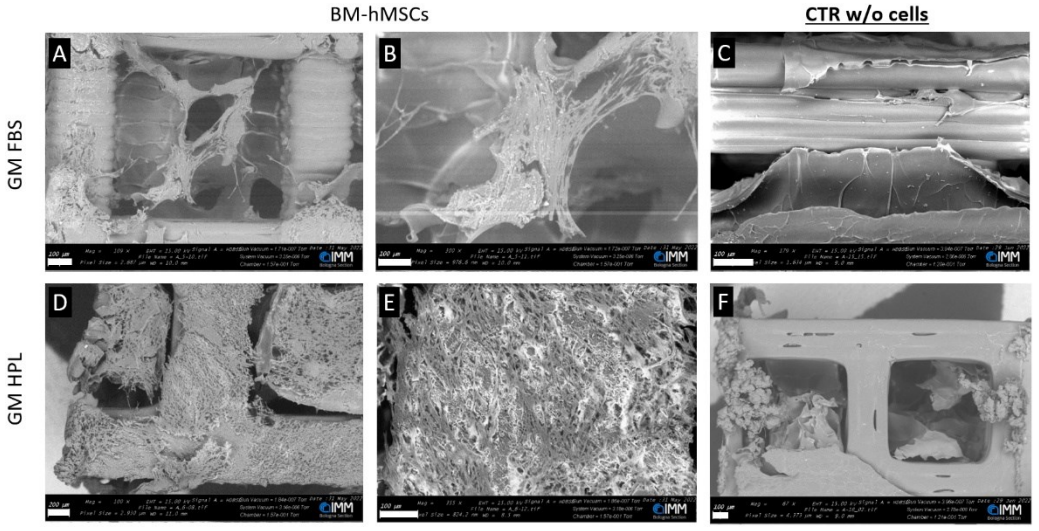

Figure 3.15. SEM micrographs of PLA-CH(M) bar slices with BM hMSCs (A,B,D,E) and without cells (C,F) in the GM FBS (A,B,C) and GM HPL (D,E,F) using SEM. Scale bar: 200 µm (A,C,D,F); 100 µm (B,E).

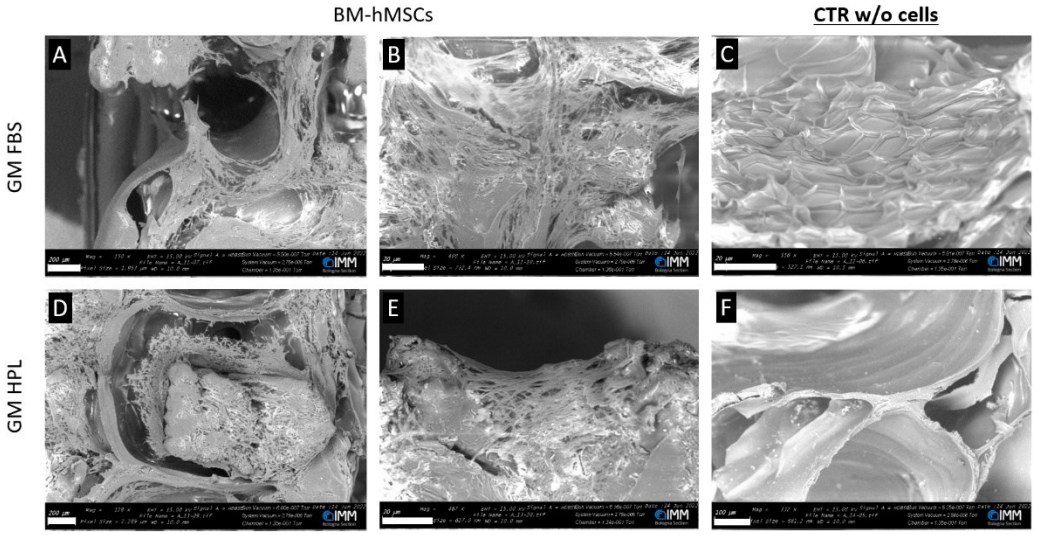

Figure 3.16. SEM micrographs of PLA-CH(H) bar slices with BM hMSCs (A,B,D,E) and without cells (C,F) in the GM FBS (A,B,C) and GM HPL (D,E,F) using SEM. Scale bar: 200 µm (A,D); 100 µm (B,C,E,F).

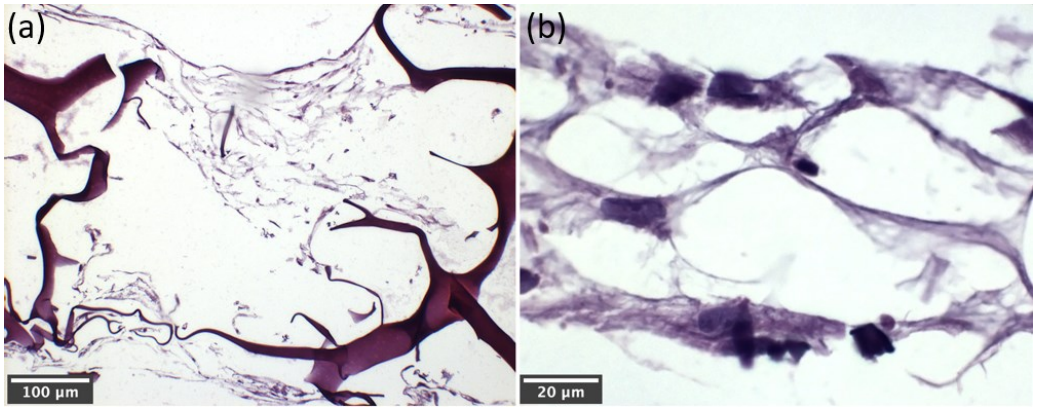

Figure 3.17. Histomorphological analysis with H&E *stain of PLA-CH(M) bar slices cultivated with BM-hMSCs in GM FBS at different magnifications at the optical microscope.*

Finally, SEM micrographs of PLA-CH(M) scaffolds seeded with BM-hMSCs in OM FBS and OM HPL (Figure 3.18) revealed their capability of supporting cell differentiation towards the osteogenic lineage. In fact, BM-hMSCs appeared to be differentiated into osteoblast cells and formation of calcium phosphate deposits was observed, especially in the hydrogel shell. Neither BM-hMSCs seeded scaffolds treated with GM FBS or GM hPL (Figure 3.14-3.16) nor the unseeded specimens used as controls (Figure 3.18) showed any presence of mineral deposits, confirming that mineralization occurred only in the scaffolds seeded with cells grown in OM.

In accordance with the findings of previous investigations on hydrogel scaffolds [64,65,71], the observed deposits can be ascribed to hydroxyapatite formation. Indeed, the elemental content measured by X-ray spectroscopy associated with SEM (SEM-EDX) revealed that the inorganic phase was mainly composed of calcium and phosphorous ions, co-localized in the same areas of the sample sections (see chemical distribution maps in Figure 3.19). These ions are typically present in mineral deposits formed during osteogenic differentiation as the main elements in hydroxyapatite nanoparticles.

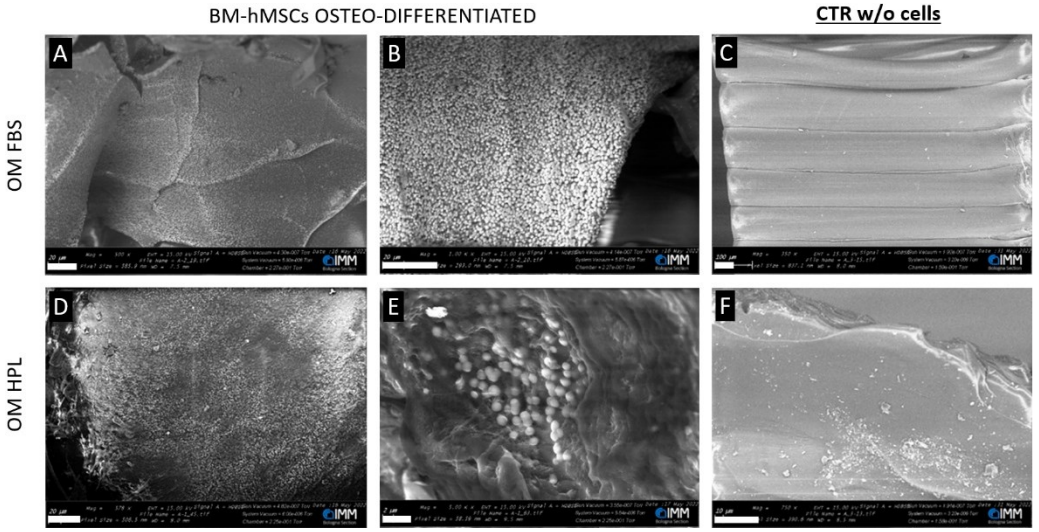

Figure 3.18. SEM micrographs of calcium phosphate deposition in PLA-CH(M) bar slices with BM-hMSCs in OM FBS (A,B) and OM HPL (D,E) at day 28. Controls without cells were also used (C,F). Scale bar: 50 μm (A-D,F); 5 μm (E).

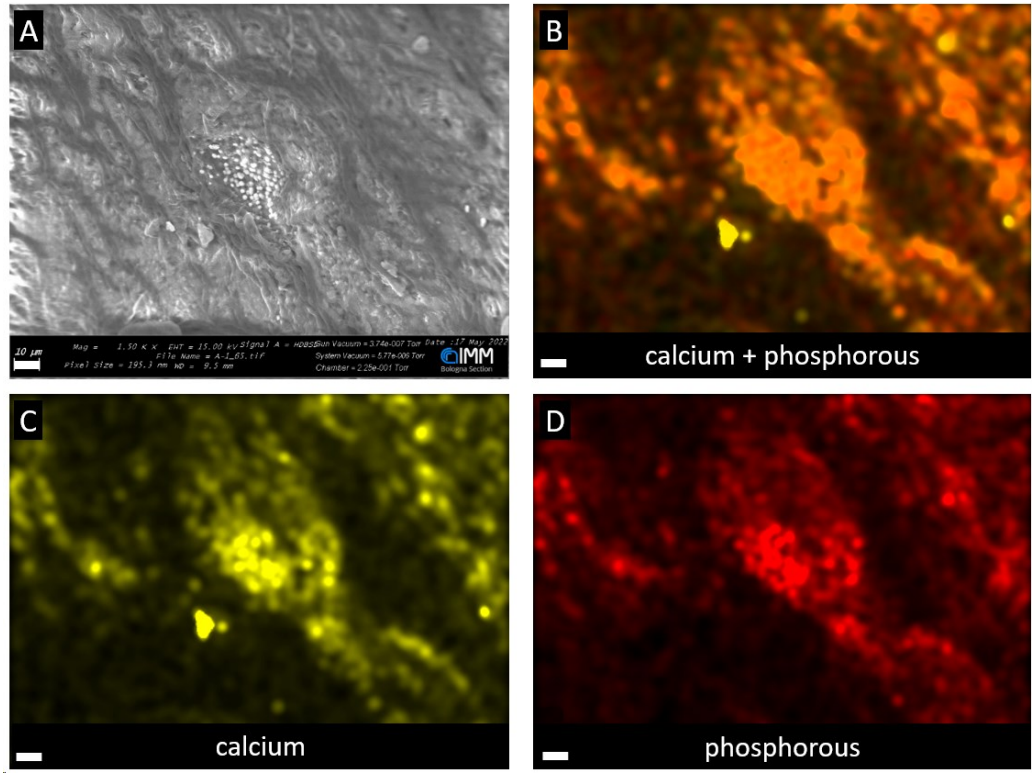

Figure 3.19. SEM image of a PLA-CH(M) bar slices seeded with BM-hMSCs in OM HPL (A) and corresponding EDX spectrum images of the distribution of calcium and phosphorous together (B), calcium alone (C), and phosphorus alone (D). Scale bar: 10 µm.

3.5. Conclusions

Bioresorbable scaffolds with innovative core-shell architecture were realized by grafting a bioactive gelatin-chitosan hydrogel shell onto a stiff 3D-printed PLA core. The two components were selected in order to provide the scaffolds with complementary functions to better match the multiple requirements for bone tissue engineering applications.

The PLA core was designed with lattice structures having different void volume fractions, corresponding to different values of stiffness and strength in the range of bone tissue mechanical properties, consistently with the results of the extensive mechanical characterization in Chapter 2. These properties were observed to be stable for at least 7 weeks, as demonstrated by hydrolytic degradation experiments. Dimensional stability upon heating was also verified for temperatures below 60 °C, corresponding to PLA glass transition.

The bioactive shell filled the entire void volume of the core lattices, resulting in proportional values of hydrogel content. While several scientific papers on composite scaffolds exploit hydrogels only as matrices for the release of specific drugs or osteogenic biomolecules, the gelatin-chitosan shell here presented constitutes a privileged site for cell colonization and new extracellular matrix deposition, thanks to its hierarchical interconnected porous structure and to its efficacy in promoting osteogenic differentiation of hMSCs.

In fact, *in vitro* experiments proved that all the core-shell scaffolds are able to sustain cell viability and proliferation, and SEM analyses evidenced good cell adhesion and mineral deposits ascribed to the presence of osteogenic differentiated cells. Noteworthily, instead of introducing calcium phosphate particles in the scaffold production, increasing the risk of brittleness problems, a gradual deposition of natural hydroxyapatite can be here guaranteed on a fully polymeric composite when seeded with hMSCs. Besides, the hydrogel was found to undergo gradual

degradation, leaving space to new bone tissue formation, and it has still the potential to be integrated with proper therapeutic/osteogenic agents.

Overall, the core-shell scaffolds proved to be biocompatible and promising for bone tissue regeneration and personalized medicine, offering unprecedented customization possibilities. In fact, their versatile multi-material design and the use of additive manufacturing allow fine tuning of their physical-mechanical and biological properties. During the customization of the scaffolds, it is fundamental to reach good balance in mechanical support and regenerative potential by properly designing the core-shell proportions and architecture.

In the next chapter, the specific case of mandibular bone regeneration in a rabbit model is addressed, illustrating how the core-shell scaffolds were customized for this target application and produced with medical-grade poly-L-lactic acid core structures, having higher enantiomeric purity with respect to the commercial PLA used in the experiments of Chapter 2 and Chapter 3. Chapter 4 also deals with the translational potential of these systems, on the basis of preliminary results of *in vivo* experiments on rabbits.

4. Customization of Composite Core-Shell Scaffolds for Mandible Regeneration in a Rabbit Model

PLA-hydrogel core-shell scaffolds have shown interesting hierarchical morphology and tunable mechanical performances, as extensively discussed in Chapter 2. Moreover, hydrolytic degradation and *in vitro* experiments in Chapter 3 highlighted their bioresorbability, biocompatibility, and capability to sustain cell proliferation and osteogenic differentiation. These features are highly desirable in the field of bone regenerative medicine and make the scaffolds promising for future clinical use as biomaterials with different therapeutic purposes.

In light of such attractive specifications, surgeons from the Department of Neurosciences of the University of Padua[5] requested *ad hoc* scaffolds for preclinical tests in a rabbit model. In response, customized core lattices were designed to fit mandibular bone defects and 3D-printed with medical-grade filament, which is composed of high-purity poly(L-lactic acid) (PLLA).

The new core material (PLLA) has higher enantiomeric purity with respect to the commercial grade (PLA) employed in Chapter 2 and Chapter 3, but their thermal and mechanical properties were found to be overall similar for the purpose of the study. The core lattice design and its build direction were specifically tailored to follow the surgeons' requests and to achieve a good balance between mechanical performance and hydrogel content in the final core-shell scaffolds. The experimental work conducted for the development of these customized scaffolds is described in paragraphs 4.1 (materials and methods) and 4.2 (results and discussion).

[5] Collaboration: Prof. Piero Nicolai's team (Section of Otorhinolaryngology—Head and Neck Surgery, Department of Neurosciences, University of Padua—"Azienda Ospedale Università di Padova", 35129 Padua, Italy).

Sterilized scaffolds have been tested on a rabbit animal model (New Zealand immunocompetent rabbit, *Oryctolagus Cuniculus*) in several *in vivo* experiments, which were carried out by surgeons of the University of Padua at GTx Lab (Princess Margaret Cancer Research Tower, Toronto, Canada)[6]. Both scaffolds rehydrated without cells and scaffolds seeded with human mesenchymal stromal cells (hMSCs) were employed.

These studies were conducted with the aim of exploring the translational potential of the core-shell scaffolds for future applications in clinical practice in the field of head and neck district pathology. In particular, they investigated the possibility of using the scaffolds for healing marginal and segmental mandibular defects, as well as the eventuality of biomaterial interactions with irradiated tissues and with the microenvironment generated after tumor resection. Translational applications tested up to date are illustrated more in detail in paragraph 4.3.

[6] Collaboration: Prof. Johnatan C. Irish and Prof. Ralph. W. Gilbert's team (Princess Margaret Cancer Centre, Department of Otolaryngology—Head and Neck Surgery/Surgical Oncology, University Health Network, Toronto, ON M5G 2A2, Canada).

4.1. Materials and methods

4.1.1. Materials

Raise3D Premium PLA filament for first customized prototypes was provided by Raise 3D Technologies, Inc. (Irvine, CA, USA) [133]. Lactoprene® 100M filament for specimens used in *in vivo* analyses was kindly supplied by Poly-Med, Inc. (Anderson, SC, USA); Lactoprene® 100M is a high-purity poly(L-lactic acid) (PLLA) bioresorbable filament for medical devices that meets all the requirements of the guidelines set forth by the Biological Test for Plastics, USP Class VI and acceptance criteria of ISO 10993-5 Cytotoxicity testing [146].

Pharmaceutical grade type A gelatin (280 bloom, viscosity 4.30 mPs) was provided by Italgelatine (Cuneo, Italy). Poly(ethylene glycol) diglycidyl ether (PEGDGE) (molecular weight 526 Da) and chitosan (molecular weight 50,000 ÷ 190,000 Da, degree of deacetylation 75–85%) were supplied by Sigma-Aldrich Co (Milan, Italy). Ethylene diamine (EDA) and acetic acid were provided by Fluka (Milan, Italy).

4.1.2. Preparation of *ad hoc* core-shell scaffolds

Specimens for *in vivo* experiments on rabbits were designed with a similar lattice structure (parallelepipedal cells with $t = 0.6$ mm) and with external shape matching the surgical anatomical sites selected by surgeons (mandibular full segmental defects with elliptical cross-section, as well as other mandibular defects of different size: XS, S, M, and L). Their dimensions are specified in Figure 4.1.

PLA core prototypes were obtained as previously described by 3D printing the commercial filament (see paragraph 2.1.2). For PLLA specimens, the same procedures and printing parameters were applied to the medical-grade filament, except for the selection of the build direction. In fact, after mechanical check-tests on specimens obtained by adopting a different build direction (x, y or z) for the 3D-printed core, the build direction was set along the smallest of their principal dimensions (*i.e.*, along the y axis).

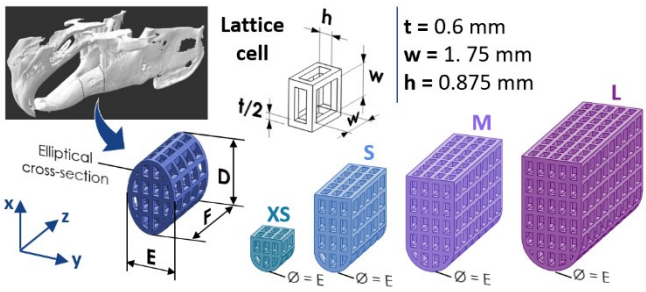

Size	D [mm]	E [mm]	F [mm]
Mandible segment	10.000	6.500	10.000
XS	5.300	5.025	5.300
S	10.000	5.025	12.350
M	12.350	6.500	17.050
L	14.700	7.975	21.750

Figure 4.1. Dimensions of specimens for in vivo *experiments (mandibular full segmental defects or defects with size XS, S, M, and L).*

Finally, core-shell composite scaffolds were prepared by grafting a hydrogel shell onto the core specimens, following the procedure described in paragraph 2.1.2.

4.1.3. Thermal characterization of filaments and 3D-printed materials

Differential scanning calorimetry (DSC) tests were carried out on PLLA filaments and 3D-printed PLLA according to the same procedure previously used for commercial PLA (paragraph 3.1.4.1).

Thermogravimetric analysis (TGA) was performed on both PLA and PLLA filaments. Samples of about 10 mg were tested by means of a TGA Q500 (TA Instruments), heating them from 20 °C to 600 °C at 50 °C/min.

4.1.4. Physical and mechanical characterization of lattices and scaffolds

Core and core-shell specimens were characterized as described in detail in paragraph 2.1.3, through microscope observations, core void volume fraction and hydrogel content evaluation, water uptake measurements, compression tests and bending tests.

Equations of normalized load (P_N, eq. 2.8) and normalized displacement (u_N, eq. 2.9) were updated for specimens with elliptical cross-section tested under transversal compression, as follows:

$$P_N[MPa] = \frac{P}{A'} \tag{4.1}$$

$$u_N[mm/mm] = \frac{u}{L'} \tag{4.2}$$

For compression along x, $A' = EF$ and $L' = D$, whereas for compression along y, $A' = DF$ and $L' = E$; D, E, F and the coordinate system xyz are all defined in Figure 4.1. Failure under transversal compression was associated with the second peak or knee of the curves, since the first deviation from linearity was due to flattening of the curved surface in contact with the plates, which did not significantly compromise the specimen integrity and functionality.

Bending tests on specimens with elliptical cross-section were performed with span equal to 30 mm and load parallel to the x direction.

4.2. Customization of the scaffolds for rabbit mandible regeneration

Core-shell scaffolds for the regeneration of segmental defects in rabbit mandibles were created according to the specifications indicated by surgeons of the University of Padua. Their thermal, physical, and mechanical characterization is here discussed, whereas paragraph 4.3 deals with their application in preclinical studies.

4.2.1. Thermal analyses on commercial PLA and medical-grade PLLA

For preclinical studies, commercial PLA was substituted with Lactoprene® 100M, a medical-grade bioresorbable filament kindly provided by Poly-Med, Inc. This is a poly-L-lactic filament having high optical purity, and is therefore referred to as PLLA in this thesis. The thermal behavior of the PLLA filament and of 3D-printed PLLA is here presented and compared to that of commercial PLA.

DSC thermograms of PLLA before and after 3D printing are presented in Figure 4.2 for all thermal scans (1st heating, cooling, 2nd heating), whereas Table 4.1 reports the properties measured on the two heating scans: glass transition temperature (T_g), cold crystallization temperature (T_{cc}), cold crystallization enthalpy (ΔH_{cc}), melting temperature (T_m), melting enthalpy (ΔH_m), and crystallinity content before the scan (X_c, calculated according to eq. 3.1).

As expected from its high enantiomeric purity, PLLA presents the typical T_g and T_m values of poly-L-lactic acid (about 60 °C and 180 °C, respectively) [143]. The pristine filament curve shows only the inflection due to glass transition and an endothermal melting peak immediately preceded by a small exothermal cold crystallization peak; the calculated initial crystallinity is around 46%. Conversely, subsequent heating scans show much more evident cold crystallization signals around 100-105 °C, besides smaller signals right before melting. In these scans, ΔH_m is higher than the total ΔH_{cc}, indicating that part of the crystallization occurs also under the cooling rates experienced both during DSC and during 3D printing.

In the case of the filament, the crystallization peak in the cooling scan is rather broad and poorly visible, and only 12% crystallinity is measured on the 2nd heating scan. In the case of 3D-printed PLLA, the 1st heating scan reveals that the scaffold core lattices are about 10% crystalline; moreover, 3D printing is likely to affect the orientation of PLLA molecules, favoring cold crystallization (lower T_{cc} in the 1st heating scan). Crystallization seems to be favored also during the DSC cooling scan of 3D-printed PLLA, finally leading to a higher value of crystallinity measured on its 2nd heating scan (about 28%).

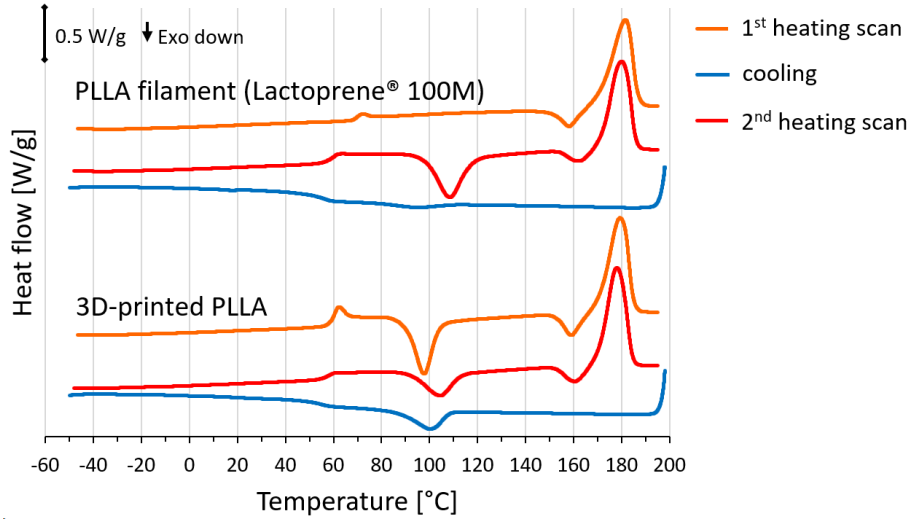

Figure 4.2. DSC traces of the PLLA filament and of 3D-printed PLLA.

Table 4.1. PLLA glass transition temperature (T_g), cold crystallization temperature (T_{cc}), cold crystallization enthalpy (ΔH_{cc}), melting temperature (T_m), melting enthalpy (ΔH_m), and crystallinity (X_c) evaluated by DSC on the filament and after 3D printing.

Material	Heating scan	T_g [°C]	T_{cc} [°C]	ΔH_{cc} [J/g]	T_m [°C]	ΔH_m [J/g]	X_c [%]
PLLA filament	1st	69.1	158.2	7.0	181.6	50.4	46.4
	2nd	59.0	108.7; 162.2	38.9	180.0	50.5	12.4
3D-printed PLLA	1st	60.6	97.7; 159.0	41.5	179.3	51.0	10.1
	2nd	58.0	104.6; 160.6	25.2	178.0	51.5	28.1

In order to facilitate the comparison between PLLA and PLA thermal properties, their first DSC scans and their TGA traces are reported together in Figure 4.3a and Figure 4.3b, respectively, whereas the key properties derived from these graphs are shown in Table 4.2.

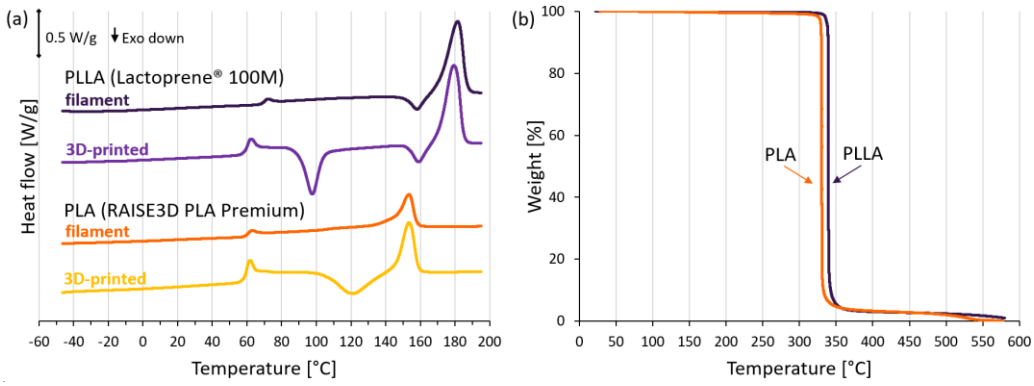

Figure 4.3. Comparison of thermal analyses on medical-grade PLLA and commercial PLA: (a) DSC first heating scans of filaments and 3D-printed materials; (b) TGA traces of filaments.

Table 4.2. Comparison of PLLA and PLA thermal data from DSC 1st heating scans (on filaments and 3D-printed parts) and from TGA (on filaments): glass transition temperature (T_g); cold crystallization temperature (T_{cc}); cold crystallization enthalpy (ΔH_{cc}); melting temperature (T_m); melting enthalpy (ΔH_m); crystallinity (X_c); TGA inflection point temperature (T_{deg}); TGA residual weights at 205 °C and 570 °C ($W_{205\,°C}$ and $W_{570\,°C}$).

Material	T_g [°C]	T_{cc} [°C]	ΔH_{cc} [J/g]	T_m [°C]	ΔH_m [J/g]	X_c [%]	T_{deg} [°C]	$W_{205\,°C}$ [%]	$W_{570\,°C}$ [%]
PLLA filament	69.1	158.2	7.0	181.6	50.4	46.4	338.0	99.86	1.25
3D-printed PLLA	60.6	97.7; 159.0	41.5	179.3	51.0	10.1			
PLA filament	60.8	-	-	153.5	22.6	24.1	328.5	99.58	0.15
3D-printed PLA	60.0	121.5	29.8	153.6	29.0	≈ 0*			

*at the beginning of the heating scan, the polymer is completely amorphous

DSC analyses show that the two materials are both thermally stable until their glass transition around 60 °C, whereas their melting transitions occur at different temperatures (about 155 °C for PLA and 180 °C for PLLA). The higher melting temperature of PLLA is a consequence of its higher optical purity, implying higher stereoregularity of its polymer chains; for the same reason, PLLA also exhibits higher values of crystallinity [144].

Both 3D-printed materials show exothermal signals due to cold crystallization, indicating that the cooling rate they experience during FDM is too fast for complete crystallization. More specifically, 3D-printed PLA is fully amorphous, whereas 3D-printed PLLA achieves a small degree of crystallinity (about 10%), which may be ascribed once again to its higher purity. In addition, while 3D-printed PLA cold crystallization is associated to a single broad signal covering a region between 100 °C and the melting peak, the curve of 3D-printed PLLA shows a sharper exothermal peak around 100 °C and a smaller one immediately before the melting transition, the latter also visible in the thermogram of PLLA filament (*i.e.*, a few crystals seem to form right before melting).

Finally, a similar thermal degradation behavior is revealed by TGA of commercial PLA and medical-grade PLLA. Figure 4.3b shows TGA traces, while Table 4.2 reports the inflection point temperatures (T_{deg}) and the residual weights at 205 °C and 570 °C ($W_{205\,°C}$ and $W_{570\,°C}$). Both filaments present negligible weight loss at their process temperature (*i.e.*, the 3D printer nozzle temperature, 205 °C), ensuring that no significant degradation occurs while printing. At higher temperatures, a sharp weight loss occurs around T_{deg} (about 330 °C for PLA and 340 °C for PLLA), and both polymers are almost completely degraded at the end of the tests ($W_{570\,°C}$ of about 1% or less).

In conclusion, despite the differences due to the higher enantiomeric purity of PLLA, the thermal properties of the two materials are overall similar for the scaffold purpose; in fact, they are both stable until about 60 °C and they do not degrade

during 3D printing. The main difference is that, after 3D printing, PLLA shows a certain degree of crystallinity, while PLA appears fully amorphous. This may cause differences in their mechanical properties, but compression tests in paragraph 4.2.3 show that this is not the case. In addition, a higher crystallinity may prolong the life of these materials *in vivo*, because their hydrolysis is controlled by water diffusion in the polymer amorphous phase [144]; however, a precise comparison of PLA and PLLA core lattices in terms of bioresorption time and rate is difficult to make, since both degradation and crystallization kinetics should be jointly considered, and real *in vivo* conditions are typically different from *in vitro* ones.

4.2.2. Optimization of lattice cell dimensions and build direction

First core prototypes with elliptical cross-section (see Figure 4.1) were printed with commercial PLA and characterized as described in paragraph 4.1.4, aiming at the optimization of lattice cell dimensions and build direction for mandibular full segmental defects in rabbits. The lattices were designed to perfectly fit the dimensions of segmental bone defects planned by surgeons (elliptical cross-section of 10 mm x 6.5 mm; length of 10 mm).

The balance between mechanical support and bioactive hydrogel content was also given special consideration. In the case of mandibular defects, particular attention must be paid to the forces generated by chewing. For this reason, rather dense lattices were created, obtaining void volume fraction values of 69-74%, between those of PLA-CH(L) and PLA-CH(M) in Chapter 3. These core structures can still host a significant amount of bioactive hydrogel, which was found capable of sustaining cell proliferation and differentiation during *in vitro* tests.

The two alternative designs in Figure 4.4a were initially considered: (i) one with parallelepipedal holes of 1.75 mm x 1.75 mm x 1.5 mm, similar to those of PLA-CH(M) in Chapter 3, and (ii) one with additional struts in the xy plane, reducing hole dimensions down to 1.75 mm x 1.75 mm x 0.785 mm. Special attention was directed to the x direction because it is the main chewing direction. High compression loads

may be expected in portions of mandible underneath teeth, while bending may also interest the diastema region between incisors and premolars. For more details, thorough studies conducted by Weijs *et al.* [147,148] report orientation and magnitude of bite forces in young and adult rabbits.

Compression tests on core prototypes (commercial PLA; z build direction) show that stiffness (Figure 4.4b) and load at failure (Figure 4.4c) are superior in the reinforced specimens, especially for compression along x and z. Noteworthily, the stiffness along the x axis can be doubled and the load at failure along the x axis can be increased by 50% by choosing the scaffolds with additional struts instead of those with bigger holes. Such a significant improvement is obtained at the cost of a modest reduction of the core void volume fraction (69% *versus* 74% ca.), therefore the reinforced lattices appear the best of the two alternatives.

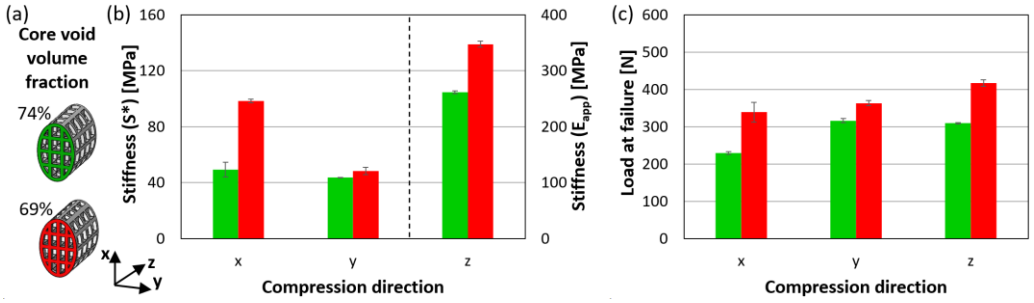

Figure 4.4. Evaluation of first PLA core prototypes designed for mandibular full segmental defects in rabbits: effect of lattice cell dimensions on void volume fraction (a), compression stiffness (b) and compression load at failure (c); compression tests were carried out along x, y and z axes.

Finally, the influence of the build direction (x, y, or z in Figure 4.5a) on the mechanical properties was evaluated on PLA core prototypes under compression and bending conditions. The determination of an optimal solution is not straightforward if based only on compression stiffness (Figure 4.5b) and load at failure (Figure 4.5c), because different layer orientations present different benefits and drawbacks. Even considering a same loading direction, stiffness and strength do not seem to follow a same trend.

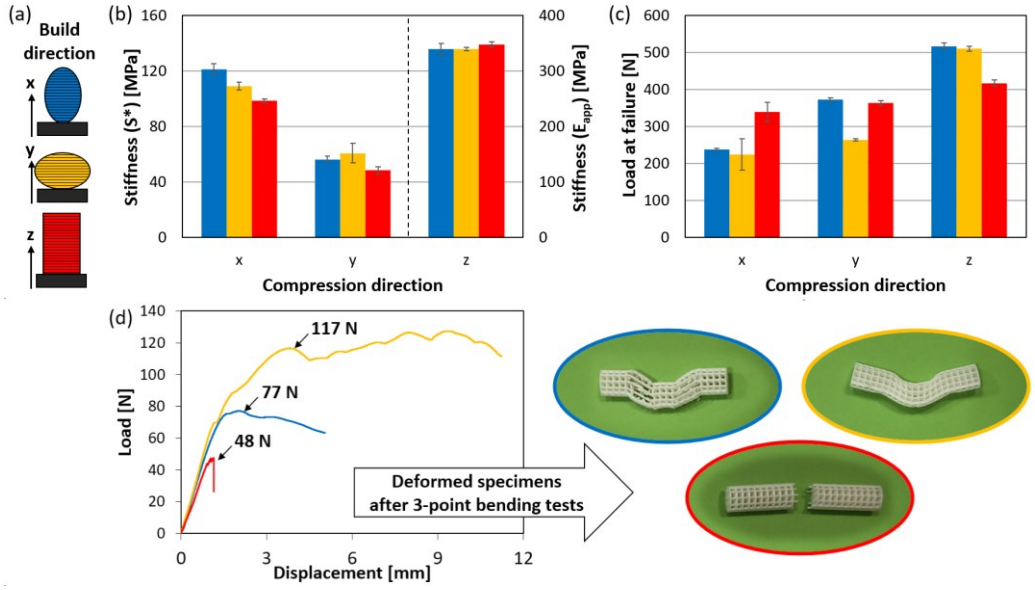

Figure 4.5. (a) Scheme of PLA core prototypes with elliptical cross-section printed with different orientations, represented by different colors as legend. (b-d) Effect of build direction on compression stiffness (b), compression load at failure (c), and bending response (d); compression tests were carried out along x, y and z axes, three-point bending tests along x.

However, the results of bending tests (three-point bending configuration; x loading direction) led to select y as build direction. In fact, as shown in Figure 4.5d, specimens built along y can bear significantly higher bending loads along x and their failure occurs gradually, as progressive plastic deformation. On the contrary, specimens built along z exhibit catastrophic failure for much lower loads. Finally, specimens built along x present intermediate failure load and deformation behavior, overall maintaining their integrity but showing several signs of local brittle failures. In summary, the criticality of the loading condition depends on how much the interface between printing layers in put under stress.

4.2.3. Implementation with medical-grade PLLA core and hydrogel shell

Once the core design was defined (lattice holes of 1.75 mm x 1.75 mm x 0.785 mm; y build direction), the mechanical properties of the scaffolds were finally verified upon substitution of commercial PLA with medical-grade PLLA as well as integration with the gelatin-chitosan shell (about 19% hydrogel content).

Figure 4.6 shows the results obtained by testing three core specimens and one core-shell specimen for each material and for each compression direction. No relevant differences in stiffness (Figure 4.6a) or strength (Figure 4.6b) are observed. Noteworthily, PLLA-hydrogel specimens were tested in wet conditions after sterilization with ^{60}Co gamma rays, so they represent exactly the final scaffolds. Moreover, the stiffness of the scaffolds appears properly tailored, since the values of apparent modulus (350 MPa ca., along z) are comparable with those of the stiffest system evaluated *in vitro*, *i.e.* PLA-CH(L) in Chapter 3.

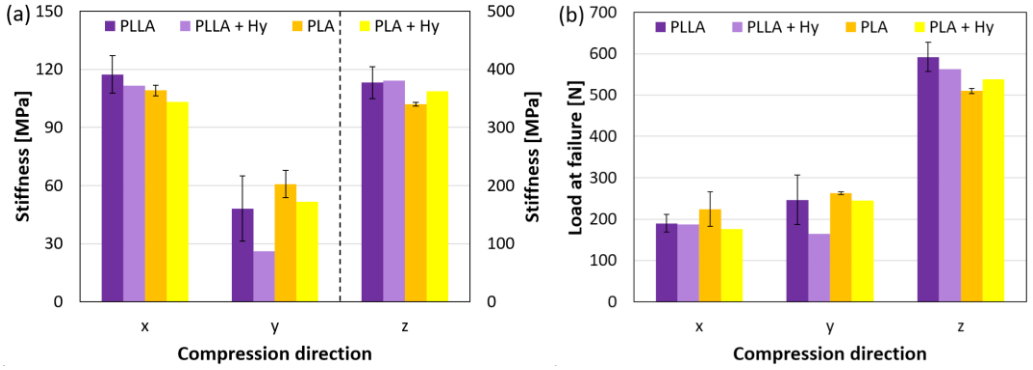

Figure 4.6. Stiffness (a) and load at failure (b) of PLLA and PLA core lattices for segmental mandible defects tested under compression along x, y and z axes; data of the corresponding core-shell scaffolds are also shown (PLLA + Hy, which were tested after sterilization; PLA + Hy).

Interestingly, the scaffolds could guarantee mechanical support against compression loads up to about 200 N along x. According to bite forces values reported by Weijs *et al.* [147,148], this may ensure biting capability comparable to healthy rabbits at least in young individuals (bite forces within 100 N ca.) and in correspondence of incisors in adults (bite forces around 200 N). Adult premolar/molar bite forces can reach some hundreds of N in healthy animals, but it must be remembered that a good bioactive scaffold should not merely provide mechanical support, but rather promote regeneration of new bone tissue in fast times to finally restore full mandible functionality. In the meantime, considering for instance the first month post-surgery, the proposed scaffolds could still perform

better than some common mandible treatments such as mandible distraction [149] or fracture fixation with biodegradable fixation devices [150]. The scaffold stiffness is also superior to that of typical rabbit food such as pellets or wet hay [151].

At the end of the engineering process described, PLLA lattices customized for mandibular full segmental defects and the corresponding core-shell scaffolds in wet conditions appear as shown in Figure 4.7. Moreover, Figure 4.8 highlights how aqueous fluids can easily permeate the interconnected porous structure of the hydrogel in these scaffolds: after deposition of some droplets of distilled water at the bottom of a dry scaffold, the liquid is fast absorbed and it can be seen flowing through the hydrogel pores and wetting the whole specimen. The scaffold permeability is important not only for bone regeneration *in vivo*, but also for hMSCs seeding and culture that precede surgery.

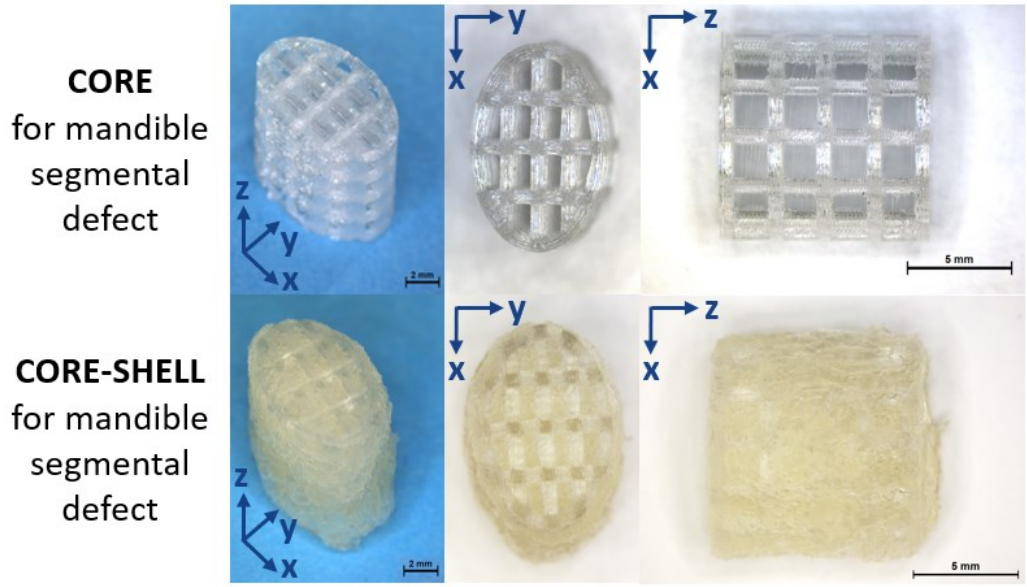

Figure 4.7. PLLA core lattices and wet PLLA-hydrogel core-shell scaffolds for mandibular full segmental defects in a rabbit model.

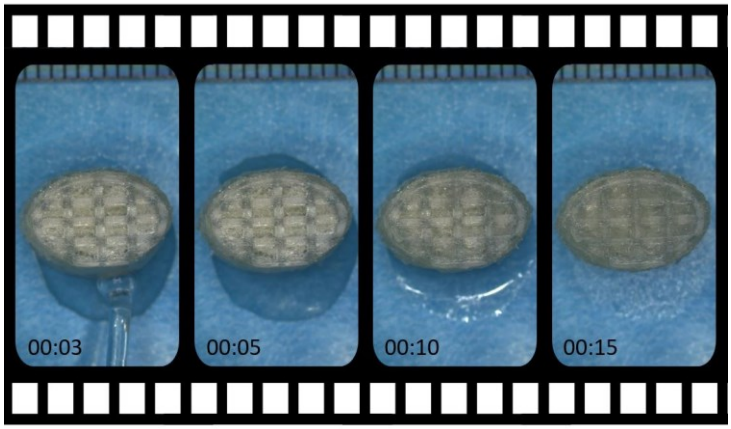

Figure 4.8. Water absorption in a PLLA-hydrogel scaffold prepared for in vivo *experiments.*

In addition, surgeons also requested scaffolds having the same core lattice cell as those with elliptical cross-section but fitting mandibular portions of different sizes (extra-small, XS; small, S; medium, M; large, L); all the dimensions are reported in Figure 4.1. Figure 4.9. shows prototypes of XS, S, M, and L lattices printed with commercial PLA (a), the lyophilization of the final core-shell scaffolds (b) and their appearance in dry conditions (c), including magnifications making the porosity of the shell more visible.

The precise values of core void volume fraction and hydrogel content for all the customized scaffolds can be read in Table 4.3; their slight increase with the scaffold size simply depends on the presence of incomplete lattice cells in correspondence of the curved lateral surface of the core.

All scaffolds were sterilized with a dose of 25 kGy ^{60}Co gamma rays by Gammatom Srl before being used in preclinical studies. This sterilization method was selected because previous studies on gelatin-chitosan hydrogel showed minor effects of gamma irradiation on the hydrogel properties [68]. Most literature considers it suitable for the sterilization of PLA-based medical devices as well [152], and the preservation of high mechanical properties in sterilized PLLA-hydrogel core-shell scaffolds (Figure 4.6) further supports this choice.

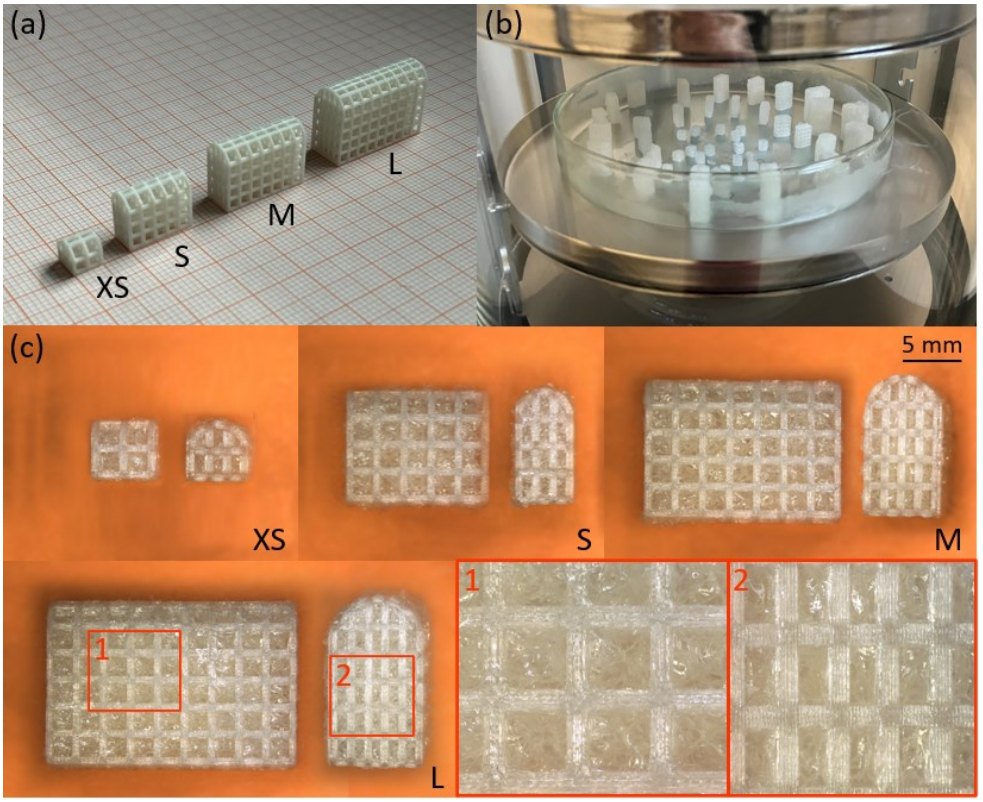

Figure 4.9. Scaffolds prepared in different sizes (XS, S, M, and L) for in vivo *experiments: (a) PLA core lattice prototypes; (b) lyophilization of PLLA-hydrogel core-shell scaffolds; (c) final appearance of PLLA-hydrogel scaffolds in dry conditions.*

Table 4.3. Designed core void volume fraction and measured hydrogel content (weight fraction) of PLLA-hydrogel scaffolds with different sizes for mandible regeneration in a rabbit model.

Size	**Core void volume fraction, th [%]**	**Hydrogel content, exp [%]**
Mandible segment	69.0	19.3
XS	67.0	15.5
S	71.5	17.4
M	72.7	18.0
L	73.4	19.0

4.3. Potential translational applications explored

4.3.1. *In vivo* regeneration of marginal and segmental mandibular defects

First preclinical preclinical studies on the rabbit model involved marginal mandibular defects filled with scaffolds consisting of polylactic acid-based core and gelatin-chitosan hydrogel shell [71], either seeded with hMSCs or only rehydrated. These experiments demonstrated that bone regeneration can be boosted by reconstruction with the scaffolds and, above all, with hMSC-seeded scaffolds. In fact, the two treatments achieved, respectively, 50% and 65% restoration of presurgical bone density in 4 months, compared to 40% restoration seen in spontaneous regeneration.

Next studies aimed at the reconstruction of critical-sized bone defects, with the final ambitious target of complete segmental defects. Looking for improved control over the mechanical properties and hydrogel content of the core-shell systems, scaffolds with 3D-printed PLLA core were prepared. These scaffolds were seeded with hMSCs and used in preliminary experiments on 5 animals with mandible marginal defects of 10 mm in length. No toxicity events were registered, but suboptimal regeneration results were obtained, which was mainly due to the fact that the scaffolds were not properly fixed to the mandible bone.

However, the feasibility of segmental mandibulectomy and reconstruction, a particularly complex surgical intervention, was demonstrated in a rabbit specimen. A horizontal segment on the left mandible side, including a tooth (first molar), was removed and replaced with a core-shell scaffold having elliptical cross-section of 10 mm x 6.5 mm and length of 10 mm (Figure 4.7). Figure 4.10 illustrates the location of the segmental defect in the mandible (a) and the positioning of the core-shell scaffold inside the defect (b). The scaffold was fixed to the mandible stumps with bioresorbable polyester screws and plate.

The animal survived the procedure, returned to oral feeding since the second postoperative day, and survived without difficulty for 4 months after implantation.

This proves the possibility to study mandible segmental defect regeneration with core-shell scaffolds when proper fixation to the bone is ensured. Of course, also for these interventions the scaffolds should be seeded with hMSCs to achieve the best results.

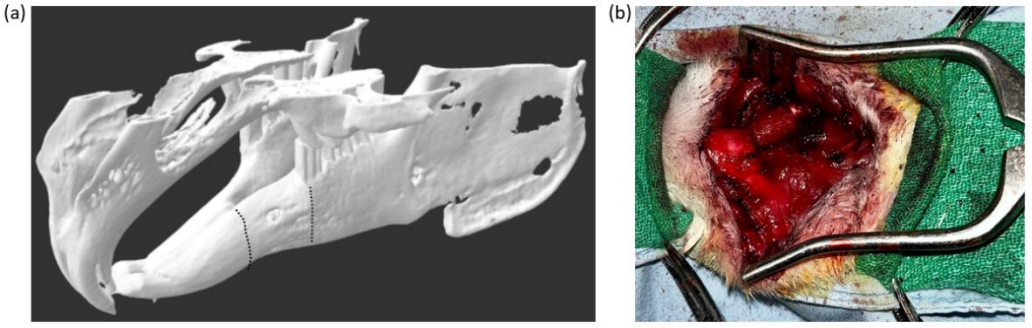

Figure 4.10. (a) Location of the segmental defect created in the rabbit mandible. (b) PLLA-hydrogel core-shell scaffold inserted in the mandible defect.

4.3.2. *In vivo* reconstruction of bone defects after removal of osteoradionecrotic portions of mandible

In this experimental phase, a first investigation on the regenerative properties of PLLA-hydrogel core-shell scaffolds after resection of osteoradionecrotic bone tissue. This highly unfavorable setting, in which bone tissue presents altered properties and reduced vascularization due to irradiation treatments, is of utmost applicative interest in bone regenerative medicine.

External beam radiotherapy with photons (X-rays) was performed on 9 rabbits, irradiating their mandible left side with 35 Gy divided in fractions of 7 Gy (therapeutic dose normally used in clinical practice); the right side received about 65% of the dose. The bidimensional target of the radiotherapy treatment (10 x 10 x 10 mm ca.) is shown in Figure 4.11, together with the area destined to reconstruction with a scaffold of 5 x 5 x 5 mm ca. (size XS in Figure 4.9). Follow-up with magnetic resonance imaging (MRI) and computer tomography (CT) was carried out until first signs of osteoradionecrosis, observed after about 4 months.

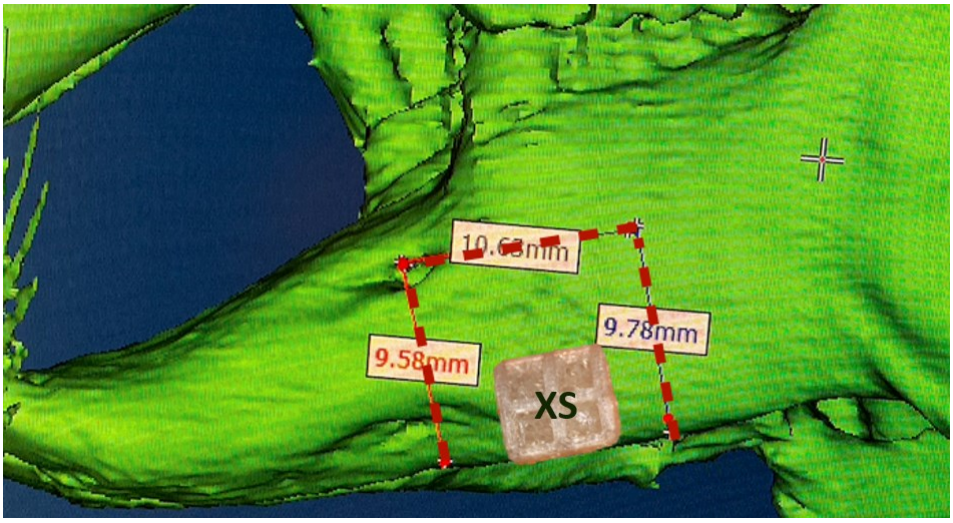

Figure 4.11. CT scan of a rabbit mandible with indication of the bidimensional target of the radiotherapy treatment on the left side (red dashed line) and of the bone resection area to be reconstructed with a PLLA-hydrogel core-shell scaffold of size XS (ca. 5 x 5 x 5 mm).

The center of the irradiated area was removed, creating marginal defects of about 5 x 5 x 5 mm on both mandible sides. The rabbits were divided in three groups: (i) 3 specimens left without reconstruction; (ii) 3 specimens treated with a scaffold without cells; (iii) 3 specimens treated with a scaffold seeded with hMSCs.

Bone defect regeneration around 25% was obtained after 4 months in rabbits treated with seeded scaffolds, a result that currently needs improvement. However, it is fundamental that nor toxicity events nor superinfections occurred, demonstrating excellent scaffold biocompatibility, and that the osteoradionecrosis process did not progress in any of the specimens, probably restrained by the tissue engineering procedure.

4.3.3. *In vivo* reconstruction of bone defects after ablation of a tumor grown in proximity of the mandible

Another important bone regeneration setting for clinical translation is represented by bone defects generated by oncological ablation of tumors. Therefore, another experimental chapter was opened to test the interaction between PLLA-

hydrogel scaffolds seeded with hMSCs and the microenvironment after tumor resection, with probable presence of micro-residues of tumoral cell nests.

Preliminary experiments were conducted on 3 rabbits subjected to oncological ablation of a tumor (VX2 cellular line) grown in proximity of the mandible. Marginal bone defects (5 x 5 x 5 mm ca.) were created in the portion of mandible adjacent to the tumor and reconstructed with hMSC-seeded scaffolds of corresponding XS size.

According to preliminary data, the presence of core-shell scaffolds and hMSCs does not favor any local tumor relapse. This is a particularly relevant result, because it states the safety of the employed regenerative model from the oncological point of view. Such promising feedback would be ideally confirmed by a higher number of experiments.

4.3.4. Ethics

The protocol for animal experimentation (AUP#6010; "Primary reconstruction of maxillary and mandibular defects with computer-aided designing, computer-aided manufacturing bioengineered composite scaffolds") was approved by the University Health Network Animal Care Committee (Princess Margaret Cancer Centre, University Health Network, University of Toronto).

4.4. Conclusions

Studies on PLA-hydrogel core-shell scaffolds have shown encouraging results in view of personalized bone regenerative medicine, as extensively discussed in Chapter 2 and Chapter 3 in terms of physical, thermal, mechanical, degradation, osteoconductive, and osteoinductive properties. As logical progression of the research, this chapter explored the potential use of the scaffolds in specific bone tissue engineering applications *in vivo*.

To this end, *ad hoc* scaffolds with medical-grade PLLA core were prepared to fit mandibular defects in a rabbit model. The new core material has certified biocompatibility and a higher enantiomeric purity with respect to the previous commercial PLA, but their thermal and mechanical behavior revealed to be overall similar for the purpose of this research; the main difference is that 3D-printed PLA is amorphous, while the crystallinity content in 3D-printed PLLA is about 10%, which may slow down its hydrolytic degradation process. In order to assess the actual time required for complete degradation of core lattices, it would be necessary to carry out longer *in vivo* studies than the preliminary experiments here described.

In order to customize the scaffolds for the segmental mandible defects planned by the surgeons, a core with elliptical cross section was designed and reinforced against bite forces by adding apposite lattice struts and carefully selecting the build direction. After 3D printing with medical-grade PLLA, grafting with bioactive gelatin-chitosan hydrogel (measured content of about 19 wt%), and sterilization by gamma irradiation, the customized scaffolds were found capable of withstanding considerable loads along the direction of rabbit bite forces.

These scaffolds, as well as similar specimens differing only for their external shape/dimensions, were employed in *in vivo* experiments on rabbit specimens, which provided interesting preliminary results in view of application in challenging clinical cases, such as regeneration of critical-sized defects, bone tissue damaged by irradiation, or post-tumor resection defects.

The preclinical experiments here presented showed encouraging results in terms of rabbit survival, absence of toxicity events or superinfections, and early oral feeding possibility. The absence of osteoradionecrosis progression in rabbits treated with radiotherapy and of local tumor relapse in rabbits subjected to tumor ablation are also very important achievements.

These preliminary findings must be confirmed and enriched by further elaboration of the experimental data collected by surgeons and by continuation of ongoing experiments on more rabbit specimens, as well as by further studies under different experimental conditions. In particular, for current experiments, not all computer tomography data are available, and euthanized rabbit mandibles require histomorphological and immunohistochemical analyses. For future studies, all experimental pathways here presented (treatment of critical-sized bone defects, bone regeneration after radiotherapy, and reconstruction of bone post-tumor resection) should be pursued more in depth.

5. Prediction of the Mechanical Properties of Lattice Structures by Analytical, Numerical and Data-Driven Models

This chapter[7] presents an extended discussion on useful modeling approaches to describe the correlations between the mechanical properties and the structure of composite core-shell scaffolds. The approaches here proposed represent different alternatives to the Gibson-Ashby power model employed in Chapter 2, which was found in previous literature on lattice structures and allowed correlation of relative modulus and relative strength with relative density by fitting experimental data. Their benefits and drawbacks are commented as conclusion to this chapter.

Since the mechanical properties of the scaffolds are provided by their core lattices, the models here discussed are representative of 3D lattice structures, an important class of metamaterials, whose properties are hugely influenced by their specific internal architecture. These structures are obtained by repetition of a unit cell in a 3D space, and they are typically produced thanks to additive manufacturing techniques due to their geometrical complexity. The strategies presented in this chapter enable the prediction of strength and stiffness of untested lattice configurations based on their geometrical features, which could be exploited early on during the design stage for faster examination of a large number of possible designs.

In summary, the proposed approaches include: (i) a simplified analytical model; (ii) a semi-empirical model combining analytical equations with experimental correction factors; (iii) an artificial neural network trained on experimental data; (iv)

[7] The paper relative to this work is under preparation at the moment of printing this thesis: G. Scalet, C. Pasini, S. Pandini, *Model-based and data-driven approaches for the prediction of the mechanical properties of lattice structures* (provisional title).

numerical simulations by finite element analyses. All of them have been applied to the case of commercial PLA lattices, for which a large number of mechanical test results was available from Chapter 2. The development of the artificial neural network and the numerical simulations were carried out at the University of Pavia[8].

The following paragraph 5.1 presents in detail the methods employed for each approach. Then, paragraph 5.2 deals with the results of analytical and semi-empirical models (i-ii). Finally, paragraph 5.3 investigates the accuracy of the artificial neural network with respect to experimental data and numerical simulations (iii-iv).

[8] Collaboration: Prof. Giulia Scalet (Department of Civil Engineering and Architecture, University of Pavia, via Ferrata 3, 27100 Pavia, Italy) took care of artificial neural network and numerical simulation approaches.

5.1. Materials and methods

5.1.1. Investigated lattice structures

As shown in Figure 5.1, this chapter investigates cubic lattice structures like those that constitute the core of the scaffolds in Chapter 2, drawn using Solidworks CAD software. Each structure is composed of a periodic arrangement of a unit cell along the x, y, and z axes. In particular, simple cubic, simple tetragonal, body-centered cubic (with internal diagonals), and face-centered cubic (with wall diagonals) unit cells are analyzed. Accordingly, labels SC, ST, BCC, FCC are used to denote the resulting structures.

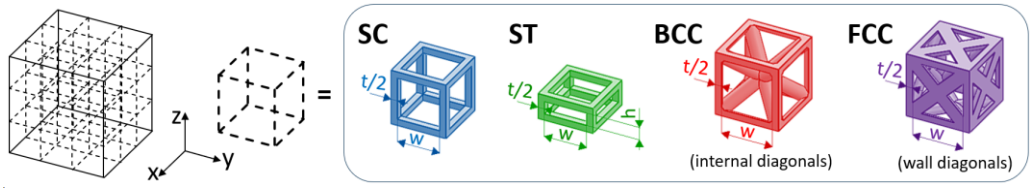

Figure 5.1. Representation of the unit cells of the investigated cubic lattices from Chapter 2: SC (simple cubic); ST (simple tetragonal); BCC (body-centered cubic); FCC (face-centered cubic).

Table 5.1 summarizes the main geometric features of each investigated structure. As it can be observed, the wall thickness, t, is kept fixed and equal to 0.6 mm, while the hole width, w, and the hole height, h, are variable parameters; for SC, BCC and FCC lattices, h is equal to w. Accordingly, the structures are labelled by means of the following notation: (i) SC_w for cubic unit cells; (ii) ST_w_h for tetragonal unit cells; (iii) BCC_w for body-centered cubic unit cells (with internal diagonals); (iv) FCC_w for face-centered cubic unit cells (with wall diagonals). The cells are then repeated periodically along the x, y, and z axes. The repetition is defined by the number of holes along these axes (N along x and y; M along z). The repetition is chosen in such a way to generate a lattice structure, having, as much as possible, an external cubic volume equal to 1000 mm^3 (side lengths of 10 mm). The theoretical void volume fraction ($V_{v,th}$) is computed as the ratio between the void volume and the external cubic volume of CAD models. Finally, the last column of Table 5.1

specifies whether the structures have been subjected to mechanical tests (compression tests in Chapter 2) or not; untested configurations are only introduced in this chapter as unseen inputs for the artificial neural network in paragraph 5.1.5.

Table 5.1. Geometrical dimensions of the investigated structures, according to definitions in Figure 5.1. In addition, N is the number of unit cells along x and y, M is the number of unit cells along z, $V_{v,th}$ is the theoretical void volume fraction, and the experimental test column reports the loading direction and the number of repetitions of compression tests.
[The table continues in the next page]

Label: type_w_h	Diagonals	t [mm]	w [mm]	h [mm]	N	M	Cube volume [mm³]	$V_{v,th}$ [%]	Exp. test
SC_0.5	/	0.6	0.5	0.5	9	9	1158	39	xy (3) z (3)
SC_0.7	/	0.6	0.7	0.7	8	8	1331	51	xy (1) z (1)
SC_1	/	0.6	1	1	6	6	1061	63	xy (3) z (3)
SC_1.5	/	0.6	1.5	1.5	5	5	1368	75	xy (1) z (1)
SC_2	/	0.6	2	2	4	4	1331	82	xy (3) z (3)
SC_2.5	/	0.6	2.5	2.5	3	3	970	85	Not tested
SC_3	/	0.6	3	3	3	3	1482	89	xy (1) z (1)
SC_3.5	/	0.6	3.5	3.5	3	3	2147	91	Not tested
SC_4	/	0.6	4	4	2	2	941	91	xy (3) z (3)
ST_1_0.6	/	0.6	1	0.6	6	8	1061	57	xy (3) z (3)
ST_1_0.8	/	0.6	1	0.8	6	7	1082	61	Not tested
ST_1.5_0.6	/	0.6	1.5	0.6	5	8	1257	66	xy (1) z (1)
ST_1.5_0.8	/	0.6	1.5	0.8	5	7	1281	69	Not tested
ST_1.5_1	/	0.6	1.5	1	5	6	1257	71	Not tested
ST_2_0.6	/	0.6	2	0.6	4	8	1234	72	xy (3) z (3)
ST_2_0.8	/	0.6	2	0.8	4	7	1258	74	Not tested
ST_2_1	/	0.6	2	1	4	6	1234	76	Not tested

Table 5.1. Geometrical dimensions of the investigated structures, according to definitions in Figure 5.1. In addition, N is the number of unit cells along x and y, M is the number of unit cells along z, $V_{v,th}$ is the theoretical void volume fraction, and the experimental test column reports the loading direction and the number of repetitions of compression tests.
[The table continues from the previous page]

Label: type_w_h	Diagonals	t [mm]	w [mm]	h [mm]	N	M	Cube volume [mm³]	$V_{v,th}$ [%]	Exp. test
ST_2_1.5	/	0.6	2	1.5	4	5	1343	80	Not tested
ST_2.5_0.6	/	0.6	2.5	0.6	3	8	1000	75	Not tested
ST_3_0.6	/	0.6	3	0.6	3	8	1326	78	xy (1) z (1)
ST_3_0.8	/	0.6	3	0.8	3	7	1352	80	Not tested
ST_3_1	/	0.6	3	1	3	6	1326	82	Not tested
ST_3_1.5	/	0.6	3	1.5	3	5	1443	85	Not tested
ST_3_2	/	0.6	3	2	3	4	1430	87	Not tested
ST_3_2.5	/	0.6	3	2.5	3	3	1287	88	Not tested
ST_3.5_0.6	/	0.6	3.5	0.6	3	8	1697	81	Not tested
ST_4_0.6	/	0.6	4	0.6	2	8	980	81	xy (3) z (3)
BCC_1.4	internal	0.6	1.4	1.4	5	5	1191	54	xy (1) z (1)
BCC_2	internal	0.6	2	2	4	4	1331	68	Not tested
BCC_2.4	internal	0.6	2.4	2.4	3	3	885	74	xy (1) z (1)
BCC_3	internal	0.6	3	3	3	3	1482	81	Not tested
BCC_3.4	internal	0.6	3.4	3.4	3	3	2000	84	xy (1) z (1)
FCC_1.4	wall	0.6	1.4	1.4	5	5	1191	45	xy (1) z (1)
FCC_2	wall	0.6	2	2	4	4	1331	60	Not tested
FCC_2.4	wall	0.6	2.4	2.4	3	3	885	67	xy (1) z (1)
FCC_3	wall	0.6	3	3	3	3	1482	75	Not tested
FCC_3.4	wall	0.6	3.4	3.4	3	3	2000	79	xy (1) z (1)

5.1.2. Realization of lattice structures and experimental tests

The lattice structures are realized by fused deposition modelling (FDM) 3D printing with Raise3D Premium PLA filament (details regarding the additive manufacturing process are provided in paragraph 2.1.2.1). The build direction is parallel to the z axis in Figure 5.1 for all the specimens realized.

For each specimen, the experimental value of the void volume fraction ($V_{v,exp}$) is also evaluated according to the methods in paragraph 2.1.3.1 (eq. 2.1).

Compression tests are performed as described in paragraph 2.1.3.5, testing each lattice structure along both the build direction (z) and the transverse direction (xy); the number of specimens for each condition is indicated in the last column of Table 5.1, for a total of 64 experimental tests. The results are represented as apparent stress (eq. 2.6) *vs.* apparent strain (eq. 2.7) curves, on which the following quantities are calculated: (i) compressive apparent modulus (E_{app}), evaluated as the first slope of the curves; (ii) compressive apparent failure stress ($\sigma_{app,f}$), evaluated at the first peak or knee of the curves. Since the considered loading directions are two, the measured quantities are here denoted as: $E_{app,xy}$ and $\sigma_{app,f,xy}$ for the x (or y) testing direction; $E_{app,z}$ and $\sigma_{app,f,z}$ for the z testing direction.

5.1.3. Analytical equations

The first approach used to describe the correlation between the mechanical properties and the void volume fraction of lattice structures is an analytical model that recalls the rule of mixtures (ROM) typically employed in composite materials [153]. Only lattice struts parallel to the loading direction are considered as actually contributing to the material stiffness and strength; according to the analogy with composite materials, these struts may be seen as uniaxial composite fibers inside in a matrix with zero stiffness and strength. By applying the ROM to the modulus (E_{ROM}) and to the failure stress ($\sigma_{ROM,f}$), the following equations are obtained:

$$E_{ROM}[MPa] = E_c V_{//} \tag{5.1}$$

$$\sigma_{ROM,f}[MPa] = \sigma_{c,f} V_{//} \tag{5.2}$$

where E_c = 2000 MPa and $\sigma_{c,f}$ = 59 MPa are, respectively, the modulus and the failure stress of the bulk material (*i.e.*, 3D-printed PLA), while $V_{//}$ is the volume fraction of struts parallel to the loading direction.

More in detail: 3D-printed PLA modulus is identified based on finite element analysis (see paragraph 5.1.6) and experimental apparent stress-strain curves of structure SC_3; 3D-printed PLA compressive strength is calculated as 125% of the tensile strength in the datasheet of Raise3D Premium PLA [133]; $V_{//}$ can be written also as ratio between the area occupied by the cross-sections of struts parallel to the loading direction and the total cross-section of the specimen.

5.1.3.1. Analytical equations for SC and ST unit cells

Considering SC and ST unit cells, the ratio between the mechanical properties of the lattices and those of PLA results as follows:

$$\frac{E_{ROM}}{E_c} = \frac{\sigma_{ROM,f}}{\sigma_{c,f}} = V_{//} = \begin{cases} \frac{t^2}{(w+t)^2} & along\ z \\ \frac{t^2}{(w+t)(h+t)} & along\ xy \end{cases} \tag{5.3}$$

The relative density (ρ_{rel}, eq. 2.12) of SC and ST unit cells can be calculated as ratio between the volume occupied by their struts and the total cell volume, resulting in the following equation:

$$\rho_{rel} = \left(\frac{t}{w+t}\right)^2 \left(\frac{2w+h+t}{h+t}\right) \tag{5.4}$$

In the specific case of SC cells, h is equal to w, so that eq. 5.3 and eq. 5.4 become:

$$\frac{E_{ROM}}{E_c} = \frac{\sigma_{ROM,f}}{\sigma_{c,f}} = \left(\frac{t}{w+t}\right)^2 \qquad along\ z\ and\ xy \tag{5.5}$$

$$\rho_{rel} = 3\left(\frac{t}{w+t}\right)^2 - 2\left(\frac{t}{w+t}\right)^3 \tag{5.6}$$

Finally, eq. 5.5 and 5.6 can be combined in the following analytical model:

$$\rho_{rel} = 3\frac{E_{ROM}}{E_c} - 2\left(\frac{E_{ROM}}{E_c}\right)^{3/2} = 3\frac{\sigma_{ROM,f}}{\sigma_{c,f}} - 2\left(\frac{\sigma_{ROM,f}}{\sigma_{c,f}}\right)^{3/2} \tag{5.7}$$

In the specific case of ST cells having h = 0.6 mm = t, eq. 5.3 and eq. 5.4 become:

$$\frac{E_{ROM}}{E_c} = \frac{\sigma_{ROM,f}}{\sigma_{c,f}} = \begin{cases} \left(\frac{t}{w+t}\right)^2 & along\ z \\ \frac{t}{2(w+t)} & along\ xy \end{cases} \quad (5.8)$$

$$\rho_{rel} = \frac{t}{w+t} \quad (5.9)$$

Finally, eq. 5.8 and 5.9 can be combined in the following analytical model:

$$\frac{E_{ROM}}{E_c} = \frac{\sigma_{ROM,f}}{\sigma_{c,f}} = \begin{cases} {\rho_{rel}}^2 & along\ z \\ 0.5\rho_{rel} & along\ xy \end{cases} \quad (5.10)$$

5.1.3.2. Analytical equations for BCC and FCC unit cells

Considering BCC and FCC unit cells, simple relative density expressions cannot be found because of the complexity of calculating the exact volume occupied by their struts. Therefore, such volume is extracted from CAD models using Solidworks, and ρ_{rel} is separately calculated for each lattice structure.

Moreover, when applying eq. 5.1 and eq. 5.2 to calculate the mechanical properties of FCC and BCC lattices, the number of struts parallel to the loading direction is corrected in the attempt of considering also the contribution of diagonal struts. In particular, each strut parallel to the loading direction counts as 1, while diagonal struts are decomposed along the axes x, y and z as if they were vectors (Figure 5.2).

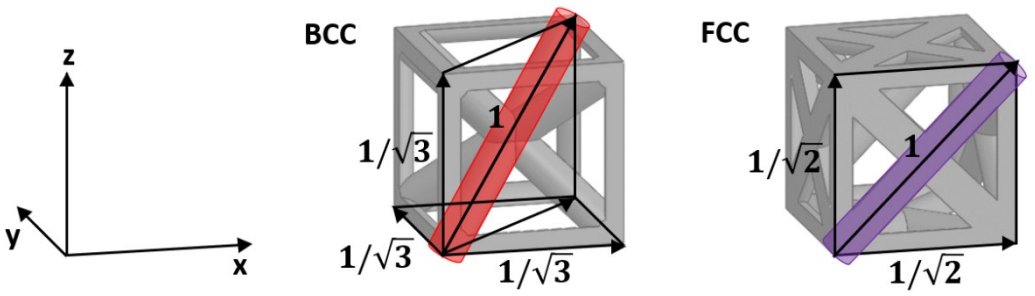

Figure 5.2. Decomposition of diagonal struts along the axes x, y and z in BCC and FCC lattice structures.

5.1.4. Semi-empirical equations

In a second approach to describe the correlation between the mechanical properties and the void volume fraction of lattice structures, the contribution of all struts to the stiffness and strength of the lattices is taken into account, in order to compensate for possible underestimations in the former approach, which considers only the contribution of struts parallel to the loading direction.

Considering the complexity of the geometry of the additional struts, a semi-empirical model is developed. The stiffness and the strength of the lattices are calculated as the sum of two contributions: (i) the contribution of struts parallel to the loading conditions, which is again described according to the ROM (eq. 5.1 and 5.2); (ii) the contribution of additional struts (ΔE or $\Delta\sigma_f$), which is expressed as a function of their volume fraction (V_{add}), resulting in the following equation:

$$\frac{\Delta E}{E_c} = \frac{\Delta\sigma_f}{\sigma_{c,f}} = K_0 + K_1 V_{add} \tag{5.11}$$

where $V_{add} = 1 - V_v - V_{//}$, while the values of K_0 and K_1 are derived as best fit parameters from experimental data on PLA lattices, more specifically from $\Delta E/E_c$ *versus* V_{add} plots for each lattice family.

Final values of moduli and failure stresses are obtained as:

$$E[MPa] = E_{ROM} + \Delta E = E_c(V_{//} + K_0 + K_1 V_{add}) \tag{5.12}$$

$$\sigma_f[MPa] = \sigma_{ROM,f} + \Delta\sigma = \sigma_{c,f}(V_{//} + K_0 + K_1 V_{add}) \tag{5.13}$$

5.1.5. Artificial neural network

The Department of Civil Engineering and Architecture of the University of Pavia collaborates to the study of structure-property relationships in the scaffold core structures by working on the development of an artificial neural network (ANN) model for accurate prediction of their mechanical properties. The modeling and implementation of the network are conducted using a code developed in the neural network environment of the software MATLAB (MathWorks®, Natick, MA, USA), as summarized in the following paragraphs. The network is then used to predict

compression stiffness and strength for both tested and untested configurations listed in Table 5.1.

5.1.5.1. Data pre-processing

The ANN takes the key inputs to define the geometry of the lattice structure and relates them to the output variables describing the mechanical properties of interest. In particular, the inputs are the hole width (w), the hole height (h), the number of holes in x (or y) direction (N), the number of holes in z direction (M), and the type of diagonal struts (none for SC and ST cells, internal diagonal for BCC cells, and wall diagonal for FCC cells); the outputs are the apparent moduli ($E_{app,xy}$ and $E_{app,z}$) and failure stresses ($\sigma_{app,f,xy}$ and $\sigma_{app,f,z}$).

Since the input and output variables have a wide span, they need to be properly normalized and scaled (values between 0 and 1) to improve the efficiency of the learning process. Being the type of diagonal a categorical variable, it must be converted into a numerical format that algorithms can understand. The adopted encoding (one-hot encoding) is represented in Table 5.2.

Table 5.2. Encoding adopted for representing the type of diagonals.

No diagonals	Internal diagonals	Wall diagonals
1	0	0
0	1	0
0	0	1

5.1.5.2. Network setup and hyperparameters

The overall architecture of the ANN is shown in Figure 5.3. To improve the network accuracy, its configuration is optimized in terms of the following hyperparameters:

(i) Number of hidden layers: a single hidden layer of neurons (shallow network) is used between the inputs and the outputs, which generally gives better performance than multiple hidden layers (deep network) when dealing with small datasets [154], such as the case considered here.

(ii) Number of nodes (neurons) in the hidden layers: two nodes have been adopted for the hidden layer.

(iii) Activation function in the hidden nodes: the "logsig" activation function is selected among those available in MATLAB environment to process the weighted sum of the inputs and determine the output of the node.

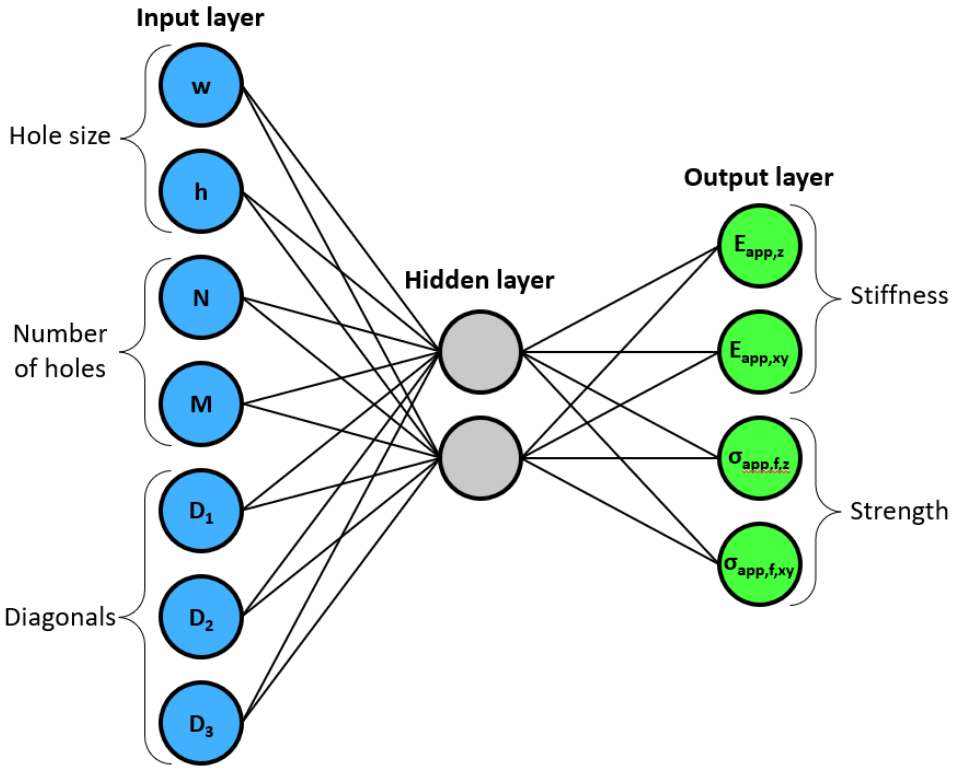

Figure 5.3. Architecture of the ANN.

5.1.5.3. Learning process

In order to apply the neural network approach, the data need to be divided into three groups: (i) training data, (ii) validation data, and (iii) test data. Experimental data on PLA lattices are here split into 70/20/10 proportions by "divideint" MATLAB function.

A back-propagation learning algorithm (MATLAB "trainbr" network training function) is used to iteratively update the internal parameters of the network.

During the training phase, the mean square error between the outputs of the network and the first group of experimental data (70% of the total) is minimized by adjusting the weights of the synapses in the network.

The second data set (20%) is then used for validation of the network. If the validation error is poor, the parameters used for training the network are adjusted and finally saved at the minimum of the validation set error.

Finally, test data (10%) are used to assess how good the network is at predicting the results for entirely unseen data.

5.1.6. Finite element modeling

A last approach for the prediction of the apparent modulus of core structures consists in simulations of compression tests by means of finite element analyses (FEA). To simulate the mechanical tests on PLA lattice structures under uniaxial compression, a quasistatic analysis is performed at the University of Pavia by means of the commercial finite element software Abaqus (Simulia, Providence, RI, USA).

Since FEA is here used for elastic moduli predictions, an isotropic linear elastic constitutive model is adopted. The Young's modulus value employed in the model (2000 MPa) is identified on apparent stress-strain curves obtained for 3D-printed PLA structure SC_3, while Poisson's ratio value is assumed equal to 0.35, which is a reasonable value for thermoplastic polymers and is consistent with literature data on poly-L-lactic acid filaments [155].

A displacement is applied on a face of the structure (along the test direction), while the opposite face is constrained along the three axes. The structures are meshed as shown in Figure 5.4 (eight-node brick elements for SC and ST lattices; four-node tetrahedral elements for BCC and FCC lattices).

Once the FEA is completed, apparent stresses and strains are computed from displacement *vs* reaction force curve, and values of apparent moduli and failure stresses are derived from stress-strain curves, following the methods described in paragraph 2.1.3.5.

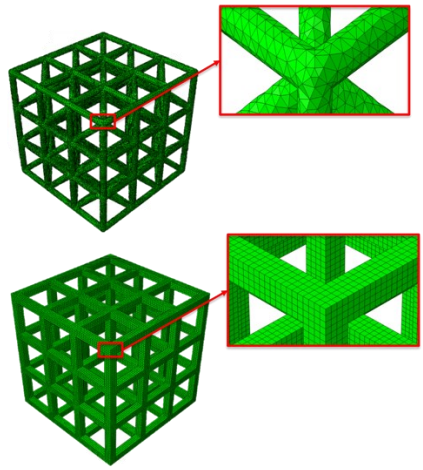

Figure 5.4. Examples of meshes adopted for (a) SC and ST lattices, and for (b) BCC and FCC lattices.

5.2. From analytical equations to a semi-empirical modeling approach

As a first approach towards modeling of PLA lattice structure-property correlations, simple analytical equations are investigated. As described in paragraph 5.1.3, these equations are based on the rule of mixtures (ROM) typically employed in composite materials [153], considering lattice struts parallel to the loading direction as fibers and the voids as matrix. Perpendicular struts are neglected, while diagonal struts contribute only with their parallel component.

In its simplicity, this analytical model is able to capture the qualitative trend of apparent modulus and failure stress plotted against the lattice void volume fraction, but fails in providing good quantitative predictions of mechanical properties. In fact, stiffness (Figure 5.5a) and strength (Figure 5.5b) of SC and ST lattices tend to be underestimated with respect to their experimental values, suggesting that the constraint provided by struts perpendicular to the loading direction is not negligible and improves the lattice performance to some extent. Conversely, stiffness (Figure 5.5c) and strength (Figure 5.5d) of BCC and FCC lattices are overestimated by the analytical model, which may be due to the simplicity of the assumption that the contribution of diagonal struts can be decomposed into parallel (contributing) and perpendicular (not contributing) components, but could also be ascribed to the anisotropic nature of FDM 3D-printed materials; in fact, the interface between layers is a potential source of weakness, that appeared mostly negligible under compression (see Chapter 2), but may reduce the performance of diagonal struts, in which the layers are not orthogonal with respect to the strut axis.

In light of such limitations of the analytical model, a semi-empirical model (eq. 5.12-13) is developed as described in paragraph 5.1.4. As said, the mechanical properties of PLA lattices are expressed as the sum of two contributions: (i) E_{ROM} or $\sigma_{ROM,f}$, which is a purely analytic component, associated to struts parallel to the

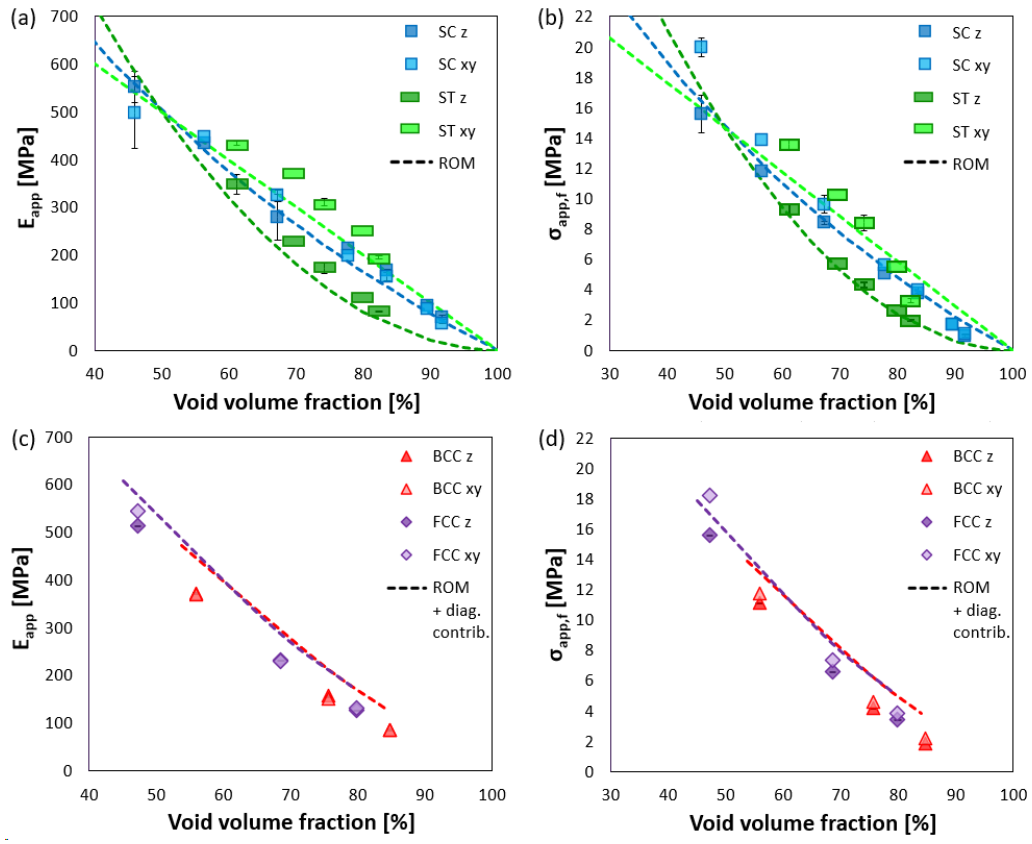

Figure 5.5. Experimental values and analytical model predictions (ROM) of apparent modulus (a,c) and failure stress (b,d) plotted against void volume fraction, for PLA lattices with SC and ST unit cells (a,b) and with BCC and FCC unit cells (c,d).

loading direction and derived according to the ROM; (ii) ΔE or $\Delta\sigma_f$, which is experimentally measured and associated to the additional struts.

ΔE can be normalized with respect to PLA stiffness (E_c) and plotted as a function of the volume fraction of additional struts (V_{add}), as shown in Figure 5.6. This plot clearly highlights two possible responses from the lattice structures: (i) in the case of SC and ST unit cells, additional struts provide a moderate contribution to the lattice stiffness, which is apparently not influenced by the volume occupied, at least in the range of V_{add} values here covered; (ii) in the case of BCC and FCC unit cells, thanks to diagonal struts, the lattice stiffness receives a higher additional contribution, which seems to increase linearly with V_{add}.

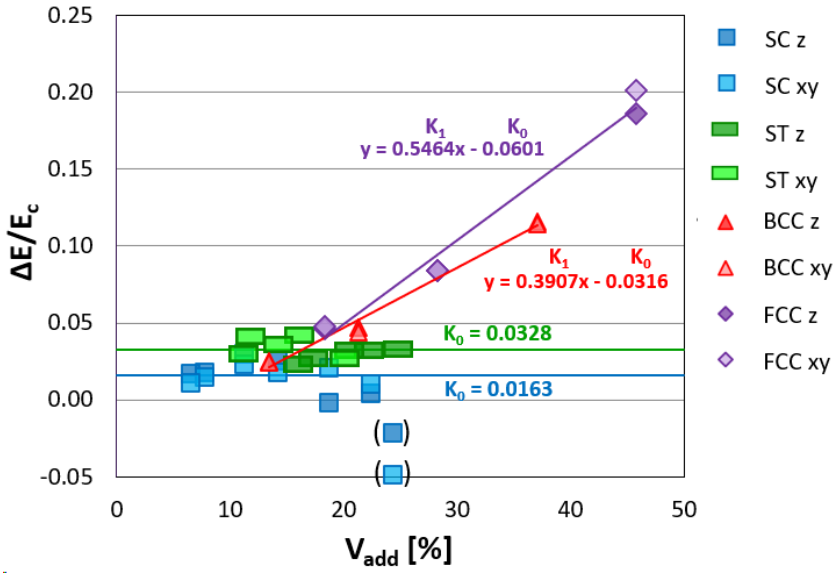

Figure 5.6. Graph used for the determination of fudge factors K_0 (intercept) and K_1(slope) for the semi-empirical model of PLA lattice structure-property correlations: the contribution of additional struts to the modulus (ΔE) is normalized with respect to PLA modulus (E_c) and plotted against the volume fraction of additional struts (V_{add}); data in brackets are excluded from the fitting.

Table 5.3. Fitting constants K_0 and K_1 derived from $\Delta E/E_c$ vs V_{add} plots for PLA lattice structures (Figure 5.6).

Lattice unit cell	K_0	K_1
SC	0.0163	0
ST	0.0328	0
BCC	-0.0316	0.3907
FCC	-0.0601	0.5464

The plot can be used to determine the values of the constants K_0 and K_1 in the semiempirical model, according to eq. 5.11: K_0 corresponds to the intercept, while K_1 corresponds to the slope of the experimental trends; data points between bracket correspond to exceptionally dense SC lattice structures ($w = 0.5$ mm $< t$), which fall out of the trend and cannot be included in the analysis. The two fitting constants assume specific values for the various lattice families, as reported in Table 5.3.

In SC and ST lattices, the addition of struts perpendicular to the loading direction is found to give a small positive contribution ($K_0 > 0$, corresponding to about 2-3% of 3D-printed PLA Young's modulus), independently of the volume occupied (*i.e.*, $K_1 = 0$).

Conversely, in BCC and FCC lattices, ΔE is proportional to the volume fraction of additional struts ($K_1 > 0$), and a negative intercept results from the fitting ($K_0 < 0$). In fact, mechanical properties increase significantly with the number of diagonal struts having a component parallel to the loading direction, but additional struts in BCC and FCC lattices also include several struts that are perpendicular to the load and contribute less; therefore, the negative value of K_0 compensates for these struts. Moreover, as expected, the constant K_1 is higher for FCC lattices than for BCC lattices, because wall diagonals are less inclined than internal diagonals with respect to the loading direction.

From all these considerations, it is clear that the introduced constants are not simply "fudge" factors to produce better fits, but meaningful parameters to properly account for additional struts in the model. In particular, K_0 is useful for including the effect of struts perpendicular to the loading direction, which was neglected in the previous analytical model, while the experimental evaluation of K_1 allows for a better estimation of the contribution of diagonal struts.

As a result, semi-empirical model predictions are much closer to the experimental data on PLA lattice structures, as reported in Figure 5.7. Noteworthily, even if K_0 and K_1 are here derived from stiffness values only, the model can describe not only apparent modulus trends (Figure 5.7a,c) but also apparent failure stress trends (Figure 5.7b,d).

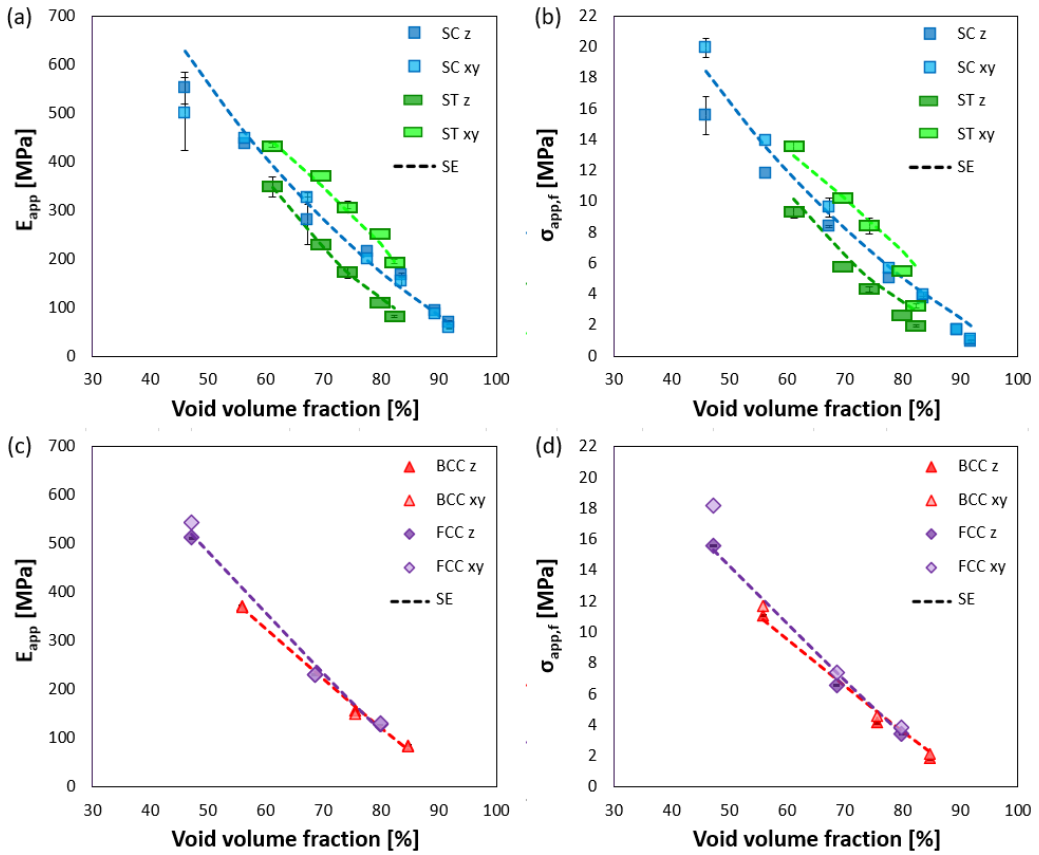

Figure 5.7. Experimental values and semi-empirical model predictions (SE) of apparent modulus (a,c) and failure stress (b,d) plotted against void volume fraction, for PLA lattices with SC and ST unit cells (a,b) and with BCC and FCC unit cells (c,d).

5.3. ANN and FEA approaches

Another data-driven model of lattice structure-property correlations can be obtained by training an artificial neural network (ANN) on the experimental data obtained for PLA lattice structures, as described in paragraph 5.1.5. The ANN receives the geometrical parameters of PLA lattices as inputs, and predicts the corresponding mechanical properties as outputs. During the machine learning process, the outputs of the ANN converge to the target experimental values.

5.3.1. Performance evaluation of the neural network

The optimum configuration of the network is determined based on the mean squared error evaluated for stiffness and strength outputs with respect to the measured experimental values. The mean squared error is reported in Figure 5.8 along the epochs (one epoch corresponds to one cycle through the full dataset), for each phase of the learning process (training, validation, test). In particular, the parameters of the network are saved at the epoch corresponding to the best validation performance (mean squared error of 1.73 x 10^{-3}, at epoch 42).

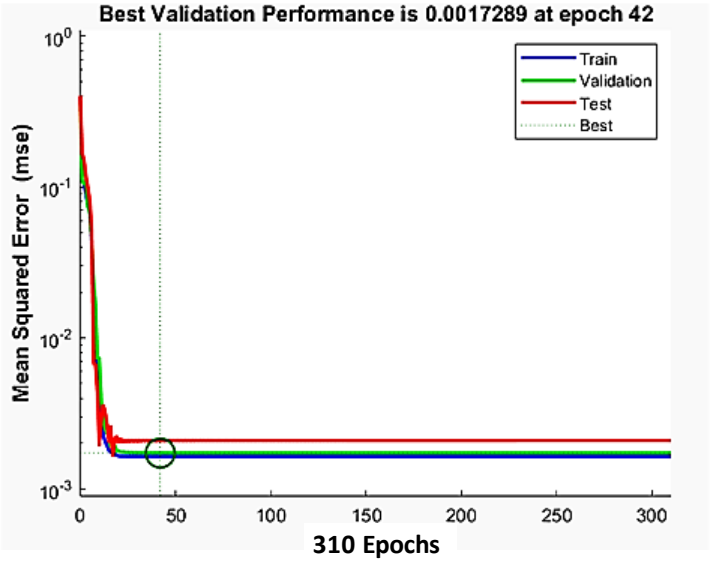

Figure 5.8. Mean squared error values obtained along the epochs for training, validation, and test phases. They are calculated for both stiffness and strength ANN outputs with respect to the corresponding experimental targets.

In order to better visualize the overall accuracy of the predictions, the correlation between experimental and ANN results is shown in Figure 5.9, together with the corresponding coefficients of correlation (*R*). Normalized values of both apparent stiffness and apparent strength of PLA lattices are considered. The first three graphs refer to the training, validation, and test datasets, while the fourth one shows the results considering all 64 data points. The 45° line corresponds to perfect matching between predictions (output) and experimental values (target).

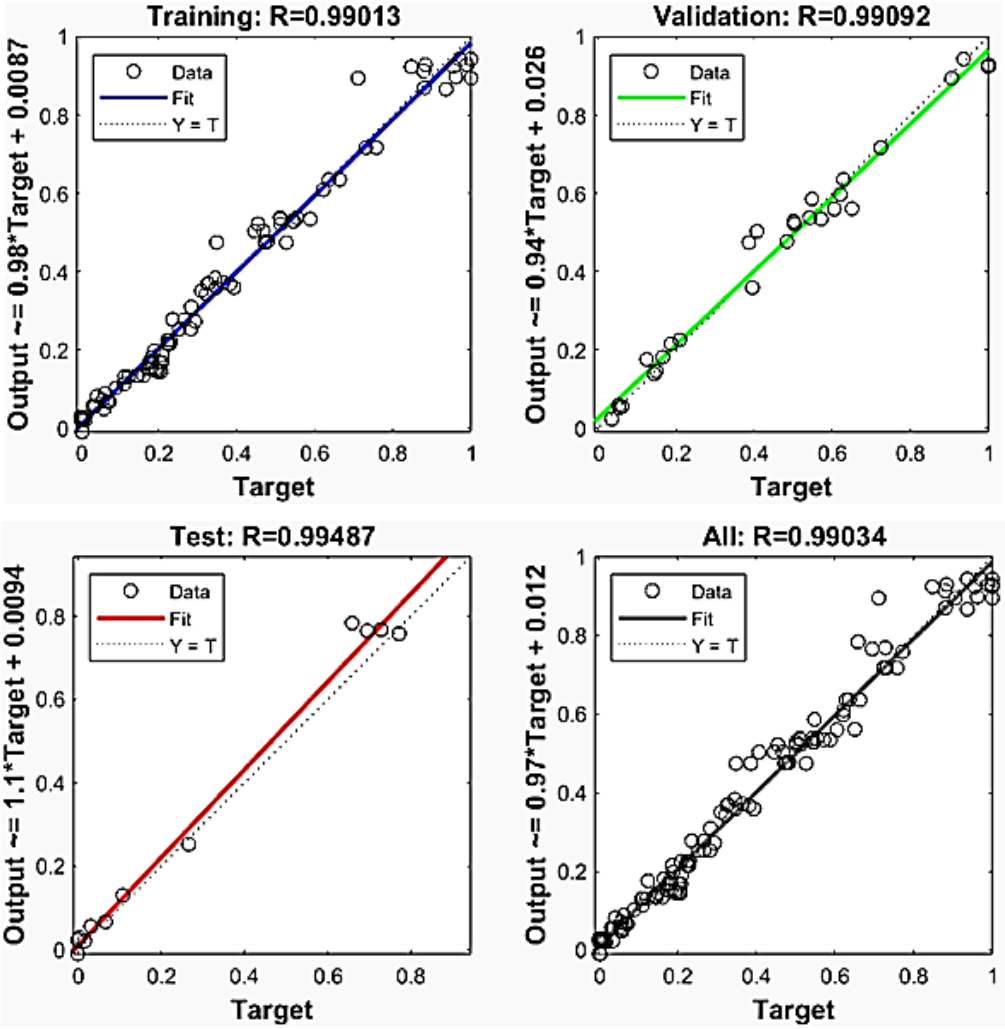

Figure 5.9. Correlation of ANN outputs with experimental target values for training, validation and test datasets, and for all datapoints considered together; normalized values of both apparent stiffness and apparent strength of PLA lattices are considered as output/target.

The predictions are of very good accuracy, since all the data fall within ±3 standard deviations. In addition, since the points are distributed uniformly above and below the 45° line, it can be concluded that there is no over- or under-prediction tendency, and the prediction errors are fairly random (no systematic error is observed).

5.3.2. ANN and FEA results

The outputs of the ANN are reported in Figure 5.10 (stiffness) and Figure 5.11 (strength) for both tested and untested lattice configurations in Table 5.1, together with experimental data points and, for stiffness only, with the results of finite element analyses (FEA, highlighted with orange color). In particular, untested configurations correspond to data points surrounded by a black border. For each PLA lattice type (SC; ST; BCC; FCC), the four outputs ($E_{app,xy}$; $E_{app,z}$; $\sigma_{app,f,xy}$; $\sigma_{app,f,z}$) are plotted against the void volume fraction.

As highlighted in the previous paragraph, the ANN is able to accurately estimate the mechanical properties of the lattices based on the inputs describing their structure. FEA results are also consistent with the experimental data, but larger deviations are observed for denser lattices (*i.e.*, low void volume fractions).

Therefore, the data-driven approach is once again more effective. In particular, the ANN model is the most accurate among the proposed prediction strategies, being able to capture very well even the behavior of denser lattices. Finally, the network can also be used to evaluate the properties of untested PLA core structures (data points with black contour), which are found to be consistent with the overall trend of lattices having the same unit cell type.

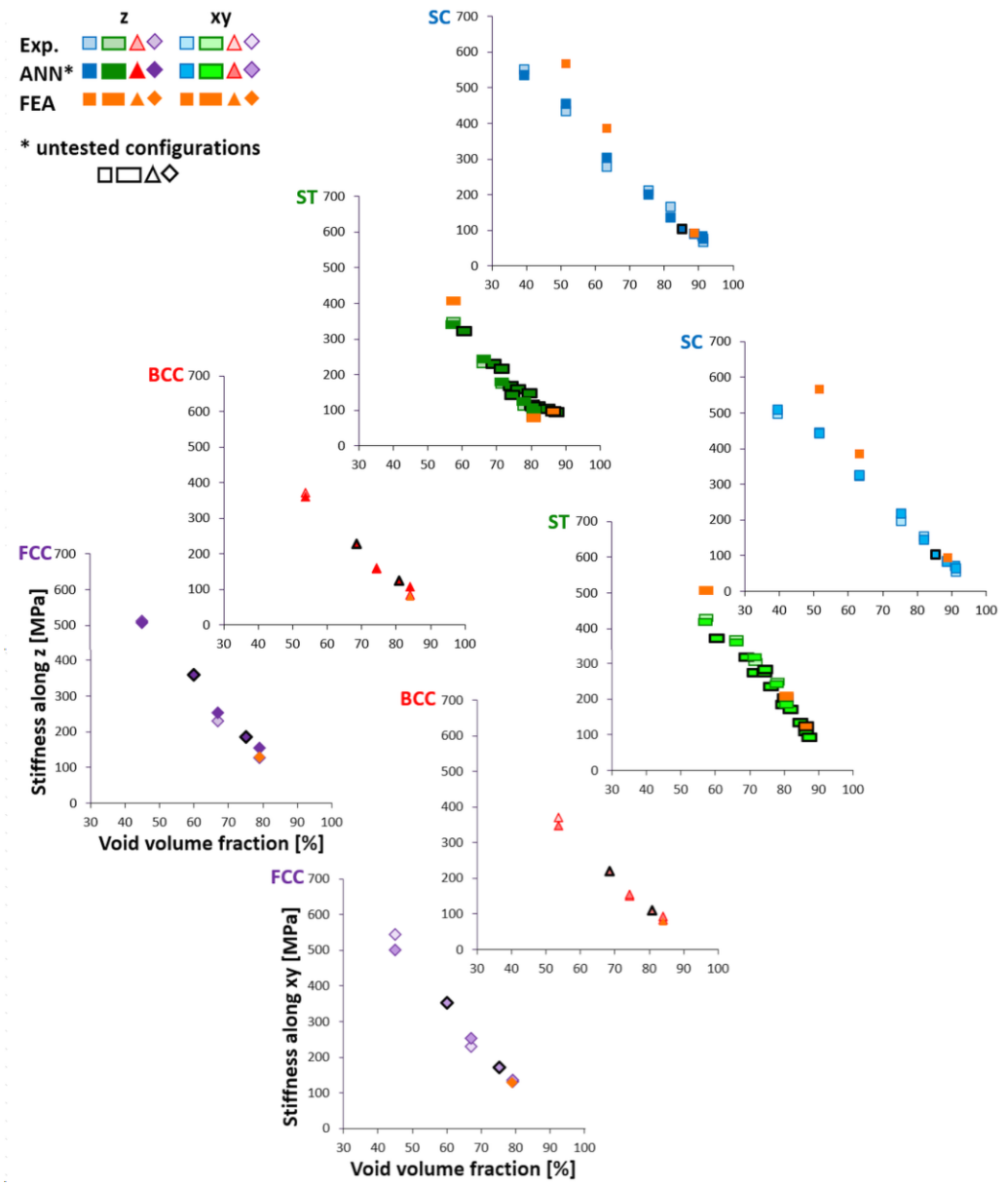

Figure 5.10. PLA lattice compression stiffness along z and xy directions, according to experiments, artificial neural network (ANN) and finite element analyses (FEA).

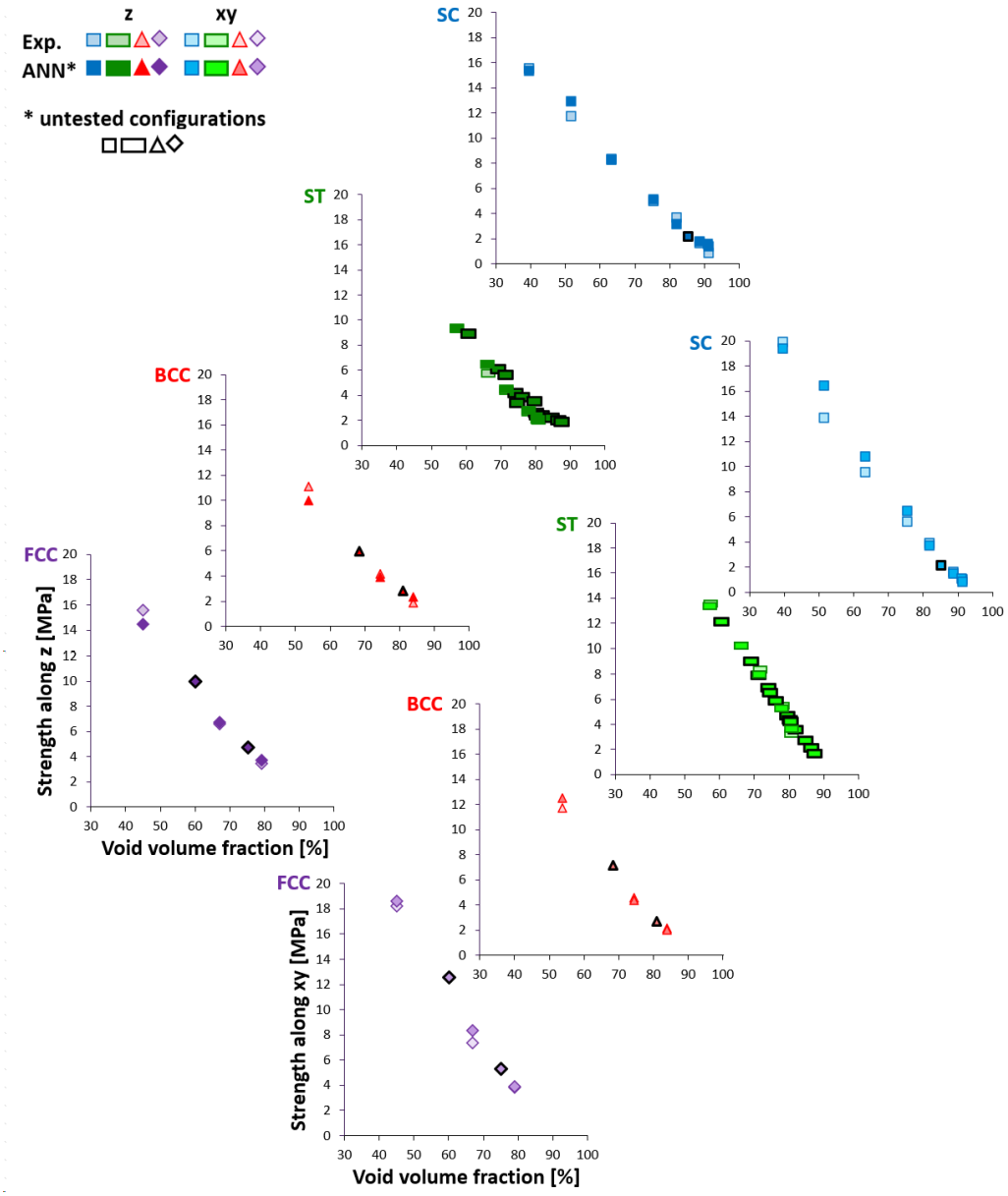

Figure 5.11. PLA lattice compression strength along z and xy directions, according to experiments and artificial neural network (ANN).

5.4. Conclusions

There are several modeling approaches that can be adopted for the prediction of the mechanical properties of lattice structures. This chapter explored a selection of models belonging to different categories and applied them to the case of PLA core structures for tunable core-shell composite scaffolds, aiming to develop helpful tools for their design.

The first approach presented, consisting of analytical equations based on the rule of mixtures, is very simple and has the advantage of being purely theoretical. Therefore, it can be easily applied during the very first design stages to estimate how the lattice properties vary with their architecture. However, it introduces significant approximations, especially neglecting the contribute of struts perpendicular to the loading direction, and cannot be considered quantitatively accurate.

Another strategy employing theoretical calculations relies on finite element analyses. Numerical simulations require higher computational effort to evaluate large numbers of geometrical configurations, but they are able to correctly consider the effect of all lattice struts and to provide additional information on stress and strain distributions. They may help optimizing lattices at later design stages, though the specific setting here investigated shows limitations in the analysis of denser lattices. It should be noted that this model does not take into account the layered nature of 3D-printed specimens, which leaves space for improvement.

Due to the complex microstructure of PLA lattice structures realized by additive manufacturing, building a reliable theoretical model can be particularly cumbersome, but it is possible to exploit a set of experimental results to create a predictive tool for new untested configurations. Indeed, the data-driven models here proposed performed very well, both in the case of semi-empirical mathematical equations and in the case of machine learning; the Gibson-Ashby model used in Chapter 2 also falls in the category of data-driven approaches, deriving its constants by fitting experimental data. Noteworthily, concerning machine learning, a rather small

training dataset was found sufficient to obtain a qualified artificial neural network with very low validation mean squared error.

Finally, the possibility of extending the predictions to core materials other than PLA should be considered. The work here presented is still limited to the case of PLA lattices, but the same strategies may be in principle applied to any other material. For example, the case of soft TPE core structures may be addressed after some additional experimental tests with respect to those reported in Chapter 2 (which include only lattices with simple cubic unit cells).

6. 4D Fabrication of Two-Way Shape Memory Polymeric Composites by Electrospinning and Melt Electrowriting

This chapter is devoted to a separate work[9] with respect to the main project of core-shell scaffolds presented in this thesis. In fact, five months of the last year of doctoral studies were spent in a foreign laboratory (Prof. Ionov's Biofabrication Laboratory, University of Bayreuth), which provided the opportunity of learning different biofabrication techniques and studying smart biopolymers.

The research activities carried out abroad were dedicated to the study of electrospinning and melt electrowriting techniques and to the development of a different type of biocompatible polymeric composites, in which the combination of multiple materials and fiber spinning processes is meant to achieve distinctive stress-free bidirectional actuation capabilities and high flexibility. Noteworthily, these systems share with the core-shell scaffolds not only the use of biocompatible polymers, but also the design freedom guaranteed by additive manufacturing techniques and the possibility of tailoring their properties by changing the proportions and the structure of their components.

More in detail, this chapter describes a new method for 4D fabrication of two-way shape memory materials, that are capable of reversible shapeshifting upon application of heating and cooling cycles. In the biomedical field, the use of these smart materials has been proposed in applications such as bandages, temporary

[9] This work is presented in a paper which is under review at the moment of printing this thesis: C. Pasini, Z.V. Soreño, D. Schönfeld, T. Pretsch, G. Constante, I. Sadilov, L. Ionov, *4D fabrication of two-way shape memory polymeric composites by electrospinning and melt electrowriting*. Research activities were carried out during a period of five months spent in Germany with Prof. Leonid Ionov's team (Faculty of Engineering Sciences, University of Bayreuth, Ludwig Thoma Str. 36A, 95447 Bayreuth, Germany).

fixation parts, active devices to help disabled people, shape-switching drug carriers, and dynamic mechanical stimulation of cell cultures.

The innovative solution here presented consists in the combination of highly stretched electrospun shape memory polymer (SMP) nanofibers with a melt electrowritten elastomer. More specifically, the electrospun nanofibers are made of a biocompatible thermoplastic polyurethane (TPU) with crystallizable soft segments[10], and a commercial TPU filament is employed for the elastomer component.

The stretched SMP represents the active layer, undergoing melt-induced contraction and crystallization-induced elongation upon heating and cooling, respectively. Reversible actuation during crystallization becomes possible thanks to the elastic recovery of the passive component, *i.e.* the melt electrowritten elastomer. Thanks to the design freedom offered by additive manufacturing, the elastomer structure has also the role of guiding the shape transformation. As final result, a smart 4D object is achieved (3D shape + transformation along time in response to thermal stimuli).

The experimental work started from the optimization of process parameters for two well-known biofabrication techniques, electrospinning and melt electrowriting, until obtaining composites capable of two-way shape memory effect (SME). The two components were then combined in different proportions with the aim of tailoring the two-way SME, taking into account the effect of design parameters such as the SMP content, the elastomer pattern, and the composite thickness.

[10] The shape memory TPU employed in this work was developed by Thorsten Pretsch's team (Shape Memory Polymers Group, Fraunhofer Institute for Applied Polymer Research IAP, Geiselbergstr. 69, 14476 Potsdam, Germany).

6.1. Materials and methods

6.1.1. Materials

As shape memory polymer (SMP), a thermoresponsive polyester urethane was employed. For its synthesis, the following materials were purchased: poly(1,4-butylene adipate) (PBA) diol Desmophen 2505 from Covestro Deutschland AG (Leverkusen, Germany); 4,4´-diphenylmethane diisocyanate (MDI) from Fisher Scientific (Schwerte, Germany); 1,4-butanediol (BD) and a molecular sieve with a pore size of 4 Å from Alfa Aesar (Kandel, Germany). For SES, the following solvents were provided by Merck (Darmstadt, Germany): acetone; dimethylformamide (DMF); chloroform ($CHCl_3$); tetrahydrofuran (THF). Rhodamine B dye (C.I. 45170) was obtained from Carl Roth GmbH + Co KG (Karlsruhe, Germany).

As elastomer, a commercial thermoplastic polyurethane (TPU) filament was employed. The selected TPU was Filaflex 70A Ultra-Soft by Recreus Industries, S.L. (Elda, Spain).

6.1.2. Preparation of shape memory composite materials

6.1.2.1. Synthesis of TPU PBA-75

PBA-based polyester urethane (TPU PBA-75) was synthesized with 75% PBA-based soft segments, following the prepolymer method described in a previous paper [156]. In summary, 0.037 mol of dried PBA-diol and 0.157 mol of MDI reacted at 120 °C for 90 min, forming a isocyanate prepolymer, which then further reacted with 0.12 mol of dried BD. The obtained melt was poured onto a plate covered with a polytetrafluoroethylene film. After a final curing in oven at 80 °C for 120 min, TPU PBA-75 was ground into granules.

6.1.2.2. Solution Electrospinning (SES) of TPU PBA-75

A custom-made electrospinning device was employed for SES of TPU PBA-75. The setup consisted of a syringe pump (Omnifix® 1 ml and 5 ml syringes were used

with a 21G needle, *i.e.* 0.5 mm inner diameter), a 30 kV voltage controller, and a metallic collector (either two conductive bars separated by a 4 cm gap and fixed at 15 cm from the tip of the needle, or a rotating drum having a 5 cm diameter and placed at 25 cm from the tip of the needle). Glass slides and aluminum foil were used as substrates for fiber deposition in the case of the two-bar collector and of the rotating drum, respectively.

TPU PBA-75 solutions were obtained by dissolving the polymer granules in different solvent mixtures (DMF-acetone with a volume ratio of 2:3; DMF-$CHCl_3$-THF with volume ratios of 2:2:1), with polymer concentration varying between 6 w/v% and 10 w/v%. A slight amount of rhodamine B was added as dye. The solutions were stirred overnight at ambient temperature and centrifuged for 10 min (8000 rpm, 6010 g, 15 °C), in order to obtain a homogeneous solution.

Looking for the optimal set of process parameters, different values of solution flow rate (0.25-0.5-1 mL/h) and of applied voltage between the tip of the needle and the collector (20-25-30 kV) were considered. For the rotating drum collector, a speed of 8000 rpm was adopted. For optical microscope observation, the electrospinning process was stopped after about 5 minutes, whereas specimens for other analyses had longer production times (30 min – 1 hour).

6.1.2.3. Melt Electrowriting (MEW) of TPU Filaflex

MEW of TPU Filaflex was performed by means of a custom-made device composed of four elements: a three-axis (XYZ) precision stage, a dual-gear feeder system, a thermal control system, and a high voltage supply (LNC 30000, Heinzinger electronic GmbH, Rosenheim, Germany). The control system was created through the software Repetier Host (Hot-World GmbH & Co. KG, Knickelsdorf, Germany). The device was equipped with a 0.2 mm nozzle, which was kept at a 3 mm distance from the collector.

Several parallel long and short filaments were deposited for the selection of optimized process parameters (long filaments: 70 mm length and 1.5 mm spacing;

short filaments: 20 mm length and 1 mm spacing; width and height of the filaments were both set to a nominal value of 30 μm in the G-code). The following parameter values were considered: nozzle temperature of 230-240 °C; applied voltage of 1.5-2.5-3.5 kV; collector speed between 300 and 1800 mm/min.

Composite systems were obtained by deposition of multiple TPU Filaflex layers onto electrospun TPU PBA-75 mats collected on a rotating drum. A quasi-isotropic sequence ($[0°/45°/90°/-45°]_s$) was repeated one or two times. After each set of 4 filament orientations was deposited, the nozzle-collector distance was increased of 0.1 mm. For each orientation, parallel filaments were spaced of 0.5 mm (higher density areas) or 1 mm (standard density areas) and their nominal width and height in the G-code was equal to 30 μm. By changing the thickness and/or the density of the MEW layer in different areas of a same specimen, it was possible to design different shape transformation patterns (see shape memory experiments in paragraph 6.1.3.5.). The obtained samples were stored in a freezer at -20 °C.

6.1.3. Morphological, thermal and shape memory characterizations

6.1.3.1. Optical and electron microscopy

Images of fibers obtained by SES and MEW fibers were recorded by means of an optical microscope Eclipse Ti2 (Nikon, Japan) and a scanning electron microscope (SEM) Gemini Sigma 300 VP (Zeiss, Germany). Prior to SEM observation, samples were attached onto pin stubs with copper tape, and their conductivity was ensured by sputtering with platinum (~2 nm) by means of a Cressington 108 auto sputter coater (Cressington Scientific Instruments Ltd., Watford, UK). Image analyses were carried out by using the software ImageJ (National Institutes of Health, US).

6.1.3.2. Differential Scanning Calorimetry (DSC)

DSC analysis of TPU PBA-75 was carried out with a Mettler Toledo DSC3 (USA). About 10 mg of granules were closed inside an aluminum crucible. The following heating-cooling cycle was repeated four times, each maintaining the

sample at a different cooling temperature, T_{low}: (i) heating up to 80 °C at 5 °C/min; (ii) maintaining at 80 °C for 5 min; (iii) cooling down to T_{low} = (10, 0, -10, or -20) °C at 5 °C/min; (iv) maintaining at T_{low} for 4 h. A last heating step (i) completed the analysis.

From DSC data, the crystallinity of the PBA-based soft segment phase (X_c) was calculated according to the following equation:

$$X_c[\%] = \frac{\Delta H_m - \Delta H_{cc}}{\Delta H_m^0 \times 0.75} \times 100 \quad (6.1)$$

where ΔH_m is the melting enthalpy, ΔH_{cc} is the cold crystallization enthalpy (which was set to 0 J/g because the thermograms did not show exothermal signals), and ΔH_m^0 is the reference melting enthalpy (135 J/g) for 100% crystalline PBA [157].

6.1.3.3. Preliminary shrinking assessments on electrospun mats

In order to verify if TPU PBA-75 fibers were sufficiently stretched during the electrospinning process, the shrinking of electrospun mats was observed at room temperature (T_{room}) and at T_{high} = 60 °C. Samples with starting dimensions in the order of 1-2 cm were first detached from the collector at T_{room}, and then heated up to T_{high}. Pictures of the samples before and after shrinking were taken with a Nikon Coolpix B700 camera, and their dimensions were measured with ImageJ.

6.1.3.4. Rheological analyses

The rheological properties of molten TPU Filaflex were evaluated by using the MCR 702 Multidrive Anton Paar (Ostfildern, Germany). Parallel plate geometry of 25 mm diameter was used to measure the viscosity at 230 °C and 240 °C for shear rates between 0.01 s^{-1} and 1000 s^{-1}.

6.1.3.5. Shape memory experiments

The shape memory behavior of the composites was investigated on two types of samples, designed to take on a C shape (Figure 6.1a) or an S shape (Figure 6.1b). C-shaped specimens were obtained by MEW of one or two $[0°/45°/90°/-45°]_s$ sequences with standard density on top of electrospun mats of 1 cm x 1 cm. S-

shaped specimens were realized by MEW areas with proper density and thickness on the top and bottom of electrospun mats of about 3 cm x 1 cm, according to the design reported in Figure 6.1b.

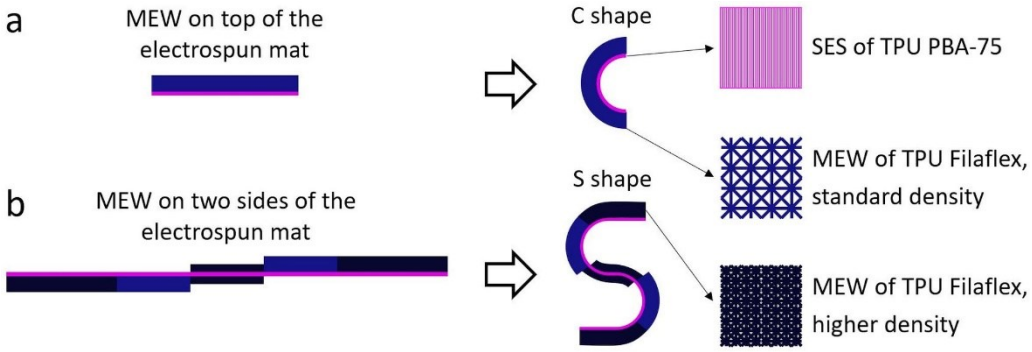

Figure 6.1. Schematic representation of specimens designed to take on a C shape (a) or an S shape (b), with indication of fabrication techniques and materials employed for areas highlighted in different colors.

While the thickness of TPU Filaflex could be easily selected by varying the number of MEW layers, that of TPU PBA-75 varied according to the SES process duration and to the specific position occupied on the surface of the metallic collector. Therefore, for each SES batch, electrospun samples of 2 cm x 2 cm were collected in different positions and weighted. Three mat types were identified as representative of low, medium or high thickness (nominal weight of 0.5 mg, 1 mg or 2 mg). MEW samples of 2 cm x 2 cm were also weighted, so that the mass fraction of SMP (v_{SMP}) could be identified for each thickness combination of TPU PBA-75 and TPU Filaflex, according to the following equation:

$$v_{SPM}[wt\%] = \frac{m_{SMP}}{m_{SMP}+m_E} \times 100 \qquad (6.2)$$

where m_{SMP} is the mass of the SMP (TPU PBA-75) and m_E is the mass of the elastomer (TPU Filaflex).

A Canon EOS 800D camera was used to record the initial shrinking of samples at T_{room} as well as their reversible shape transformations upon permanence in hot water (T_{high} = 60 °C) or cold water (T_{low} = 0 °C) for selected times. More

specifically, a heating step of 3 min or 10 min was applied to C-shaped and S-shaped specimens, respectively, and followed by a cooling step of 10 min or 1 h for both sample geometries; additionally, the effect of cooling for 24 hours or 1 week in water at T_{room} was explored. In the case of 10 min cooling at T_{low}, three sequential heating-cooling cycles were performed.

For C-shaped samples, a quantitative evaluation of their deformation was obtained by measuring their curvature (κ) with ImageJ. During the shape memory cycles, the curvature changed from an initial value of 0 m^{-1} to different measured values κ_N, numbered in chronological order ($N = 0$ after shrinking, $N = 1$ after the first heating step, $N = 2$ after the first cooling step, *etc.*). Normalized curvature variations ($\Delta\kappa_{norm}$) were calculated with respect to the curvature produced by the first heating step, as follows:

$$\Delta\kappa_{norm}[\%] = -\frac{\kappa_N - \kappa_{N-1}}{\kappa_1} \times 100 \quad (6.3)$$

This equation associates positive $\Delta\kappa_{norm}$ values with an opening of the C shape.

6.2. Working principle and fabrication of shape memory composites

The two-way shape memory effect (SME) of the materials presented in this paper relies on the combination of a pre-stretched shape memory polymer (SMP) with an elastomer, which is among the strategies proposed by the literature to achieve such effect [123]. Compared to more conventional casting/molding methods previously described [127–129], a new fabrication process is here proposed which (i) integrates pre-stretching directly in the SMP manufacturing phase by solution electrospinning (SES), and (ii) guarantees higher flexibility in the design of shape changes thanks to additive manufacturing of the elastomer component by melt electrowriting (MEW). More in detail, the steps concerning the realization and thermal activation of these smart materials are represented in Figure 6.2.

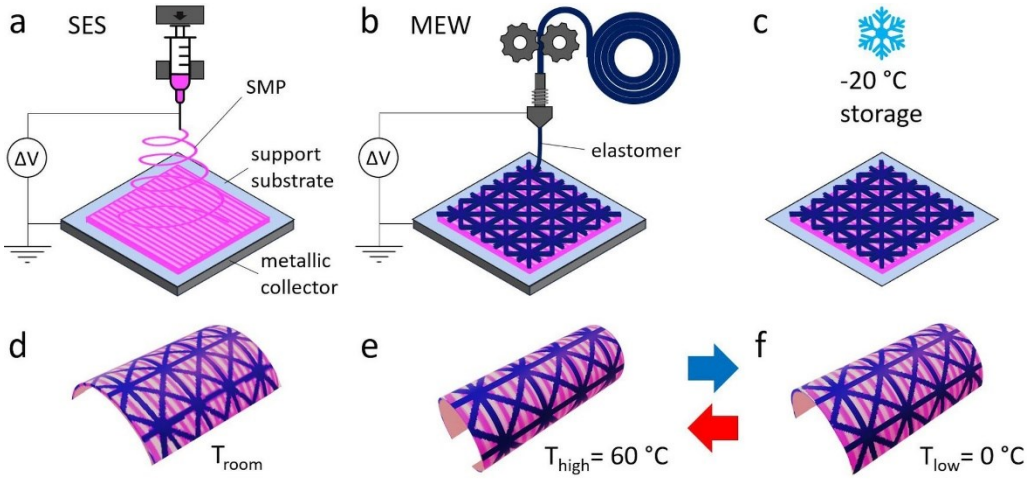

Figure 6.2. Steps for 4D fabrication of the two-way shape memory composites: (a) SES of the SMP on a support; (b) MEW of the elastomer onto the SMP; (c) cooling and storage in a freezer; (d) shrinking upon support removal at T_{room}; (e) closed configuration upon heating up to T_{high}; (f) open configuration upon cooling down to T_{low}. The transformation between (e) and (f) is reversible and repeatable.

First, TPU PBA-75 is synthesized and employed in the production of the active layer. This TPU has already shown good SME in one-way and two-way shape memory cycles, as well as excellent biocompatibility [158–160]. Its

thermoresponsive behavior is given by its physically cross-linked molecular structure, containing 75% PBA-based crystallizable soft segments. In fact, the polymer can be deformed into a temporary shape above PBA melting temperature (T_m) and cooled down below PBA crystallization temperature (T_c) to crystallize the soft segments and fix the deformation; in a second moment, it can be heated up above T_m to melt the PBA crystals and recover the original shape stored in the hard segments. Another study [160] also highlighted important advantages of TPU PBA-75 for applications in soft tissue engineering, including biocompatibility, biodegradability and low elastic modulus in the range of a few MPa. TPU PBA-75 is dissolved in organic solvents to be processed by SES (Figure 6.2a). The electrospinning parameters, solution composition and collector type are adjusted as described in paragraph 6.2.1., aiming at obtaining a mat of highly stretched nanofibers on the support substrate.

In a second stage (Figure 6.2b), an elastomer is deposited onto the electrospun mat as passive component, intended to guide the overall shape transformation and to ensure its reversibility. To these ends, MEW technique is adopted for higher control over the geometry of the system, and a commercial elastomer (TPU Filaflex) is selected for being stable above PBA T_m and good at storing and recovering deformations in the elastic field. Also this second material has low elastic modulus (about 7 MPa [161]), guaranteeing sufficient deformation upon actuation. The MEW pattern, thickness and process parameters are tailored as reported in paragraph 6.2.2. The obtained samples, still attached to the support substrate, are then stored in a freezer (Figure 6.2c) to fix the electrospun nanofibers in their stretched configuration by crystallization of TPU PBA-75 soft segments.

The tensile deformation in the nanofibers is partially lost when the samples are detached from the support substrate at T_{room} (Figure 6.2d), and further released by melting PBA-based crystals at $T_{high} > T_m$ (Figure 6.2e). However, the presence of the elastomer hinders the contraction of the SMP, resulting in bending of the

specimens towards the SMP side. By cooling the composite material down to T_{low} < T_c, the deformed elastomer is expected to provide sufficient stress for crystallization-induced elongation in the SMP, reducing bending of the specimens (Figure 6.2f), similarly to what has been previously observed when an external stress is applied to TPU PBA-75 during heating-cooling cycles [159]. Further applications of T_{high} and T_{low} should lead again to the more closed configuration in Figure 6.2e and the more open configuration in Figure 6.2f, respectively, therefore achieving reversible and repeatable two-way SME.

Aiming to choose suitable values of T_{high} and T_{low}, DSC analysis was carried out on TPU PBA-75, with particular focus on observing the crystallization during isothermal stages at different T_{low} values (10 °C; 0 °C; -10 °C; -20 °C). For each temperature considered, a complete heating-cooling cycle was performed, *i.e.* heating up to 80 °C, waiting for 5 min, cooling down to T_{low}, and maintaining for 4 h. The thermograms of all DSC heating scans are displayed in Figure 6.3a, while Figure 6.3b plots the specific heat flow against time during the cooling steps and the isothermal steps at T_{low}; the origin of the time axis is set at the beginning of the isothermal tracts.

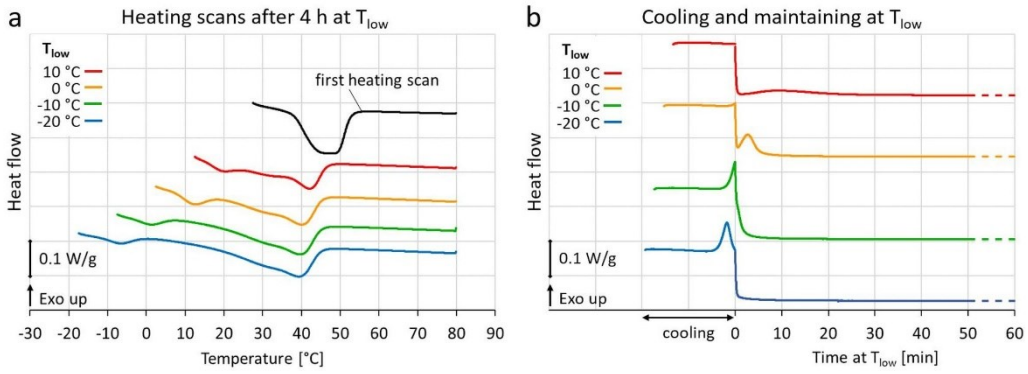

Figure 6.3. Results of DSC analyses: (a) heating scans as a function of temperature; (b) cooling and isothermal steps as a function of time.

*Table 6.1. TPU PBA-75 melting temperature (T_m), melting enthalpy (ΔH_m), and crystallinity (X_c) evaluated by DSC on granules in their pristine conditions and after 4 h at T_{low} (*in some scans the baseline could not be properly drawn).*

Heating scan	T_m [°C]	ΔH_m [J/g]	X_c [%]
First scan	46.1	16.7	16.5
After 4 h at T_{low} = 10 °C	42.2	-*	-*
After 4 h at T_{low} = 0 °C	40.1	-*	-*
After 4 h at T_{low} = -10 °C	39.4	16.4	16.2
After 4 h at T_{low} = -20 °C	39.2	17.0	16.8

The heating scans present a main endothermal peak around 40–45 °C (detailed values are reported in Table 6.1), which is associated with the melting transition of the soft segments. When heating follows one of the 4-h isotherms at T_{low}, the melting process begins earlier and the peak temperature tends to be reduced with respect to the first heating scan; such differences could be explained considering that PBA crystallized segments in the original granules had much more time to rearrange and stabilize their molecular structure at T_{room} ($< T_m$) with respect to those formed during 4 h at T_{low}. However, in all the cases, the melting process is concluded within 50–55 °C, so that T_{high} can be reasonably set to 60 °C during the shape memory experiments. Furthermore, a degree of crystallinity (X_c) of approximately 16-17% can be estimated through eq. 6.1 for the soft segment phase, comparing the melting enthalpy of 100% crystalline PBA (ΔH_m^0 = 135 J/g) [157] with that in the thermograms (ΔH_m = 16–17 J/g,); detailed values of ΔH_m and X_c are reported in Table 6.1 when applicable (*i.e.* when a sufficiently reliable baseline could be defined).

The effect of the selected T_{low} on the crystallization of SMP soft segments can be appreciated by looking at the associated exothermal signals in Figure 6.3b. At 10 °C, a long time is required for crystallization, which mostly occurs in less than 10 min at 0 °C and even before the beginning of the isothermal stage for the lowest

values of T_{low}. In fact, the nucleation of crystals is faster at lower temperatures. At the light of these findings, the specimens were stored in a freezer at -20 °C to promptly fix the electrospun nanofibers in their stretched configuration, whereas the shape memory experiments were performed with T_{low} = 0 °C, which was more convenient to handle and still allowed short cooling times. However, it should be specified that, while crystal nucleation slows down when approaching T_m, crystal growth becomes faster, still allowing to obtain high crystallinity in the long time.

6.2.1. SES setup

A good pre-stretching of the SMP is fundamental for the achievement of the two-way SME without applying any external stress to the SMP-elastomer composites. Therefore, the effects of several variables were considered until obtaining nanofibers with the desired morphology and shrinking upon heating.

Firstly, different values of flow rate (0.25-0.5-1 mL/h), applied voltage (20-25-30 kV) and solution concentration (6-8-10 w/v%) were compared. A DMF-acetone mixture with volume ratio of 2:3 was employed as solvent, based on the previous use of these two chemicals in touch-spinning of a TPU PBA-75 solution [160]. All conditions allowed SES except for the highest TPU concentration (10%), which appeared to excessively increase the solution viscosity. The nanofibers were collected on glass slides on two parallel conductive bars and observed at the optical microscope (images in Figure 6.4a). Looking for thin nanofibers with a regular morphology, the voltage was set at 25 kV, the flow rate at 1 mL/h and the concentration at 6 w/v%. In particular, the fiber diameter (Figure 6.4b) did not significantly vary with the voltage and flow rate; conversely, reducing the solution concentration to 6 w/v% was more effective, though the final fibers had still quite large diameter (2 μm).

For fibers obtained with the selected process parameters, a further morphology check by SEM and some shrinking tests were carried out. SEM images revealed several areas in which the fibers appeared fused together due to incomplete

evaporation of the solvent (Figure 6.5a), which led to substitute DMF-acetone (2:3) with a new mixture of solvents. Figure 6.5b reports the improvement achieved by using DMF-$CHCl_3$-THF with volume ratios of 2:2:1, which was employed in the production of all specimens from here on. Furthermore, the shrinkage of electrospun mats at 60 °C was barely noticeable (Figure 6.6a). It was concluded that the application of high voltage was insufficient to effectively stretch TPU PBA-75, probably because of its high molecular weight (about 1.4×10^5 g mol^{-1} [160]). For this reason, the electrospinning setup was finalized by using a rotating drum as collector and selecting a high rotation speed (8000 rpm), aiming at mechanically drawing the fibers. The values of fiber diameter obtain before and after this improvement are illustrated in Figure 6.5c, and SEM images of the new materials are provided in Figure 6.5d-f. While fibers collected on parallel bars are randomly oriented and rather thick (diameter of about 1.6 μm), the new samples consist of thinner nanofibers (diameter of about 0.4 μm) mainly aligned along the circumferential direction of the rotating drum; an overall thickness of a few microns is achieved in 1 h of SES.

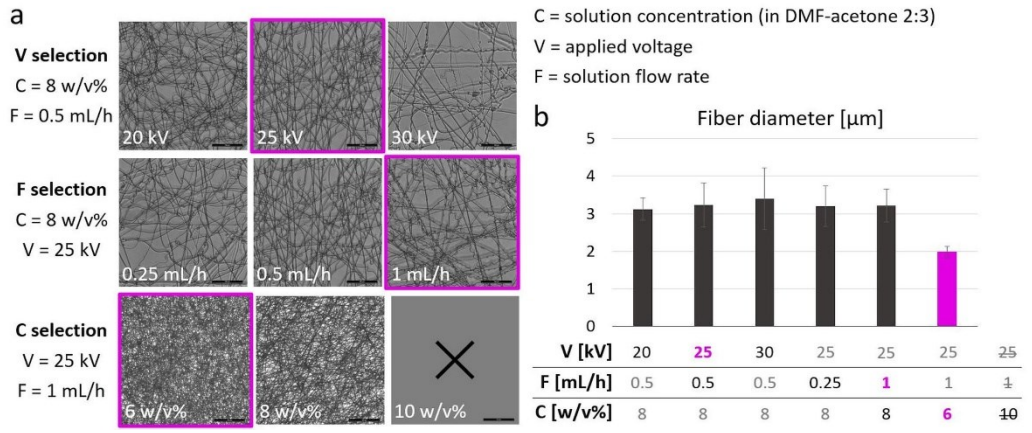

Figure 6.4. Selection of SES parameters based on (a) optical microscope images (marker: 100 μm) and (b) fiber diameter measurements; electrospinning was not feasible with the highest solution concentration.

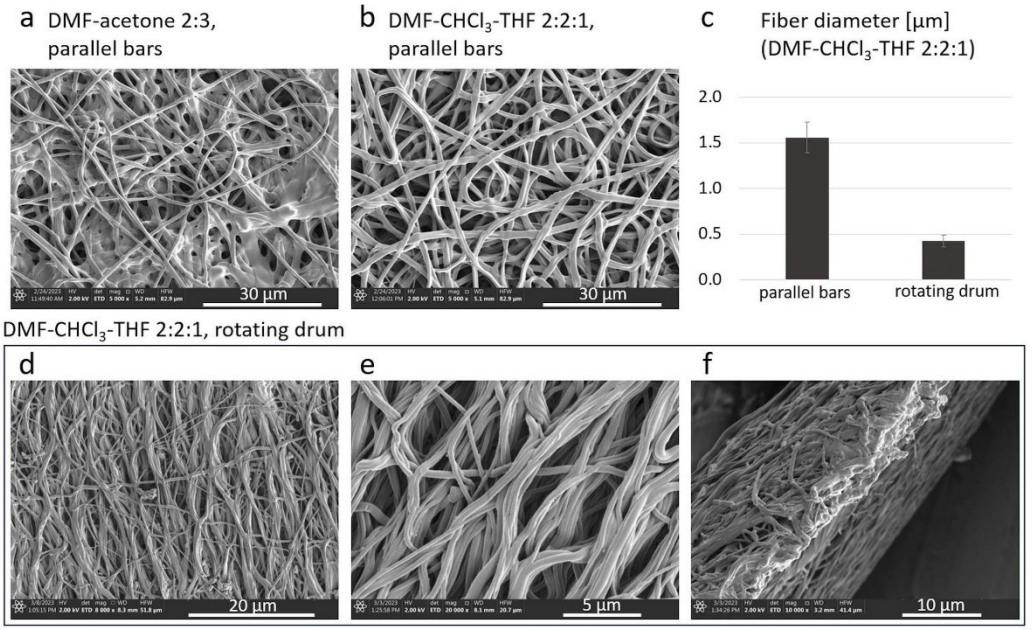

Figure 6.5. SEM images of electrospun fibers obtained by using different solvents and collectors (a; b; d-f) and diameter values for fibers obtained with the best solvent on different collectors (c).

The reduced diameter of the nanofibers is indicative of their stretched state, that is confirmed by the significative shrinking of the electrospun mats after freezing (to fix the deformation at best) and detaching from the collector. Due to the preferential alignment of the nanofibers, most of the shrinkage occurs along the circumferential direction of the drum (about 15%), while the axial contraction is limited (about 5%). At T_{high} = 60 °C, the crystalline domains responsible for shape fixation melt, and the specimens further contract until reaching shrinking values of about 50% in the circumferential direction and 10% in the axial direction (Figure 6.6b). This experiment highlights that while both parallel bars and rotating drum allow production of nanofibers, the fibers produced by the two methods are different: fibers produced using a rotating drum are strongly oriented and stretched while those produced using parallel bars are not.

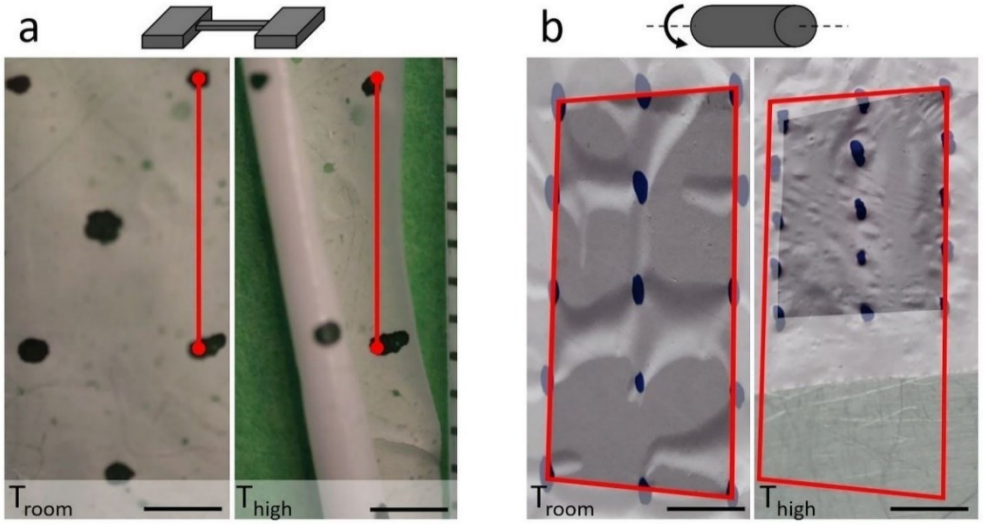

Figure 6.6. TPU PBA-75 specimens electrospun on parallel bars (a) and rotating drum (b) and photographed before and after heating (T_{room} and T_{high}), with red lines as fixed references to highlight dimensional changes; marker = 2 mm.

6.2.2. MEW setup

The next step was the selection of MEW parameters for TPU Filaflex. The effects of nozzle temperature and applied voltage were first explored, maintaining the collector speed at its maximum value (1800 mm/min) and a distance of 3 mm between nozzle and collector. Figure 6.7a shows diameter values and optical microscope images of the obtained fibers, as well as viscosity *versus* shear rate curves and viscosity *versus* shear stress curves at 230 °C and 240 °C. The highest voltage applied (3.5 kV) excessively accelerates the molten polymer flow, so that the collector is not fast enough to collect straight fibers, and wavy thin fibers are produced. Better results are obtained by reducing the voltage, leading to less stretched fibers having larger diameter. More in detail, for a nozzle temperature of 230 °C, a voltage decrease from 3.5 kV to 1.5 kV increases the diameter from about 50 μm to about 110 μm. For a temperature of 240 °C, the lower viscosity of the melt seems to ease the flow of a larger amount of material through the nozzle (corresponding to thicker fibers, *e.g.* 80 μm diameter with a voltage of 3.5 kV) and to produce more irregular fibers (especially under application of 1.5 kV, resulting in

counter-trend thin filaments interrupted by long bead defects [162]). Moreover, rheological curves at 240 °C are more irregular; while deviations at low stress seem to indicate a thixotropic behavior, probably occurring when hydrogen bonds between polymer chains break and the polymer melt starts flowing, deviations at high stress may be ascribed to transition to elastic regime and failure. In the end, a nozzle temperature of 230 °C and an applied voltage of 2.5 kV were selected as most reliable parameters. The final fiber diameter is around 80 µm, slightly increasing up to about 90 µm when printing on top of electrospun mats, because covering part of the conductive collector with the SMP mitigates the voltage effect to some degree.

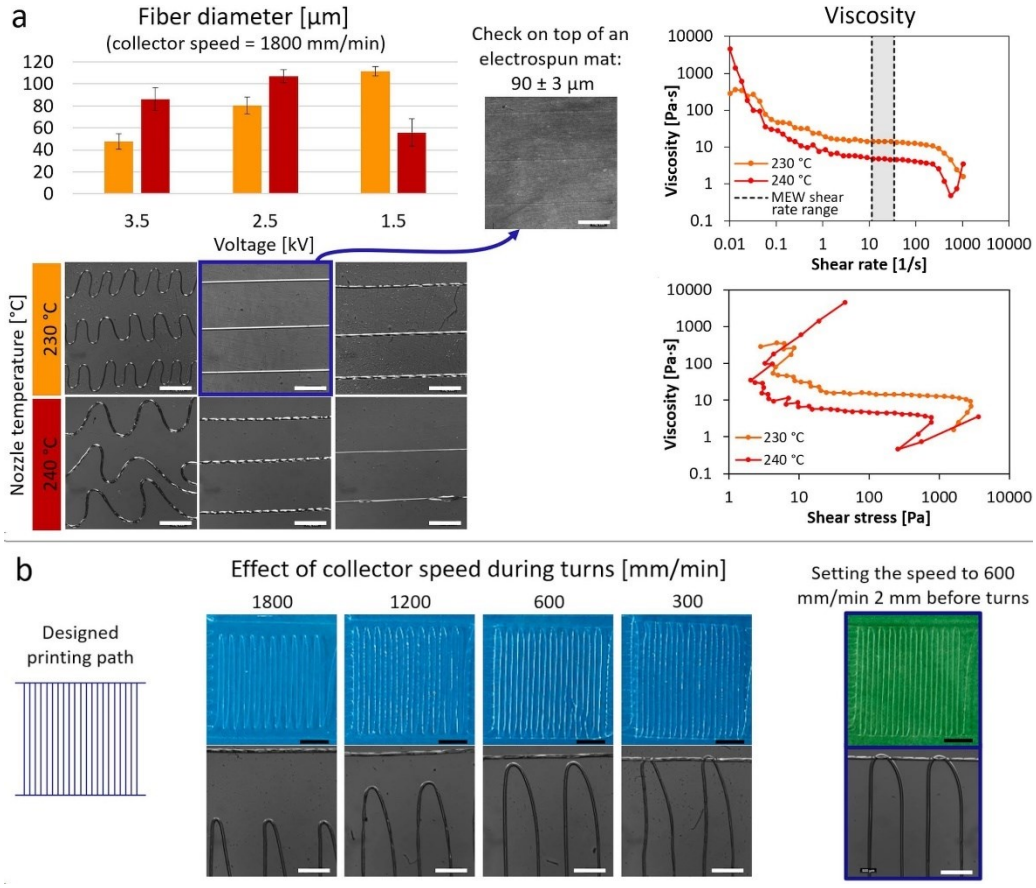

Figure 6.7. Selection of MEW parameters based on fiber diameter measurements, optical microscope images (white marker: 1 mm), photographs (black marker: 5 mm), and viscosity measurements: (a) voltage and nozzle temperature; (b) collector speed during/ approaching turns.

In addition, it was observed that MEW was not accurate when changing the travelling direction of the extruder, due to jet lagging. This problem was solved by reducing the collector speed in correspondence of turns in the deposition path. As reported in Figure 6.7b, the highest accuracy is achieved by setting the collector speed to 600 mm/min since 2 mm before changing travelling direction, until the turn is completed. It was also noticed that, regardless of the selected speed, the deceleration of the extruder in proximity of turning points inevitably causes some accumulation of material, and a consequent local increase in fiber diameter (up to 120-150 μm).

6.2.3. Fabrication of SMP-elastomer composites

The composite nature of the shape memory materials here proposed provides versatility to the adopted 4D fabrication strategy. In fact, the shape transformation can be modulated by acting on the stiffness of each component. In particular, the electrospun mat stiffness depends on its thickness (which is directly proportional to the associated nominal mass of 4 cm^2 samples), while that of the MEW part can be locally tailored by designing and printing specific patterns, as well as by changing the number of printed layers. Both the thickness ratio of the active and passive components and the total thickness of the specimen are expected to affect the final result.

Table 6.2 summarizes all the SMP-elastomer combinations that have been explored, labeling them according to their SMP/elastomer thickness ratio. The SMP layer has three possible values of associated nominal mass (0.5-1-2 mg), corresponding to different values of surface density. Moreover, the MEW part has four possible values of surface density, depending both on the number of printed quasi-isotropic sequences (N = 1 or N = 2) and on the density of single layers (the standard corresponds to 1 mm fiber spacing, while higher density areas have 0.5 mm fiber spacing and are indicated with a "d" in the label in Table 6.2).

Table 6.2. Summary of all explored SMP-elastomer combinations

Label	SES		MEW		
	Nominal mass (4 cm^2) [mg]	Surface density [mg/cm^2]	Number of sequences ($[0°/45°/90°/-45°]_s$) [%]	Surface density [mg/cm^2]	Estimated thickness ratio
2/2	2	0.49 ± 0.03	2	15.6 ± 1.1	1/50
2/2d	2	0.49 ± 0.03	2 with higher density	31.2 ± 2.2	
1/2	1	0.26 ± 0.03	2	15.6 ± 1.1	1/100
1/2d	1	0.26 ± 0.03	2 with higher density	31.2 ± 2.2	
0.5/2	0.5	0.13 ± 0.02	2	15.6 ± 1.1	1/200
0.5/1	0.5	0.13 ± 0.02	1	7.8 ± 0.6	1/100

The appearance of quasi-isotropic MEW structures is displayed in Figure 6.8a for standard density and N = 1 or N = 2. Furthermore, Figure 6.8b reports SEM images of a 0.5/1 composite, providing a first rough estimation of the SMP/elastomer proportions based on thickness measurements, *i.e.* (3.7 ± 0.9) μm for 0.5 mg electrospun mats and (360 ± 70) μm for MEW structures with N = 1. As detailed in Table 6.2, the thickness ratio of 0.5/1 and 1/2 composites is around 1/100, while that of 0.5/2 composites is around 1/200 and that of 2/2 composites is around 1/50. SMP mass fraction values are also calculated on the basis of the surface density of the two components, and illustrated in Figure 6.8c for all the considered alternatives. Small TPU PBA-75 contents are obtained, overall ranging between 0.7% and 3%.

Two specimen shapes were created for shape memory experiments: (i) a C shape is simply achieved for specimens having uniform thickness and thickness ratio (Figure 6.1a); (ii) a S shape is the result of a more complex MEW pattern, combining two standard density areas printed on different sides of the electrospun mat (the two curves of the S) and three higher density areas (extremities and center of the S), as shown in Figure 6.1b.

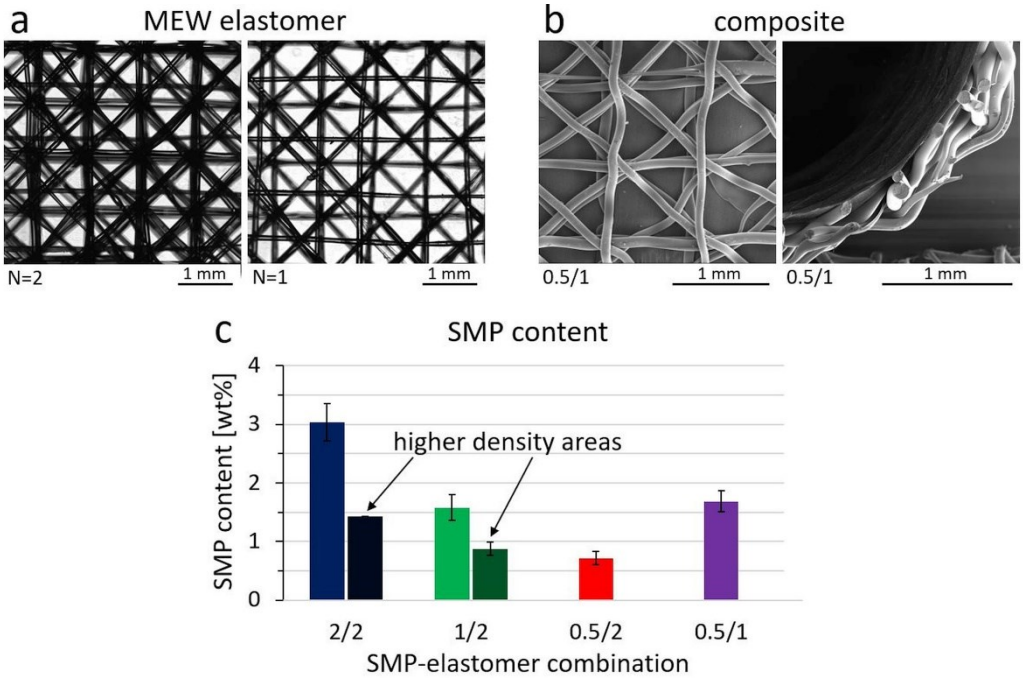

Figure 6.8. (a) N quasi-isotropic sequences printed by MEW and observed at the optical microscope. (b) Example of shape memory composite observed at SEM from the top and side views. (c) Mass fraction of SMP for all SMP-elastomer combinations in Table 6.2.

6.3. Two-way SME characterization

The shape memory behavior of SMP-elastomer composites and its tunability were investigated by applying proper heating-cooling cycles in water, therefore minimizing possible gravity and friction effects. C-shaped samples were employed to study the possibility of achieving a stress-free two-way SME, as well as the impact of specimen thickness and SMP content. More specifically, C-shaped specimens were prepared with SMP/elastomer thickness ratio equal to 2/2, 1/2, 0.5/2, and 0.5/1.

Figure 6.9a shows that all specimens partially bend at T_{room} upon removal of their stiff substrate, and further bend upon heating up to 60 °C; the resulting values of curvature (κ) are reported in Figure 6.9b. The observed curvature depends on the balance between the force generated by contracting electrospun fibers and the mechanical resistance of the passive layers. Therefore, remarkable shapeshifting occurs when heating above TPU PBA-75 transition temperature, due to the release of the tensile deformation stored in PBA-based crystalline domains.

The most evident effect is that of the total thickness of the specimens. In fact, considering a same thickness ratio of 1/100 (*i.e.*, 0.5/1 and 1/2 composites), thinner constructs exhibit remarkably higher κ values (380 m^{-1} *vs* 85 m^{-1} at T_{room}; 1200 m^{-1} *vs* 450 m^{-1} at T_{high}). The excessive coiling of 0.5/1 composites at T_{high} does not favor the two-way SME, which may be hindered by friction between contact surfaces.

Conversely, the effect of the SMP content appears modest when comparing specimens consisting of the same MEW structure (2 quasi-isotropic sequences) but different electrospun layer thickness, namely 2/2, 1/2, and 0.5/2 composites. At T_{room}, overall similar curvatures are measured, but some 0.5/2 specimens bend more than the others due to partial delamination starting at their edges; delamination at the interface between the double MEW structure and the thinnest electrospun

mat becomes complete upon heating, leading to discard this combination. At T_{high}, higher SMP content corresponds to slightly increased κ values (520 m^{-1} for 2/2 composites *vs* 450 m^{-1} for 1/2 composites); even if these values are rather close from a statistical point of view, this trend appears reasonable because the contraction of SMP pre-stretched fibers is indeed the driving force for the composite bending.

These data allow drawing two guidelines for further investigations: (i) among the SMP-elastomer combinations considered, only 2/2 and 1/2 appear promising in view of SME reversibility; (ii) the total thickness of the systems plays a major role in their shape transformations and it is does not significantly change with the SMP content, since the microscopic thickness of the electrospun mats can be reasonably neglected.

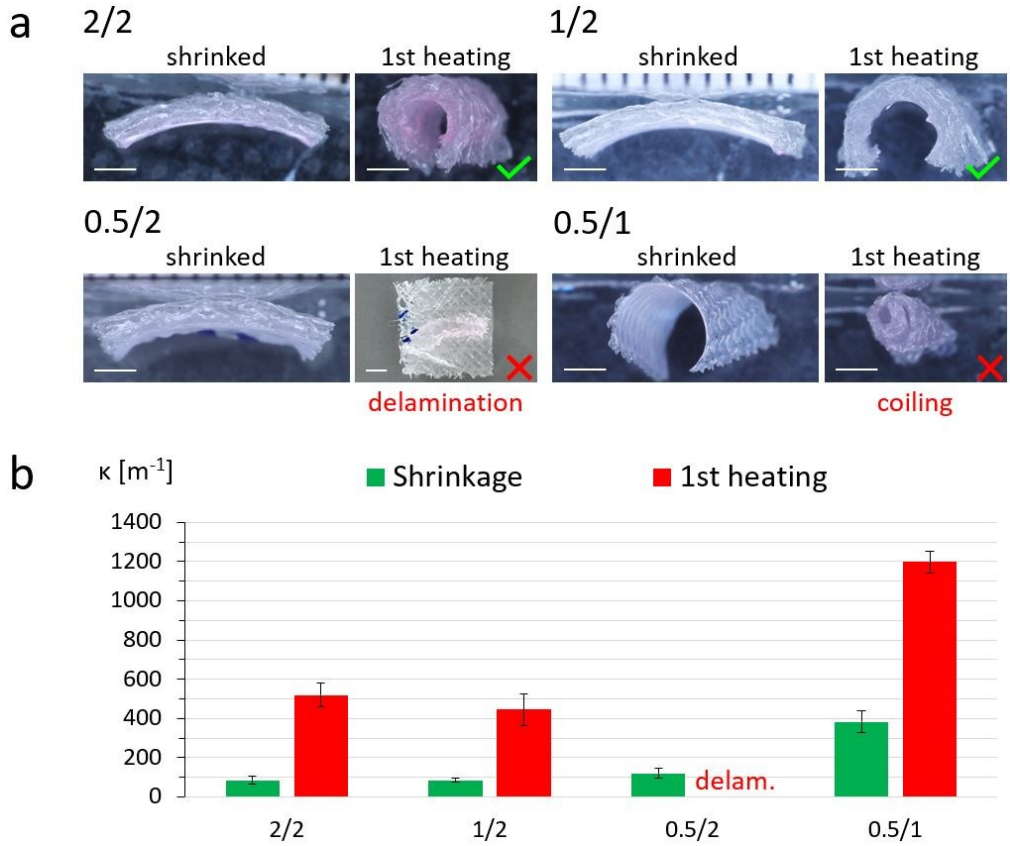

Figure 6.9. Images (marker: 2 mm) (a) and curvature measurements (b) of various SMP-elastomer combinations after shrinking at T_{room} and after first heating at 60 °C.

Once the desired C shape is guaranteed upon heating, the two-way SME can be assessed. While heating triggers the contraction of the electrospun SMP, cooling under an external tensile stress induces recrystallization of its soft segments in a stretched configuration. Here, the stress is provided by the elastic recovery of the elastomer, which is expected to decrease the C curvature.

The results of this approach are documented in Figure 6.10 and Figure 6.11, reporting the effect of various heating-cooling cycles on 2/2 and 1/2 composites. More in detail, images and κ values of 2/2 and 1/2 specimens are illustrated in Figure 6.10a and 6.10b, respectively, for three thermal histories: (i) 3 min at 60 °C followed by 10 min at 0 °C, repeated for three successive cycles; (ii) 3 min at 60 °C followed by 1 h at 0 °C; (iii) 3 min at 60 °C followed by 1 week at about 25 °C (collecting data after 1 day and 1 week at T_{room}).

Both types of specimens exhibit reversible SME, closing at T_{high} and opening at T_{low}, and the feasibility of multiple actuations is also demonstrated in both cases. More precisely, the effect is clearly visible when the cooling temperature is equal to 0 °C, after 10 minutes as well as after 1 hour, whereas the opening of samples maintained at T_{room} is barely perceptible. This is consistent with DSC data, showing that a temperature of 10 °C or higher is not optimal for efficient crystallization of TPU PBA-75.

In addition, Figure 6.11 better highlights the amount of deformation that is reversibly gained and released at each cooling or heating step following the big transformation at first heating. For each step of the various thermal histories applied, curvature variations were normalized with respect to those occurring at first heating. The resulting average values ($\Delta\kappa_{norm}$) are reported in Figure 6.11a and 6.11b for composites 2/2 and 1/2, respectively. Positive values are associated to opening of the C shape (cooling steps), while negative values correspond to its closure (heating steps).

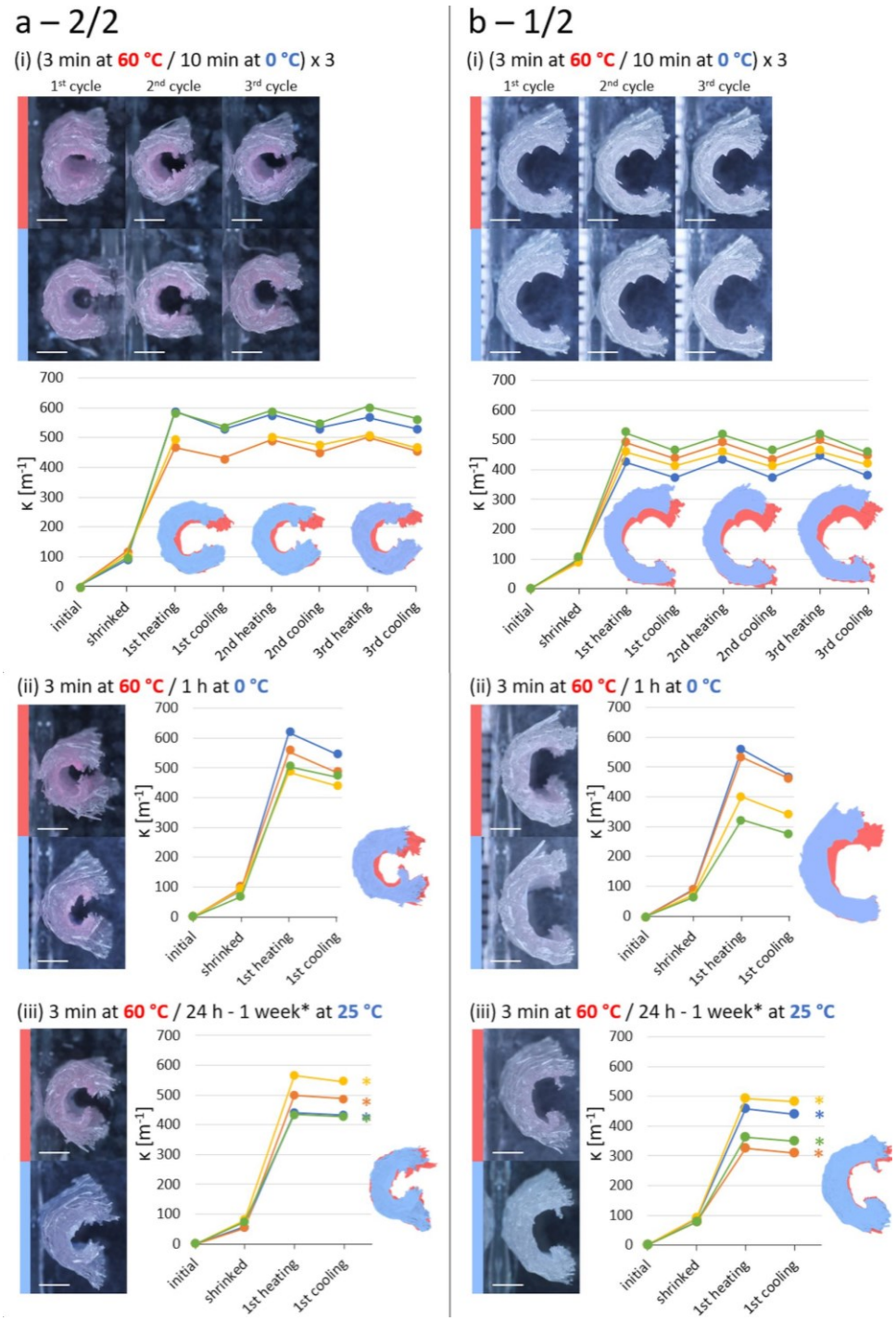

Figure 6.10. Two-way SME of 2/2 (a) and 1/2 (b) C-shaped specimens during various heating-cooling cycles (i-iii): images (marker: 2 mm); curvature measurements (4 repetitions); visual comparison (hot specimen in red, cold specimen in blue).

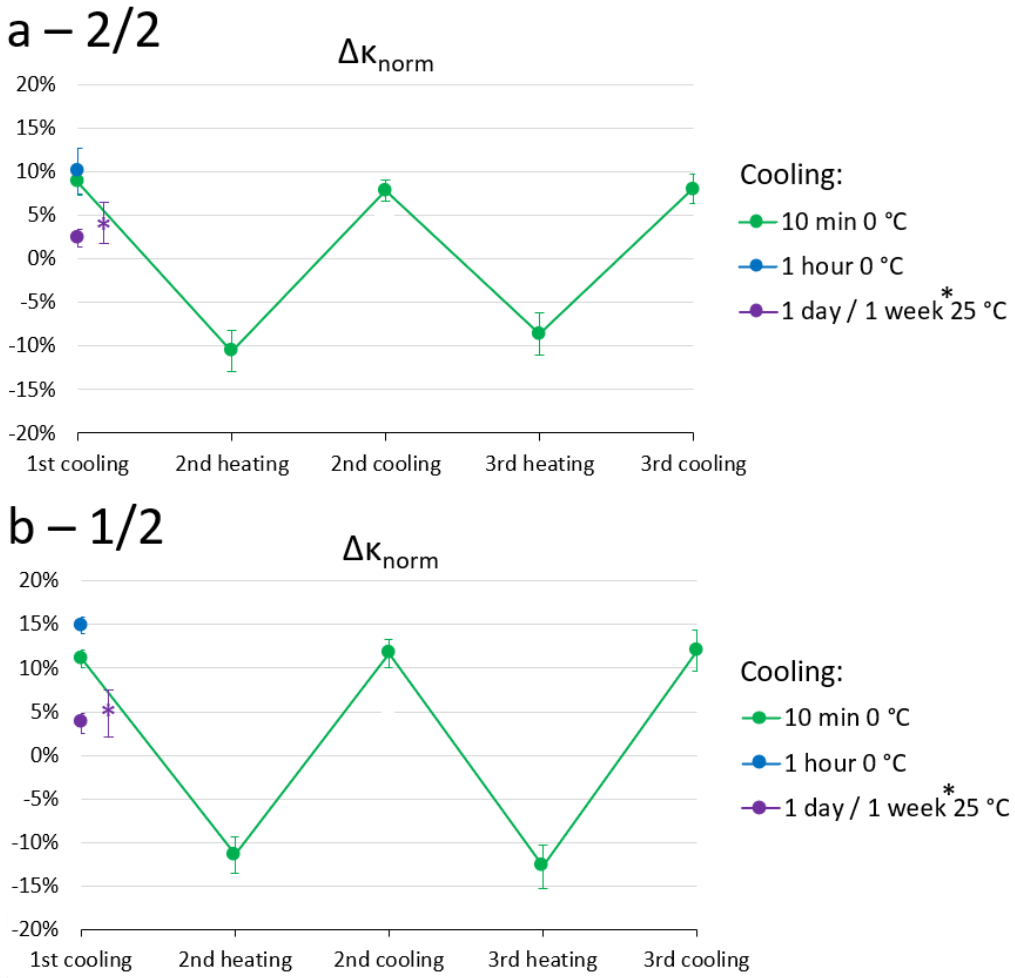

Figure 6.11. Normalized curvature variations ($\Delta\kappa_{norm}$) of 2/2 (a) and 1/2 (b) C-shaped specimens during various heating-cooling cycles (3 min at 60 °C / cooling as specified in the legend); curvature values are normalized with respect to the effect of first heating.

The curvature variation during the first cooling phase, which is always smaller compared to the major shape transformation occurring in the first heating phase, is proved to be reversible. In fact, when multiple thermal cycles are applied, the same variation is observed during each following step.

Moreover, $\Delta\kappa_{norm}$ varies according to the SMP content and to the cooling temperature and time. For T_{low} = 0 °C, 2/2 composites can recover about 9-10% of the initial transformation in 10 min, whereas $\Delta\kappa_{norm}$ of 1/2 specimens is around

12-15%. The values obtained after cooling for 1 h tend to be slightly higher, but most of the actuation occurs within 10 min at 0 °C. As for samples maintained 1 day at T_{room}, only a very small fraction of the initial transformation is recovered (about 2% and 4% for 2/2 and 1/2 specimens, respectively), and even after 1 week $\Delta\kappa_{norm}$ remains within 4-5%.

Finally, the possibility of creating 4D objects having more complex geometries were explored, using S-shaped specimens as proof of concept. MEW was performed on both sides of the electrospun mats to introduce multiple curves, with the SMP on the inside and the elastomer on the outside. Once again, 2/2 and 1/2 combinations were selected for the two curves of the S, while denser MEW structures (2/2d and 1/2d in Table 6.2) were deposited on the extremities and in the central part to make them stiffer and, consequently, flatter. Images of the samples after shrinking at T_{room} and during shape memory experiments are shown in Figure 6.12, for two thermal histories: (i) 10 min at 60 °C followed by 10 min at 0 °C, repeated for three successive cycles; (ii) 10 min at 60 °C followed by 1 h at 0 °C. The longer heating step is necessary because of the high amount of TPU filaments deposited by MEW, forming a dense hydrophobic network that requires some time to be penetrated by hot water. All specimens have reached the designed S configuration and show good reversibility of their shape transformation during both types of thermal cycles, confirming the feasibility of modulating the curvature in different areas of the composites and thereby obtaining complex shapes. Such modulation should take into account several parameters, including the total thickness, the SMP/elastomer ratio, the stiffness of both components, and the stretching of the SMP during SES (which may be controlled through the drum rotation speed).

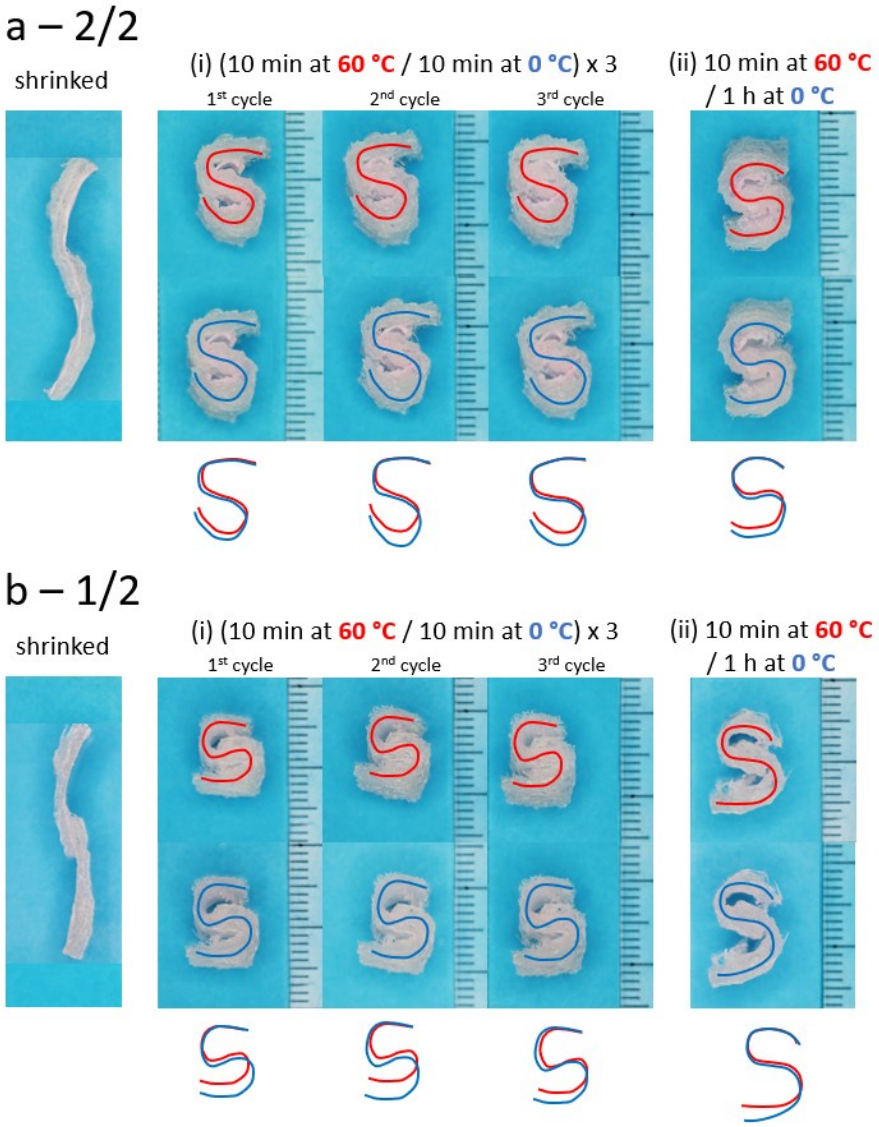

Figure 6.12. Two-way SME of S-shaped specimens: images of 2/2 (a) and 1/2 (b) specimens after shrinking at T_{room} and during various thermal cycles (i-ii).

6.4. Conclusions

This chapter sets the bases of an innovative fabrication method for smart SMP-elastomer composites that evolve in space and time (4D), changing their shape when a thermal stimulus is applied, and that can be reversibly actuated, exhibiting the so-called two-way shape memory effect.

Electrospinning of the SMP proved to be an excellent strategy to integrate pre-stretching of the SMP directly in its manufacturing phase. To this end, the use of a drum collector at high rotational speed was fundamental, and determined the anisotropic behavior of the material, undergoing contraction/expansion mainly along the drum circumferential direction.

The elastomer component was equally important for the achievement of reversible shape memory. Additive manufacturing by MEW allowed for easy modulation of the elastomer structure in terms of geometric pattern and thickness, the combination of which determines its stiffness and, as a consequence, the final shape of the composite.

A preliminary study on specimens with simple geometry showed that both the SMP/elastomer ratio and the total thickness of the composite play an important role and should be carefully selected to modulate the shapeshifting behavior. When these parameters were properly chosen, a reversible and repeatable shape memory effect was obtained. The relatively small actuation amplitude obtained could be ascribed to the tendency of fibrous structures to undergo partially irreversible deformation and dissipate energy (high tan delta value), that is due to bending and displacement of fibers with respect to each other.

There is still space for the SME optimization of these novel systems, which may benefit from experiments on further composite configurations, considering for example more composition and thickness combinations, or also the degree of fiber pre-stretching (depending on the drum collector rotational speed and diameter). Mechanical and thermomechanical testing should also be performed in order to gain

understanding of the mechanical behavior of these structures and how it changes during the applied thermal cycles.

Moreover, proof-of-concept experiments on S-shaped specimens open the road towards more complex objects with multiple curvatures, achievable by working on the design of the MEW layers. The design of such devices should aim at specific applications in the biomedical field (*e.g.* thermally stimulated drug delivery, deployable stents, smart rehabilitation solutions), but also in flexible electronics or in soft robotics, given their flexibility and bidirectional actuation capabilities. Importantly, for medical applications, appropriate evaluation of the biocompatibility of SMP-elastomer composites is still required; in particular, the complete remotion of the solvent after electrospinning must be ensured, and biological properties of the elastomer must also be investigated.

Conclusions

This thesis addressed the development of biocompatibile advanced materials and fabrication processes that can bring innovation to the biomedical sector, and specifically to the field of regenerative medicine.

Core-shell design of bioresorbable composite scaffolds was conceived as a versatile strategy to address the complex set of requirements of tissue engineering. A thermoplastic core was dedicated to the function of temporary mechanical support and shaped as a lattice structure by additive manufacturing, which further extended the customization possibilities, whereas the shell was obtained by grafting and freeze-drying of a bioactive hydrogel, in order to provide an interconnected porous structure capable not only of hosting cells but also to promote stem cell proliferation and differentiation.

A vast number of core types was realized with different materials (PLA, PLLA or TPE) and lattice structures (changing external shape, unit cell size, strut arrangement, and build direction), and mechanically tested under various loading conditions. These experiments highlighted the scaffold stiffness and strength tunability in a range that can be associated to different types of bone tissue (especially with PLA or PLLA core) and cartilage tissue (especially with TPE core). Importantly, the core can be tailored to support loads along the most relevant directions for a given anatomical site.

The shell grafting procedure resulted in full penetration of significant amounts of gelatin-chitosan hydrogel inside the core, exhibiting highly interconnected porosity and water absorption similar to the unconstrained hydrogel. Moreover, it was possible to also modulate the hydrogel content by varying the core void volume fraction. While showing no effect on the mechanical properties, the hydrogel

incorporation is essential for its bioactive role, previously demonstrated to support osteogenic and chondrogenic differentiation.

The potential of PLA-hydrogel scaffolds was specifically investigated for bone tissue engineering applications, carrying out further experiments on their hydrolytic degradation and interaction with cells. While the core revealed to be mechanically stable for several weeks, promising to provide temporary mechanical support while new bone tissue is forming, the shell was observed to gradually leave space for new ECM deposition. Therefore, the core/shell ratio was found to influence the scaffold bioresorption behavior as well. Moreover, *in vitro* experiments showed that the hydrogel was the preferred site of cell adhesion and was able to support viability, proliferation and osteogenic differentiation of hMSCs, which led to scaffold mineralization with hydroxyapatite particles.

Given these promising results, *ad hoc* PLLA-hydrogel scaffolds were prepared for *in vivo* experiments on rabbit mandibular defects, reinforcing them along the direction of bite forces and realizing their core with biomedical grade PLLA. These studies were carried out to investigate the feasibility of important translational applications such as the regeneration of marginal and segmental mandibular defects, and the reconstruction of bone defects after removal of osteoradionecrotic bone or after tumor resection. From preliminary results, the scaffolds showed excellent biocompatibility and with their support they allowed oral feeding of the rabbits since the second post-operative day.

Furthermore, the combination of the core-shell strategy with additive manufacturing appeared particularly valuable in view of personalizing the scaffolds and extending the target towards tissues with different properties. Aiming to find guidelines to properly modulate the scaffold properties, the results of mechanical tests were further analyzed to find useful structure-property correlations between core structure, mechanical performances, and hydrogel content. In particular data-driven models based on semi-empirical equations and artificial neural networks were

applied to the determination of the core stiffness and strength, achieving high output accuracy and enabling mechanical property prediction of new untested structures.

Finally, a different kind of advanced composite biomaterials was also explored, together with the combination of two different unconventional manufacturing techniques, namely electrospinning and melt-electrowriting. The two processes were combined in an innovative fabrication process for SMP-elastomer composites capable of reversible shape memory, a behavior that was observed to be influenced by the system composition and structure. Indeed, this study highlighted once more the benefits of composite materials and additive manufacturing in terms of property tunability. Moreover, it suggested a new promising approach to achieve reversible shapeshifting, a smart feature with great potential for the creation of active biomedical devices, dynamic scaffolds or stimuli-responsive drug delivery systems.

Acknowledgements

The author is highly grateful to Poly-Med, Inc. (Anderson, SC, USA) for kindly supplying Lactoprene® 100M 3D-printing filament and to Gammatom Srl (Guanzate, Italy) for gamma sterilization of scaffolds for *in vitro* and *in vivo* studies.

Moreover, the author sincerely thanks the Materials Science and Technology Laboratory (Department of Mechanical and Industrial Engineering, University of Brescia), for hosting and assisting the author over the course of the doctoral program, with special thanks to the thesis supervisor Prof. Luciana Sartore, to the co-supervisors Prof. Stefano Pandini and Prof. Francesco Baldi, and to Prof. Giorgio Ramorino and his collaborators in the spin-off society ITL – Italian Technology Lab Srl.

The author also wishes to acknowledge all other research teams who collaborated to the research on core-shell composite scaffolds: Prof. Domenico Russo's team, especially Dr. Federica Re, and Prof. Elisa Borsani (Department of Clinical and Experimental Sciences, University of Brescia), for *in vitro* experiments; Prof. Matteo Ferroni (Department of Civil, Environmental, Architectural Engineering and Mathematics, University of Brescia) and Prof. Giovanna Cornacchia (Department of Mechanical and Industrial Engineering, University of Brescia), for SEM analyses; Prof. Piero Nicolai's team, especially Dr. Stefano Taboni and Dr. Alessandra Ruaro (Section of Otorhinolaryngology – Head and Neck Surgery, Department of Neurosciences, University of Padua), and Prof. Johnathan Irish and Prof. Ralph W. Gilbert's team (Princess Margaret Cancer Centre, Department of Otolaryngology – Head and Neck Surgery/Surgical Oncology, University Health Network, Toronto), for *in vivo* experiments; Prof. Giulia Scalet (Department of Civil Engineering and Architecture, University of Pavia), for the work on ANN and FEA modeling approaches.

Finally, for the work on smart polymeric composites, further acknowledgments are addressed to collaborators in Germany: Prof. Leonid Ionov's team, especially Zhander Vohr Soreño, Gissela K. Constante Ibarra, and Ilia Sadilov (Faculty of Engineering Sciences, University of Bayreuth), for hosting and assisting the author in the research; Prof. Thorsten Pretsch's team (Shape Memory Polymers Group, Fraunhofer Institute for Applied Polymer Research IAP, Potsdam), for synthesizing and providing TPU PBA-75 granules for the shape memory component of the developed systems.

References

[1] F. Asghari, M. Samiei, K. Adibkia, A. Akbarzadeh, S. Davaran, Biodegradable and biocompatible polymers for tissue engineering application: a review, Artif. Cells, Nanomedicine Biotechnol. 45 (2017) 185–192. https://doi.org/10.3109/21691401.2016.1146731.

[2] A. Abalymov, B. Parakhonskiy, A.G. Skirtach, Polymer-and hybrid-based biomaterials for interstitial, connective, vascular, nerve, visceral and musculoskeletal tissue engineering, Polymers (Basel). 12 (2020) 620. https://doi.org/10.3390/polym12030620.

[3] M.S.B. Reddy, D. Ponnamma, R. Choudhary, K.K. Sadasivuni, A Comparative Review of Natural and Synthetic Biopolymer Composite Scaffolds, Polymers (Basel). 13 (2021) 1105. https://doi.org/10.3390/polym13071105.

[4] D.F. Williams, Definitions in biomaterials, in: Proc. a Consens. Conf. Eur. Soc. Biomater., Chester, England, 1986. https://www.worldcat.org/it/title/Definitions-in-biomaterials-:-proceedings-of-a-consensus-conference-of-the-European-Society-for-Biomaterials-Chester-England-March-3-5-1986/oclc/16351683.

[5] J. Conde, Q. Chen, Y. Tang, E. Lu, J. Liu, Y. Lv, B. Wang, G. Liu, K. Xie, C. Lan, Z. Qin, L. Wang, Metal Material, Properties and Design Methods of Porous Biomedical Scaffolds for Additive Manufacturing: A Review, (2021). https://doi.org/10.3389/fbioe.2021.641130.

[6] K.H. Vining, D.J. Mooney, Mechanical forces direct stem cell behaviour in development and regeneration, Nat. Rev. Mol. Cell Biol. 18 (2017) 728–742. https://doi.org/10.1038/nrm.2017.108.

[7] K. Dey, E. Roca, G. Ramorino, L. Sartore, Progress in the mechanical

modulation of cell functions in tissue engineering, Biomater. Sci. 8 (2020) 7033–7081. https://doi.org/10.1039/d0bm01255f.

[8] M. Mabrouk, H.H. Beherei, D.B. Das, Recent progress in the fabrication techniques of 3D scaffolds for tissue engineering, Mater. Sci. Eng. C. 110 (2020) 110716. https://doi.org/10.1016/j.msec.2020.110716.

[9] M. Wasyłeczko, W. Sikorska, A. Chwojnowski, Review of synthetic and hybrid scaffolds in cartilage tissue engineering, Membranes (Basel). 10 (2020) 348. https://doi.org/10.3390/membranes10110348.

[10] A.P. Kishan, E.M. Cosgriff-Hernandez, Recent advancements in electrospinning design for tissue engineering applications: A review, J Biomed Mater Res Part A. 105 (2017) 2892–2905. https://doi.org/10.1002/jbm.a.36124.

[11] D. Puppi, F. Chiellini, Biodegradable Polymers for Biomedical Additive Manufacturing, Appl. Mater. Today. 20 (2020). https://doi.org/10.1016/j.apmt.2020.100700.

[12] L. Zhang, G. Yang, B.N. Johnson, X. Jia, Three-dimensional (3D) printed scaffold and material selection for bone repair, Acta Biomater. 84 (2019) 16–33. https://doi.org/10.1016/j.actbio.2018.11.039.

[13] A.P. Moreno Madrid, S.M. Vrech, M.A. Sanchez, A.P. Rodriguez, Advances in additive manufacturing for bone tissue engineering scaffolds, Mater. Sci. Eng. C. 100 (2019) 631–644. https://doi.org/10.1016/j.msec.2019.03.037.

[14] T.D. Brown, P.D. Dalton, D.W. Hutmacher, Direct Writing By Way of Melt Electrospinning, Adv. Mater. 23 (2011) 5651–5657. https://doi.org/10.1002/adma.201103482.

[15] T.D. Brown, A. Slotosch, L. Thibaudeau, A. Taubenberger, D. Loessner, C. Vaquette, P.D. Dalton, D.W. Hutmacher, Design and Fabrication of Tubular Scaffolds via Direct Writing in a Melt Electrospinning Mode, Biointerphases. 7 (2012) 13. https://doi.org/10.1007/s13758-011-0013-7.

[16] X.-X. He, J. Zheng, G.-F. Yu, M.-H. You, M. Yu, X. Ning, Y.-Z. Long, Near-Field Electrospinning: Progress and Applications, J. Phys. Chem. C. 121 (2017) 8663–8678. https://doi.org/10.1021/acs.jpcc.6b12783.

[17] P.D. Dalton, Melt electrowriting with additive manufacturing principles, Curr. Opin. Biomed. Eng. 2 (2017) 49–57. https://doi.org/10.1016/j.cobme.2017.05.007.

[18] J.C. Kade, P.D. Dalton, Polymers for Melt Electrowriting, Adv. Healthc. Mater. 10 (2021) 2001232. https://doi.org/10.1002/adhm.202001232.

[19] G. Hochleitner, E. Fürsattel, R. Giesa, J. Groll, H.-W. Schmidt, P.D. Dalton, Melt Electrowriting of Thermoplastic Elastomers, Macromol. Rapid Commun. 39 (2018) 1800055. https://doi.org/10.1002/marc.201800055.

[20] Z. Shao, H. Chen, Q. Wang, G. Kang, J. Jiang, X. Wang, W. Li, Y. Liu, G. Zheng, Melt Electrowriting Ordered TPU Microfibrous Mesh for On-Demand Colorimetric Wearable Sweat Detection, IEEE Sens. J. 22 (2022) 18560–18566. https://doi.org/10.1109/JSEN.2022.3199406.

[21] A.S. Cavalcanti, R.S. Diaz, E.C.L. Bolle, N. Bartnikowski, J.F. Fraser, D. McGiffin, F.M. Savi, A. Shafiee, T.R. Dargaville, S.D. Gregory, In vivo evaluation of skin integration with ventricular assist device drivelines, J. Hear. Lung Transplant. 41 (2022) 1032–1043. https://doi.org/10.1016/J.HEALUN.2022.03.014.

[22] L. Edgar, K. McNamara, T. Wong, R. Tamburrini, R. Katari, G. Orlando, Heterogeneity of scaffold biomaterials in tissue engineering, Materials (Basel). 9 (2016). https://doi.org/10.3390/ma9050332.

[23] K. Dey, S. Agnelli, M. Serzanti, P. Ginestra, G. Scarì, P. Dell'Era, L. Sartore, Preparation and properties of high performance gelatin-based hydrogels with chitosan or hydroxyethyl cellulose for tissue engineering applications, Int. J. Polym. Mater. Polym. Biomater. 68 (2019) 183–192.

https://doi.org/10.1080/00914037.2018.1429439.

[24] D.A. Gyles, L.D. Castro, J.O.C. Silva, R.M. Ribeiro-Costa, A review of the designs and prominent biomedical advances of natural and synthetic hydrogel formulations, Eur. Polym. J. 88 (2017) 373–392. https://doi.org/10.1016/j.eurpolymj.2017.01.027.

[25] S.C. Neves, L. Moroni, C.C. Barrias, P.L. Granja, Leveling Up Hydrogels: Hybrid Systems in Tissue Engineering, Trends Biotechnol. 38 (2020) 292–315. https://doi.org/10.1016/j.tibtech.2019.09.004.

[26] F. Re, E. Borsani, R. Rezzani, L. Sartore, D. Russo, Bone Regeneration Using Mesenchymal Stromal Cells and Biocompatible Scaffolds: A Concise Review of the Current Clinical Trials, Gels. 9 (2023) 389. https://doi.org/10.3390/gels9050389.

[27] M. Dominici, K. Le Blanc, I. Mueller, I. Slaper-Cortenbach, F.C. Marini, D.S. Krause, R.J. Deans, A. Keating, D.J. Prockop, E.M. Horwitz, Minimal criteria for defining multipotent mesenchymal stromal cells. The International Society for Cellular Therapy position statement, Cytotherapy. 8 (2006) 315–317. https://doi.org/10.1080/14653240600855905.

[28] D. Sipp, P.G. Robey, L. Turner, Clear up this stem-cell mess, Nature. 561 (2018) 455–457. https://doi.org/10.1038/D41586-018-06756-9.

[29] H.F. Pereira, I.F. Cengiz, F.S. Silva, R.L. Reis, J.M. Oliveira, Scaffolds and coatings for bone regeneration, J. Mater. Sci. Mater. Med. 31 (2020) 27. https://doi.org/10.1007/s10856-020-06364-y.

[30] B. Lei, B. Guo, K.J. Rambhia, P.X. Ma, Hybrid polymer biomaterials for bone tissue regeneration, Front. Med. 13 (2019) 189–201. https://doi.org/10.1007/s11684-018-0664-6.

[31] J.H. Lee, H.W. Kim, Emerging properties of hydrogels in tissue engineering, J. Tissue Eng. 9 (2018). https://doi.org/10.1177/2041731418768285.

[32] C.D. Spicer, Hydrogel scaffolds for tissue engineering: the importance of polymer choice, Polym. Chem. 11 (2020) 184–219. https://doi.org/10.1039/C9PY01021A.

[33] F. Taraballi, M. Sushnitha, C. Tsao, G. Bauza, C. Liverani, A. Shi, E. Tasciotti, Biomimetic Tissue Engineering: Tuning the Immune and Inflammatory Response to Implantable Biomaterials, Adv. Healthc. Mater. 7 (2018). https://doi.org/10.1002/adhm.201800490.

[34] J.Y. Park, S.H. Park, M.G. Kim, S.H. Park, T.H. Yoo, M.S. Kim, Biomimetic Scaffolds for Bone Tissue Engineering, Adv. Exp. Med. Biol. 1064 (2018) 109–121. https://doi.org/10.1007/978-981-13-0445-3_7.

[35] H. Bakht Khosh Hagh, F. Farshi Azhar, Reinforcing materials for polymeric tissue engineering scaffolds: A review, J. Biomed. Mater. Res. - Part B Appl. Biomater. 107 (2019) 1560–1575. https://doi.org/10.1002/jbm.b.34248.

[36] T. Hoffman, A. Khademhosseini, R. Langer, Chasing the Paradigm: Clinical Translation of 25 Years of Tissue Engineering, Tissue Eng. - Part A. 25 (2019) 679–687. https://doi.org/10.1089/ten.tea.2019.0032.

[37] P. Gunatillake, R. Mayadunne, R. Adhikari, Recent developments in biodegradable synthetic polymers, Biotechnol. Annu. Rev. 12 (2006) 301–347. https://doi.org/10.1016/S1387-2656(06)12009-8.

[38] R.N. Darie-Niţă, M. Râpă, S. Frąckowiak, Special Features of Polyester-Based Materials for Medical Applications, Polymers (Basel). 14 (2022) 951. https://doi.org/10.3390/polym14050951.

[39] L. Sartore, N. Inverardi, S. Pandini, F. Bignotti, F. Chiellini, PLA/PCL-based foams as scaffolds for tissue engineering applications, Mater. Today Proc. 7 (2019) 410–417. https://doi.org/10.1016/j.matpr.2018.11.103.

[40] L. Sartore, S. Pandini, K. Dey, F. Bignotti, F. Chiellini, A versatile cell-friendly approach to produce PLA-based 3D micro-macro-porous blends

for tissue engineering scaffolds, Materialia. 9 (2020) 100615. https://doi.org/10.1016/j.mtla.2020.100615.

[41] L. Sartore, S. Pandini, F. Baldi, F. Bignotti, L. Di Landro, Biocomposites based on poly(lactic acid) and superabsorbent sodium polyacrylate, J. Appl. Polym. Sci. 134 (2017). https://doi.org/10.1002/app.45655.

[42] N.R. Richbourg, N.A. Peppas, V.I. Sikavitsas, Tuning the biomimetic behavior of scaffolds for regenerative medicine through surface modifications, J. Tissue Eng. Regen. Med. 13 (2019) 1275–1293. https://doi.org/10.1002/term.2859.

[43] Z.J. Chen, Y. Zhang, L. Zheng, H. Zhang, H.H. Shi, X.C. Zhang, B. Liu, Mineralized self-assembled silk fibroin/cellulose interpenetrating network aerogel for bone tissue engineering, Mater. Sci. Eng. C. 134 (2021) 112549. https://doi.org/10.1016/j.msec.2021.112549.

[44] M. Vishnu Priya, A. Sivshanmugam, A.R. Boccaccini, O.M. Goudouri, W. Sun, N. Hwang, S. Deepthi, S. V Nair, R. Jayakumar, Injectable osteogenic and angiogenic nanocomposite hydrogels for irregular bone defects, Biomed. Mater. 11 (2016) 035017. https://doi.org/10.1088/1748-6041/11/3/035017.

[45] T.T. Li, Y. Zhang, H.T. Ren, H.K. Peng, C.W. Lou, J.H. Lin, Two-step strategy for constructing hierarchical pore structured chitosan–hydroxyapatite composite scaffolds for bone tissue engineering, Carbohydr. Polym. 260 (2021). https://doi.org/10.1016/J.CARBPOL.2021.117765.

[46] S.E. El-Habashy, A.H. El-Kamel, M.M. Essawy, E.-Z.A. Abdelfattah, H.M. Eltaher, Engineering 3D-printed core–shell hydrogel scaffolds reinforced with hybrid hydroxyapatite/polycaprolactone nanoparticles for in vivo bone regeneration, Biomater. Sci. 9 (2021) 4019–4039. https://doi.org/10.1039/D1BM00062D.

[47] V. V. Filipović, M.M. Babić Radić, J.S. Vuković, M. Vukomanović, M.

Rubert, S. Hofmann, R. Müller, S.L. Tomić, Biodegradable Hydrogel Scaffolds Based on 2-Hydroxyethyl Methacrylate, Gelatin, Poly(β-amino esters), and Hydroxyapatite, Polym. 2022, Vol. 14, Page 18. 14 (2021) 18. https://doi.org/10.3390/POLYM14010018.

[48] A.M. Haaparanta, E. Järvinen, I.F. Cengiz, V. Ellä, H.T. Kokkonen, I. Kiviranta, M. Kellomäki, Preparation and characterization of collagen/PLA, chitosan/PLA, and collagen/chitosan/PLA hybrid scaffolds for cartilage tissue engineering, J. Mater. Sci. Mater. Med. 25 (2014) 1129–1136. https://doi.org/10.1007/s10856-013-5129-5.

[49] D. Enea, S. Cecconi, S. Calcagno, A. Busilacchi, S. Manzotti, C. Kaps, A. Gigante, Single-stage cartilage repair in the knee with microfracture covered with a resorbable polymer-based matrix and autologous bone marrow concentrate, Knee. 20 (2013) 562–569. https://doi.org/10.1016/j.knee.2013.04.003.

[50] M.M. Kareem, T. Hodgkinson, M.S. Sanchez, M.J. Dalby, K.E. Tanner, Hybrid core–shell scaffolds for bone tissue engineering, Biomed. Mater. 14 (2019) 025008. https://doi.org/10.1088/1748-605X/aafbf1.

[51] P. Chen, L. Liu, J. Pan, J. Mei, C. Li, Y. Zheng, Biomimetic composite scaffold of hydroxyapatite/gelatin-chitosan core-shell nanofibers for bone tissue engineering, Mater. Sci. Eng. C. 97 (2019) 325–335. https://doi.org/10.1016/j.msec.2018.12.027.

[52] F. Sharifi, S. Irani, G. Azadegan, M. Pezeshki-Modaress, M. Zandi, M. Saeed, Co-electrospun gelatin-chondroitin sulfate/polycaprolactone nanofibrous scaffolds for cartilage tissue engineering, Bioact. Carbohydrates Diet. Fibre. 22 (2020) 100215. https://doi.org/10.1016/j.bcdf.2020.100215.

[53] B.S. Kim, K.E. Park, M.H. Kim, H.K. You, J. Lee, W.H. Park, Effect of nanofiber content on bone regeneration of silk fibroin/poly(ε-caprolactone) nano/microfibrous composite scaffolds, Int. J. Nanomedicine. 10 (2015)

485–502. https://doi.org/10.2147/ijn.s72730.

[54] C. Paredes, F.J. Martínez-Vázquez, A. Pajares, P. Miranda, Co-continuous calcium phosphate/polycaprolactone composite bone scaffolds fabricated by digital light processing and polymer melt suction, Ceram. Int. 47 (2021) 17726–17735. https://doi.org/10.1016/J.CERAMINT.2021.03.093.

[55] N. Raja, H.S. Yun, A simultaneous 3D printing process for the fabrication of bioceramic and cell-laden hydrogel core/shell scaffolds with potential application in bone tissue regeneration, J. Mater. Chem. B. 4 (2016) 4707–4716. https://doi.org/10.1039/C6TB00849F.

[56] C. Liu, Z. Wang, X. Wei, B. Chen, Y. Luo, 3D printed hydrogel/PCL core/shell fiber scaffolds with NIR-triggered drug release for cancer therapy and wound healing, Acta Biomater. 131 (2021) 314–325. https://doi.org/10.1016/j.actbio.2021.07.011.

[57] C. Wang, W. Huang, Y. Zhou, L. He, Z. He, Z. Chen, X. He, S. Tian, J. Liao, B. Lu, Y. Wei, M. Wang, 3D printing of bone tissue engineering scaffolds, Bioact. Mater. 5 (2020) 82–91. https://doi.org/10.1016/j.bioactmat.2020.01.004.

[58] L. Dong, S.J. Wang, X.R. Zhao, Y.F. Zhu, J.K. Yu, 3D-printed poly (ϵ-caprolactone) scaffold integrated with cell-laden chitosan hydrogels for bone tissue engineering, Sci. Rep. 7 (2017) 4–12. https://doi.org/10.1038/s41598-017-13838-7.

[59] A.C. Daly, G.M. Cunniffe, B.N. Sathy, O. Jeon, E. Alsberg, D.J. Kelly, 3D Bioprinting of Developmentally Inspired Templates for Whole Bone Organ Engineering, Adv. Healthc. Mater. 5 (2016) 2353–2362. https://doi.org/10.1002/adhm.201600182.

[60] C. Erggelet, K. Neumann, M. Endres, K. Haberstroh, M. Sittinger, C. Kaps, Regeneration of ovine articular cartilage defects by cell-free polymer-based implants, Biomaterials. 28 (2007) 5570–5580.

https://doi.org/10.1016/j.biomaterials.2007.09.005.

[61] C. Vasile, D. Pamfil, E. Stoleru, M. Baican, New developments in medical applications of hybrid hydrogels containing natural polymers, Molecules. 25 (2020). https://doi.org/10.3390/molecules25071539.

[62] K. Dey, S. Agnelli, F. Re, D. Russo, G. Lisignoli, C. Manferdini, S. Bernardi, E. Gabusi, L. Sartore, Rational Design and Development of Anisotropic and Mechanically Strong Gelatin-Based Stress Relaxing Hydrogels for Osteogenic/Chondrogenic Differentiation, Macromol. Biosci. 19 (2019). https://doi.org/10.1002/mabi.201900099.

[63] L. Sartore, C. Manferdini, Y. Saleh, K. Dey, E. Gabusi, G. Ramorino, N. Zini, C. Almici, F. Re, D. Russo, E. Mariani, G. Lisignoli, Polysaccharides on gelatin-based hydrogels differently affect chondrogenic differentiation of human mesenchymal stromal cells, Mater. Sci. Eng. C. 126 (2021) 112175. https://doi.org/10.1016/J.MSEC.2021.112175.

[64] F. Re, L. Sartore, E. Borsani, M. Ferroni, C. Baratto, A. Mahajneh, A. Smith, K. Dey, C. Almici, P. Guizzi, S. Bernardi, G. Faglia, F. Magni, D. Russo, Mineralization of 3D osteogenic model based on gelatin-dextran hybrid hydrogel scaffold bioengineered with mesenchymal stromal cells: A multiparametric evaluation, Materials (Basel). 14 (2021). https://doi.org/10.3390/ma14143852.

[65] F. Re, L. Sartore, V. Moulisova, M. Cantini, C. Almici, A. Bianchetti, C. Chinello, K. Dey, S. Agnelli, C. Manferdini, S. Bernardi, N.F. Lopomo, E. Sardini, E. Borsani, L.F. Rodella, F. Savoldi, C. Paganelli, P. Guizzi, G. Lisignoli, F. Magni, M. Salmeron-Sanchez, D. Russo, 3D gelatin-chitosan hybrid hydrogels combined with human platelet lysate highly support human mesenchymal stem cell proliferation and osteogenic differentiation, J. Tissue Eng. 10 (2019). https://doi.org/10.1177/2041731419845852.

[66] S. Bernardi, F. Re, K. Bosio, K. Dey, C. Almici, M. Malagola, P. Guizzi, L.

Sartore, D. Russo, Chitosan-Hydrogel Polymeric Scaffold Acts as an Independent Primary Inducer of Osteogenic Differentiation in Human Mesenchymal Stromal Cells, Materials (Basel). 13 (2020) 3546. https://doi.org/10.3390/ma13163546.

[67] C. Manferdini, E. Gabusi, L. Sartore, K. Dey, S. Agnelli, C. Almici, A. Bianchetti, N. Zini, D. Russo, F. Re, E. Mariani, G. Lisignoli, Chitosan-based scaffold counteracts hypertrophic and fibrotic markers in chondrogenic differentiated mesenchymal stromal cells, J. Tissue Eng. Regen. Med. 13 (2019) 1896–1911. https://doi.org/10.1002/term.2941.

[68] K. Dey, S. Agnelli, L. Sartore, Effects of gamma sterilization on the physicomechanical and thermal properties of gelatin-based novel hydrogels, Polym. Eng. Sci. 59 (2019) 2533–2540. https://doi.org/10.1002/pen.25178.

[69] K. Dey, S. Agnelli, L. Sartore, Dynamic freedom: Substrate stress relaxation stimulates cell responses, Biomater. Sci. 7 (2019) 836–842. https://doi.org/10.1039/c8bm01305e.

[70] L. Sartore, D. Russo, S. Pandini, P. Nicolai, M. Ferrari, R. Gilbert, J. Irish, Integrated core–shell bioactive structure for the regeneration of bone and osteochondral tissues, European Patent PCT/IB2021/056113, 2021.

[71] L. Sartore, C. Pasini, S. Pandini, K. Dey, M. Ferrari, S. Taboni, H.H.L. Chan, J. Townson, S. Viswanathan, S. Mathews, R.W. Gilbert, J.C. Irish, F. Re, P. Nicolai, D. Russo, Hybrid Core-Shell Polymer Scaffold for Bone Tissue Regeneration, Int. J. Mol. Sci. 23 (2022) 4533. https://doi.org/10.3390/ijms23094533.

[72] H. Wang, E. Wang, Y. Huang, X. Li, Hybrid hydrogel based on stereocomplex PDLA/PLLA and gelatin for bone regeneration, J. Appl. Polym. Sci. 137 (2020) 49571. https://doi.org/10.1002/app.49571.

[73] V.P. Ribeiro, S. Pina, J.B. Costa, I.F. Cengiz, L. García-Fernández, M.D.M. Fernández-Gutiérrez, O.C. Paiva, A.L. Oliveira, J. San-Román, J.M.

Oliveira, R.L. Reis, Enzymatically Cross-Linked Silk Fibroin-Based Hierarchical Scaffolds for Osteochondral Regeneration, ACS Appl. Mater. Interfaces. 11 (2019) 3781–3799. https://doi.org/10.1021/acsami.8b21259.

[74] D.R. Pereira, R.F. Canadas, J. Silva-Correia, A. da Silva Morais, M.B. Oliveira, I.R. Dias, J.F. Mano, A.P. Marques, R.L. Reis, J.M. Oliveira, Injectable gellan-gum/hydroxyapatite-based bilayered hydrogel composites for osteochondral tissue regeneration, Appl. Mater. Today. 12 (2018) 309–321. https://doi.org/10.1016/j.apmt.2018.06.005.

[75] J. Li, X. Liu, J.M. Crook, G.G. Wallace, Electrical stimulation-induced osteogenesis of human adipose derived stem cells using a conductive graphene-cellulose scaffold, Mater. Sci. Eng. C. 107 (2020) 110312. https://doi.org/10.1016/j.msec.2019.110312.

[76] M. Kashi, F. Baghbani, F. Moztarzadeh, H. Mobasheri, E. Kowsari, Green synthesis of degradable conductive thermosensitive oligopyrrole/chitosan hydrogel intended for cartilage tissue engineering, Int. J. Biol. Macromol. 107 (2018) 1567–1575. https://doi.org/10.1016/j.ijbiomac.2017.10.015.

[77] R.A. Perez, H.W. Kim, Core-shell designed scaffolds for drug delivery and tissue engineering, Acta Biomater. 21 (2015) 2–19. https://doi.org/10.1016/j.actbio.2015.03.013.

[78] F. Ghasemkhah, M. Latifi, A. Hadjizadeh, M.A. Shokrgozar, Potential core–shell designed scaffolds with a gelatin-based shell in achieving controllable release rates of proteins for tissue engineering approaches, J. Biomed. Mater. Res. - Part A. (2019) 1393–1405. https://doi.org/10.1002/jbm.a.36653.

[79] F.P.W. Melchels, M.A.N. Domingos, T.J. Klein, J. Malda, P.J. Bartolo, D.W. Hutmacher, Additive manufacturing of tissues and organs, Prog. Polym. Sci. 37 (2012) 1079–1104. https://doi.org/10.1016/J.PROGPOLYMSCI.2011.11.007.

[80] B. Derby, Printing and prototyping of tissues and scaffolds, Science (80-.). 338 (2012) 921–926. https://doi.org/10.1126/SCIENCE.1226340/ASSET/E2028590-DA57-4752-A4B9-1795B5DCF86B/ASSETS/GRAPHIC/338_921_F6.JPEG.

[81] I. Matai, G. Kaur, A. Seyedsalehi, A. McClinton, C.T. Laurencin, Progress in 3D bioprinting technology for tissue/organ regenerative engineering, Biomaterials. 226 (2020) 119536. https://doi.org/10.1016/j.biomaterials.2019.119536.

[82] M. Mirkhalaf, Y. Men, R. Wang, Y. No, H. Zreiqat, Personalized 3D printed bone scaffolds: A review, Acta Biomater. 156 (2023) 110–124. https://doi.org/10.1016/J.ACTBIO.2022.04.014.

[83] L. Moroni, J.R. De Wijn, C.A. Van Blitterswijk, 3D fiber-deposited scaffolds for tissue engineering: Influence of pores geometry and architecture on dynamic mechanical properties, Biomaterials. 27 (2006) 974–985. https://doi.org/10.1016/j.biomaterials.2005.07.023.

[84] S.M. Bittner, B.T. Smith, L. Diaz-Gomez, C.D. Hudgins, A.J. Melchiorri, D.W. Scott, J.P. Fisher, A.G. Mikos, Fabrication and mechanical characterization of 3D printed vertical uniform and gradient scaffolds for bone and osteochondral tissue engineering, Acta Biomater. 90 (2019) 37–48. https://doi.org/10.1016/J.ACTBIO.2019.03.041.

[85] Z.B. Velioglu, D. Pulat, B. Demirbakan, B. Ozcan, E. Bayrak, C. Erisken, 3D-printed poly(lactic acid) scaffolds for trabecular bone repair and regeneration: scaffold and native bone characterization, Connect. Tissue Res. 60 (2019) 274–282. https://doi.org/10.1080/03008207.2018.1499732.

[86] E. Nyberg, A. O'Sullivan, W. Grayson, scafSLICR: A MATLAB-based slicing algorithm to enable 3D-printing of tissue engineering scaffolds with heterogeneous porous microarchitecture, PLoS One. 14 (2019) e0225007. https://doi.org/10.1371/JOURNAL.PONE.0225007.

[87] K.C.R. Kolan, Y.W. Huang, J.A. Semon, M.C. Leu, 3D-printed Biomimetic Bioactive Glass Scaffolds for Bone Regeneration in Rat Calvarial Defects, Int. J. Bioprinting. 6 (2020) 1–17. https://doi.org/10.18063/IJB.V6I2.274.

[88] P. Egan, X. Wang, H. Greutert, K. Shea, K. Wuertz-Kozak, S. Ferguson, Mechanical and Biological Characterization of 3D Printed Lattices, 3D Print. Addit. Manuf. 6 (2019) 73–81. https://doi.org/10.1089/3DP.2018.0125/ASSET/IMAGES/LARGE/FIGURE7.JPEG.

[89] D.N. Heo, N.J. Castro, S.J. Lee, H. Noh, W. Zhu, L.G. Zhang, Enhanced bone tissue regeneration using a 3D printed microstructure incorporated with a hybrid nano hydrogel, Nanoscale. 9 (2017) 5055–5062. https://doi.org/10.1039/C6NR09652B.

[90] S.L. Marshall, T.D. Jacobsen, E. Emsbo, A. Murali, K. Anton, J.Z. Liu, H.H. Lu, N.O. Chahine, Three-Dimensional-Printed Flexible Scaffolds Have Tunable Biomimetic Mechanical Properties for Intervertebral Disc Tissue Engineering, ACS Biomater. Sci. Eng. 7 (2021) 5836–5849. https://doi.org/10.1021/ACSBIOMATERIALS.1C01326.

[91] C. Pasini, L. Sartore, S. Pandini, G. Ramorino, Hybrid scaffolds with a 3D-printed polymer lattice core and a bioactive hydrogel shell for bone regeneration, Mater. Today Proc. 70 (2022) 230–236. https://doi.org/10.1016/j.matpr.2022.09.026.

[92] L.J. Gibson, M.F. Ashby, Cellular solids: Structure and properties, second edition, Cambridge University Press, 2014. https://doi.org/10.1017/CBO9781139878326.

[93] V.S. Deshpande, M.F. Ashby, N.A. Fleck, Foam topology: bending versus stretching dominated architectures, Acta Mater. 49 (2001) 1035–1040. https://doi.org/10.1016/S1359-6454(00)00379-7.

[94] E. Cuan-Urquizo, F. Shalchy, A. Bhaskar, Compressive stiffness of

staggered woodpile lattices: Mechanics, measurement, and scaling laws, Int. J. Mech. Sci. 187 (2020) 105932. https://doi.org/10.1016/J.IJMECSCI.2020.105932.

[95] G. Rotta, T. Seramak, K. Zasińska, Estimation of Young's Modulus of the Porous Titanium Alloy with the Use of Fem Package, Adv. Mater. Sci. 15 (2015) 29–37. https://doi.org/10.1515/ADMS-2015-0020.

[96] S. Altamimi, D.W. Lee, I. Barsoum, R. Rowshan, I.M. Jasiuk, R.K. Abu Al-Rub, On Stiffness, Strength, Anisotropy, and Buckling of 30 Strut-Based Lattices with Cubic Crystal Structures, Adv. Eng. Mater. 24 (2022) 2101379. https://doi.org/10.1002/ADEM.202101379.

[97] A.M. Abou-Ali, O. Al-Ketan, R. Rowshan, R. Abu Al-Rub, Mechanical Response of 3D Printed Bending-Dominated Ligament-Based Triply Periodic Cellular Polymeric Solids, J. Mater. Eng. Perform. 28 (2019) 2316–2326. https://doi.org/10.1007/S11665-019-03982-8/FIGURES/11.

[98] T. Maconachie, M. Leary, B. Lozanovski, X. Zhang, M. Qian, O. Faruque, M. Brandt, SLM lattice structures: Properties, performance, applications and challenges, Mater. Des. 183 (2019) 108137. https://doi.org/10.1016/J.MATDES.2019.108137.

[99] M.D.B. Barrera, F. Franco-Martínez, A.D. Lantada, Artificial Intelligence Aided Design of Tissue Engineering Scaffolds Employing Virtual Tomography and 3D Convolutional Neural Networks, Mater. 2021, Vol. 14, Page 5278. 14 (2021) 5278. https://doi.org/10.3390/MA14185278.

[100] Y. Lu, T. Gong, Z. Yang, H. Zhu, Y. Liu, C. Wu, Designing anisotropic porous bone scaffolds using a self-learning convolutional neural network model, Front. Bioeng. Biotechnol. 10 (2022) 1784. https://doi.org/10.3389/FBIOE.2022.973275/BIBTEX.

[101] H. Kang, C.Y. Lin, S.J. Hollister, Topology optimization of three dimensional tissue engineering scaffold architectures for prescribed bulk

modulus and diffusivity, Struct. Multidiscip. Optim. 42 (2010) 633–644. https://doi.org/10.1007/S00158-010-0508-8/FIGURES/9.

[102] J. Hu, J.H. Wang, R. Wang, X.B. Yu, Y. Liu, D.A. Baur, Analysis of biomechanical behavior of 3D printed mandibular graft with porous scaffold structure designed by topological optimization, 3D Print. Med. 2019 51. 5 (2019) 1–14. https://doi.org/10.1186/S41205-019-0042-2.

[103] C. Wu, J. Fang, A. Entezari, G. Sun, M. V. Swain, Y. Xu, G.P. Steven, Q. Li, A time-dependent mechanobiology-based topology optimization to enhance bone growth in tissue scaffolds, J. Biomech. 117 (2021) 110233. https://doi.org/10.1016/J.JBIOMECH.2021.110233.

[104] H.M. El-Husseiny, E.A. Mady, L. Hamabe, A. Abugomaa, K. Shimada, T. Yoshida, T. Tanaka, A. Yokoi, M. Elbadawy, R. Tanaka, Smart/stimuli-responsive hydrogels: Cutting-edge platforms for tissue engineering and other biomedical applications, Mater. Today Bio. 13 (2022) 100186. https://doi.org/10.1016/J.MTBIO.2021.100186.

[105] J. Li, Y. Zhang, L. Zhu, K. Chen, X. Li, W. Xu, Smart Nucleic Acid Hydrogels with High Stimuli-Responsiveness in Biomedical Fields, Int. J. Mol. Sci. 2022, Vol. 23, Page 1068. 23 (2022) 1068. https://doi.org/10.3390/IJMS23031068.

[106] J. Xie, P. Yu, Z. Wang, J. Li, Recent Advances of Self-Healing Polymer Materials via Supramolecular Forces for Biomedical Applications, Biomacromolecules. 23 (2022) 641–660. https://doi.org/10.1021/acs.biomac.1c01647.

[107] M.R. Pfau, M.A. Grunlan, Smart scaffolds: shape memory polymers (SMPs) in tissue engineering, J. Mater. Chem. B. 9 (2021) 4287. https://doi.org/10.1039/d1tb00607j.

[108] A. Lendlein, S. Kelch, Shape-memory polymers, Angew. Chemie - Int. Ed. 41 (2002). https://doi.org/10.1002/1521-3773(20020617)41:12<2034::aid-

anie2034>3.0.co;2-m.

[109] L. Du, S. Yang, W. Li, H. Li, S. Feng, R. Zeng, B. Yu, L. Xiao, H.-Y. Nie, M. Tu, Scaffold composed of porous vancomycin-loaded poly(lactide-co-glycolide) microspheres: A controlled-release drug delivery system with shape-memory effect, (2017). https://doi.org/10.1016/j.msec.2017.04.099.

[110] C. Wang, Y. Zhou, M. Wang, In situ delivery of rhBMP-2 in surface porous shape memory scaffolds developed through cryogenic 3D plotting, Mater. Lett. 189 (2017) 140–143. https://doi.org/10.1016/J.MATLET.2016.11.039.

[111] F.S. Senatov, M.Y. Zadorozhnyy, K. V. Niaza, V. V. Medvedev, S.D. Kaloshkin, N.Y. Anisimova, M. V. Kiselevskiy, K.C. Yang, Shape memory effect in 3D-printed scaffolds for self-fitting implants, Eur. Polym. J. 93 (2017) 222–231. https://doi.org/10.1016/J.EURPOLYMJ.2017.06.011.

[112] T. Li, L. Chen, Y. Yuan, R. Shi, The Current Status, Prospects, and Challenges of Shape Memory Polymers Application in Bone Tissue Engineering, Polym. 2023, Vol. 15, Page 556. 15 (2023) 556. https://doi.org/10.3390/POLYM15030556.

[113] M. Zare, P. Davoodi, S. Ramakrishna, Electrospun Shape Memory Polymer Micro-/Nanofibers and Tailoring Their Roles for Biomedical Applications, Nanomaterials. 11 (2021) 933. https://doi.org/10.3390/nano11040933.

[114] L. Wang, F. Zhang, Y. Liu, J. Leng, Shape Memory Polymer Fibers: Materials, Structures, and Applications, Adv. Fiber Mater. 4 (2022) 5–23. https://doi.org/10.1007/s42765-021-00073-z.

[115] A. Liguori, S. Pandini, C. Rinoldi, N. Zaccheroni, F. Pierini, M.L. Focarete, C. Gualandi, Thermoactive Smart Electrospun Nanofibers, Macromol. Rapid Commun. 43 (2022) 2100694. https://doi.org/10.1002/marc.202100694.

[116] V. Salaris, A. Leonés, D. Lopez, J.M. Kenny, L. Peponi, Shape-Memory

Materials via Electrospinning: A Review, Polymers (Basel). 14 (2022) 995. https://doi.org/10.3390/polym14050995.

[117] F. Momeni, S. M.Mehdi Hassani.N, X. Liu, J. Ni, A review of 4D printing, Mater. Des. 122 (2017) 42–79. https://doi.org/10.1016/j.matdes.2017.02.068.

[118] G. Constante, I. Apsite, H. Alkhamis, M. Dulle, M. Schwarzer, A. Caspari, A. Synytska, S. Salehi, L. Ionov, 4D Biofabrication Using a Combination of 3D Printing and Melt-Electrowriting of Shape-Morphing Polymers, ACS Appl. Mater. Interfaces. 13 (2021) 12767–12776. https://doi.org/10.1021/acsami.0c18608.

[119] J. Uribe-Gomez, A. Posada-Murcia, A. Shukla, M. Ergin, G. Constante, I. Apsite, D. Martin, M. Schwarzer, A. Caspari, A. Synytska, S. Salehi, L. Ionov, Shape-Morphing Fibrous Hydrogel/Elastomer Bilayers Fabricated by a Combination of 3D Printing and Melt Electrowriting for Muscle Tissue Regeneration, ACS Appl. Bio Mater. 4 (2021) 1720–1730. https://doi.org/10.1021/acsabm.0c01495.

[120] H.C. Koch, D. Schmelzeisen, T. Gries, S. Pandini, 4D Textiles Made by Additive Manufacturing on Pre-Stressed Textiles-An Overview, (2021). https://doi.org/10.3390/act10020031.

[121] S.J.P. Callens, N. Tümer, A.A. Zadpoor, Hyperbolic origami-inspired folding of triply periodic minimal surface structures, Appl. Mater. Today. 15 (2019) 453–461. https://doi.org/10.1016/j.apmt.2019.03.007.

[122] C. Zhang, D. Cai, P. Liao, J.W. Su, H. Deng, B. Vardhanabhuti, B.D. Ulery, S.Y. Chen, J. Lin, 4D Printing of shape-memory polymeric scaffolds for adaptive biomedical implantation, Acta Biomater. 122 (2021) 101–110. https://doi.org/10.1016/J.ACTBIO.2020.12.042.

[123] M. Zare, M.P. Prabhakaran, N. Parvin, S. Ramakrishna, Thermally-induced two-way shape memory polymers: Mechanisms, structures, and

applications, Chem. Eng. J. 374 (2019) 706–720. https://doi.org/10.1016/j.cej.2019.05.167.

[124] M. Saatchi, M. Behl, U. Nöchel, A. Lendlein, Copolymer networks from oligo (ε -caprolactone) and n -butyl acrylate enable a reversible bidirectional shape-memory effect at human body temperature, Macromol. Rapid Commun. 36 (2015). https://doi.org/10.1002/marc.201400729.

[125] T. Gong, K. Zhao, W. Wang, H. Chen, L. Wang, S. Zhou, Thermally activated reversible shape switch of polymer particles, J. Mater. Chem. B. 2 (2014) 6855–6866. https://doi.org/10.1039/C4TB01155D.

[126] K.A. Davis, K.A. Burke, P.T. Mather, J.H. Henderson, Dynamic cell behavior on shape memory polymer substrates, Biomaterials. 32 (2011). https://doi.org/10.1016/j.biomaterials.2010.12.006.

[127] K.K. Westbrook, P.T. Mather, V. Parakh, M.L. Dunn, Q. Ge, B.M. Lee, H.J. Qi, Two-way reversible shape memory effects in a free-standing polymer composite, Smart Mater. Struct. 20 (2011) 065010. https://doi.org/10.1088/0964-1726/20/6/065010.

[128] S. Chen, J. Hu, H. Zhuo, Properties and mechanism of two-way shape memory polyurethane composites, Compos. Sci. Technol. 70 (2010) 1437–1443. https://doi.org/10.1016/j.compscitech.2010.01.017.

[129] T.-H. Kang, J.-M. Lee, W.-R. Yu, J.H. Youk, H.W. Ryu, Two-way actuation behavior of shape memory polymer/elastomer core/shell composites, Smart Mater. Struct. 21 (2012) 035028. https://doi.org/10.1088/0964-1726/21/3/035028.

[130] Q. He, Z. Wang, Y. Wang, Z. Wang, C. Li, R. Annapooranan, J. Zeng, R. Chen, S. Cai, Electrospun liquid crystal elastomer microfiber actuator, Sci. Robot. 6 (2021). https://doi.org/10.1126/scirobotics.abi9704.

[131] J.-S. Ahn, W.-R. Yu, J.H. Youk, H.Y. Ryu, In situ temperature tunable pores of shape memory polyurethane membranes, Smart Mater. Struct. 20

(2011) 105024. https://doi.org/10.1088/0964-1726/20/10/105024.

[132] S. Pandini, S. Agnelli, A. Merlettini, F. Chiellini, C. Gualandi, K. Paderni, M.L. Focarete, M. Messori, M. Toselli, Mutifunctional Electrospun Nonwoven Mats with Two-Way Shape Memory Behavior Prepared from Sol–Gel Crosslinked Poly(ε-Caprolactone), Macromol. Mater. Eng. 302 (2017). https://doi.org/10.1002/mame.201600519.

[133] Raise3D Technologies Inc., Raise3D Premium PLA Technical Data Sheet, (2022). https://s1.raise3d.com/2020/12/PLA-Data-Sheet.zip (accessed July 20, 2023).

[134] FILOALFA®, BioFlex Technical Data Sheet, (2020). https://www.filoalfa3d.com/img/cms/MSDS & TDS/TDS BIOFLEX.pdf.

[135] FILOALFA®, BioFlex Compatibility Tests, (n.d.). https://www.filoalfa3d.com/it/flexible/296-266-bioflex-8050327032385.html.

[136] M.F. Ashby, Cellular Solids – Scaling of Properties, in: M. Scheffler, P. Colombo (Eds.), Cell. Ceram. Struct. Manuf. Prop. Appl., Wiley-VCH Verlag GmbH & Co. KGaA, Weinheim, 2005: pp. 1–17. https://doi.org/10.1002/3527606696.ch1a.

[137] K.A. Verner, M. Lehner, L.P. Lamas, R.P. Main, Experimental tests of planar strain theory for predicting bone cross-sectional longitudinal and shear strains, J. Exp. Biol. 219 (2016) 3082–3090. https://doi.org/10.1242/JEB.134536/262220/AM/EXPERIMENTAL-TESTS-OF-PLANAR-STRAIN-THEORY-FOR.

[138] C. Pasini, S. Pandini, G. Ramorino, L. Sartore, Tailoring the properties of composite scaffolds with a 3D-Printed lattice core and a bioactive hydrogel shell for tissue engineering, J. Mech. Behav. Biomed. Mater. 150 (2024) 106305. https://doi.org/10.1016/j.jmbbm.2023.106305.

[139] A. Haryńska, I. Carayon, P. Kosmela, K. Szeliski, M. Łapiński, M. Pokrywczyńska, J. Kucińska-Lipka, H. Janik, A comprehensive evaluation of flexible FDM/FFF 3D printing filament as a potential material in medical application, Eur. Polym. J. 138 (2020) 109958. https://doi.org/10.1016/J.EURPOLYMJ.2020.109958.

[140] D. da Silva, M. Kaduri, M. Poley, O. Adir, N. Krinsky, J. Shainsky-Roitman, A. Schroeder, Biocompatibility, biodegradation and excretion of polylactic acid (PLA) in medical implants and theranostic systems, Chem. Eng. J. 340 (2018) 9–14. https://doi.org/10.1016/J.CEJ.2018.01.010.

[141] P. Gnatowski, K. Gwizdała, A. Kurdyn, A. Skorek, E. Augustin, J. Kucińska-Lipka, Investigation on Filaments for 3D Printing of Nasal Septum Cartilage Implant, Materials (Basel). 16 (2023). https://doi.org/10.3390/MA16093534.

[142] E.W. Fischer, H.J. Sterzel, G. Wegner, Investigation of the structure of solution grown crystals of lactide copolymers by means of chemical reactions, Z. Polym. 251 (1973) 980–990.

[143] Y. Ikada, H. Tsuji, Biodegradable polyesters for medical and ecological applications, Macromol. Rapid Commun. 21 (2000) 117–132. https://doi.org/10.1002/(SICI)1521-3927(20000201)21:3<117::AID-MARC117>3.0.CO;2-X.

[144] L. Fambri, C. Migliaresi, Crystallization and Thermal Properties, in: Poly(Lactic Acid) Synth. Struct. Prop. Process. Appl. End Life, John Wiley & Sons, Ltd, 2022: pp. 135–151. https://doi.org/10.1002/9781119767480.CH8.

[145] S. Tonello, A. Bianchetti, S. Braga, C. Almici, M. Marini, G. Piovani, M. Guindani, K. Dey, L. Sartore, F. Re, D. Russo, E. Cantù, N.F. Lopomo, M. Serpelloni, E. Sardini, Impedance-based monitoring of mesenchymal stromal cell three-dimensional proliferation using aerosol jet printed

sensors: A tissue engineering application, Materials (Basel). 13 (2020). https://doi.org/10.3390/ma13102231.

[146] Poly-Med Inc., Lactoprene 100M Technical Data Sheet, (2022). https://poly-med.com/wp-content/uploads/2022/08/Lactoprene®-100M-3DP-Filament.pdf.

[147] W.A. Weijs, P. Brugman, E.M. Klok, The growth of the skull and jaw muscles and its functional consequences in the New Zealand rabbit (Oryctolagus cuniculus), J. Morphol. 194 (1987) 143–161. https://doi.org/10.1002/JMOR.1051940204.

[148] G.E.J. Langenbach, W.A. Weijs, J.H. Koolstra, Biomechanical changes in the rabbit masticatory system during postnatal development, Anat. Rec. 230 (1991) 406–416. https://doi.org/10.1002/AR.1092300313.

[149] T. Bulut, E. Durmuş, A. Mihmanl, D. Dolanmaz, A. Kalayc, H. Salam, Distracted mandible does not reach the same strength as normal mandible in rabbits, Oral Surg. Oral Med. Oral Pathol. Oral Radiol. 114 (2012). https://doi.org/10.1016/J.OOOO.2011.09.024.

[150] O. Atali, A. Varol, S. Basa, C. Ergun, S. Hartomacioğlu, Comparison and validation of finite element analysis with a servo-hydraulic testing unit for a biodegradable fixation system in a rabbit model, Int. J. Oral Maxillofac. Surg. 43 (2014) 32–39. https://doi.org/10.1016/J.IJOM.2013.06.007.

[151] M.J. Ravosa, J. Ning, D.B. Costley, A.N. Daniel, S.R. Stock, M.S. Stack, Masticatory biomechanics and masseter fiber-type plasticity, J. Musculoskelet. Neuronal Interact. 10 (2010) 46–55.

[152] S. Pérez Davila, L. González Rodríguez, S. Chiussi, J. Serra, P. González, How to Sterilize Polylactic Acid Based Medical Devices?, Polym. 2021, Vol. 13, Page 2115. 13 (2021) 2115. https://doi.org/10.3390/POLYM13132115.

[153] W. Voigt, Ueber die Beziehung zwischen den beiden Elasticitätsconstanten isotroper Körper, Ann. Phys. 274 (1889) 573–587.

https://doi.org/10.1002/ANDP.18892741206.

[154] K. Pasupa, W. Sunhem, A comparison between shallow and deep architecture classifiers on small dataset, in: Proc. 2016 8th Int. Conf. Inf. Technol. Electr. Eng. Empower. Technol. Better Futur. ICITEE 2016, 2017. https://doi.org/10.1109/ICITEED.2016.7863293.

[155] R.T.L. Ferreira, I.C. Amatte, T.A. Dutra, D. Bürger, Experimental characterization and micrography of 3D printed PLA and PLA reinforced with short carbon fibers, Compos. Part B Eng. 124 (2017) 88–100. https://doi.org/10.1016/J.COMPOSITESB.2017.05.013.

[156] D. Schönfeld, D. Chalissery, F. Wenz, M. Specht, C. Eberl, T. Pretsch, Actuating Shape Memory Polymer for Thermoresponsive Soft Robotic Gripper and Programmable Materials, Mol. 2021, Vol. 26, Page 522. 26 (2021) 522. https://doi.org/10.3390/MOLECULES26030522.

[157] T. Debuissy, E. Pollet, L. Avérous, Synthesis of potentially biobased copolyesters based on adipic acid and butanediols: Kinetic study between 1,4- and 2,3-butanediol and their influence on crystallization and thermal properties, Polymer (Guildf). 99 (2016) 204–213. https://doi.org/10.1016/J.POLYMER.2016.07.022.

[158] G. Constante, I. Apsite, P. Auerbach, S. Aland, D. Schönfeld, T. Pretsch, P. Milkin, L. Ionov, Smart Mechanically Tunable Surfaces with Shape Memory Behavior and Wetting-Programmable Topography, ACS Appl. Mater. Interfaces. 14 (2022) 20208–20219. https://doi.org/10.1021/acsami.2c01078.

[159] M. Bothe, T. Pretsch, Two-Way Shape Changes of a Shape-Memory Poly(ester urethane), Macromol. Chem. Phys. 213 (2012) 2378–2385. https://doi.org/10.1002/macp.201200096.

[160] J. Uribe-Gomez, D. Schönfeld, A. Posada-Murcia, M. Roland, A. Caspari, A. Synytska, S. Salehi, T. Pretsch, L. Ionov, Fibrous Scaffolds for Muscle

Tissue Engineering Based on Touch-Spun Poly(Ester-Urethane) Elastomer, Macromol. Biosci. 22 (2022) 2100427. https://doi.org/10.1002/mabi.202100427.

[161] A. Georgopoulou, B. Vanderborght, F. Clemens, Fabrication of a Soft Robotic Gripper With Integrated Strain Sensing Elements Using Multi-Material Additive Manufacturing, Front. Robot. AI. 8 (2021) 615991. https://doi.org/10.3389/FROBT.2021.615991/BIBTEX.

[162] G. Hochleitner, A. Youssef, A. Hrynevich, J.N. Haigh, T. Jungst, J. Groll, P.D. Dalton, Fibre pulsing during melt electrospinning writing, BioNanoMaterials. 17 (2016) 159–171. https://doi.org/10.1515/bnm-2015-0022.

[163] C. Pasini, S. Pandini, F. Re, M. Ferroni, E. Borsani, D. Russo, L. Sartore, New Poly(lactic acid)–Hydrogel Core–Shell Scaffolds Highly Support MSCs' Viability, Proliferation and Osteogenic Differentiation, Polym. 2023, Vol. 15, Page 4631. 15 (2023) 4631. https://doi.org/10.3390/POLYM15244631.


PROF. STEFANO
PROF. SARTORE
MAMMA
PAPÀ
PROF. MASTI
MASTI LAB
PROF. RAMORINO & ITL TEAM
PROF. IONOV
IONOV'S LAB
PROF. BALDI
PROF. NICOLAI
PROF. PRETSCH
PROF. RUSSO
PROF. CORNACCHIA
PROF. BORSANI
PROF. FERRONI
PROF. IRISH & GILBERTI
GILBERTI
MARZIA
JACOPO
CLARISSA
SILVIA
GIULIA
MICHELE
IRENE
ZHANDER
SARA
ILIA
GISSELA
FEDERICA
ALESSANDRA
ANNA B.
ANNA G.
STEFANO T.
GLORIA & ISA
FA & FEO
ASSE
STE